University of Alberta

Numerical Analysis of Static Liquefaction

by

Abbas Soroush

A thesis submitted to the Faculty of Graduate Studies and Research in partial fulfillment of the requirements for the degree of Doctor of Philosophy

in

Geotechnical Engineering

Department of Civil and Environmental Engineering

Edmonton, Alberta

Fall 1996

National Library
of Canada

Acquisitions and
Bibliographic Services Branch

395 Wellington Street
Ottawa, Ontario
K1A 0N4

Bibliothèque nationale
du Canada

Direction des acquisitions et
des services bibliographiques

395, rue Wellington
Ottawa (Ontario)
K1A 0N4

Your file Votre référence

Our file Notre référence

The author has granted an irrevocable non-exclusive licence allowing the National Library of Canada to reproduce, loan, distribute or sell copies of his/her thesis by any means and in any form or format, making this thesis available to interested persons.

L'auteur a accordé une licence irrévocable et non exclusive permettant à la Bibliothèque nationale du Canada de reproduire, prêter, distribuer ou vendre des copies de sa thèse de quelque manière et sous quelque forme que ce soit pour mettre des exemplaires de cette thèse à la disposition des personnes intéressées.

The author retains ownership of the copyright in his/her thesis. Neither the thesis nor substantial extracts from it may be printed or otherwise reproduced without his/her permission.

L'auteur conserve la propriété du droit d'auteur qui protège sa thèse. Ni la thèse ni des extraits substantiels de celle-ci ne doivent être imprimés ou autrement reproduits sans son autorisation.

ISBN 0-612-18110-3

Canada

University of Alberta

Library Release Form

Name of Author: Abbas Soroush

Title of Thesis: Numerical Analysis of Static Liquefaction

Degree: Doctor of Philosophy

Year this Degree Granted: 1996

Permission is hereby granted to the University of Alberta Library to reproduce single copies of this thesis and to lend or sell such copies for private, scholarly, scientific research purposes only.

The author reserves all other publication and other rights in association with the copyright in the thesis, and except as herein before provided, neither the thesis nor the any substantial portion thereof may be printed or otherwise reproduced in any material form whatever without the author's prior written permission.

A. SOROUSH

236 RH Michener Park, Edmonton,
Alberta, T6H 4M5

Dated: Aug. 16, 1996

University of Alberta

Faculty of Graduate Studies and Research

The undersigned certify that they have read, and recommend to the Faculty of Graduate Studies and Research for acceptance, a thesis entitled Numerical Analysis of Static Liquefaction submitted by Abbas Soroush in partial fulfillment of the requirements for the degree of Doctor of Philosophy in Geotechnical Engineering.

Dr. N.R. Morgenstern
(Supervisor)

Dr. P.K. Robertson

Dr. D. Chan

Dr. N. Rajaratnam

Dr. J.K. Szymanski

Dr. V.K. Garga
(External Examiner)

To My Wife, Our Two Sons and

To My Father and Late Mother

ABSTRACT

Liquefaction-induced deformation of saturated granular soils is a major source of damage to soil structures, buried lifeline facilities, foundations, canals and roads. Liquefaction can occur in saturated loose to medium dense sands when subjected to rapid cyclic or monotonic loading. Finite element techniques using the concepts of steady state strength and collapse surface are employed here to perform deformation analyses of liquefaction.

Post-earthquake deformation analysis of the Upper San Fernando Dam, San Fernando Valley, California, which suffered large deformations as a result of the 1971 San Fernando earthquake, is carried out. Deformations comparable with the deformations observed shortly after the earthquake are obtained.

A literature review on earthquake-induced lateral spreading of gently sloping granular deposits is performed. Based on the information provided from the literature, it is suggested that large deformations in lateral spreading are triggered by gravity. The notion is reinforced by the observation of delayed response. According to this phenomenon, response of saturated soil structures to earthquakes continue long after the earthquake. A simplified numerical model, based on the method of post-earthquake deformation analysis, is suggested for analysis of lateral spreads.

The problem of static liquefaction is studied by numerical modeling and analyses of three centrifuge model tests and a full-scale field event. The liquefiable material in the centrifuge tests and the field event was Syncrude sand from Syncrude, Canada. The analyses indicated that the finite element model is capable of capturing the liquefaction-induced failure mechanics and pore pressure response of the sand.

ACKNOWLEDGMENTS

The author wishes to express his deepest appreciation to his Supervisor, Professor N.R. Morgenstern, for his guidance and encouragement. His ideas, consultations and supports were invaluable.

The author would also like to express his appreciation to Dr. D.H. Chan for his valuable consultation and guidance on the numerical analyses of the CANLEX Project. Sincere appreciation is expressed to Dr. P.K. Robertson for his time and suggestions during the analyses. Dr. W. H. Gu's help in the early stages of the research is also appreciated.

Thanks to all support staff in the Civil and Environmental Engineering Department, especially those in the Geotechnical Office. And thanks to the CANLEX staff for providing the data for the Analysis.

The author also wishes to thank his wife Razyeh Hashemi and sons Ali Soroush and Mohammad Soroush for their understanding, patience and encouragement during the process.

The author acknowledges the financial support provided by the Ministry of Science and Higher Education of Islamic Republic of Iran, and the encouragement and support from Dr. S.R. Hosseini, the Higher Education Advisory at the Embassy of I.R. of Iran in Ottawa, Canada. The financial support provided by the Natural Sciences and Engineering Research Council of Canada (NSERC) is also acknowledged. The computer facilities in the Geotechnical Division of the Department is acknowledged.

Finally, the author extends his deepest gratitude to his father, Shojaedin Soroush and his late mother, Nosrat Amiri for their love and patience.

TABLE OF CONTENTS

Chapter **page**

1 INTRODUCTION....1

1.1 Liquefaction History....1

1.2 Delayed Response in Liquefaction Effects....4

1.3 Deformation Analysis of Liquefaction....9

1.4 Outline of the Thesis....11

2 PRINCIPLES OF LIQUEFACTION....13

2.1 Introduction....13

2.2 Definitions of Liquefaction....14

2.3 Steady State Line....15

2.4 Collapse Surface....21

2.5 Summary of Behavior of Saturated Granular Soils....23

2.5.1 Soils Subjected to Monotonic Loading....23

2.5.2 Soils Subjected to Cyclic Loading....23

2.6 Definitions for Different Types of Liquefaction....24

2.6.1 Gravitational (flow) Liquefaction....24

2.6.2 Seismic Liquefaction....26

2.7 Summary....27

3 NUMERICAL MODELING OF LIQUEFACTION DEFORMATION ANALYSIS....28

3.1 Introduction....28

3.2 Undrained Behavior of Soil....29

3.3 State Boundary Surface for Liquefiable Soils....32

3.4 An Elasto-plastic Model for Liquefiable Soils....39

3.4.1 The Yielding Surface for Strain Softening 40
3.4.2 Hyperbolic Strain Softening Model 42
3.5 Adoption of the Model for Static Liquefaction 48
3.6 Further Development of the Model 50

4 POST-EARTHQUAKE DEFORMATION ANALYSIS OF THE UPPER SAN FERNANDO DAM 54
4.1 Introduction 54
4.2 Literature Review 57
4.2.1 Construction of the Dam 57
4.2.2 Soil Properties of the Dam 58
4.2.3 Effects of the Earthquake on the Dam 63
4.3 Earthquake Analysis 67
4.3.1 Pseudo-static Analysis 67
4.3.2 Dynamic Analysis 67
4.3.3 Comments on the Previous Numerical Works 69
4.3.4 Post-earthquake Deformation Analysis 70
4.4 Post-earthquake Deformation Analysis of the Upper San Fernando Dam 75
4.4.1 Initial Effective Stress Analysis 75
4.4.2 Liquefaction and Post-earthquake Deformation Analysis 85
4.4.2.1 Material Properties 86
4.4.2.2 Results of the Analysis 92
4.4.2.3 Deformation Patterns in the Dam 93
4.4.2.4 Discussion 93
4.5 Summary and Conclusion 94

5 NUMERICAL MODELING AND ANALYSIS OF CANLEX PROJECT EXPERIMENTS 102
5.1 GENERAL INTRODUCTION 102

5.2 LIQUEFACTION ANALYSIS OF THE CENTRIFUGE MODEL TESTING 105
5.2.1 Introduction 105
5.2.2 Centrifuge Model Tests 106
5.2.3 Numerical Modeling and Analysis 116
5.2.3.1 Results of the Analysis 118
5.2.3.2 Discussion on Steady State Strength, S_u 120
5.2.3.3 Limit Equilibrium Analysis versus Liquefaction Analysis 122
5.2.4 Summary 122
5.3 LIQUEFACTION ANALYSIS OF THE FIELD EVENT 144
5.3.1 Introduction 144
5.3.2 Proposed Field Event 146
5.3.2.1 Numerical Modeling and Analysis 147
5.3.2.2 Results 147
5.3.3 Liquefaction Analysis of the Final Designed Field Event 156
5.3.3.1 Pre-Event Analyses 158
5.3.3.2 During-Event Analyses 169
5.3.3.3 Post-Event Comments 177
5.3.3.4 Summary of the Event Analysis 179
6 LATERAL SPREADING DUE TO EARTHQUAKE-INDUCED LIQUEFACTION 185
6.1 Introduction 185
6.2 Case Histories of Lateral Spreading 190
6.3 Effects of Spreading on In-ground Structures 196
6.4 Conclusions from Case Studies 197
6.5 Empirical Prediction of Lateral Spreading 203
6.6 Experimental Studies on Liquefaction-Induced Ground Displacement 207

6.6.1 Shaking Table Test Under 1g Gravitational Stress 207
6.6.2 Centrifuge Modeling of Lateral Spreading 209
6.6.3 Laboratory Tests on Post-Liquefaction Behavior of Sand 210
6.7 Analytical Modeling of Liquefaction-Induced Ground Displacement 213
6.7.1 Behavior As A Fluid 213
6.7.2 Sliding Soil Blocks Model 214
6.7.3 Behavior As A Solid 216
6.8 Discussion 219
6.8.1 Comparison between Behaviour of Liquefied Soil in Model Tests and in the Field. 219
6.8.2 Trigger Mechanism in Lateral Spreading 220
6.9 Numerical Model for Lateral Spreading Analysis 221
6.10 Mitigating Methods of Liquefaction and Lateral Spreading 225
6.11 Summary and Conclusion 227

7 CONCLUSIONS AND RECOMMENDATIONS 228
7.1 Conclusions 228
7.2 Recommendations 232

BIBLIOGRAPHY 234

List of Tables

Table **Page**

1.1(a) Delayed Response in Liquefaction Effects, Earth and Tailing Dams. 5

1.1(b) Delayed Response in Liquefaction Effects, Level Ground Cases. 7

4.1 Soil Parameters Used in Static Analysis of the Upper San Fernando Dams (after Lee et al., 1975). 63

4.2 Soil Parameters Used in Non-linear Deformation Analysis by Serf et al. (1976). 73

4.3 Soil Parameters Used in Initial Effective Stress Analysis. 76

4.4 Soil Parameters Used in Post-earthquake Deformation Analysis. 88

4.5 Steady State Strength of Hydraulic Fill in Lower San Fernando Dam, psf (kpa). 89

4.6 Overall Estimate of Pre-earthquake S_u at Base of Upstream Hydraulic Fill. 89

4.7 $S_{u,cy}/S_{u,nc}$ of Clay Core for Different Pore Water Pressure Ratio ($\Delta u/p'i$). 91

5.2.1 Properties of Oil Sand Tailings [after Phillips and Byrne, 1993]. 107

5.2.2 Parameters Used in Analysis of Triaxial Test. 116

5.2.3 Material Parameters Used in Finite Element Liquefaction Analysis. 117

5.2.4 CANLEX 3- Observed and Computed Pore Pressures at PPTs, (kPa). 120

5.3.1 Material properties of Tailings Used in Liquefaction Analysis of the Proposed Field Event. 152

5.3.2 Parameters Used in Effective Stress Static Analysis of the Field Event. 159

5.3.3 Sequence of Fully Drained Analysis of Clay Embankment. 160

5.3.4 Maximum Allowed Excess Pore Pressure in the Tailings in order to

Safely Construct the Embankment.....162
5.3.5 Parameters of Tailings Sand Used in Liquefaction Analysis of the Final Designed Field Event.....163
5.3.6 Summary of the Analyses of Loading due to Contained Tailings. 170
5.3.7 Comparison between the Observed and Calculated Changes in Water Level for Case 3 in Line 1 of the Instrumented Section (changes in water level in meter). 178

6.1 Summary of Lateral Spread Case Histories. 188

List of Figures

Figure **Page**

2.1 Zero Effective Stress Definition of Liquefaction; (a) isotropically consolidated conditions, (b) anisotropically consolidated conditions. 17

2.2 Effects of Shearing on the Volume of Dry (or drained) Sand, Concept of Critical Void Ratio Introduced by Casagrande (1936). 18

2.3 Definition of Liquefaction in terms of Loss in Shear Strength. 19

2.4 The Steady State Line (SSL). 20

2.5 Typical Result of Triaxial Test on Very Loose Sand [after Sladen et al., 1985]. 22

2.6 Collapse Surface [after Sladen et al., 1985]. 22

2.7 Behavior of Granular Soils Subjected to Monotonic Undrained Triaxial Compression [after Robertson, 1994]. 25

2.8 Behavior of Granular Soils Subjected to Cyclic Undrained Triaxial Compression. [after Robertson, 1994]. 25

3.1 The Critical State Boundary Surface Defined by Roscoe et al. (1958).....30

3.2 Idealized Soil Behavior under Undrained Monotonic Loading. 34

3.3 Soil Behavior on Undrained Planes [after Ishihara et al., 1991].....35

3.4 Idealized Soil Behavior under Undrained Cyclic Loading. 36

3.5 State Boundary Surface for Liquefiable Soils. 37

3.6 Constant Volume and Undrained Stress Paths [after Sasitharan et al., 1992]. 38

3.7 Three Zones for Liquefiable Soils.....45

3.8 The Hyperbolic Strain Softening Model [after Chan, 1986].....45
3.9 Hyperbolic Strain Softening Model for Liquefiable Soils
[after Gu et al., 1994].....46
3.10 Contraction of Yield Surface.....47
3.11 Pore Pressure during Contraction of Yield Surface.....47
3.12 Potential Stress Paths in Static Liquefaction.....53
3.13 Steady State Line in *ln*(p') - e plane.....53

4.1 Cross-section through Upper San Fernando Dam (1 ft = 0.305 m)
[modified after L. A. Dept. of Water and Power].....56
4.2 Results of Standard Penetration Tests (SPT) in Lower San Fernando Dam
[modified after Seed et al., 1975].....60
4.3 Relative Densities Determined from Standard Penetration Tests Data
in Upper San Fernando Dam [modified after Seed et al., 1975].....61
4.4 Grain Size Distribution in Hydraulic Fill from outer Shell towards
Center of Embankment [modified after Lee et al., 1975].....62
4.5 Displacements Measured after Earthquake [modified after Serf et al., 1976].....65
4.6 Changes in Water Level in Piezometers Following the Earthquake
(1 ft = 0.305 m), [modified after Seed et al., 1975].....66
4.7 Analysis of Response of Upper San Fernando Dam during San Fernando
Earthquake during San Fernando Earthquake to Base Motion Determined
from Modified Pacoima Record [modified after Seed et al., 1975].....71
4.8 Strain Potential in Hydraulic Fill of Upper San Fernando dam Resulted
from Dynamic Analysis [modified after Seed et al., 1973].....72
4.9 Displacements Computed by Serf et al. (1976), (a) using non-linear
modified modulus, (b) using nodal force method analysis with soft

central zone. 74
4.10 Finite Element Mesh of the Upper San Fernando Dam. 77
4.11 Contours of Equipotentials in Seepage Analysis (m). 78
4.12 Contours of Equal Pressures in Seepage Analysis (kPa). 79
4.13 Flow Vectors in Seepage Analysis. 80
4.14 Contours of Initial Vertical Effective Stress, σ_y (kPa). 81
4.15 Contours of Initial Horizontal Effective Stress, σ_x (kPa). 82
4.16 Contours of Shear Stress, τ_{xy} (kPa). 83
4.17 Initial Effective Stress in Hydraulic Fill of Upper San Fernando Dam. 84
4.18 Definition of Maximum Pore Water Pressure in Post-earthquake Deformation analysis. 96
4.19 Elements with Maximum Pore Water Pressure Ratio. 97
4.20 Displacements Computed Using Non-modified Shear Strength of Clay Core. 98
4.21 Computed Displacements in Liquefaction Analysis (S_u = 19 kPa, final analysis). 99
4.22 Comparison between Measured and Computed Deformations at the Surface of the Dam. 100
4.23 Computed Displacement Field from Post-earthquake Deformation Analysis (displacement = 0.5 x arrow). 101

5.1.1 Role of Centrifuge Modeling and Field Event in CANLEX Project [modified after Phillips and Byrne, 1993]. 104
5.2.2 Grain Size Distribution of Oil Sand. 110
5.2.2 Summary of Triaxial Test Results [modified after Phillips and Byrne, 1993]. 111

5.2.3 CANLEX 1 and 2- Initial Configuration of Model Slope.....112
5.2.4 CANLEX 2- Observed Post-failure Configuration.....112
5.2.5 CANLEX 2- Model Slope after Failure [modified after Phillips and Byrne, 1993].....113
5.2.6 CANLEX 3- Model Test Configuration. 114
5.2.7 CANLEX 3- Pre- & Post-test Surface Profiles. 115
5.2.8 CANLEX 3- Observed Deformation Field. 115
5.2.9 Axisymmetric Finite Element Model of Triaxial Test.....124
5.2.10 Triaxial Test (Laval #3), Measured and Calculated Results.....125
5.2.11 Schematic Steps of Numerical Modeling. 126
5.2.12 CANLEX 1 and 2- Finite Element Idealization.....127
5.2.13 CANLEX 3- Finite Element Idealization. 128
5.2.14 CANLEX 1- Effective Stress Distribution after Drop of Weight.....129
5.2.15 CANLEX 1- Yield Zone after Stress Redistribution. 130
5.2.16 CANLEX 1- Contours of Excess Pore Pressures Induced by Dropping the Weight (kPa).....131
5.2.17 CANLEX 1- Comparison between Computed and Observed Pore Pressures.....132
5.2.18 CANLEX 2- Effective Stress Distribution after Drop of Weight.....133
5.2.19 CANLEX 2- Yield Zone after Drop of Weight and before Stress Redistribution.....134
5.2.20 CANLEX 2- Deformed Mesh after Liquefaction Analysis. 135
5.2.21 CANLEX 2- Displacement Field after Liquefaction Analysis. 136
5.2.22 CANLEX 2- Contours of Excess Pore Pressures Induced by Dropping the Weight (kPa).....137
5.2.23 CANLEX 2- Comparison between Computed and Observed Pore

Pressures. 138
5.2.24 CANLEX 3- Deformed Mesh after Liquefaction Analysis, S_u = 0.2 p'
[surcharge is simulated by rigid elements]. 139
5.2.25 CANLEX 3- Displacement Field after Liquefaction Analysis, S_u = 0.2 p'
[surcharge is simulated by rigid elements]. 140
5.2.26 CANLEX 3- Deformed Mesh after Liquefaction Analysis, S_u = 20 kPa
[surcharge is simulated by boundary pressure]....141
5.2.27 CANLEX 3- Displacement Field after Liquefaction Analysis, S_u = 20 kPa
[surcharge is simulated by boundary pressure]....142
5.2.28 Syncrude Sand Steady State Results in e-lnp' Plane
[modified after Cunning, 1993]. 143
5.3.1 Proposed Plan of the Field Event. 149
5.3.2 Section A-A of the Proposed Field Event. 150
5.3.3 Illustration of Field Event Modeling. 151
5.3.4 Displacement Field after Liquefaction Analysis
(H_{berm} = 15 m, S_u/p' = 0.2). 153
5.3.5 Deformed Mesh after Liquefaction Analysis (H_{berm} = 15m, Su/p' = 0.2). 154
5.3.6 Failure Cases of the Field Event. 155
5.3.7 Plan View of the Field Event in J-Pit. 157
5.3.8 Field Event Geometry and Soil Types. 157
5.3.9 Cross-section of the Final designed Field Event. 165
5.3.10 Finite Element Idealization of the Field Event. 166
5.3.11 Maximum Excess Pore Pressure at Mid-depth of Tailings Sands
(under centre-line of embankment) for Safe Construction of Embankment. ..167
5.3.12 Deformed Mesh after Liquefaction Analysis (Su/p' = 0.1). 168
5.3.13 Contours of Equal Potential in Seepage Analysis (m). 174

5.3.14 Deformed Mesh after Liquefaction Analysis [Case 2]. 175
5.3.15 Contours of Excess Pore Pressures at the End of Loading (kPa) [Case 3].....176
5.3.16 Location of Piezometer Tips of Line 1 Instrumented Section.. 181
5.3.17 Comparison of Observed and Computed Pore Pressures at P18A, Line 1.....182
5.3.18 Triaxial Compression and Extension Undrained Behavior of Water Pluviated Syncrude Sand [after Vaid et al., 1995]. 183
5.3.19 Contours of the Angle (α) between Major Principle Stress ($\sigma 1$) and Depositional (vertical) Direction (α in degree).. 184

6.1 A Model of Liquefaction Effects. 187
6.2 Ground Displacements, Fissures and Sand Boils in the Vicinity of the Ogata Primary School during the 1964 Niigata Earthquake [modified after Hamada et al., 1994]. 192
6.3 Soil Conditions, Ground Displacement and Estimated Liquefied Layer along Section A-A' at Ebigase area in Niigata City [modified after Hamada et al., 1994]. 193
6.4 Liquefaction-induced Ground Displacement, East of Upper Van Norman Reservoir (1971 San Fernando Earthquake) [after O'Rourke et al., 1992]. 194
6.5 Soil Profile at Cross Section A-A', East of Upper Van Norman Reservoir, (1971 San Fernando Earthquake) [modified after O'Rourke et al., 1992]. 195
6 6 Damages to the Foundation Piles [modified after Doi and Hamada, 1992]. 199
6.7 Horizontal Displacement of the Ground Surface and Movement of Sewage Pipe.....201
6.8 Ground Displacement and Movement of Sewage Pipe

in Cross-section A-A' of Figure 7. 202

6.9 Measured Displacements versus Predicted Displacements [modified after Bartlett and Youd, 1992]. 206

6.10 Comparison of the Predicted Ground Displacement with the Observed Ground Displacement [modified after Hamada et al., 1986]....206

6.11 Experiment on Liquefaction-induced Ground Displacement [modified after Hamada et al., 1986]....211

6.12 Viscose Flow of Ground Displacement. 211

6.13 Case History Study in Ogata Area[modified after Towhata et al., 1992]. 212

6.14 Newmark Sliding Block Model. 218

6.15 Two-Block Soil Model for Analysis of Spreading with Free Face and Graben Proposed by Dobry and Baziar (1992)....218

6.16 Simplified Process during and after Earthquake. 223

6.17 Mechanism of Earthquake-induced Liquefaction and Lateral Spreading....224

Chapter 1

INTRODUCTION

1.1 LIQUEFACTION HISTORY

Liquefaction can occur in saturated loose to medium sands when subjected to rapid cyclic or monotonic loading. Liquefaction is often followed by a substantial loss of strength and stiffness resulting in large deformations.

Casagrande (1936) appears to have been the first to study this phenomenon. In this work, Casagrande elaborated characteristics of cohesionless soils affecting the stability of slopes and earth fills. Although he did not use the term liquefaction at that time, he clearly established the concept and the meaning of the phenomenon.

Casagrande described liquefaction by means of some simple model tests and noted some case histories of that time. He showed that a slight disturbance of a loose saturated sand may lead to rapid deformation, resulting in a change of the sand structure and the formation of hydrodynamic stresses. He noted that the stresses quickly spread through the entire mass and so decreased the internal friction angle of the saturated sand. One of the

Casagrande's conclusions clearly describes the liquefaction phenomenon; it is worthwhile to quote it here:

> "The density in the loose state of many cohesionless soils, particularly medium to fine, uniform sands, is considerably under their critical density. Such materials in their loose state tend to reduce their volume if exposed to continuous deformation. If the voids are filled with water and the water cannot escape as quickly as the deformation is produced, then a temporary transfer of load on the water takes place, and the resulting reduction in friction angle impairs the stability of the mass, which can lead, in extreme cases to a flow slide."

Terzaghi and Peck (1948) used the term *spontaneous liquefaction* to indicate the sudden change of loose deposits of sand into flows much like viscous fluid, triggered by a slight disturbance. They considered the phenomenon the main cause of slope failures in saturated deposits of fine silty sands.

The 1964 earthquake of Niigata, Japan, attracted broader attention to the phenomenon of liquefaction and underlined the importance of earthquake-induced liquefaction. During and following the earthquake, extensive damage to structures occurred due to liquefaction of the sandy deposits on which they were placed. Seed and Idriss (1967) provided valuable information on the damage due to the earthquake. The significance of the loss of life and property damage caused by the liquefaction during this earthquake, generated a large amount of research to evaluate the phenomenon and to provide mitigative measures against damage.

After the Niigata earthquake, many other earthquakes have occurred around the world and liquefaction of soils has been a significant source of damage to both in- and on- ground structures. The earthquake of San Fernando 1971 resulted in liquefaction and almost catastrophic failure of the upstream embankment of the Lower San Fernando Dam. The earthquake also resulted in large deformations of the Upper San Fernando Dam. In the following years, extensive research and laboratory tests were carried out to clarify the

liquefaction behaviour of soils. The research was primarily concentrated on earthquake-induced liquefaction.

With the development of structural engineering codes, direct earthquake-induced damage to super-structures has been significantly reduced. However, damage to sub-structures and in-ground structures has remained significant due to the complex behaviour of natural materials involved in liquefaction.

Extensive efforts have been made to evaluate the stability and deformation of soil structures during and after an earthquake. The effect of an earthquake on earth structures becomes more complicated with presence of pore water in the soil. Earthquake shaking increases pore water pressures and may lead to liquefaction of the soil.

A number of numerical models for calculating seismic stability of soil structures have been developed during the last three decades (Newmark, 1965; Seed et al., 1975; Zienkiewicz et al., 1990; Kuwana and Ishihara, 1991 and Finn et al., 1990). An exact deformation analysis of the earthquake-induced liquefaction involves the effect of both cyclic and gravity forces. Few practical analyses have been developed to couple the above two effects, due to the complexity of the phenomenon. The progress of research on liquefaction of soils and its consequences has been discussed in detail by Seed (1979), Finn (1991) and Ishihara (1993).

Earthquake-induced liquefaction of a soil structure is a complicated process involving seismic loading, excess pore water pressure generation, strain softening, stress redistribution and reconsolidation both during and after an earthquake. The deformation induced directly by the seismic loading is small due to the reversed nature of the loading. During the collapse of elements liquefied directly by the earthquake, a major part of the load previously carried by these elements will be transferred to the neighboring elements, causing further liquefaction and yielding. This process of stress redistribution may result in continual progressive deformation until the whole body of the soil structure comes to a new equilibrium. If that part of the structure which is liquefied directly by the earthquake

is sufficiently large, stress redistribution may cause large deformations or complete failure of the structure.

Excess pore water pressures can be induced by either earthquake motion or stress redistribution. Hence, liquefaction can occur by either an earthquake or stress redistribution. The liquefied zone after the stress redistribution may be much larger than the initial liquefied zone triggered directly by the earthquake. Progressive deformation is not an instantaneous phenomenon; rather it is a process in time. This time could vary from a few seconds to several hours depending on a variety of conditions, including the permeability and the boundary conditions of the soil structure.

1.2 DELAYED RESPONSE IN LIQUEFACTION EFFECTS

The observation of delayed response (or failure) supports the view that post-earthquake deformation and stress redistribution are essential in the evaluation of liquefaction stability of soil structures. Delayed response is common in liquefaction effects on all kinds of soil structures, including earth dams, natural slopes and gently sloping ground. Seed (1979) has given a comprehensive discussion about liquefaction effects on earth dams. He cited the conclusion of Akiba and Semba (1941) that few failures of earth dams have occurred during the earthquake motion. Most dams failed sometime after the earthquake, ranging from a few hours to 24 hours.

Seed concluded that the critical period for an embankment dam subjected to earthquake shaking is not only the period of shaking itself, but also a period of hours following the earthquake. He attributed the delayed response to the piping through the cracks induced by the earthquake shaking and the pore water pressure redistribution in the body of the earth dam.

The seismoscope record on the crest of the Lower San Fernando Dam during the earthquake of 1971 showed that the slide movement involving the crest of the dam apparently did not take place during the main earthquake, but rather occurred some 30 seconds after the main shaking (Seed, 1979). Some case histories of earth dams, in which

the delayed response in liquefaction effects has been observed, are summarized in Table 1.1(a).

Table 1.1(a) Delayed Response in Liquefaction Effects, Earth and Tailing Dams.

EARTHQUAKE	LIQUEFACTION EFFECTS
Ojika Earthquake 1939	Most dams failed a few hours or up to 24 hours after the earthquake.
San Fernando Earthquake 1971	The upstream shell of the Lower San Fernando Dam failed some 30 seconds after the main shaking.
Izu-Ohshima-Kinkai Earthquake 1978	Two of three tailing dams survived the main shock (a 7.1 magnitude earthquake occurring about 40 km away) but one of the two failed about 5 hours after a magnitude of 5.4 aftershock which occurred the next day directly below the dam site.

The observation of delayed response of liquefaction is not limited only to earth dams and natural slopes. A similar response has been observed and recorded for many cases of gently sloping grounds where the gradient of the ground surface does not exceed 10%. Hamada et al. (1994) have documented valuable interviews with witnesses of the areas in which the ground displacements was induced due to liquefaction. The information provided in these interviews are significant and supportive of the delayed response phenomenon. This information can be used to investigate and clarify the mechanism of liquefaction-induced deformations. A summary of two of these interviews will be presented.

Interview 1

Some witnesses of the 1948 Fukui earthquake, when the liquefaction-induced ground displacement reached over 5 m, said that a ground fissure with a width of about 1.0 m was caused after the earthquake shaking, and the width increased about 3 m two or three hours after the earthquake. Similar comments were also reported by witnesses in Kasukabe City, where the ground moved several meters due to the 1923 Kanto earthquake. They said that they found a fissure with a width of about 1.0 m along a small river after the earthquake motion ended, and that the width of the fissure increased to 3.0 m two or three hours later.

Interview 2

The collapse of the Showa bridge as a result of the 1964 Niigata earthquake is an important case which reinforces the significance of delayed response. The bridge collapse was one of the worst cases of structural damage, and eyewitnesses reported that the girders of the bridge began to collapse sometime after the earthquake. When the earthquake shaking started people and vehicles were on the bridge, but no lives were lost since there was enough time for the people to escape. Hamada et al. concluded that liquefaction-induced displacements at the site of the bridge continued for a relatively long time after the earthquake. The ground deformation eventually deformed the foundation piles of the bridge and caused the girders to collapse.

From the remarks by the witnesses and the vivid example of the bridge itself, Hamada et al. (1994) concluded that the liquefaction-induced ground displacements had continued for a long period until the excess pore water pressures dissipated, although the earthquake shaking had stopped.

In addition to the Japanese cases, there are many similar cases of delayed response of the ground during earthquakes. The simultaneous measurements of seismically induced pore water pressures during the 1987 Superstition Hills Earthquake at Wildlife Site, California, have been reported by Holzer et al. (1989). These are probably the first measurements of pore water pressure increase to lithostatic conditions associated with

earthquake induced liquefaction. According to the pore water pressure change measurements, the pore pressures approached lithostatic conditions after the strong motion ceased. The earthquake shaking lasted for about 10 seconds, while the pore water pressures continued to increase for about 90 seconds. Table 1.1(b) presents a summary of several reported cases of delayed response due to earthquakes in level ground or gently sloping ground.

Table 1.1(b) Delayed Response in Liquefaction Effects, Level Ground Cases.

EARTHQUAKE	LIQUEFACTION EFFECTS
Assam Earthquake June 12, 1987	Water and sand continued to eject for about 30 minutes after the earthquake.
Kanto Earthquake September 1, 1923	The ejection of water and sand stopped, then continued again for a long time after the earthquake.
Bihar - Nepal Earthquake January 15, 1934	Hundreds of water spouts, throwing up water and sand, continued for about 30 minutes after the earthquake.
Bulgarian Earthquake April 18, 1928	Water spouted in Maritsa Valley for tens of minutes after the earthquake. Houses sank gradually into the ground.
Fukui (Japan) 1948	A witness said that the ground fissure with a width of about 1.0 meter was caused after earthquake motion, and that the width increased about 3.0 meters two or three hours later after the earthquake. Similar comments were also reported by witnesses in KasuKabe City, where the ground moved several meters due to the 1923 Kanto Earthquake.

Table 1.1(b) Delayed Response in Liquefaction Effects, Level Ground Cases (continued).

EARTHQUAKE	LIQUEFACTION EFFECTS
Niigata Earthquake June 16, 1964	The collapse of the Showa Bridge with a total span of 250 m, was one of the worst cases of damage. Many eyewitnesses reported that the girders began to collapse sometime after the earthquake. When the earthquake motion started, many people and vehicles were on the bridge, but no lives were lost in spite of catastrophic collapse. This suggests that there was enough time for people on the bridge to escape towards the banks.
Niigata Earthquake June 16, 1964	Fountains of water continued for about 20 minutes. Fissures and sand & water boils continued to occur after the earthquake.
Tangshan Earthquake 1976	Ejection of water and sand started after the earthquake ceased, and lasted from minutes up to one day. Structures sank into the ground sometime after the earthquake.
Superstition Hills November 24, 1987	The earthquake shaking lasted for 10 seconds; the measured Pore water pressures continued to climb to lithostatic conditions for about 90 seconds.
Manjil Earthquake (Iran) 1990	Local people testified that the sand mixed with water came up gradually from the bottom and completely filled the well. All wells in the devastated area were filled with the sand and became unstable.

1.3 DEFORMATION ANALYSIS OF LIQUEFACTION

These cases clearly establish the delayed response and provide further evidence of the importance of (1) considering post-earthquake stability of dams constructed of loose to medium dense granular soils and (2) the post-earthquake behaviour of gently sloping fluvial deposits and level grounds.

Liquefaction-induced deformation of soils occurs in the whole mass of the soil, rather than along a single slip surface. Hence, in order to evaluate the soil response during liquefaction, a load deformation analysis which includes the entire mass of the soil is required. Finite element analysis is a powerful tool for this purpose.

Gu (1992) developed an undrained elasto-plastic model for *post-earthquake deformation analyses*. The model simulates liquefaction due to earthquake, strain softening behaviour, stress redistribution and progressive flow deformation of liquefied soils. The model is useful in explaining the delayed response in liquefaction effects, although it is not intrinsically time-dependent. Gu et al. (1993a and 1993b) employed this undrained model to evaluate progressive failure of the Lower San Fernando Dam damaged by the 1971 Earthquake and liquefaction event in the Wildlife Site in California during the 1987 Earthquake.

In the post-earthquake deformation analysis of the Lower San Fernando Dam, the failure of the upstream embankment of the dam was indicated by non-converging solution in the computation process (Gu et al., 1993). A converged numerical solution could not have been obtained for this case which involved overall slope failure. In this case, where the liquefied soils failed and displaced several ten meters, the purpose of the analysis was to capture the failure and the onset (not the extent) of the deformations.

There are many case histories in the literature where earth structures subjected to earthquake and liquefaction *did not fail*. However, these structures suffered *large, although contained, deformations*. There is a need to examine and calibrate the method of post-earthquake deformation analysis for such cases. In this kind of analysis,

deformations induced by liquefaction and stress redistribution are required to be evaluated.

In addition to the earthquake-induced liquefaction, liquefaction induced by monotonic loading, namely static liquefaction, has also been a major cause of damage to soil structures. Static liquefaction can be induced by rapid undrained monotonic loading. Saturated loose granular deposits are prone to this type of liquefaction. Many cases of static liquefaction have been recorded in the literature. A number of static liquefaction failures occurred at the Suncor Tar Island Tailings Pond in the 1970's. The Stava Tailings Dam, Italy, failed catastrophically in 1985, resulting in the death of over 260 people.

A numerical model to study the undrained behaviour of liquefiable soils during static liquefaction is also required. The model should be able to simulate behaviour of liquefied soils both before and during the collapse. Effective stress analyses, in which pore pressure response of the soil during the loading and the collapse are calculated, are preferred.

Fundamental behaviour of the soil subjected to static liquefaction and earthquake-induced liquefaction are the same. However, there are differences in stress paths by which the soil is brought to the state of collapse. During an earthquake, the net change in the deviator stress (q) is zero; therefore, the stress path can be simulated by a q-constant stress path. However in static liquefaction, the stress path by which the soil is brought to the state of collapse may not be a q-constant one. When saturated soils are subjected to monotonic loading, both deviator stresses and pore water pressures in the soil may increase during loading.

A liquefaction numerical model should be able to explain fundamentals of the soil behaviour during static liquefaction. As mentioned, the behaviour of soil liquefied by monotonic loading is similar to the behaviour of soil liquefied by cyclic loading (i.e. earthquake). Therefore, the principles of the method of post-earthquake deformation analysis, which basically was developed to evaluate earthquake-induced liquefaction, can also be employed for static liquefaction analysis.

1.4 OUTLINE OF THE THESIS

The purposes of the present research are:

(1) to reevaluate and calibrate the *post-earthquake deformation analysis* method introduced by Gu et al. (1993) for a case where earthquake-induced deformations are large, but contained

(2) to adapt and extend the numerical model for a case where liquefaction of soils is induced by monotonic loading rather than by cyclic loading

(3) to extend and modify the model for a case where the undrained strength of a liquefiable soil is not a single value, but rather a function of the mean normal effective stress, which is the case for loose liquefiable sandy deposits

(4) to provide a thorough literature review on earthquake-induced spreading of gently sloping liquefiable deposits, in order to figure out the potential mechanism of spreading.

After this introductory chapter, Chapter 2 summarizes fundamental and theoretical aspects of liquefaction. *Zero effective stress* and *strain softening & collapse,* two definitions suggested to define liquefaction, are reviewed. Steady state line, collapse surface and strain softening behaviour of soils are also described. In addition, behaviour of saturated granular soils under both undrained monotonic loading and cyclic loading are discussed. Definitions for different types of liquefaction are also presented in this Chapter.

Chapter 3 summarizes the elasto-plastic model for liquefiable soils. The model, which was developed for post-earthquake deformation analysis, is adapted for static liquefaction analysis. Furthermore, the numerical model is extended for liquefaction analysis of loose sands where the undrained steady state strength of the soil is a function of confining stress.

Chapter 4 presents a post-earthquake deformation analysis of the Upper San Fernando Dam, which was deformed by the earthquake of 1971. This Chapter provides further

evaluation of the numerical model and its calibration for the case where liquefaction-induced deformations are large but contained.

A major liquefaction sand study entitled the Canadian Liquefaction Experiment (CANLEX) is being carried out by the Canadian geotechnical engineering community. Chapter 5 presents a numerical study for the CANLEX Project. This Chapter describes numerical modeling and static liquefaction analyses of three centrifuge model tests and a full-scale field event. The Chapter is organized in a number of separate sections.

Section 5.1 provides an introduction to the CANLEX Project. Section 5.2 describes numerical modeling and analyses of the centrifuge tests. The field event was designed based on the analyses of the centrifuge tests. Finally, section 5.3 describes modeling and analysis of the field event.

Chapter 6 of the Thesis presents a thorough literature review on lateral spreading of the ground induced by liquefaction of gently sloping granular materials. The literature review summarizes a number of case histories of lateral spreading where the ground moved several meters, and their damaging effects on in-ground structures. Experimental works on lateral spreading are also reviewed. The developed analytical models to evaluate liquefaction-induced ground displacements are summarized and their physical concepts are probed. A possible mechanism for lateral spreading is suggested. At the Chapter's end, mitigating methods of liquefaction-induced large ground displacements are reviewed.

Chapter 7 presents the major conclusions of this research and makes recommendations for further study.

Chapter 2

PRINCIPLES OF LIQUEFACTION

2.1 INTRODUCTION

The term "liquefaction" has been used to refer to a group of phenomena which have in common the development of high pore pressures in saturated sands due to cyclic or monotonic loading under undrained (i.e., constant volume) conditions. Several trigger mechanisms, both cyclic and monotonic, to induce liquefaction can be identified. Earthquake shaking, explosion, pile driving and vibration of vibratory equipment are cyclic trigger mechanisms whereas rapid static undrained loading, raising the water table, rapid excavation and even small mechanical disturbance (for the case of very loose sands) are static trigger mechanisms.

There are two opinions in the literature about the definition of soil liquefaction; they are as follows.

2.2 DEFINITIONS OF LIQUEFACTION

Zero Effective Stress Definition

A condition of zero effective stress following accumulation of excess pore water pressures during cyclic loading was defined as *initial liquefaction* by Seed (1966). The immediate result of this definition is that the liquefied soil will not be able to carry any shear stress. For anisotropically consolidated dense soils under undrained cyclic loading, the condition of zero effective stress will not occur if no shear stress reversal develops; hence, the zero effective stress definition is unable to define the liquefaction developed in such conditions. Therefore, certain amounts of accumulated axial strain, 5% double amplitude axial strain, were adopted to define liquefaction. Figure 2.1 presents the above definition of liquefaction.

Strain Softening and Collapse Definition

The steady state oriented definition of liquefaction is based on the concept of "critical void ratio" introduced by Casagrande (1936). The critical void ratio for non-plastic, granular materials is defined as the void ratio in which the arrangement of the soil particles is such that no volume change takes place during shearing. Figure 2.2 illustrates the concept of critical void ratio. It shows that both loose and dense states of a particular sand, after undergoing a certain amount of shear strain, will reach the same shear stress. This shear stress is associated with a void ratio which is named the critical void ratio.

Based on the concept of critical void ratio and supportive results of undrained monotonic loading tests on saturated sands, Castro (1975) suggested that liquefaction be defined as the phenomenon wherein the shear resistance of a mass of soil decreases when subjected to monotonic or cyclic loading at constant volume (i.e., undrained loading conditions) so that the mass undergoes very large unidirectional shear strains. It appears to flow until the shear stresses are as low as or lower than the reduced shear resistance. Thus, a liquefaction failure requires the presence of driving static shear stresses that exceed the reduced shear resistance of the soil. Therefore, a soil is not in itself liquefiable, but it

depends on the value of the applied driving shear stress. The reduced shear resistance was called *undrained steady state strength.*

According to this definition of liquefaction, the conditions for a seismically induced liquefaction failure to occur are twofold: first, the mass must be unstable in the sense that the driving shear stresses exceed the undrained steady state strength of the soil; secondly, the earthquake stresses must be sufficient to trigger the failure; i.e., it must be able to strain the soil sufficiently to overcome the peak strength of the soil . Figure 2.3 shows schematically the definition of liquefaction in terms of loss in shear strength.

One advantage of the definition of liquefaction proposed by Castro (1975) is that it enables one to unify descriptively liquefaction cases induced by both cyclic and monotonic loading. The second advantage is that it enables one to introduce some strength, namely residual or steady state strength, for liquefiable materials in any stability analysis.

The definition of liquefaction given by Castro is used in the thesis to consider the behaviour of contractant sands under undrained conditions. Liquefaction of saturated soils is possible if the drainage is impeded or if the rate of generation of excess pore water pressure is sufficiently higher than the rate of dissipation of the excess pore water pressure. If drainage is not impeded or dissipation of excess pore water pressure is fast enough, the void ratio of the soil will change and liquefaction will not occur.

2.3 STEADY STATE LINE

Castro et al (1975) introduced a steady state line for sands, based on the "critical void ratio" concept defined by Casagrande (1936). Supportive results were obtained from undrained monotonic load tests on saturated sands. The key element in the steady state method is *the steady state of deformation* defined by Poulos (1981). The *steady state of deformation* for any mass of particles is the state in which the mass is continuously deforming at constant volume, constant normal effective stress and constant velocity. It is achieved only after all particle orientation has reached a steady state condition and after

all particle breakage, if any, is complete so that the shear stress needed to continue deformation and the velocity of deformation remain constant.

Figure 2.4 illustrates the steady state of a particular sand as a line in p'-q-e space, where p', q and e are the mean normal effective stress, the deviator stress and the void ratio, respectively. The steady state may be also represented by the projection of the steady state line (SSL) on the e-p' plane or the e-q plane. However, in order to fully understand the behaviour of sands under monotonic or cyclic loading, it is important to follow the actual stress paths in a spatial manner in three dimensional p'-q-e space. The steady state line is very similar to the critical state line defined by Roscoe et al (1958). Projection of the steady state line in a void ratio versus effective stress (e-σ') plane was called the critical void ratio line by Casagrande (1936).

Several laboratory tests results have shown that for uniform sands, the steady state strength is independent of the effective stress path and the initial effective stress value; it only depends on the void ratio. Been et al. (1991,1992) examined the behaviour of fine to medium uniform graded quartzic sand and concluded that steady state (or critical state) of the sand is unique and independent of stress path, sample preparation and initial stress state. Vaid et al. (1990) conducted both compression and extension triaxial tests on water deposited sands and concluded that the steady state strength, at a given void ratio, is smaller in extension than in the compression and the difference increases as the sand gets looser.

Been et al. (1991) argued that the difference in the steady state strength of the sand in compression and extension is due to the difference in mapping of steady state line in the p'-q plane. In general, the friction angle at steady state is approximately the same under conditions of triaxial compression and triaxial extension and, therefore, $M = q_{ss}/p'_{ss}$ on the steady state line in extension and compression must be necessarily different, i.e., $M_{Ext.} < M_{Comp.}$. This difference gives a smaller steady state strength in the triaxial extension test than the steady state strength in the triaxial compression test.

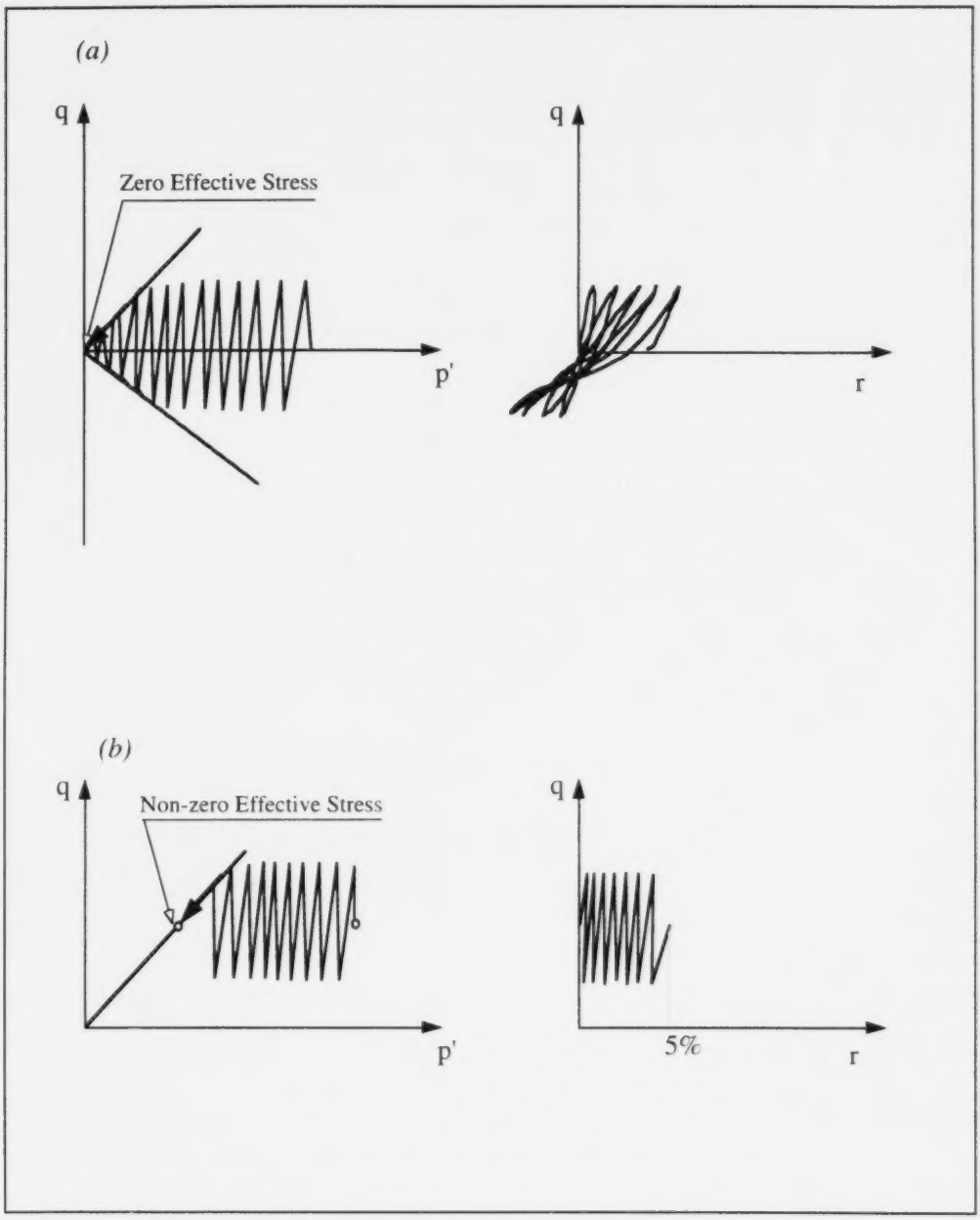

Fig. 2.1 Zero Effective Stress Definition of Liquefaction;
(a) isotropically consolidated conditions,
(b) anisotropically consolidated conditions.

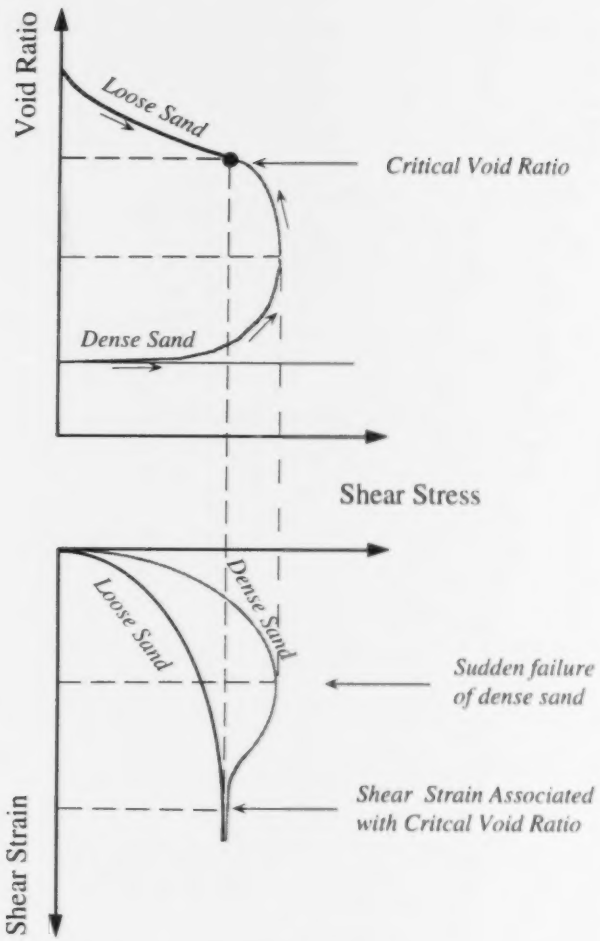

Fig. 2.2 Effects of Shearing on the Volume of Dry (or drained) Sand, Concept of Critical Void Ratio Introduced by Casagrande (1936).

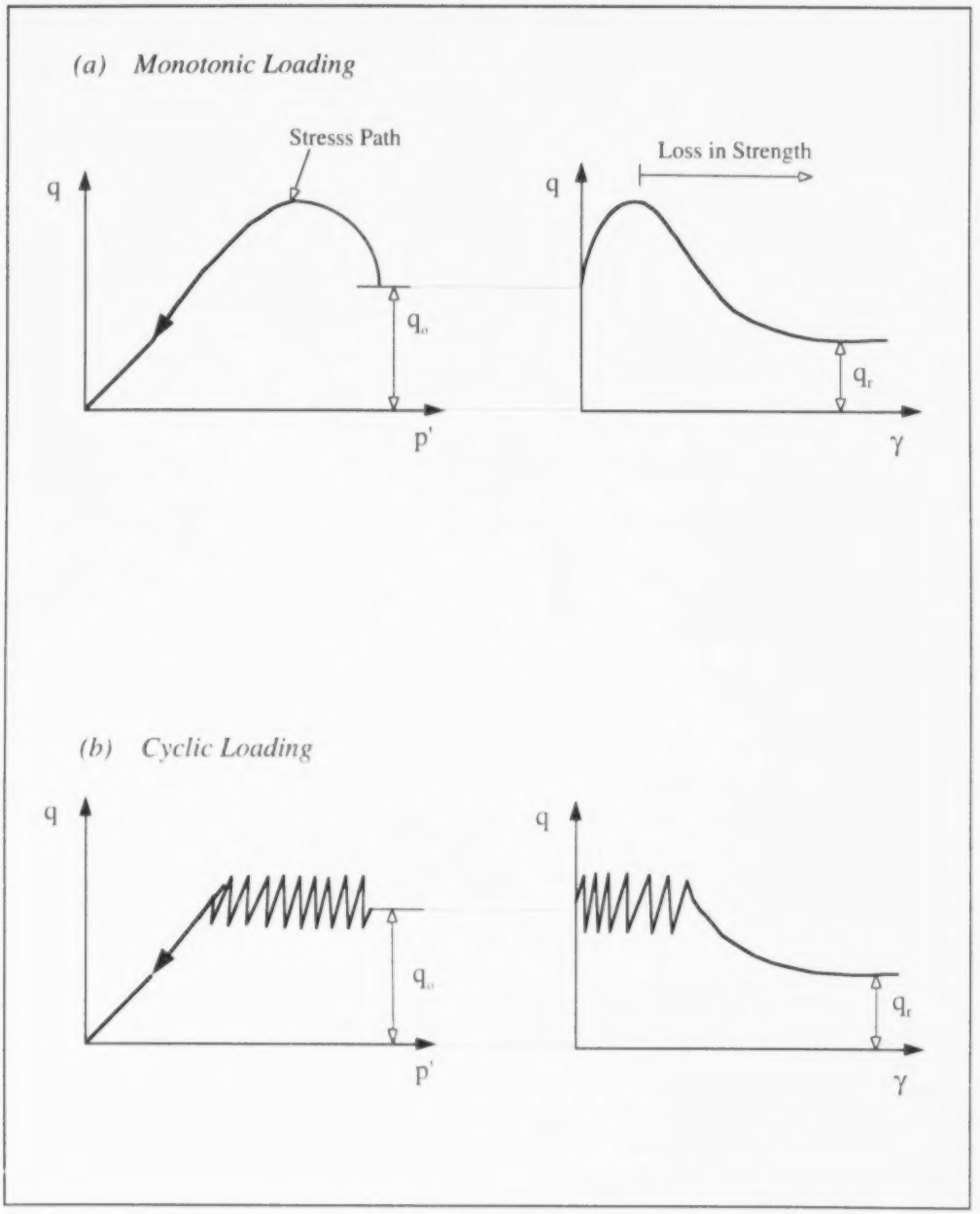

Fig. 2.3 Definition of Liquefaction in terms of Loss in Shear Strength.

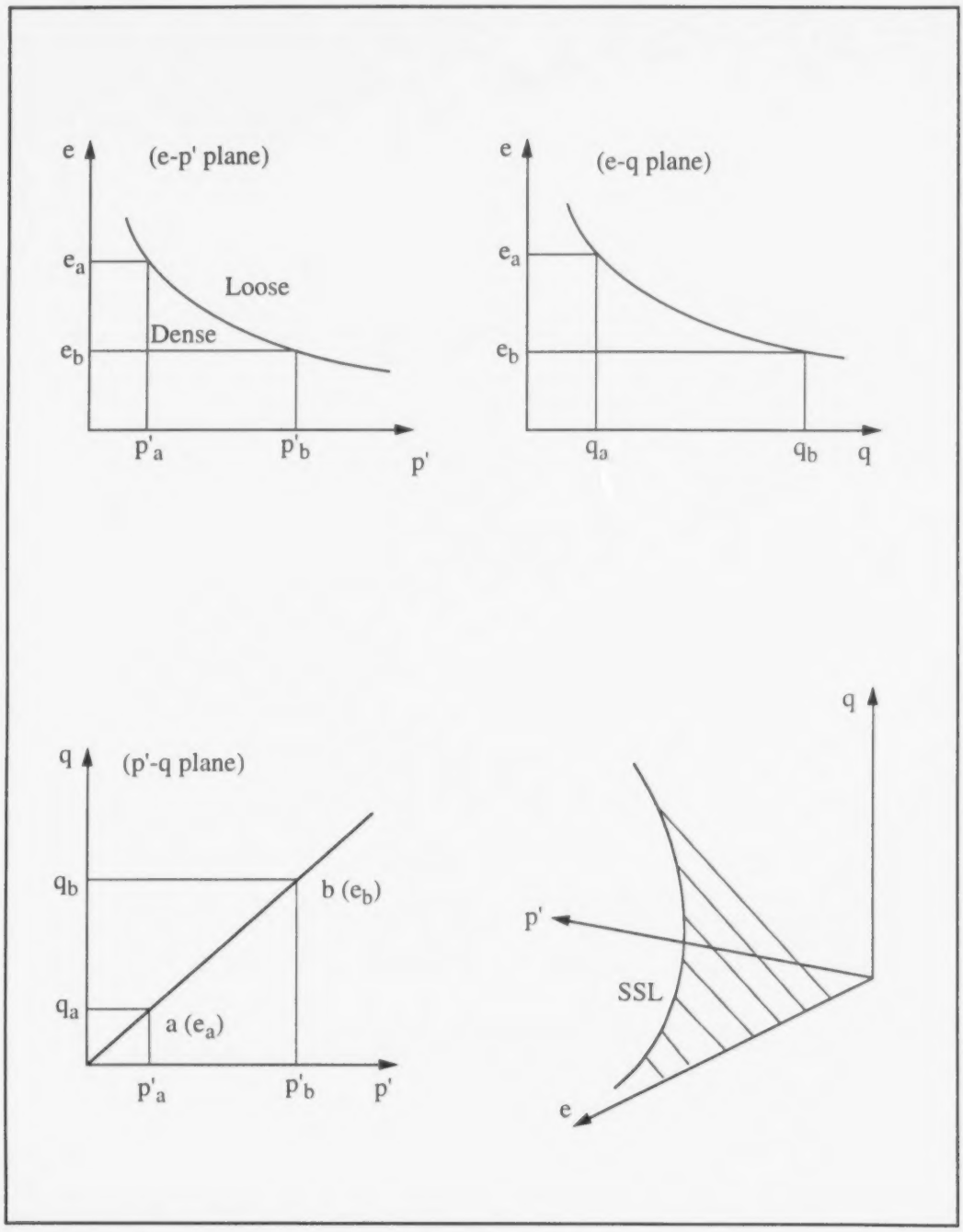

Fig. 2.4 The Steady State Line (SSL).

2.4 COLLAPSE SURFACE

Sladen et al. (1985) introduced the collapse surface concept. The collapse surface defines the trigger of collapse for loose sands subjected to undrained loading. Having conducted a series of undrained triaxial compression tests on loose sands, they showed that the sand reaches a maximum shear stress before strain softening to steady state. Figure 2.5 shows a typical result of the tests on very loose saturated sand. The deviator stress reaches a peak value at a certain strain and then drops to a reasonably constant value, or steady state level, with increasing axial strain. Pore pressure increases steadily during the tests to a constant steady state value and exhibits no clearly defined peak. For contractant saturated soils under monotonic undrained loading, strain softening behaviour may occur after the effective stress path reaches a peak point.

Test results obtained by Sladen et al. (1985) suggested that the collapse surface may be observed by plotting the results of undrained triaxial compression tests in a normalized p'-q plane. The envelope of the peak strengths on this normalized p'-q plane forms the collapse surface. Figure 2.6 shows the collapse surface suggested by Sladen et al. (1985).

The peak strength depends on the effective stress path and also on the initial stress, and the post peak strain softening behaviour depends on both void ratio and initial effective stress. For a soil with constant in situ stress, the higher the void ratio, the more brittle the post peak behaviour. For a soil with constant void ratio, the higher the in situ stress, the more brittle the soil and, hence, the higher the softening of the soil.

It is possible that the slope of the collapse surface is to some degree dependent on the stress history. The tests results on anisotropically consolidated samples reported by Castro et al. (1982), as cited by Sladen et al (1985), suggested that the collapse surface for anisotropically consolidated sands may be slightly steeper than that for isotropically consolidated sands.

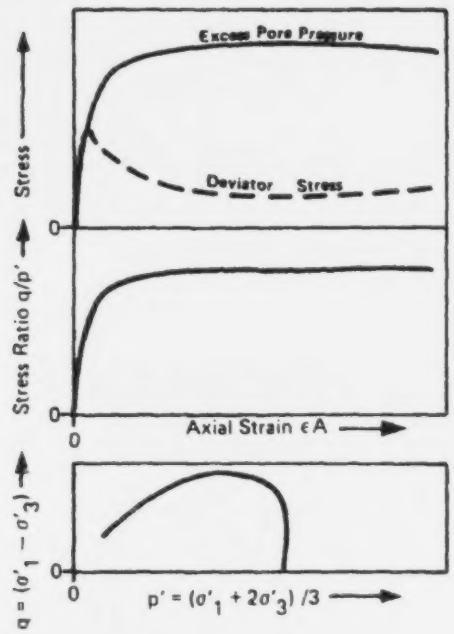

Fig. 2.5 Typical Result of Triaxial Test on Very Loose Sand [after Sladen et al., 1985].

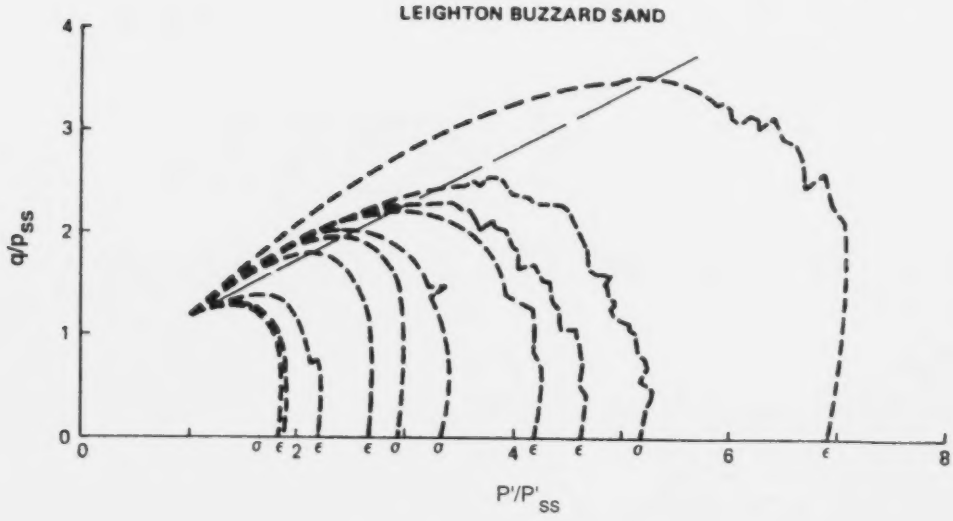

Fig. 2.6 Collapse Surface [after Sladen et al., 1985].

2.5 SUMMARY OF BEHAVIOUR OF SATURATED GRANULAR SOILS

2.5.1 Soils Subjected to Monotonic Loading

A summary of the behaviour of a granular soil subjected to monotonic undrained triaxial compression is presented in Figure 2.7. A soil with initial shear stress higher than the steady state strength will behave in a strain softening manner at large strains, while a soil with an initial shear stress lower than the steady state strength will behave in a strain hardening manner at large strains. If the initial shear stress of the soil is only a little higher than the steady state, the soil will display limited strain softening, but after passing the quasi-steady state, the final response at large strains will be strain hardening to the ultimate steady state. The soil response at quasi steady state may be controlled by the sand fabric and method of deposition.

If a saturated soil structure is composed entirely of strain softening materials and the in situ shear stresses are larger than the steady state shear strength, a collapse and liquefaction flow slide can occur if the soil is triggered to strain soften by either cyclic or monotonic loading. If a soil structure is composed entirely of stain hardening materials, collapse and flow slide will not occur even though some deformation may be induced.

2.5.2 Soils Subjected to Cyclic Loading

Figure 2.8 shows a summary of the behaviour of a granular soil subjected to cyclic undrained loading. Soils subjected to cyclic undrained loading will initially develop positive pore water pressures because of the contractant nature of the soil at small strains. If the initial shear stress of the soil (i.e. before the application of cyclic loading) is sufficiently higher than the steady state strength, the soil behaves in a strain softening manner after reaching the boundary surface. After that, the behaviour of soil will be controlled by the gravitational load and will become almost independent of the cyclic loading. In this case, cyclic loading by inducing pore pressures only brings the effective stress state of the soil to the collapse surface and then the collapse and flow failure will be caused directly by gravitational loading. If the initial shear stress of the soil is smaller

than the steady state strength, the soil behaves in a strain hardening manner after reaching the boundary surface.

If the ground is level or gently sloping and the magnitude of cyclic loading is big enough, shear stress reversal will occur and the effective stress will move to the point of zero effective confining stress. If the soil is dense and the size of cyclic loading is not big enough to develop stress reversal, the state of zero effective stress will not occur and deformations will be smaller. These deformations essentially stop when the cyclic loading stops. In this case, cyclic mobility with limited deformations will occur.

2.6 DEFINITIONS FOR DIFFERENT TYPES OF LIQUEFACTION

On the basis of the above description of granular soil behaviour under monotonic and cyclic loading, one can suggest definitions for different types of liquefaction, depending on the liquefaction mechanism. Robertson (1994) has suggested a set of comprehensive definitions of liquefaction as follows.

2.6.1 Gravitational (Flow) Liquefaction

The requirements for this kind of liquefaction are:

- post peak behaviour of the soil in undrained loading conditions should be strain softening; the loading can be either monotonic or cyclic
- initial shear stress must be higher than the steady state strength of the soil
- in order that the stress redistribution within the body of the soil structure results in progressive deformation and eventually to collapse and flow failure, sufficient volume of the soil must behave strain softening
- whether the gravitational (flow) liquefaction failure occurs or not depends on the boundary conditions

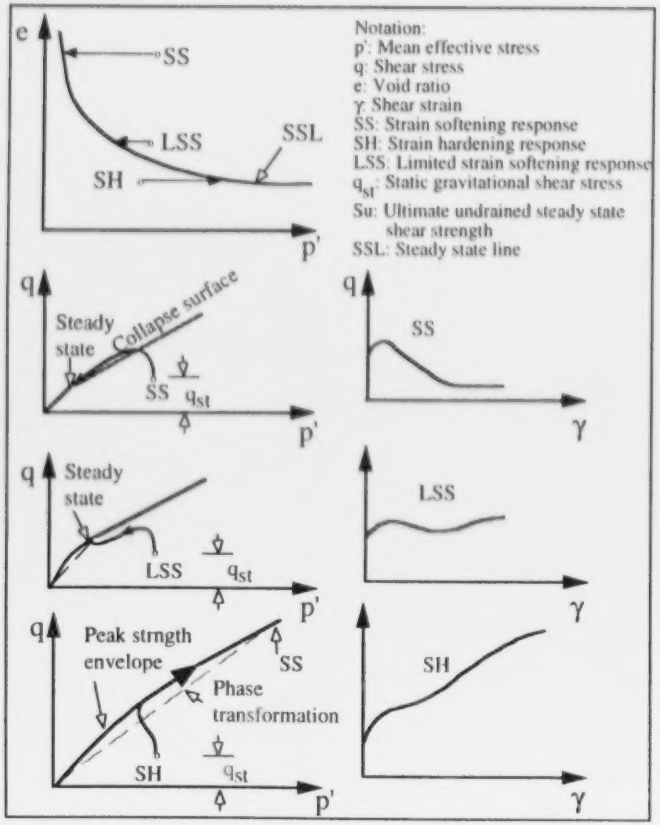

Fig. 2.7 Behavior of Granular Soil Subjected to Monotonic Undrainrd Triaxial Compression [modified after Robertson, 1994].

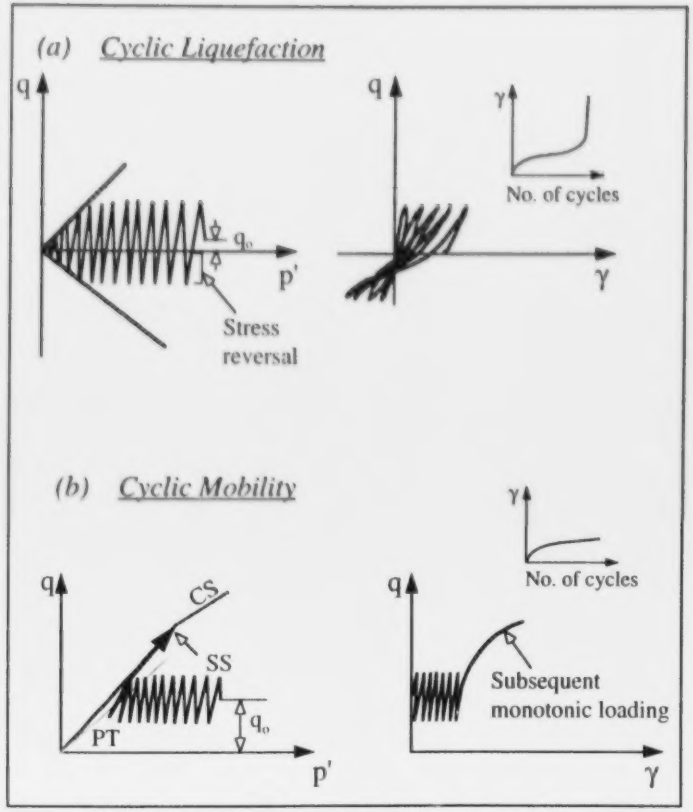

Fig. 2.8 Behavior of Granular Soil Subjected to Cyclic Undrained Triaxial Compression [modified after Robertson, 1994].

2.6.2 Seismic Liquefaction

(1) Cyclic Liquefaction

The requirements for cyclic liquefaction to occur are:

- shear stress reversal should be developed in a saturated soil under undrained cyclic loading; in order to develop shear stress reversal, the cyclic shear stress must be sufficiently higher than the in situ shear stress of the soil
- the cyclic loading should be of sufficient duration to extend the soil to the point of zero effective confining stress; in this point no shear stress can exist
- deformations during cyclic loading and at the state of zero effective confining stress can be large; if no further shear is present the soil movement will stop as the cyclic loading stops

(2) Cyclic Mobility

Cyclic mobility will occur when the following conditions are provided:

- the in situ shear stress should be high enough that no stress reversal happens during the application of cyclic loading; hence, the effective confining stress will remain always higher than zero
- deformation starts with cyclic loading and the soil movement stops as the cyclic loading stops
- the amount of deformation depends on the size and the duration of the cyclic loading

Casagrande (1936) proposed the term *cyclic mobility* for progressive softening of saturated soils that are subjected to cyclic loading in laboratory tests, but which are sufficiently dense to remain safe against liquefaction failure. In fact, both *cyclic mobility* and *cyclic liquefaction* refer to the same phenomenon which is defined as "cyclic mobility" by Casagrande (1936). The only difference between these two is that in cyclic liquefaction stress reversal occurs, whereas in cyclic mobility it will not occur.

2.7 SUMMARY

The principles of liquefaction, including definitions of liquefaction and the concepts of steady state strength and collapse surface, were summarized in this Chapter. A summary of behaviour of granular soils under monotonic and cyclic undrained triaxial tests were presented and different types of liquefaction were defined.

From all field experiences and laboratory test results, it can be reasonably concluded that gravitational flow liquefaction in the sense proposed by Casagrande and Castro can develop only in loose sands. In addition, liquefaction failure, i.e. flow of sands, will occur only if the driving shear stress is higher than the undrained steady state shear strength of the soil. The source of driving shear stress can be sloping grounds, foundation of buildings, or buoyancy because a buried structure is lighter than the displaced soil. For a given void ratio, the susceptibility to liquefaction increases with increases in confining pressure and with shear stresses acting on the sand.

Chapter 3

NUMERICAL MODELING OF LIQUEFACTION DEFORMATION ANALYSIS

3.1 INTRODUCTION

A simplified elasto-plastic model for liquefaction deformation analysis was developed by Gu (1992). The model, which simulates the collapse of liquefied soils, is based on the critical state boundary surface theory, and the concepts of steady state strength and collapse surface. Moreover, a hyperbolic strain softening model has been used to represent the post-peak behaviour of liquefied materials. Also simulated in this analysis is the process of stress redistribution followed by progressive deformation. This model has been introduced through a finite element analysis and used to perform the liquefaction failure analysis of the Lower San Fernando Dam following the 1971 earthquake (Gu et al., 1993a) and the liquefaction event at the Wildlife site following the 1987 earthquake (Gu et al., 1993b).

The elasto-plastic model was essentially developed for post-earthquake deformation analysis. In this research the model is adapted and extended for analysis of liquefaction induced by monotonic loading, namely static liquefaction. The model is also extended for

liquefaction analysis of very loose sands where the undrained steady state strength of the soil is not a single value, but a function of confining stress.

This Chapter presents a summary of this undrained model, adapting the model for static liquefaction and its extension for liquefaction analysis of loose sands.

3.2 UNDRAINED BEHAVIOUR OF SOIL

The critical state boundary surface was developed mainly for clay soils by Roscoe et al. (1958). They defined a "critical state line" as a junction between the Roscoe surface and the Hvorslev surface in a p'-q-e space, where p' is the effective normal stress, q is the deviator stress, and e is the void ratio of soil. Figure 3.1 illustrates the critical state boundary surface. Contractant behaviour occurs when the soil is sheared below the Roscoe surface and dilatant behaviour may occur when the soil is sheared below the Hvorslev surface under drained conditions. Therefore, the critical state line separates contractant behaviour from dilatant behaviour of soil. Under undrained conditions, pore pressure will increase if the soil is contractant or decrease if the soil is dilatant. In both drained and undrained conditions, the soil always fails on the critical state line.

The state boundary surface introduced by Roscoe et al. (1958) determines the yielding of materials. Elastic behaviour is defined for stress states inside the state boundary surface. For most natural soils, plastic shear strain may occur inside the state boundary surface. A modification is usually made for this problem by introducing an additional shear yielding surface.

The steady state line and the collapse surface for granular materials were introduced in the previous Chapter. The test results obtained by Sladen et al. (1985) suggested that the collapse surface may be observed by plotting the results of undrained triaxial compression tests in a normalized p'-q plane. The envelope of the peak strengths on this normalized p'-q plane forms the collapse surface.

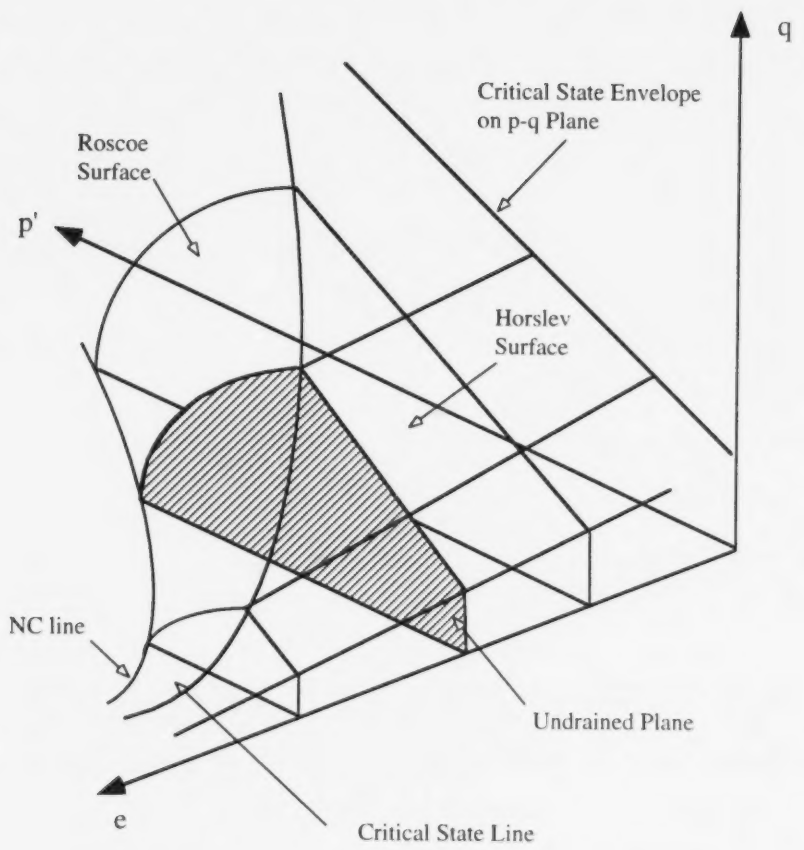

Fig. 3.1 The Critical State Boundary Surface Defined by Roscoe et al. (1958).

Peak shear stresses for samples tested at the same void ratio are dependent on the initial confining stress. It is of significance, however, that the peak strengths fall on a straight line in stress space and that this line passes through the steady state point. At a lower void ratio, the straight line will have the same slope but will pass through a higher point on the steady state line in stress space.

The observation that the peak strengths fall on a relatively straight line and that this line changes position only with void ratio has suggested the concept of a collapse surface in a three dimensional stress-void ratio space. For flow liquefaction to occur, the soil state has to reach the collapse surface and the shear stress must exceed the steady state shear strength. Another condition is the impedance of pore water drainage as the stress state approaches the collapse surface. Sands with stress states approaching or on the collapse surface will liquefy and collapse if drainage is impeded. If drainage is not impeded, the void ratio will change and the collapse line will move upward to represent the change in void ratio.

During strain softening, the pore water pressure continues to increase and causes the effective stress path to move downward along or slightly above the collapse surface. Therefore, the collapse surface defines approximately a critical state boundary and also a zone of strain softening behaviour of soils under undrained loading conditions. For very loose sands whose state lies on or very close to the collapse surface, only minimal excess pore pressure is necessary to trigger liquefaction. Loading may be essentially fully drained up to the point of failure.

The pore water pressure developed during strain softening is both the reason and the result for the collapse. If the pore water pressure can dissipate fast enough, the soil may move away from the collapse surface and experience either elastic unloading or plastic hardening. If the pore water pressure decreases, the strength of the soil will recover and the effective stress path will move up even though the steady state had been reached. This is as an elbow in the effective stress path in p'-q plane, and defined as limited liquefaction by Vaid et al. (1990).

3.3 STATE BOUNDARY SURFACE FOR LIQUEFIABLE SOILS

The idealized behaviour of contractant and dilatant sands under monotonic undrained shear is illustrated in Figure 3.2. Contractant sands reach a peak undrained strength that can be defined by the collapse surface. After passing the peak strength, contractant sands strain soften to steady state with additional increase in pore water pressure. The post-peak collapse behaviour is governed by strain softening behaviour. Dilatant sands may initially show a small increase in pore pressure before reaching the phase transformation line defined by Ishihara (1975). After passing the phase transformation line, the soil behaves in a strain hardening manner and the pore pressure decreases. The final load that can be carried by the dilatant sand is limited to the steady state strength even though some deformation may develop. The monotonic undrained triaxial tests on very loose to medium dense sands reported by Ishihara et al. (1991) confirmed the above concepts, as shown in Figure 3.3.

A similar response may be observed for contractant and dilatant sands subjected to undrained cyclic loading. Figure 3.4 illustrates this undrained cyclic response. For both contractant and dilatant sands, cyclic loads will generate positive pore pressure as effective stress path will move toward the state boundary surface. For initial static shear stresses larger than the steady state strength, strain softening will occur as the stress path reaches the collapse surface. For initial static shear stresses smaller than the steady state strength, the stress path may move beneath the steady state line and then pass to the dilatant side of steady state. When the cyclic stresses move up and down along the Hvorslev surface, cyclically-induced strains will be accumulated. These strains are defined as cyclic mobility behaviour by Casagrande (1971) and Castro et al. (1975).

For liquefiable soils, the state boundary surface under undrained conditions should be modified to include the following important characteristics.

(1) When the soil is collapsing from its peak to post-peak strength, strain softening behaviour occurs and the excess pore water pressure increases until the effective stress path reaches the steady state.

(2) A triggering condition should be defined for the strain softening behaviour and the undrained collapse of soil.

(3) Cyclic mobility should be included in the model.

(4) The effective stress path or the excess pore water pressure should be defined below the state boundary surface.

Figure 3.5 shows the proposed state boundary surface for liquefiable soils in a spatial form in p'-q-e space. This surface obviously considers the above characteristics. The steady state line is a curve in the space connecting the collapse surface and the Hvorslev surface. The collapse surface is a plane between the Hvorslev surface and the Roscoe surface. For soil on or close to the collapse surface, any small load or disturbance may result in strain softening and undrained collapse, regardless of whether it was brought to the point under a drained or undrained condition. The test results reported by Eckersley (1990) supports this type of failure. In his model test, a loose soil in an embankment model was brought to the collapse surface by raising the water table under fully drained conditions. The embankment model collapsed and large flow deformation was induced.

The laboratory test results on very loose samples of Ottawa sand, reported by Sasitharan et al.(1992), have further proved that the collapse surface is a state boundary. They conducted a drained test following the constant void ratio stress path obtained in an undrained test and two drained constant deviator stress path tests to investigate the sand behaviour close to the collapse surface. They found that the constant void ratio stress path followed under drained and undrained conditions are identical, as shown in Figure 3.6. The results of the two constant deviator stress path tests showed that slopes can collapse in undrained manner if the soil is very loose and the pore pressure rises, even if the soil is brought to the state of collapse under drained conditions.

The main difference between the proposed state boundary surface for sands, and the critical state boundary surface proposed by Roscoe et al. (1958) for clays, is the collapse surface. In reality, the Roscoe surface and the collapse surface are one curved state boundary. However, for the purpose of simplicity, the model for sands considers the strain softening part of the surface as a flat plane, i.e., the collapse surface.

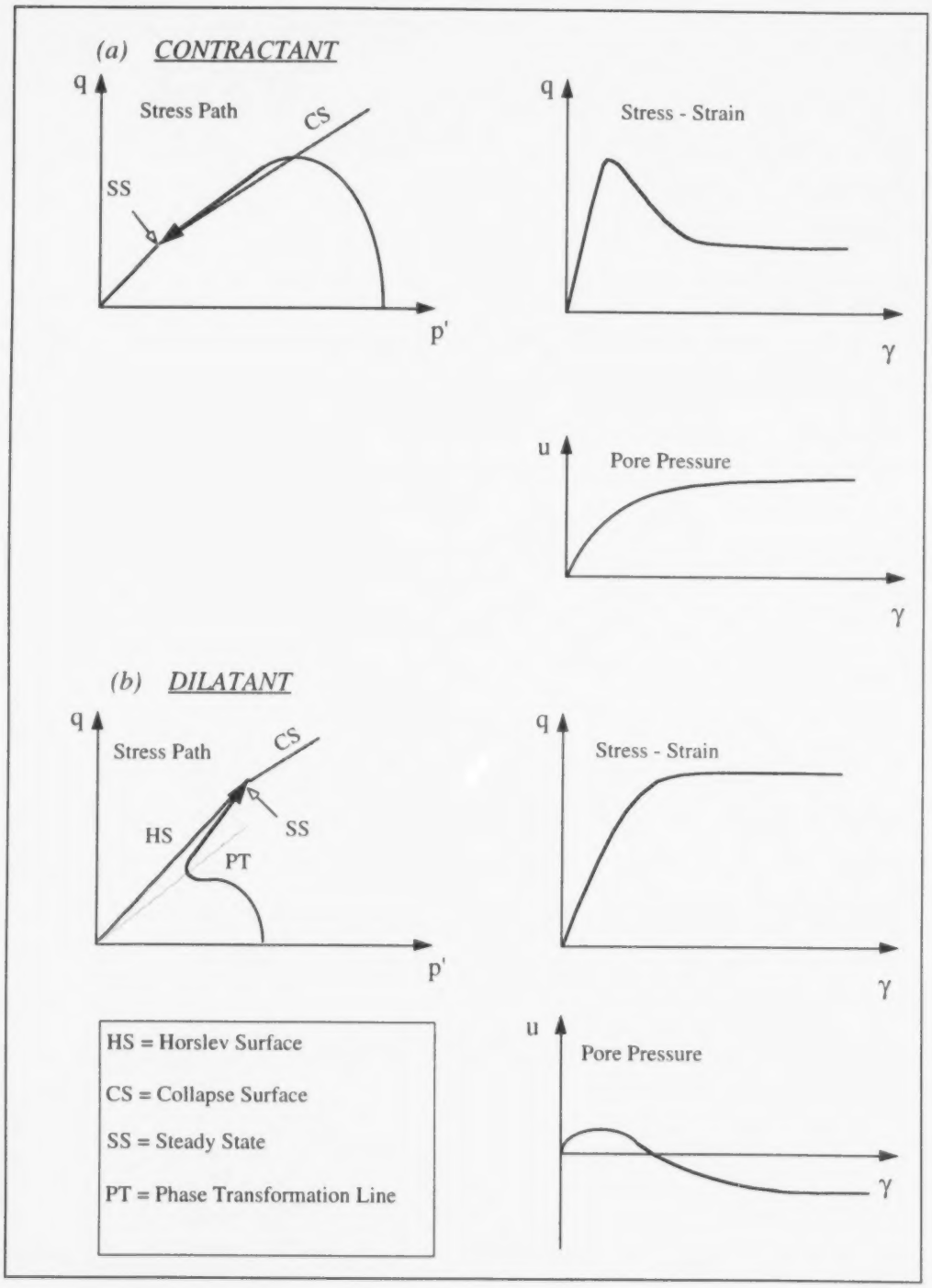

Fig. 3. 2 Idealized Soil Behavior under Undrained Monotonic Loading.

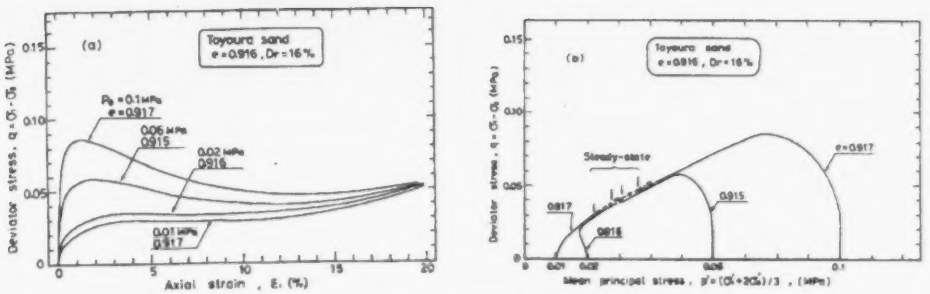

Fig. 6 Results of triaxial shear tests on very loose sand

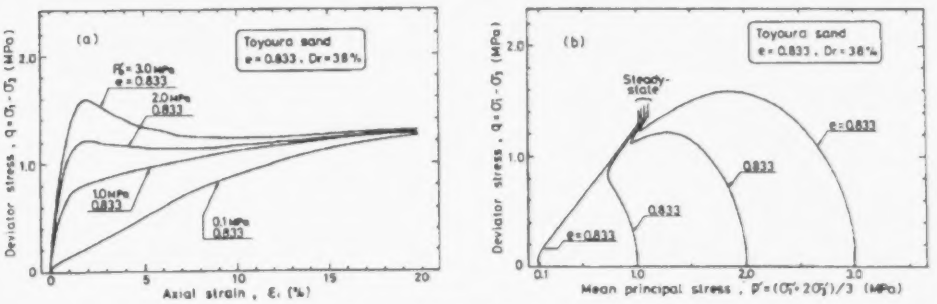
(a)
Toyoura sand
e = 0.833 , Dr = 38 %
Deviator stress , q = σ1 - σ3 (MPa)
Axial strain , ε1 (%)
(b)
Toyoura sand
e = 0.833 , Dr = 38 %
Steady-state
e=0.833
Mean principal stress , p' = (σ1' + 2σ3')/3 (MPa)

Fig. 7 Results of triaxial shear tests on loose sand

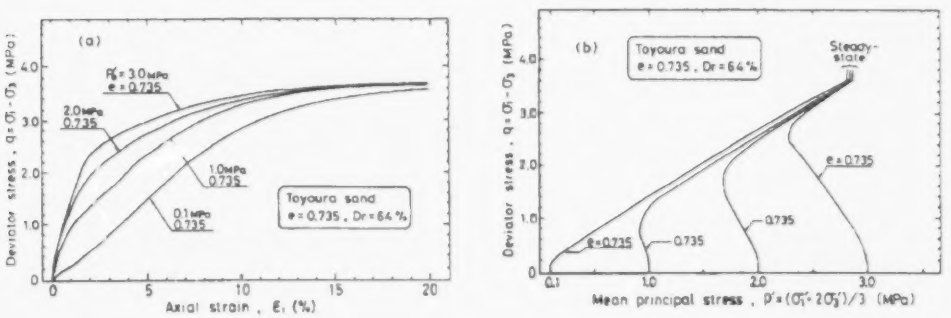
(a)
Toyoura sand
e = 0.735 , Dr = 64 %
Deviator stress , q = σ1 - σ3 (MPa)
Axial strain , ε1 (%)
(b)
Toyoura sand
e = 0.735 , Dr = 64 %
Steady-state
e=0.735
Mean principal stress , p' = (σ1' + 2σ3')/3 (MPa)

Fig. 3. 3 Soil Behaviour on Undrained Planes (after Ishihara et al., 1991).

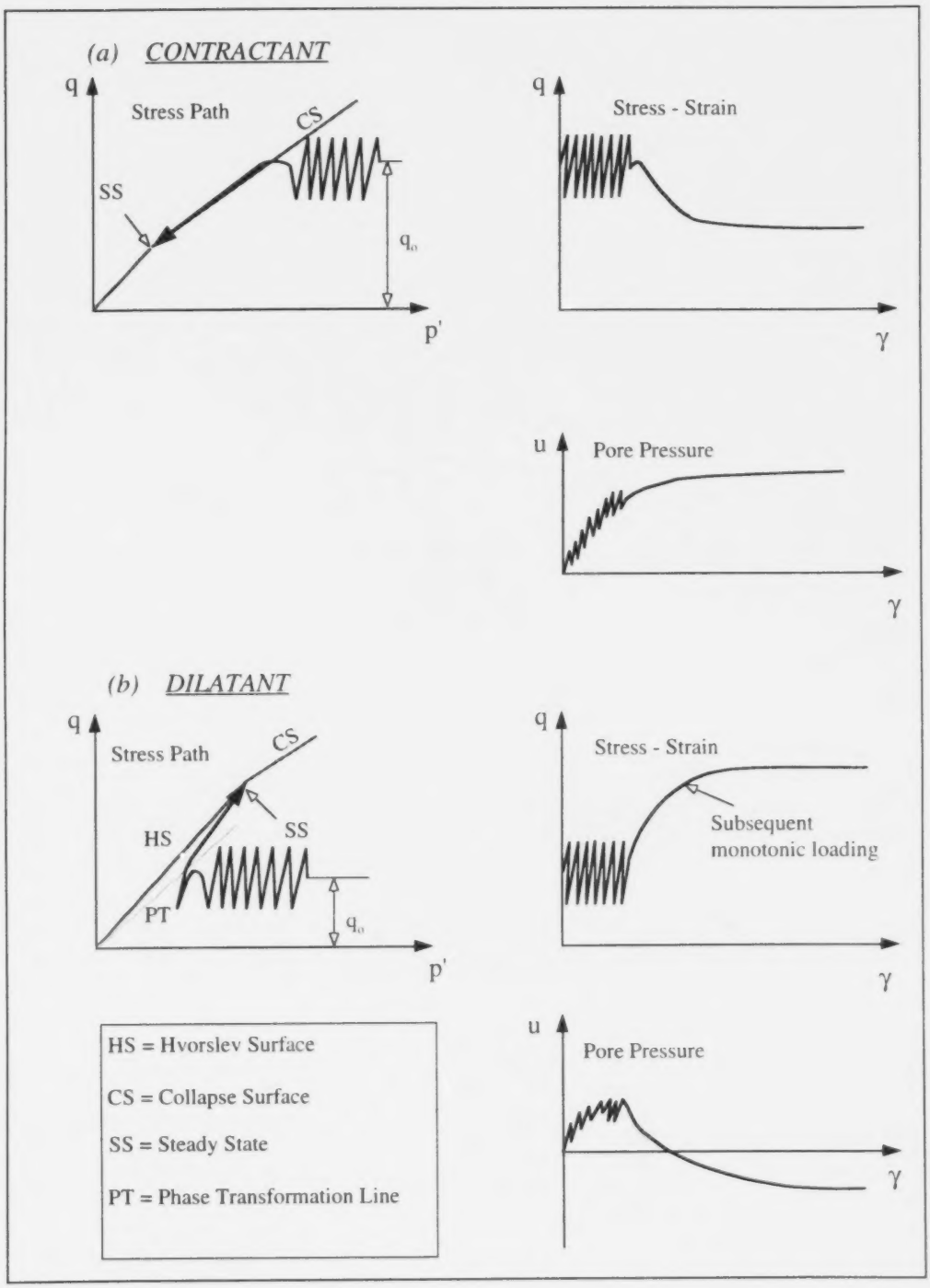

Fig. 3.4 Idealized Soil Behavior under Undrained Cyclic Loading.

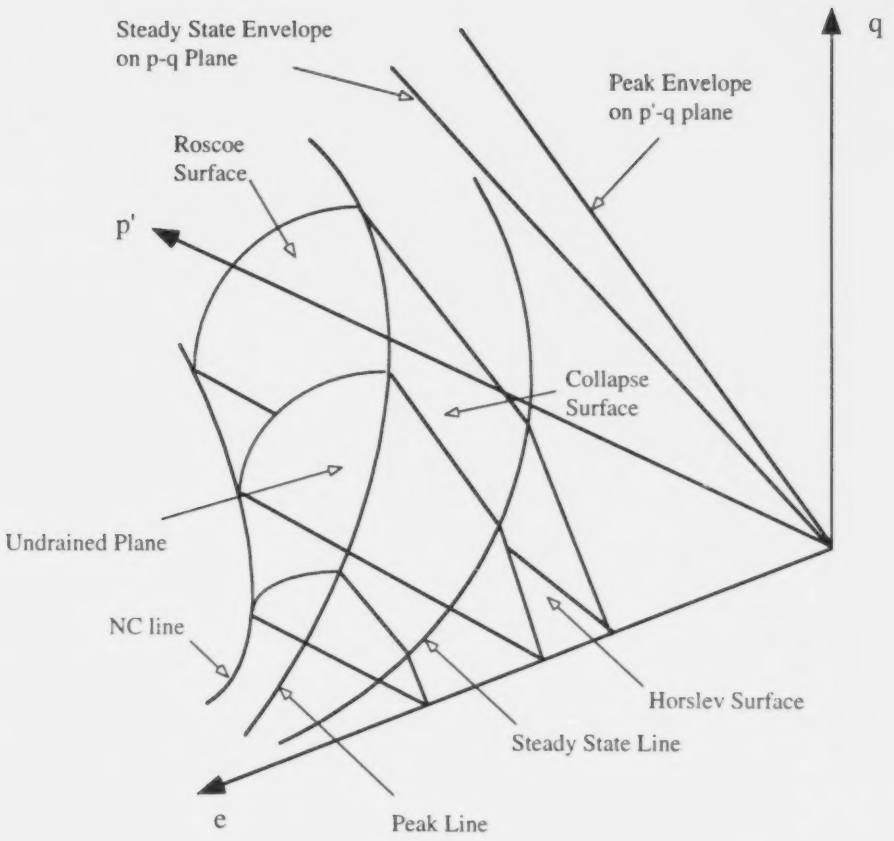

Fig. 3.5 State Boundary Surface for Liquefiable Soils [after Gu et al., 1994].

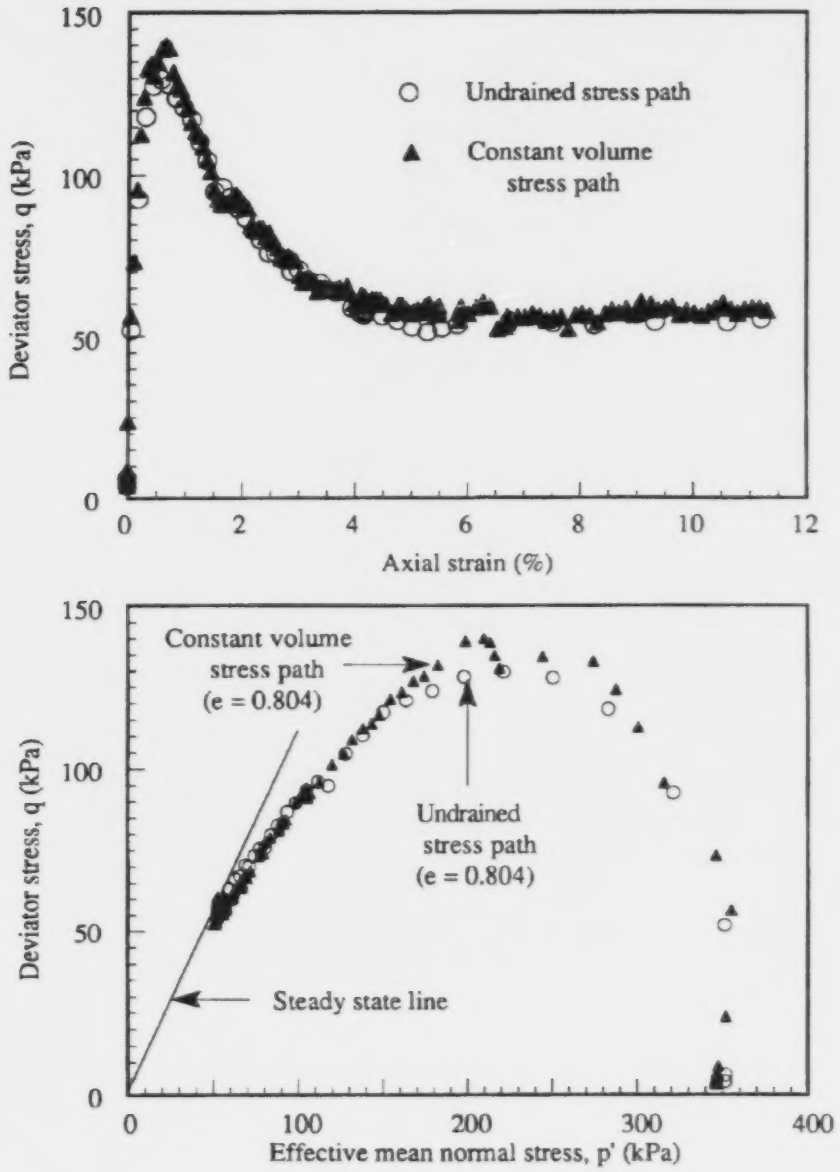

Fig. 3.6 Constant Volume and Undrained Stress Paths
[after Sasitharan et al., 1992].

3.4 AN ELASTO-PLASTIC MODEL FOR LIQUEFIABLE SOILS

In this model, liquefaction stability analysis is considered a fully undrained process. Therefore, the model for liquefiable materials is simplified to an undrained plane. This simplified model, as shown in Figure 3.7, consists of 3 zones of behaviour:

Zone 1: elastic or strain hardening behaviour occurs during loading by shear stress; excess pore water pressures will increase during monotonic or cyclic loading.

Zone 2: strain softening behaviour occurs; excess pore water pressure increases as the soil collapses and the soil reaches the steady state strength after the collapse.

Zone 3: elastic or strain hardening behaviour may occur; excess pore pressures decrease by loading of shear stress and increase by unloading of shear stress.

The effective stress path in zone 1 can be defined in laboratory undrained tests. When stress moves along these effective stress paths, total volumetric strain will not occur. Therefore, instead of defining a volumetric yield surface, an effective stress path is defined in this model. It means that the stress has to move along the effective stress path to satisfy the undrained condition in which no volumetric strain will occur.

When the driving shear stress of liquefiable soil reduces from its peak to the steady state strength, some parts of its associated energy will release, and stress redistribution within the soil structure will occur. If the liquefied soil has a relatively high driving shear stress, the stress redistribution may result in large deformation which in its excessive form can cause the flow failure of the soil structure. Whether the failure occurs or not, and what the extent of failure will be if it occurs, depends on the amount of the released driving shear stress, the drainage conditions and the boundary conditions.

The deformation caused by induced excess pore water pressures under fully saturated and undrained conditions is expected to be very small. This is inherent in the adopted assumption of incompressibility of the pore fluid and the soil particles. From a practical point of view, therefore, the liquefaction flow failure of soil structures are caused directly

by the stress redistribution and indirectly by the initially generated excess pore water pressures. In other words, the excess pore pressure brings the soil close to or to the collapse surface, but it is the stress redistribution, resulted from the driving shear stress release, which may cause the failure. The stress redistribution by itself will generate further pore pressures that in turn may cause further release in driving shear stress and further stress redistribution.

In order to consider the process of stress redistribution in liquefaction analysis of soil structures, a deformation analysis is essential. The finite element method is used for this analysis.

3.4.1 The Yielding Surface for Strain Softening

In plasticity theory, the stress strain relationship can be expressed as

$$\{d\sigma\} = [C]\ \{d\varepsilon\} \qquad [3.1]$$

in which:

$$\{d\varepsilon\} = \{d\varepsilon^e\} + \{d\varepsilon^p\} \qquad [3.2]$$

and

$$[C] = [C]^e - \frac{[C]^e \left\{\frac{\partial Q}{\partial \sigma}\right\} \left\langle \frac{\partial F}{\partial \sigma} \right\rangle [C]^e}{\left\langle \frac{\partial F}{\partial \sigma} \right\rangle [C]^e \left\{\frac{\partial Q}{\partial \sigma}\right\} - \left\langle \frac{\partial F}{\partial \varepsilon^p} \right\rangle \left\{\frac{\partial Q}{\partial \sigma}\right\}} \qquad [3.3]$$

where:

$\{d\sigma\}$ = stress increment

$\{d\varepsilon\}$ = strain increment

$\{d\varepsilon^e\}$ = elastic strain increment

$\{ d\varepsilon^p \}$ = plastic strain increment

$[C]$ = elasto-plastic constitutive matrix

$[C]^e$ = elastic constitutive matrix

F = yield function

Q = plastic potential function.

For associated flow rule assumption, $Q = F$.

For plastic shear strain, a shear yield surface should be defined in an elasto-plastic model. In plasticity theory, the material behaviour can be described by the yield function as follows:

(1) for elastic deformation

$$F\left(\sigma_{ij}, \varepsilon_{ij}^p\right) < 0, \qquad [3.4]$$

$$F\left(\sigma_{ij} + \Delta\sigma_{ij}, \varepsilon_{ij}^p + \Delta\varepsilon_{ij}^p\right) < 0 \qquad [3.5]$$

where: F is a function of yield surface, σ_{ij} are stresses and ε_{ij} are plastic strains.

(2) for elastic unloading

$$F\left(\sigma_{ij}, \varepsilon_{ij}^p\right) = 0, \qquad [3.6]$$

$$F\left(\sigma_{ij} + \Delta\sigma_{ij}, \varepsilon_{ij}^p + \Delta\varepsilon_{ij}^p\right) < 0 \qquad [3.7]$$

and

$$\left\langle \frac{\partial F}{\partial \sigma_{ij}} \right\rangle \left\{ d\sigma_{ij} \right\} < 0 \qquad [3.8]$$

(3) for plastic deformation and strain hardening

$$F\left(\sigma_{ij}, \varepsilon_{ij}^p\right) = 0, \qquad [3.9]$$

$$F\left(\sigma_{ij} + \Delta\sigma_{ij}, \varepsilon_{ij}^{p} + \Delta\varepsilon_{ij}^{p}\right) = 0 \qquad [3.10]$$

and

$$\left\langle \frac{\partial F}{\partial \sigma_{ij}} \right\rangle \left\{ d\sigma_{ij} \right\} > 0 \qquad [3.11]$$

(4) for plastic deformation and strain softening

$$F\left(\sigma_{ij}, \varepsilon_{ij}^{p}\right) = 0, \qquad [3.12]$$

$$F\left(\sigma_{ij} + \Delta\sigma_{ij}, \varepsilon_{ij}^{p} + \Delta\varepsilon_{ij}^{p}\right) = 0 \qquad [3.13]$$

and

$$\left\langle \frac{\partial F}{\partial \sigma_{ij}} \right\rangle \left\{ d\sigma_{ij} \right\} < 0 \qquad [3.14]$$

Since the plastic shear strains in zone 1 are small compared to the strains on the collapse surface and at steady state, an elastic behavior in this zone is adopted. For soils in zone 3, an elastic model is used because steady state strengths of loose soils are small.

3.4.2 Hyperbolic Strain Softening Model

For the soil behaviour during the collapse (zone 2) a hyperbolic strain softening model is used. The shear yield surface can be defined by either Von Mises, Tresca or Mohr Coulomb yield surfaces and the hyperbolic strain softening relationship defined by Chan and Morgenstern (1986,1989) is adopted. The yield function during the collapse is defined as:

$$F = q - k = 0 \qquad [3.15]$$

where:

$$k = k_{p}\left(1 - \frac{\bar{\varepsilon}^{p}}{a + b\bar{\varepsilon}^{p}}\right) \qquad [3.16]$$

and

$$\bar{\varepsilon}^p = \int d\bar{\varepsilon}^p = \text{equivalent plastic strain} \qquad [3.17]$$

$$d\bar{\varepsilon}^p = (\frac{2}{3} de_{ij}^p \; de_{ij}^p)^{1/2} \qquad [3.18]$$

$$de_{ij}^p = d\varepsilon_{ij}^p - d\varepsilon_{kk}^p \delta_{ij} / 3 \qquad [3.19]$$

$d\varepsilon_{ij}^p$ = increment of plastic strain

k_p is the peak strength and a and b are material parameters.

The features of the model enables one to specify the peak strength, residual strength, peak strain and post-peak strain softening behaviour independently. The peak strength is determined by the point of intersection between the effective stress path and the collapse surface.

Substitute $\bar{\varepsilon}^p = \infty$ into Equation [3.16],

$$b = 1/(1 - \frac{k_r}{k_p}) \qquad [3.20]$$

where k_r and k_p are the residual and the peak strengths respectively.

The parameter b depends on the amount of softening of the material. The parameter a can be determined by differentiating k with respect to ε^p in Equation [3.16].

$$\frac{\partial k}{\partial \bar{\varepsilon}^p} = -a \, k_p / (a + b\bar{\varepsilon}^p)^2 \qquad [3.21]$$

let $\bar{\varepsilon}^p = 0$

$$\frac{\partial k}{\partial \bar{\varepsilon}^p} = -(\frac{k_p}{a}) \qquad [3.22]$$

$\frac{k_p}{a}$ is the tangent of the initial slope of the post peak stress strain relationship of the material. Figure 3.8 illustrates a typical stress strain relationship of this model. The

parameter *b* defines the residual strength and the parameter *a* defines the post peak strain softening behaviour. As indicated, the lower the *a* value, the more brittle the post peak behaviour of the soil. Figure 3.9 shows the hyperbolic strain softening model for liquefiable soils.

During the stress calculation, the yield criterion should be satisfied within allowable tolerance. Then an iteration procedure is used to bring the stress state back to the yield surface. The contraction of yield surface, after the peak strength, will leave the state of stress outside the yield surface which is inadmissible and causes unbalanced loads. Therefore, the stress state after peak strength will be frequently projected onto the yield surface. The equilibrium condition must be satisfied by iterations of the unbalanced load. In this analysis, the perpendicular projection method defined by Chan (1986) is used. This method is illustrated in Figure 3.10.

For collapsible soils, the pore water pressure will increase during strain softening along the collapse surface. Figure 3.11 displays the increment of pore water pressure and the projection of the stress state for collapsible materials. As shown, the effective stress state will remain on the collapse surface.

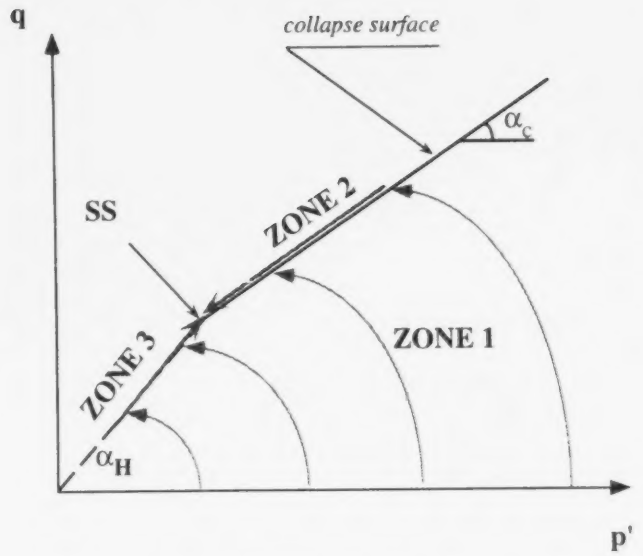

Fig. 3.7 Three Zones for Liquefiable Soils.

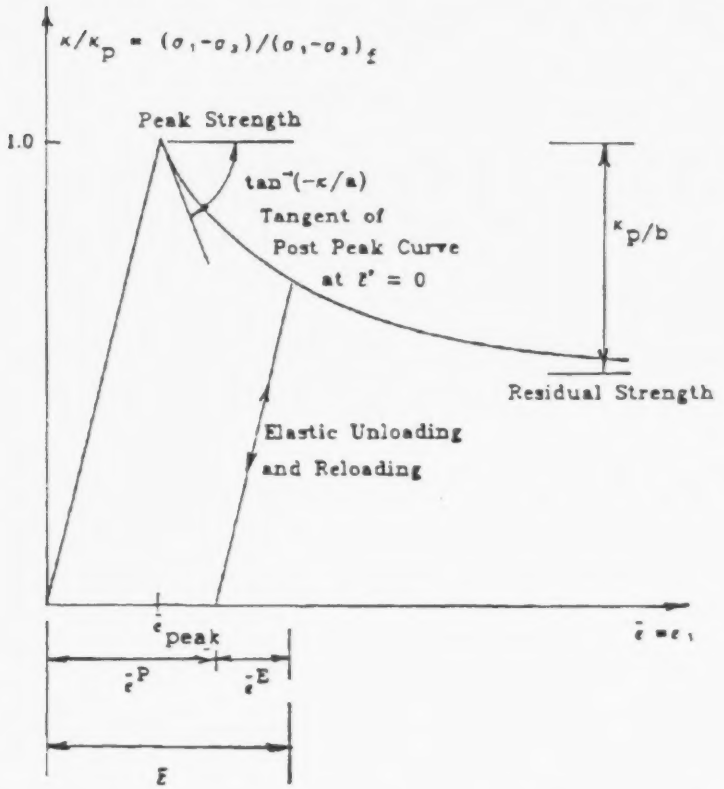

Fig. 3.8 The Hyperbolic Strain Softening Model (after Chan, 1986).

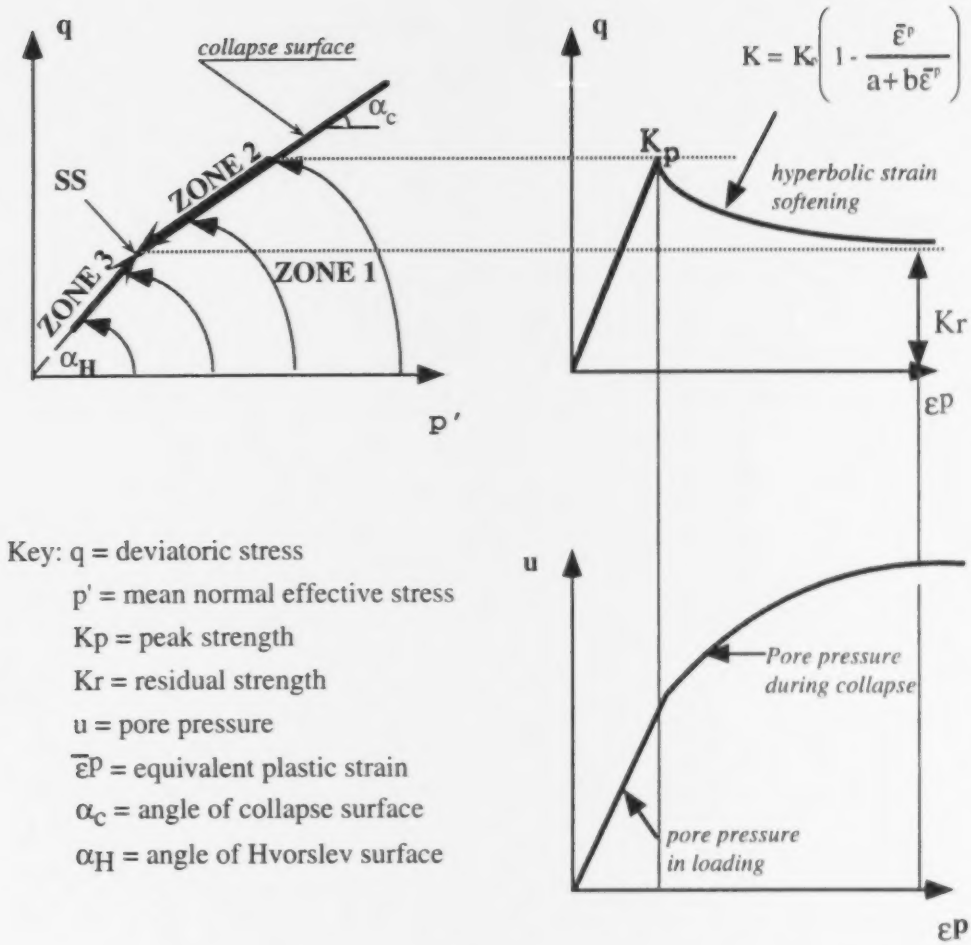

Key: q = deviatoric stress
p' = mean normal effective stress
Kp = peak strength
Kr = residual strength
u = pore pressure
$\bar{\varepsilon}^p$ = equivalent plastic strain
α_c = angle of collapse surface
α_H = angle of Hvorslev surface

Fig. 3.9 Hyperbolic Strain Softeninig Model for Liquefiable Soils [after Gu et al., 1994].

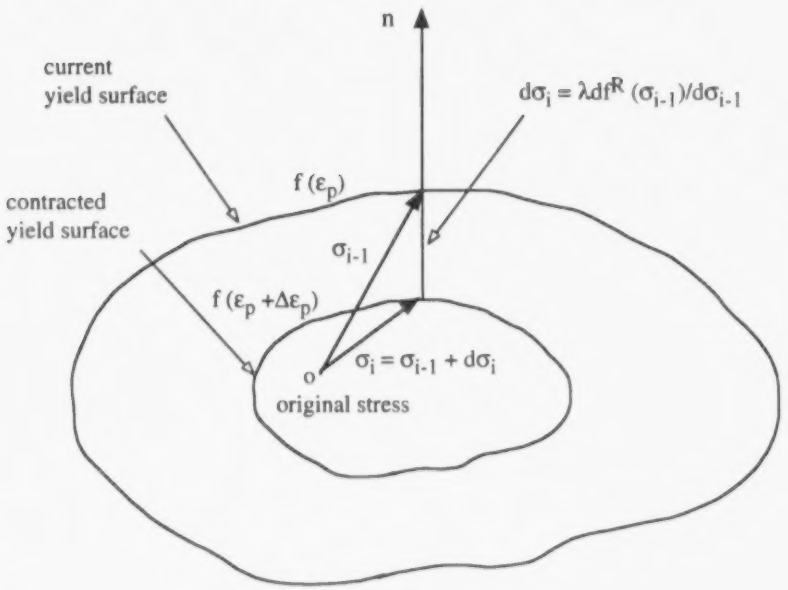

Fig. 3.10 Contraction of Yield Surface during Strain Softening.

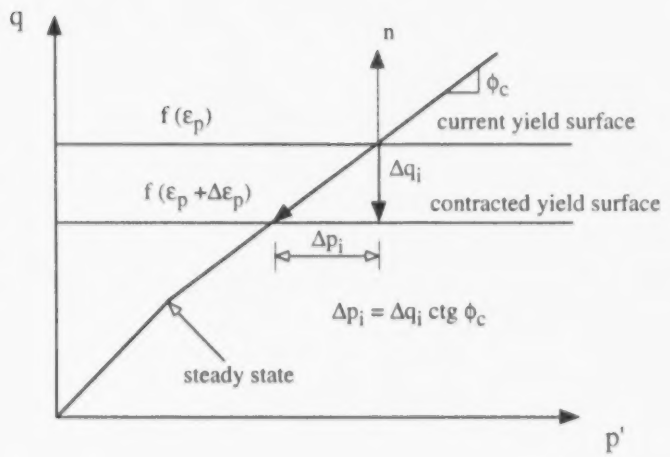

Fig. 3.11 Pore Pressure during Contraction of Yield Surface.

3.5 ADAPTING THE MODEL FOR STATIC LIQUEFACTION

The collapse surface plasticity model was essentially developed for post-earthquake deformation analysis of soil structures. A key requirement is the value of the excess pore pressure induced either by cyclic or static loading. The excess pore pressure can be introduced to the analysis as pore pressure ratios, u/u_m at the integration points of the elements, where u is the pore pressure induced directly by undrained cyclic or monotonic loading and u_m is the maximum pore pressure. The maximum pore pressure is defined as the horizontal distance between the effective stress state immediately before liquefaction and the collapse surface as shown in Figure 3.12. The following steps are involved in the analysis.

(1) Determine the effective stress distribution in the soil before earthquake, point 1 in Figure 3.12.

(2) Introduce the excess pore pressure generated in the soil by the earthquake to the program, line 1-2 in Figure 3.12.

This kind of analysis for an earthquake-induced liquefaction is relatively straightforward since the effective stress state of the soil before the earthquake is known. The net change in the deviator stress, q, is zero during the earthquake; therefore, having excess pore pressures of saturated elements of the soil, a q constant stress path can be defined in the liquefaction analysis.

If the static liquefaction is induced by a q-constant type of loading, like raising water levels in the soil, the above steps can be followed in the analysis. If the static liquefaction is induced by other means, such as rapid construction of an embankment or application of a surcharge over a loose saturated sand deposit, the stress path followed by the soil is not necessarily a q-constant stress path and therefore, the above procedure can no longer be used. Different potential stress paths, in which the deviator stress and the pore pressure change simultaneously, are shown in Figure 3.12.

In order to adapt the numerical model for static liquefaction, the following steps should be carried out during the analysis.

(1) Determine the in situ effective stress of the soil before application of the undrained loading.

(2) Perform an undrained effective stress analysis to simulate the soil behaviour at the time subjected to the undrained loading.

(3) Impose the collapse plasticity model, i. e., the boundary surface defined by the undrained steady state strength and the collapse surface (ss and cs lines in Figure 3.12), and let the computation go through the process of distribution of unbalanced load and finally reach the equilibrium.

Excess pore pressures in the undrained analysis (Step 2) will be calculated using Henkel's parameters, α and β. β is pore pressure parameter for the change in mean normal stress and α is the pore pressure parameter for the change in deviator stress. The total excess pore pressure, Δu, is calculated as:

$$\Delta u = \Delta u_\alpha + \Delta u_\beta \qquad [3.23]$$

$$\Delta u_\beta = \beta\left(\frac{\Delta\sigma_1 + \Delta\sigma_2 + \Delta\sigma_3}{3}\right) \qquad [3.24]$$

$$\Delta u_\alpha = \sqrt{(\Delta\sigma_1 - \Delta\sigma_2)^2 + (\Delta\sigma_1 - \Delta_3)^2 + (\Delta\sigma_2 - \Delta_3)^2} \qquad [3.25]$$

where $\Delta\sigma_1$, $\Delta\sigma_2$ and $\Delta\sigma_3$ are the increments of the total principle stresses.

3.6 FURTHER DEVELOPMENT OF THE MODEL

Stability analyses of sand under undrained loading conditions, such as post-liquefaction conditions, require a knowledge of the undrained steady state strength *(S_u)* of the sand. The parameter S_u is a key one in the collapse surface plasticity model. In liquefaction stability analyses of sandy soil structures, the most difficult issue is to determine what value of S_u best represents the field condition. Current practice tends to use correlations between S_u and Standard Penetration Test (SPT) or Cone Penetration Test (CPT) resistance (Seed and Harder 1990, Robertson 1990, Stark and Mesri). The above methods are reviewed and discussed by Fear and Robertson (1994).

Several researches have shown that samples of a given sand at a constant void ratio, when loaded undrained, will reach the same value of S_u despite the magnitude of the initial confining stresses (Sladen et al., 1985; Ishihara et al., 1991). The value of S_u is highly dependent on the value of void ratio. The higher the void ratio, the lower the S_u.

From a theoretical point of view, S_u can be determined from critical state soil mechanics. Fear and Robertson (1994) have presented the theoretical formulation of S_u in the following form:

$$\frac{S_u}{p'} = \frac{1}{2} M.exp\left(-\frac{\Psi}{\lambda_{ln}}\right) \qquad [3.26]$$

where

p' = initial effective confining stress

$$M = \frac{6 \sin \phi'_{ss}}{3 - \sin \phi'_{ss}}$$

ϕ'_{ss} = internal friction angle at steady state

Ψ = state parameter = e - e_{ss}

e = initial void ratio

e_{ss} = void ratio of the point on the steady state line(SSL) with the same p' as the initial state

λ_{in} = slope of SSL in e-$ln\ p'$ space

The above parameters are displayed in Figure 3.13. It can be seen that for a given sand (i.e. constant M and λ_{in}), S_u is a function of p' and state parameter Ψ, which by turn is a function of in situ void ratio, e. If S_u/p' is defined as the undrained steady state strength ratio, this ratio is exclusively a function of state parameter, Ψ.

Unfortunately, relating the undrained steady state strength (S_u) to the state parameter (Ψ), which is related to the void ratio (e), faces great difficulties due to the lack of techniques for confidently establishing in situ void ratios. The problem of establishing in situ void ratios is more crucial in very loose sands where the potential for liquefaction exists. An alternative way to overcome these difficulties is to bypass the state parameter (Ψ) in Equation [3.26], and to define a constant undrained steady state strength ratio (S_u/p').

For a given sand, a constant S_u/p' ratio applies only if the in situ consolidation line is parallel to the SSL on an e -$ln\ p'$ plot, resulting in a constant state parameter. Experiences with reconstituted sand samples in the laboratory indicate that the consolidation line for very loose sands can be approximately parallel to the SSL (Cunning, 1994). Hence, assuming a constant undrained steady state strength ratio may represent reasonably the field situation for very loose sands.

The minimum value of S_u/p' for a contractant sand (i.e., $\Psi > 0$) occurs when Ψ equals the maximum possible value, which is related to the highest possible void ratio. Considering the exponential element of Equation [3.26], one can observe that a small increase in Ψ leads to a dramatic decrease in the value of S_u/p'. Therefore from a practical point of view, the minimum value of the undrained steady state strength ratio can be evaluated as low as zero. However, the maximum value of S_u/p' for a contractant sand is related to $\Psi=0$, and equals to $0.5M$. Hence for a given sand (i.e., constant M and λ_{in}), a range for S_u/p' between 0 and $0.5M$ can be defined.

On the basis of the above discussion, the elasto-plastic model for liquefiable soils was extended for cases where the undrained steady state strength of the liquefiable soil is no longer a single value in the entire region of the liquefiable soil, rather it is a function of the mean normal effective stress, i.e., $S_u = f(p')$. In the extended version of the model, the strength parameter of the liquefiable soil is introduced to the analysis in the form of undrained steady strength ratio (S_u/p').

For very loose liquefiable soils, using an undrained steady state strength ratio is more representative of the field conditions than using a single value of steady state strength. Introducing S_u/p' to the analysis also prevents early instability and divergence in the process of finite element computation.

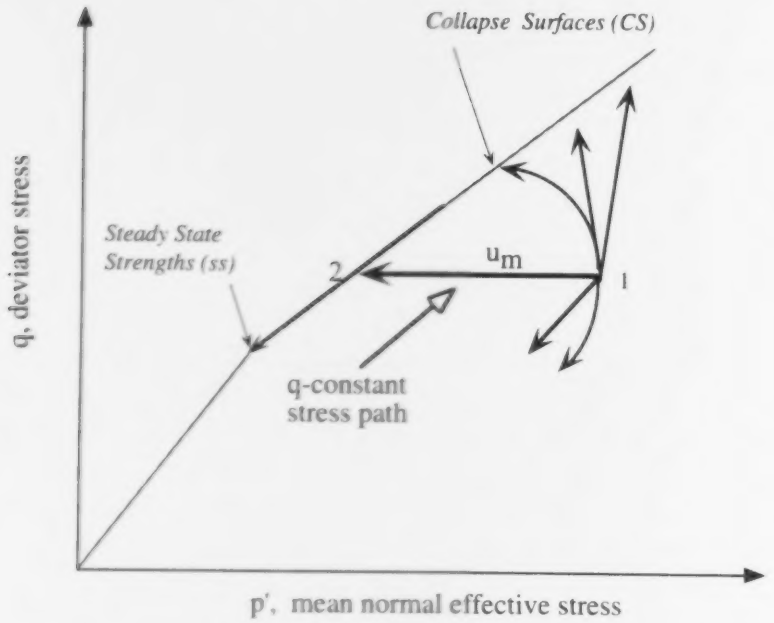

Fig. 3.12 Potential Stress Paths in Static Liquefcation.

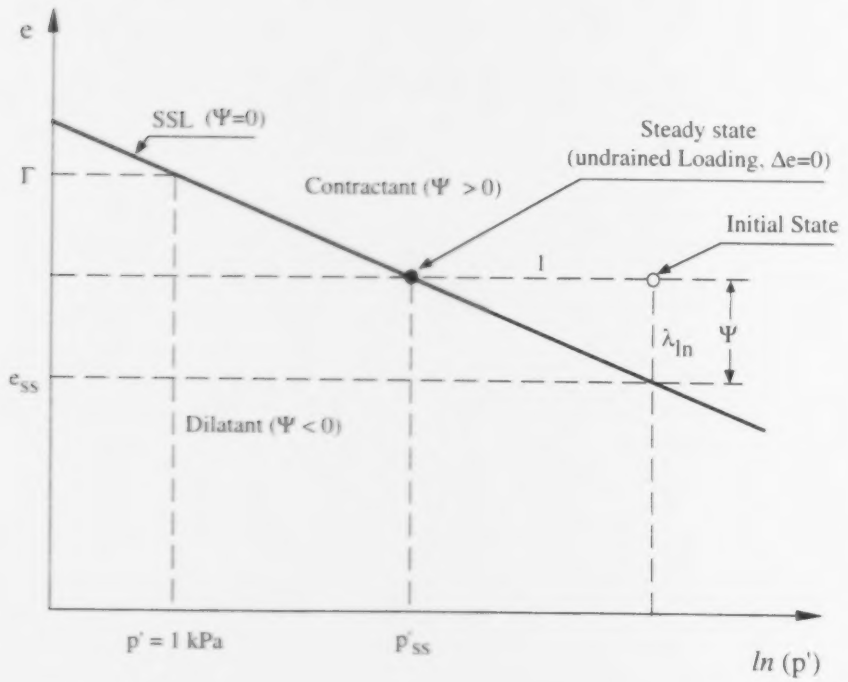

Fig. 3.13 Steady State Line in *ln*(p')-e Plane.

Chapter 4

POST-EARTHQUAKE DEFORMATION ANALYSIS OF THE UPPER SAN FERNANDO DAM[1]

4.1 INTRODUCTION

The downstream movement in the Upper San Fernando Dam was one of the major effects of the San Fernando earthquake of February 9, 1971. The earthquake had a Magnitude of 6.6 in the Richter scale and occurred at 6:00 a.m. in the San Gabriel Mountains north of the City of Los Angeles. The immediate effect of the earthquake was a downstream movement of the dam. A settlement of about 3 feet (0.9 m) and a downstream lateral movement of about 5 feet (1.5 m) at the crest of the dam was observed. The earthquake also resulted in almost catastrophic failure of the upstream embankment of the Lower San Fernando Dam.

Although the Upper San Fernando Dam did not fail due to the earthquake, the relatively large deformation of the downstream slope of the dam was alarming since the dam could

---

[1] A summarized version of this Chapter is submitted as a paper to the International Symposium: Seismic and Environmental Aspects of Dams Design, Earth, Concrete and Tailings Dams, Santiago, Chile, October 16 - 18, 1996.

have failed under more crucial conditions, i. e., a stronger earthquake and (or) a higher level of water in the reservoir.

Following the earthquake, extensive research works, including laboratory tests, in-situ tests and analytical studies, were conducted to investigate the mechanisms of the upstream failure of the Lower San Fernando Dam and the downstream movement of the Upper San Fernando Dam. The research works attributed the downstream movement of the Upper San Fernando Dam to the liquefaction of the downstream hydraulic fill of the dam (Lee et al., 1975 and Seed et al., 1975).

The movement had been triggered by liquefaction of the hydraulic fill in the lower part of the downstream shell, resulting in large deformation through the whole part of the downstream. The consequence of the downstream movement of the dam was the development of some cracks in the embankment, opening of joints in the outlet conduit through the embankment and formation of a sink-hole along the line of the conduit due to erosion through the joints. The effects of the earthquake on the dam are illustrated in Figure 4.1, which displays a cross section of the dam both before and after the earthquake. Numerical analysis of the earthquake effects on the Upper San Fernando Dam was performed by Seed et al. (1975) and Serf et al.(1976). The analyses were based on the dynamic response of the dam to the earthquake. A review of the methods and results of the above analyses will be presented later.

The purpose of this chapter is to present a post-earthquake deformation analysis of the Upper San Fernando Dam. The analysis, based on an undrained elasto plastic model, simulates the collapse of liquefied materials. The model is based on a state boundary surface, the undrained behaviour of liquefied soils and the concepts of steady state strength and collapse surface. A summary of the numerical model has been presented in Chapter 3.

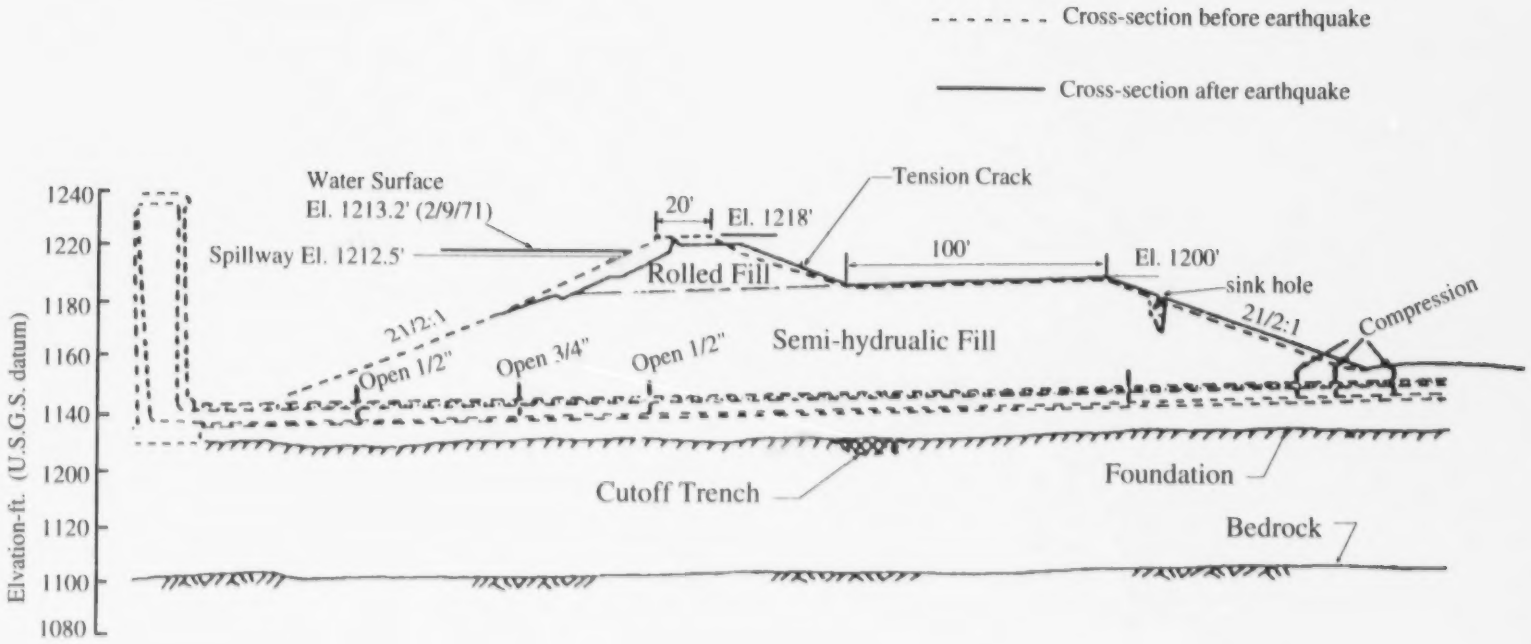

Fig. 4.1 Cross-section through Upper San Fernando Dam (1 ft = 0.305 m) [modified after L. A. Dept. of Water and Power].

Before presenting the post-earthquake deformation analysis of the Upper San Fernando Dam, the literature review, including the method used to construct the dam, the material properties of the dam, the effects of the earthquake on the dam and the numerical methods used by the other researchers to analyze the earthquake-induced deformation of the dam, will be summarized.

4.2 LITERATURE REVIEW

4.2.1 Construction of the Dam

Construction of the Upper San Fernando Dam began in 1921. In that year, the elevation of the dam was brought to 365.80 m (1200 feet). The initial plan was to raise the embankment to a final crest of 377.4 m (1238 feet). However, construction of the dam was completed by adding a rolled fill section at the upstream side of the dam, bringing the final crest elevation only to 371.3 m (1218 feet). The upstream side of the dam was protected by concrete paving .

There is no information about details of the method used to construct the dam, but the general technique employed was the "semihydraulic fill" method, a variation on the "hydraulic fill" construction method (Seed et al., 1975). In the hydraulic fill method, material for the dam is sluiced at the borrow area and conveyed to the site through pipes by pumping or gravity. It is discharged on beaches at the upstream and the downstream edges of the dam and flows toward the centre. Coarser materials deposit quickly to form the shell of the dam and finer materials settle out more slowly to form the impermeable core at the centre of the dam. Ideally, the end result is an overall gradation from coarse material at the faces, forming a strong shell, to the finer material at the centre forming an impermeable core. This method was used in construction of the Lower San Fernando Dam.

In the semihydraulic fill construction method, the fill is excavated dry in the borrow area, hauled to the edges of embankment by wagons, and dumped into place by hydraulic jets operating from floating barges. As with the hydraulic fill method, the finer material is

transported down into the pool to form the core, while the coarser materials stayed near the beaches to form the shell. This method was used in construction of the Upper San Fernando Dam. Discussions about details of the hydraulic fill and the semihydraulic fill methods is beyond the scope of this chapter. The reader interested in the subject is directed to the paper written by Whitman (1970).

4.2.2 Soil Properties of the Dam

Despite the differences in the construction methods of the Lower and the Upper San Fernando Dams, investigations by bore holes and trenches made after the earthquake of February 1971 showed no appreciable differences in the material properties of the dams (Lee et al., 1975).

The Upper Dam was constructed directly on alluvium, consisting of layers of stiff clays and clayey gravels. A cut-off trench, for the purpose of site preparation, was provided at the middle of the cross-section of the dam, as shown in Figure 4.1. To determine material properties of the alluvium foundation and the embankment in both the Lower and the Upper Dams, an extensive program, including field inspections, standard penetration tests, in-situ density tests, undisturbed sampling, index testing, seismic surveys and laboratory loading tests was conducted.

Standard penetration tests were made at both dams. In the Lower Dam, the blow counts (N) in the hydraulic fill ranged from 10 to 25 as shown in Figure 4.2; whereas in the Upper Dam, the blow counts in the hydraulic fill were less. There is no direct, detailed information about the blow counts versus the depth for the hydraulic fill of the Upper Dam (as Figure 4.2 for the Lower Dam). However, there is detailed information about relative densities determined from the standard penetration test data, which is shown in Figure 4.3. Relative densities were estimated using correlation proposed by Gibbs and Holtz (1975). Therefore, it is convenient to back figure blow counts versus depth (from Figure 4.3) for the hydraulic fill of the Upper San Fernando Dam.

Field investigations carried out in the Upper Dam consisted of excavating trenches and performing seismic surveys. Four trenches excavated along the width of the downstream

berm indicated that the hydraulic fill was made up of alternate layers of clean sand, silty sand and sandy silt. Figure 4.4 shows grain size distribution in the hydraulic fill of the dam, provided from the five samples taken from the outer shell towards the centre of the embankment along the downstream width. Figure 4.4 also shows the locations where the samples were taken.

At several locations field densities were determined by the sand cone method. In addition, a number of soil samples at each field density location was taken to determine the maximum and the minimum densities in the laboratory. The calculated average relative density for the hydraulic fill varied from 51% - 58% and for the foundation alluvium from 65% - 70%.

To determine soil strength under static loading conditions, a series of static loading triaxial tests were performed on isotropically consolidated samples at effective confining pressures ranging from 1 ton/sq. ft - 4 tons/sq. ft. (96 kN/m^2 - 380 kN/m^2). Both consolidated drained and consolidated undrained tests with pore pressure measurements were conducted. The parameters obtained from the static triaxial tests on the hydraulic fill and the alluvial soil samples are presented in Table 4.1.

Static undrained strength of the clay core was obtained by conducting vane shear tests. The vane tests were carried out on the clay seams found in the Shelby tubes and on some clay seams exposed in the inspection trenches. The measured undrained shear strength, S_u, is reported to be in good agreement with the relationship $S_u/p' = 0.24$, where p' is the effective overburden pressure.

Atterberg limit tests were performed on a number of samples of the clay found in the hydraulic fill at both the Upper and the Lower Dams. The Liquid Limit ranged from 37 - 60 and the Plasticity Index ranged from 20 - 40.

Comprehensive descriptions of the construction history and the material properties of the San Fernando Dams are given in the papers written by Lee et al. (1975) and Seed et al. (1975).

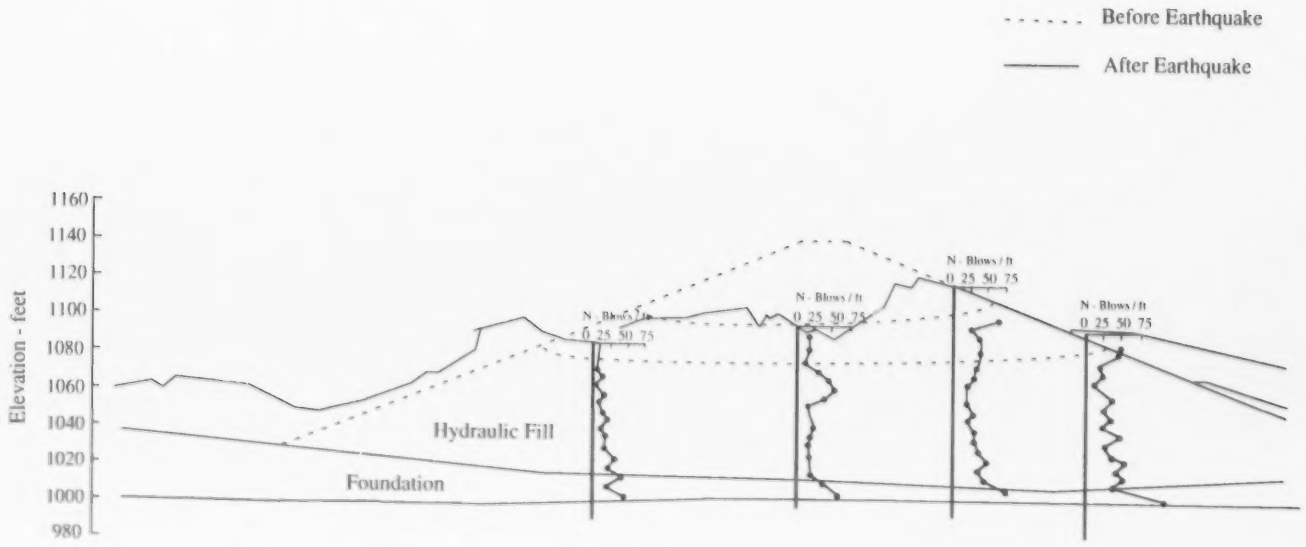

Fig. 4.2 Results of Standard Penetration Tests (SPT) in Lower San Fernando Dam [modified after Seed et al., 1975].

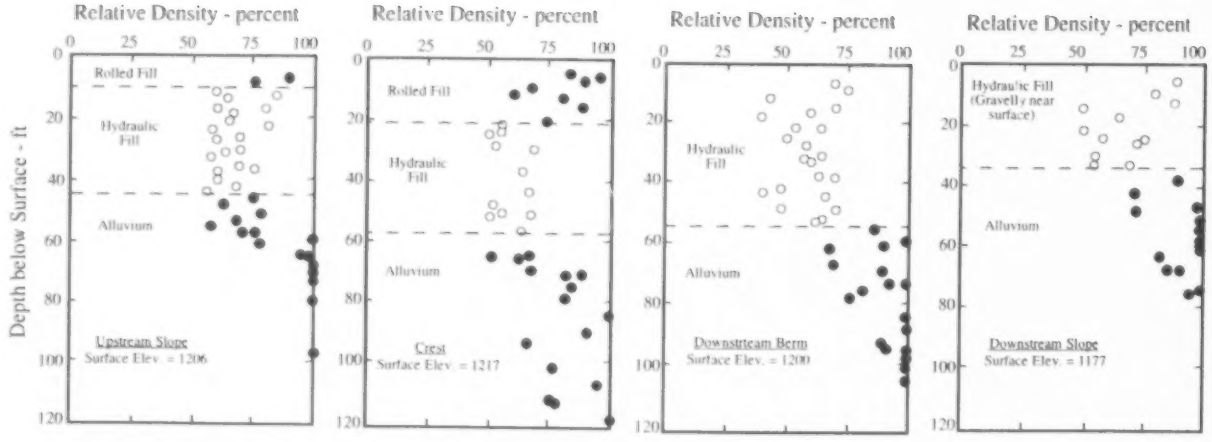

Fig 4.3 Relative Densities Determined from Standard Penetration Test Data in Upper San Fernando Dam (1 ft = 0.305 m) [modified after Lee et al., 1975].

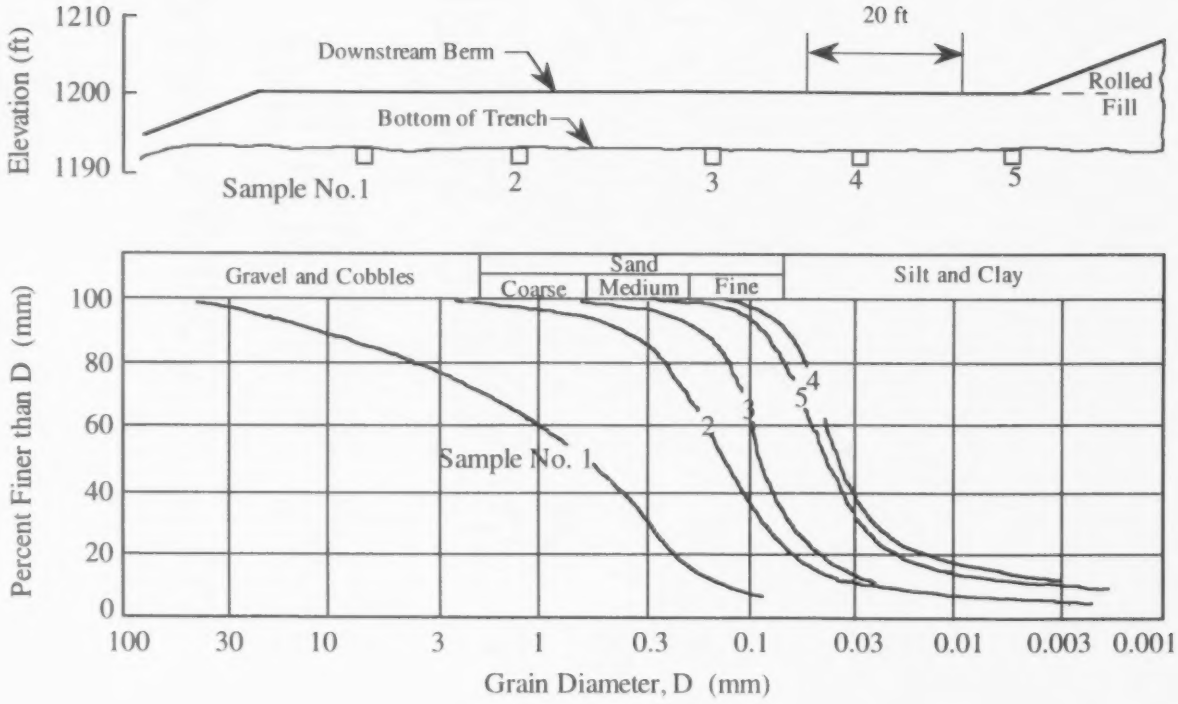

Fig. 4.4 Grain Size Distribution in Hydraulic Fill From Outer Shell towards Centre of Embankment [modified after Lee et al., 1975].

Table 4.1 Soil Parameters Used in Static Analysis of The San Fernando Dams (after Lee et al., 1975).

Soil Parameter	Symbol (units)	Upper Dam		Lower Dam	
		Hydraulic Fill	Alluvium	Hydraulic Fill	Alluvium
Dry unit weight	γ_d (kN/m^3)	18.82		16.63	17.26
Buoyant unit weight	γ_b (kN/m^3)	9.41	10.51	10.04	10.67
Strength parameters	c	0	0	0	0
	$\phi°$	37	37	37	38
	R_f	0.78	0.66	0.72	0.76
Young's modulus parameters	K	420	280	510	330
	n	0.52	0.8	0.54	0.41
Poisson's ratio parameters	G	0.33	0.32	0.41	0.40
	F	0.12	0.10	0.23	0.16
	D	10.0	9.0	9.4	5.8

Note : Data are from Consolidated Drained (CD) tests.

4.2.3 Effects of the Earthquake on the Dam

The main effect of the earthquake on the Upper San Fernando Dam was the downstream movement of the downstream hydraulic fill embankment and the crest. Shortly after the earthquake, vertical and horizontal displacements were measured at several points on the maximum section of the dam. The measured values at these points are illustrated in Figure 4.5. In addition, a two feet high pressure ridge was reported to have developed at the downstream toe of the dam. Accordingly, this ridge may have occurred in the hydraulic fill blanket somewhere below the toe of the dam. No measurements were reported from the upstream slope.

Variation of the water level in the piezometers during and after the earthquake was another important effect. Figure 4.6 illustrates locations of these piezometers and the water level changes following the earthquake. According to Seed et al. (1975), the increases for piezometers 1 and 2 were so large that the water overflowed from the top of the well casings and, therefore, the maximum changes could not be measured. Moreover, since the first observations on these piezometers were made about 24 hours after the earthquake, the actual increase in piezometer 3 was likely much higher.

In addition, the earthquake caused the following effects which could have been either directly due to the earthquake, or the consequences of the downstream movement of the embankment:

- several longitudinal cracks in the upstream and the downstream
- formation of a large sink hole in the surface above the downstream portion of the outlet conduit
- opening up of joints in the outlet conduit
- inducing sand boils in the downstream

It is not known whether the movement of the dam occurred during the earthquake or after. However, according to the reported field observations, the movements were due to the increase in pore water pressure and a corresponding weakening of the soil within a large portion of the dam. From the field observations, Seed et al. (1975) concluded that the zone of movement within the dam extended vertically over a large portion of the embankment, and was not limited to a well-defined slip surface at depth. The observed increases in piezometric levels, together with the sand boils in the fill at the downstream toe, suggest that the movements could have been associated with liquefaction of some zones within the dam.

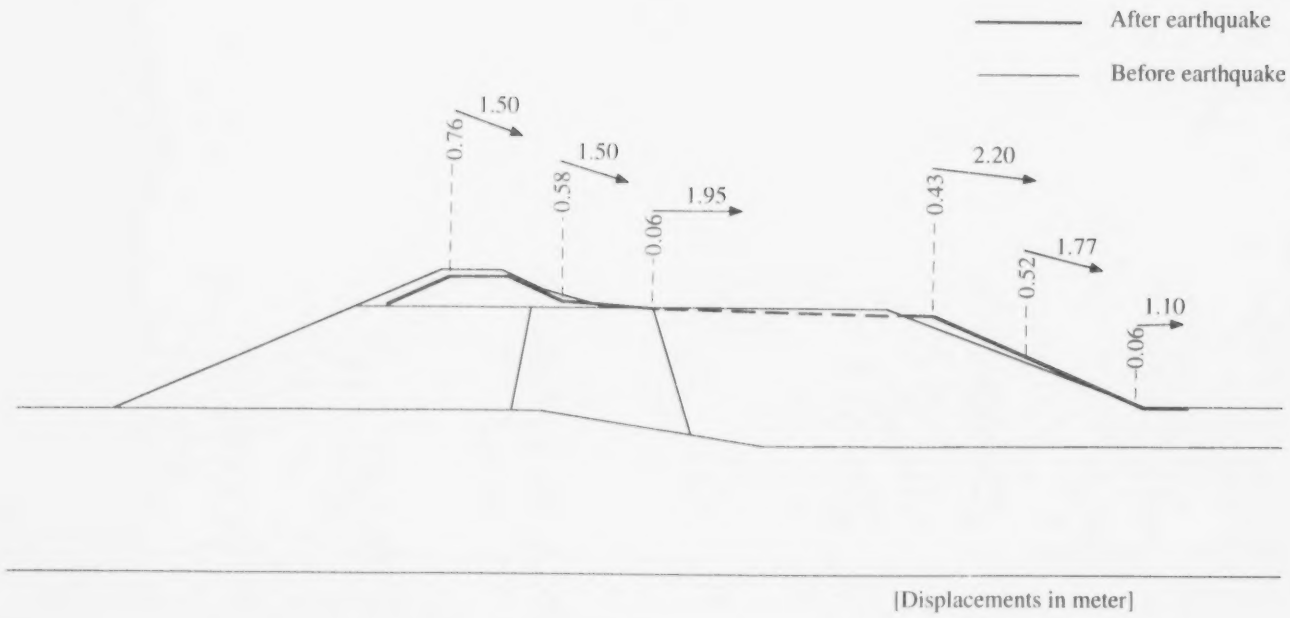

Fig. 4.5 Displacements Measured after Earthquake [modified aftr Serf et al., 1976].

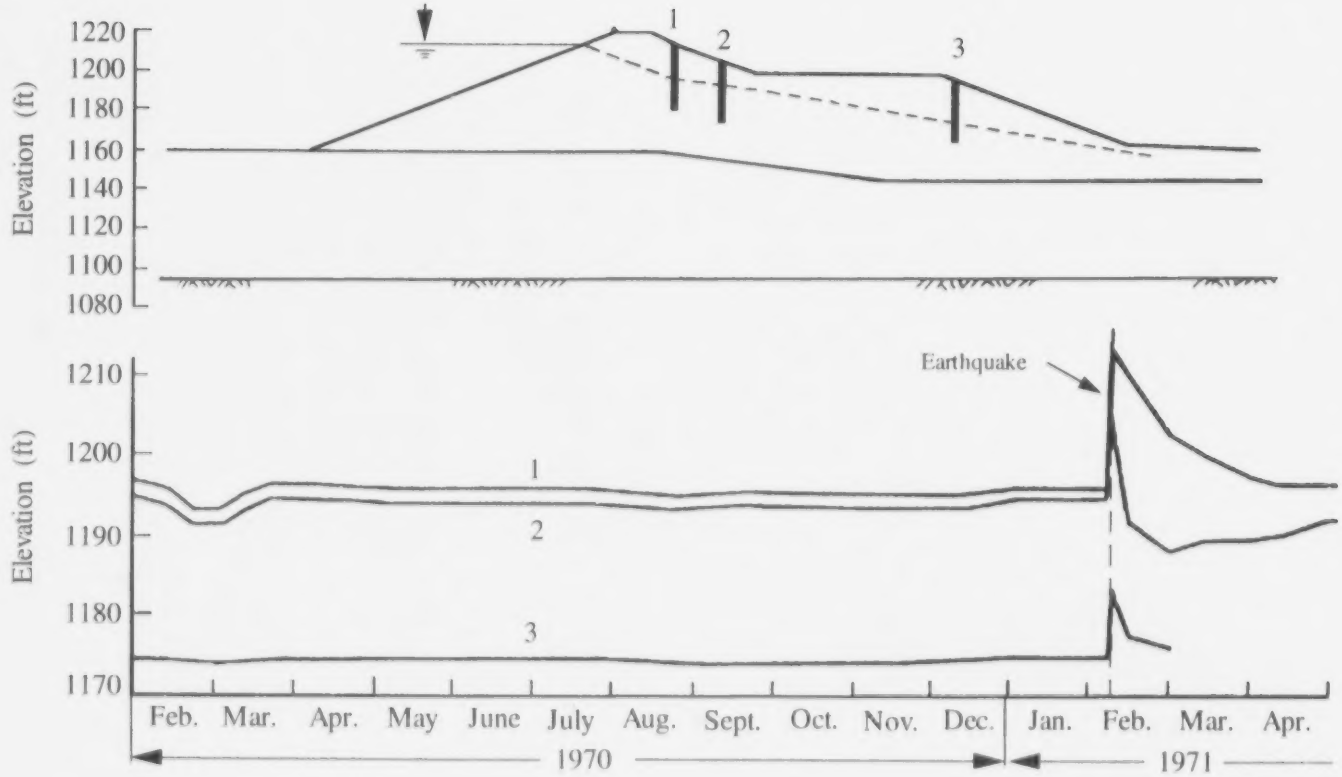

Fig. 4.6 Changes in Water Level in Piezometers Following the Earthquake (1 ft=0.305 m), [modified after Seed et al., 1975].

4.3 EARTHQUAKE ANALYSIS

Considering the historical evolution of the earthquake analysis of soil structures, three different types of analyses have been developed:

(1) pseudo-static analysis

(2) dynamic analysis

(3) post-earthquake deformation analysis

4.3.1 Pseudo-static Analysis

In this type of stability analysis, the stability of a potential sliding mass is determined as for static loading conditions. The effect of the earthquake is taken into account by including an equivalent horizontal force, acting on the potential sliding mass, in the computations. The horizontal force representing the earthquake effects is defined as the weight of the sliding mass multiplied by a seismic coefficient, K. The value of K is related to the level of seismicity of the region where the soil structure is located.

Pseudo static stability analysis of the Upper San Fernando Dam is discussed by Seed et al. (1975). For a seismic coefficient of 0.15, the computed Factor of Safety was about 2.00 for conservative soil strengths and about 2.50 for the average strengths. They showed that to compute a Factor of Safety of 1.0 (considering that the 1.5m downstream movement is about the limit of the tolerable movements), a seismic coefficient, K, in the range of 0.43 - 0.55 should be used in the computation procedure. However, in United States practice, the value of seismic coefficient for design purposes normally ranges from 0.05 to 0.15.

4.3.2 Dynamic Analysis

The dynamic finite element analysis proposed by Seed (1966) involves the following steps.

(1) Determine the initial stresses in the embankment before earthquake.

(2) Determine the characteristics for the motion developed in the rock underlying the embankment and its foundation during the earthquake.

(3) Evaluate the response of the embankment to the base rock excitation and compute the dynamic stresses induced in representative elements of the embankment.

(4) By subjecting representative samples of soil to the combinations of pre-earthquake conditions and superimposed dynamic stress applications, determine by laboratory test the effects of the earthquake-induced stresses on soil elements in the embankment. These effects will induce any evidence of liquefaction and the deformation induced by the earthquake loading.

(5) From a knowledge of the deformation induced in individual soil elements in the embankment, evaluate the overall deformation and the stability of the embankment.

Dynamic finite element analysis of the Upper San Fernando Dam was performed by Seed et al. (1973). The earthquake acceleration history used as input to the dynamic analysis was a modification of the record obtained at the Pacoima Dam, with a peak acceleration of 0.6g. Figure 4.7 presents the response analysis of the dam during the earthquake to base motions determined from the modified Pacoima record.

Figure 4.8 shows the results of the dynamic analysis, expressed as strain potential values. To approximate the deformations of the dam, the average shear strain potential for a vertical section at the centre of the dam was multiplied by the section height to obtain the downstream movement of the crest. Accordingly, the value calculated for the horizontal downstream movement was approximately 6 feet (1.83 m). This method of analysis did not permit computation of vertical movements.

Taking advantage of the shear strain potentials that resulted from the dynamic analysis, Serf et al. (1976) performed a series of static analyses using linear and nonlinear modified deformation modulii. They assumed that the effect of the earthquake on the dam was a reduction in the stiffness modulus of the materials due to the cyclic shear strain caused by

the earthquake motion. The modified modulus was calculated for each element using the initial stresses and the value of strain potential for the element. Table 4.2 presents soil parameters used by Serf et al. Figure 4.9(a) shows the deformations calculated by the nonlinear modified modulus analysis. As indicated, the deformations are much lower than the measured deformations shown in Figure 4.5.

To obtain more realistic results, Serf et al. (1976) performed a nonlinear analysis using an equivalent nodal force method. In this method, a set of nodal point forces, estimated from the strain potentials obtained from the dynamic analysis, was applied to the nodes of the finite element mesh to simulate the deforming effect of the earthquake. However, again the calculated results were much lower than those observed during the earthquake; therefore, more modifications were performed. The problem of the tension crack that arose with the elements near the centre line of the embankment was dealt with by introducing a very low stiffness modulus for these elements in the analysis. Figure 4.9(b) shows the deformations computed from the final analysis performed by Serf et al. (1976). Again, the computed results are generally lower than the measured displacements. Moreover, the left corner of the crest, according to the analysis results, has moved in the upstream direction with almost no settlement. This contradicts the measured displacements for this point of the crest, which is 1.5 m lateral movement in the downstream direction and 0.76 m settlement.

4.3.3 Comments on the Previous numerical works

The dynamic analysis suggested by Seed et al. (1975) assumes that all deformations due to the earthquake are caused directly by the shaking force. Therefore, in this type of analysis, an assumption that all deformations occur essentially during the period of earthquake shaking, not after, is embedded. This contradicts the delayed response phenomenon in liquefaction effects on soil structures. This phenomenon expresses that the critical period for an embankment dam subjected to an earthquake is not only the period of shaking itself, but also a period of hours following the earthquake.

The analysis performed by Serf et al. (1976) is essentially a static analysis which employs the dynamic analysis response. The effect of earthquake shaking is assumed to be weakening of the soil and is incorporated by reducing the stiffness modulus, and further by introducing some nodal forces to the soil elements. This approach is more realistic than the purely dynamic analysis technique because it assumes that the large deformations are caused by gravity, not the earthquake shaking. However, the analysis lacks an appropriate numerical model that is able to simulate behaviour of liquefiable soils. They used either a linear model or a hyperbolic model in the analysis.

4.3.4 Post-earthquake Deformation Analysis

Deformation analysis of the seismically-induced liquefaction of soils is very complicated and involves the effect of both cyclic and gravity forces. Few practical analyses have been developed to couple the above two effects, due to complexity of the phenomenon. The deformation induced directly by seismic loading is small. The delayed response phenomenon has been clearly established and has provided further evidence of the importance of considering post-earthquake stability of dams constructed of loose to medium dense granular soils. The delayed response suggests that most of the earthquake-induced deformations are essentially driven by gravity forces. Therefore, a deformation analysis, in which gravity is considered, is essential.

Post-earthquake deformation analysis of the Upper San Fernando Dam was carried out. The elasto-plastic model introduced in Chapter 3 is adopted in this analysis. The analysis assumes that large deformations (or failures) are caused by gravity forces. The earthquake shaking increases pore water pressures, bringing the soil on or close to the state of collapse. In other words, the gravity force is the immediate, direct cause, whereas the earthquake shaking is the indirect cause of large deformations. The earthquake also results in reduction in stiffness of the soil.

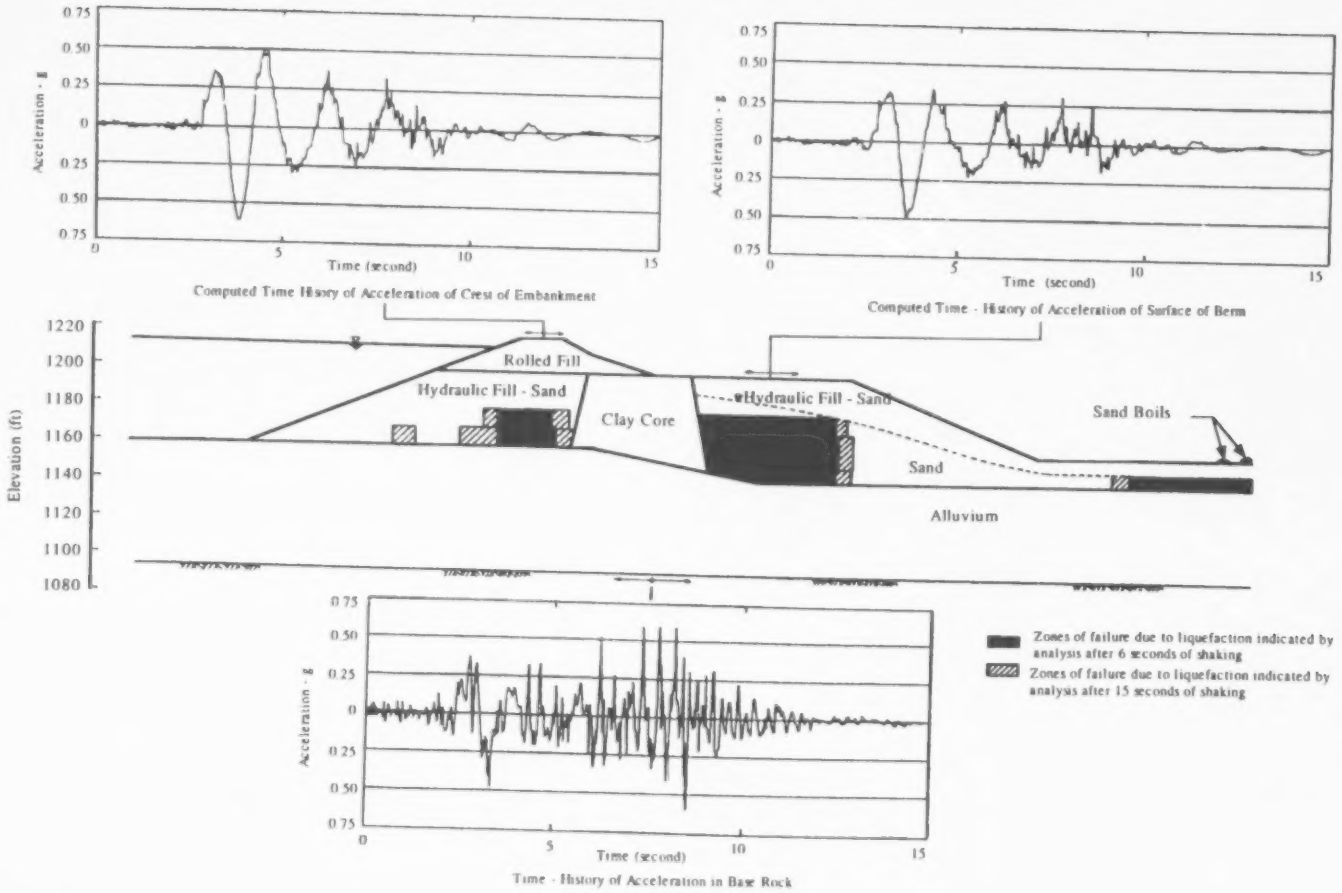

Fig. 4.7 Analysis of Response of Upper San Fernando Dam during San Fernando Earthquake to Base Motions Determined from Modified Pacoima Record [modified after Seed et al., 1975].

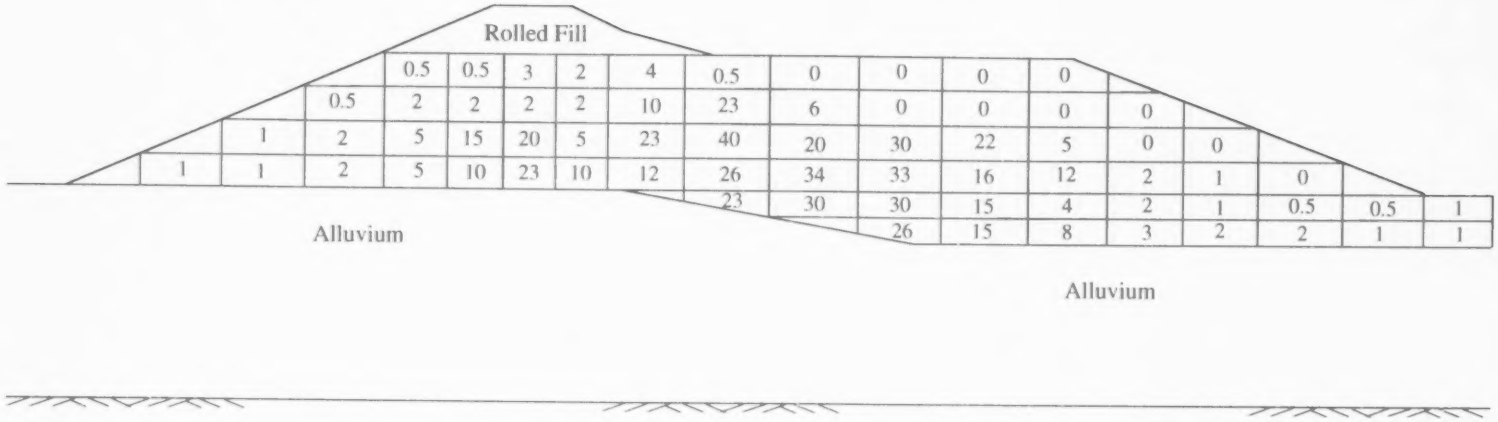

Fig. 4.8 Strain Potential in Hydraulic Fill of Upper San Fernando Dam Resulted from Dynamic Analysis [modified after Seed et al., 1973].

Table 4.2 Soil Parameters Used in Non-linear Deformation Analysis by Serf et al. (1976).

Soil Parameter	Symbol	Values used in The Analysis						
		Rolled Fill		Hydraulic Fill		Clay Core		Foundation
		Above WT	Below WT	Above WT	Below WT	Above WT	Below WT	
Unit Weight	γ (kN/m^3)	22.05	12.25	19.24	9.43	19.24	9.43	10.53
Cohesion	c (kPa)	124.5	62.25	0	26.34	48	48	34
Friction Angle	$\phi°$	25	20	37	24	0	0	32
Modulus Number	K	300	100	420	100	102	70	80
Mudulus Exponent	n	0.76	0.76	0.52	0.66	0.76	1.16	1.16
Failure Ratio	R_f	0.9	0.9	0.78	0.76	0.87	0.88	0.7
Poison's Ratio Parameters	G	0.30	0.49	0.33	0.49	0.40	0.49	0.48
	F	0.10	0	0.12	0	0	0	0
	d	3.80	0	10.0	0	0	0	0

Notes: (1) buoyant weight used for soils below the water table.

(2) data from consolidated undrained tests (CU) used to determine parameters for soils below the water table. (soil assumed impermeable during the earthquake.)

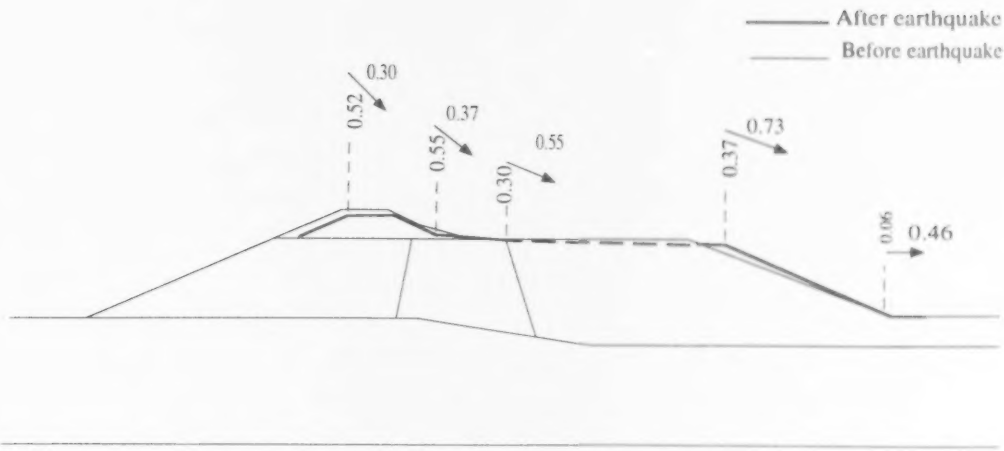

(a) Using Nonlinear Modified Modulus

[Displacements in meter]

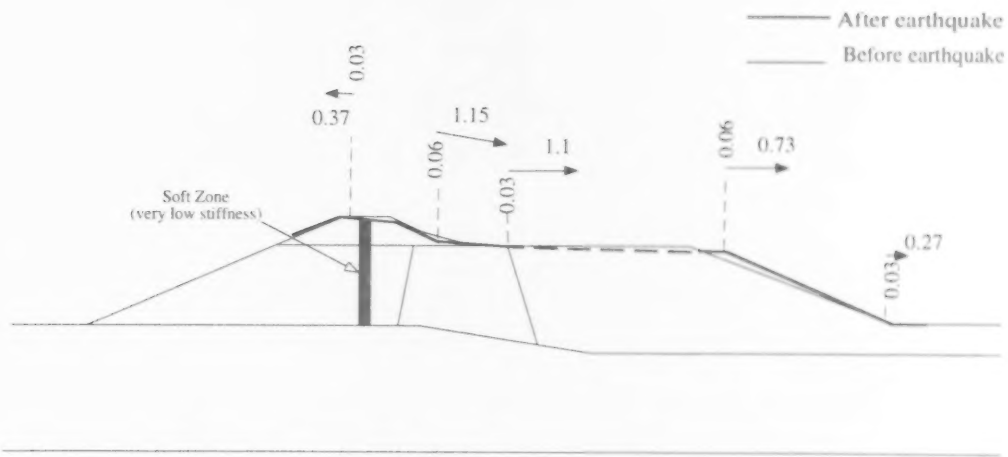

(b) Using Nodal Point Force Method Analysis with Soft Central Zone.

[Displacements in meter]

Fig. 4.9 Displacements Calculated by Serf et al. (1976).

4.4 POST-EARTHQUAKE DEFORMATION ANALYSIS OF THE UPPER SAN FERNANDO DAM

4.4.1 Initial Effective Stress Analysis

A static initial effective stress analysis was performed as a preliminary step in the stability evaluation of the Upper San Fernando Dam. The analysis was conducted using nonlinear soil properties, simulating the construction sequence of the embankment. The numerical model utilized in the analysis, the hyperbolic model, was developed by Duncan and Chang (1970) and Kulhaway et al. (1972). Table 4.3 shows material properties used in the analysis. These properties are the results of the tests conducted by Lee et al. (1975) and Serf et al. (1976).

Before performing the initial effective stress analysis, a seepage analysis was carried out to obtain the steady state pore water pressure distribution in the dam. No information about the permeability of the hydraulic fill, the clay core and the foundation of the dam is reported. The permeability values were selected so that the closest phreatic surface to that observed from the piezometric water level can be obtained from the analysis. The observed phreatic surface had been determined from the pre-earthquake water levels in the piezometers, as shown in Figure 4.6.

Figure 4.10 shows the finite element mesh used in the seepage and the static analyses. Figures 4.11 to 4.13 present, graphically, results of the seepage analysis. Figure 4.11 and 4.12 show contours of equipotentials and equal pressures respectively. Flow vectors within the body of the dam are shown in Figure 4.13. Figures 4.14 to 4.17 illustrate the output of the effective stress analysis. Figures 4.14 and 4.15 show contours of initial vertical and horizontal effective stresses respectively. Contours of shear stresses, τ_{xy} are shown in Figure 4.16. Figure 4.17 displays effective stress distribution in the hydraulic fill embankment in a p' - q plane.

Table 4.3 Soil Parameters Used in Initial Static Stress Analysis.

Symbol	Values Used in the Analysis			
	Rolled Fill	Hydraulic Fill	Clay Core	Foundation
γ_s (kN/m^3)	22.04	19.24	19.24	20.34
γ_b (kN/m^3)	12.25	9.43	9.43	10.53
c (kPa)	124	0	0	0
ϕ (°)	25	37	37	37
K	300	420	420	280
n	0.76	0.52	0.52	0.80
R_f	0.90	0.78	0.78	0.66
G	0.30	0.33	0.33	0.32
F	0.10	0.12	0.12	0.10
d	3.8	10	10	9
k (m/s)	0.0001	0.0001	0.00001	0.0001

Key: γ_s = saturated unit weight
γ_b = submerged unit weight
c = cohesion
ϕ = friction angle
K, n, R_f, G, F, and d = parameters used in hyperbolic model
k = permeability

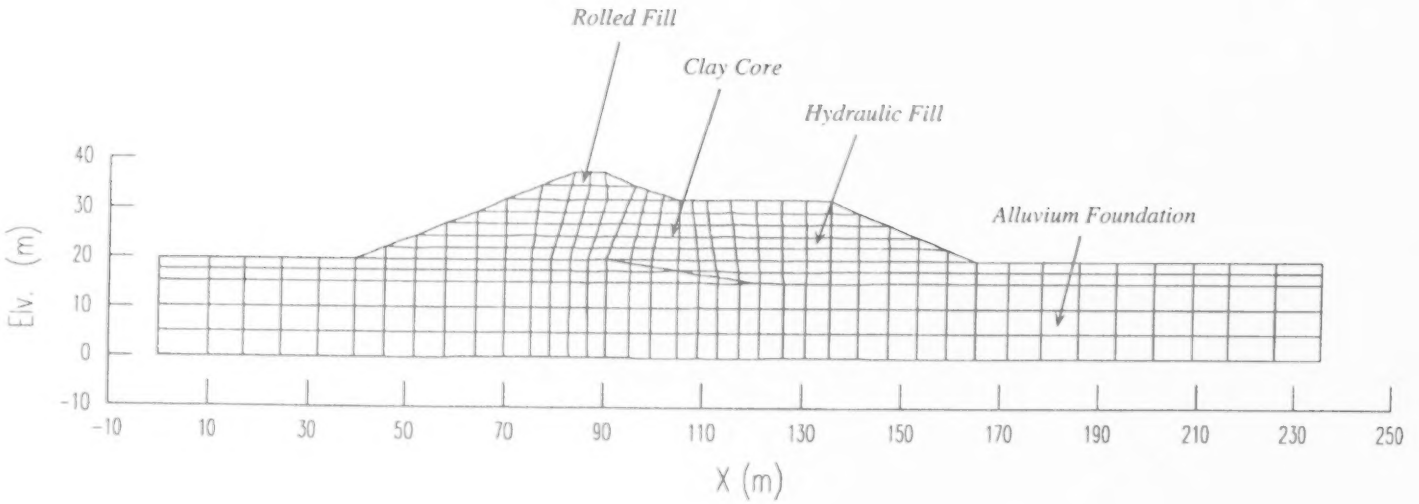

Fig. 4.10 Finite Element Mesh of the Upper San Fernando Dam.

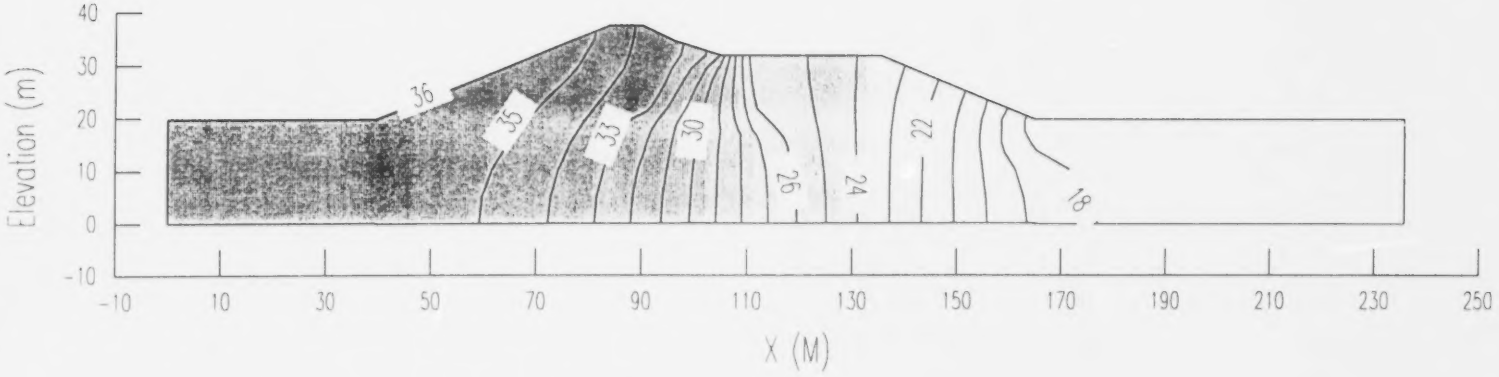

Fig. 4.11 Contours of Equipotentials in Seepage Analysis (m).

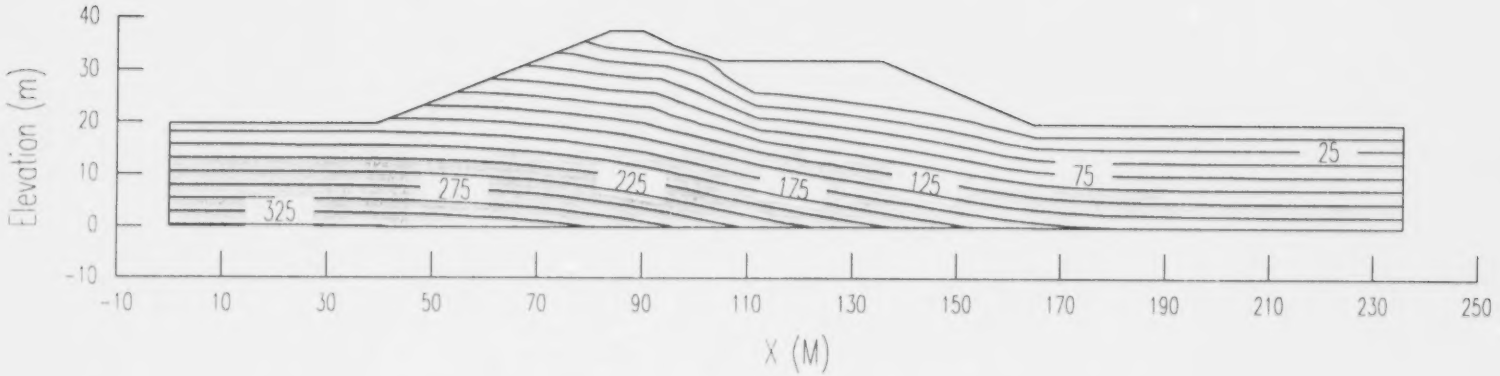

Fig. 4.12 Contours of Equal Pressures in Seepage Analysis (kPa).

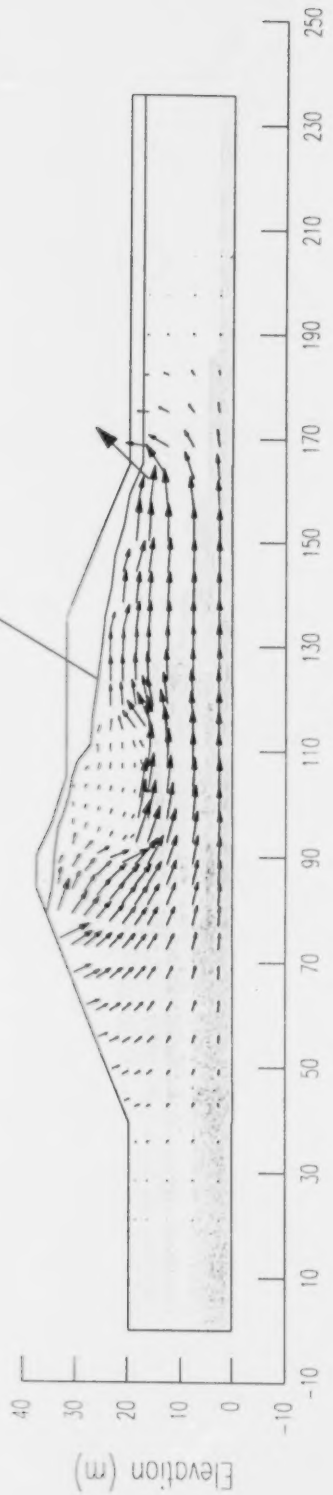

Fig. 4.13 Flow Vectors in Seepage Analysis.

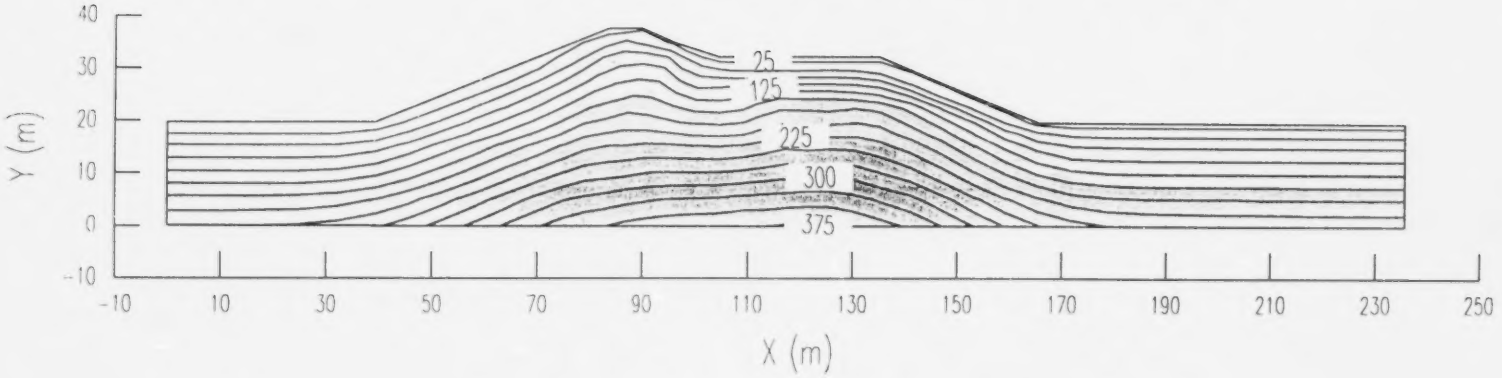

Fig. 4.14 Contours of Initial Vertical Effective Stress, σ_y (kPa).

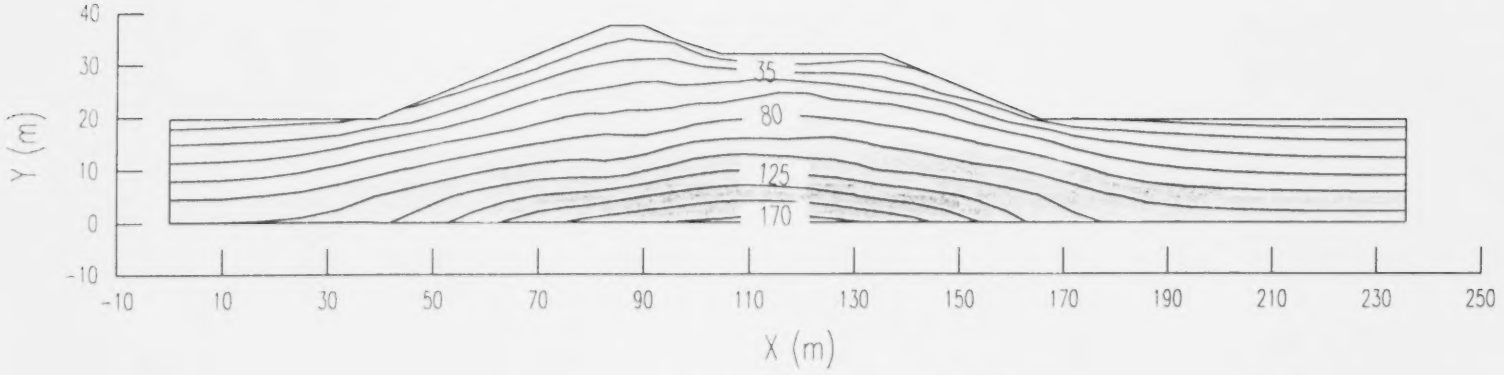

Fig. 4.15 Contours of Initial Horizontal Effective Stress, σ_x (kPa).

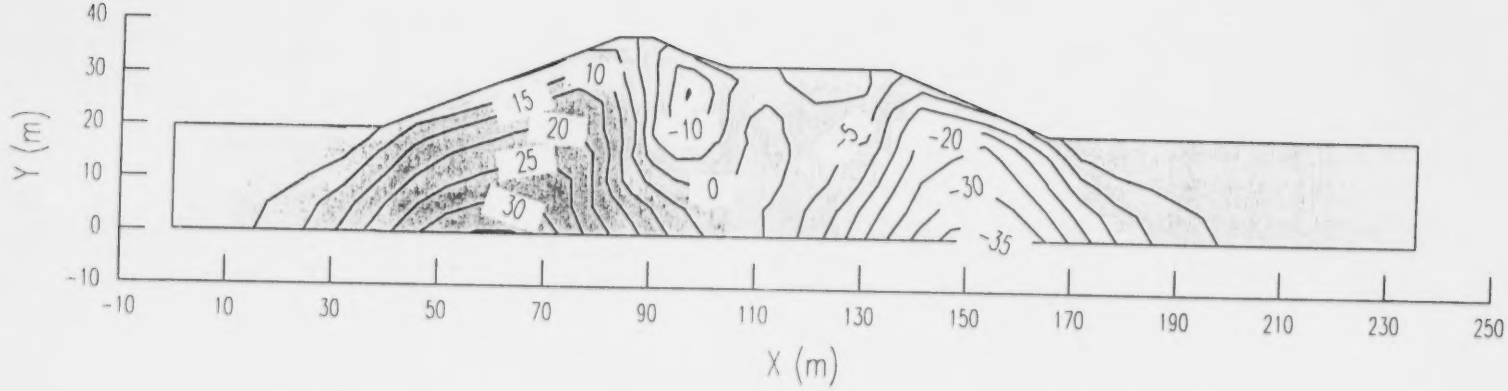

Fig. 4.16 Contours of Shear Stress, $\tau_{x\,y}$ (kPa).

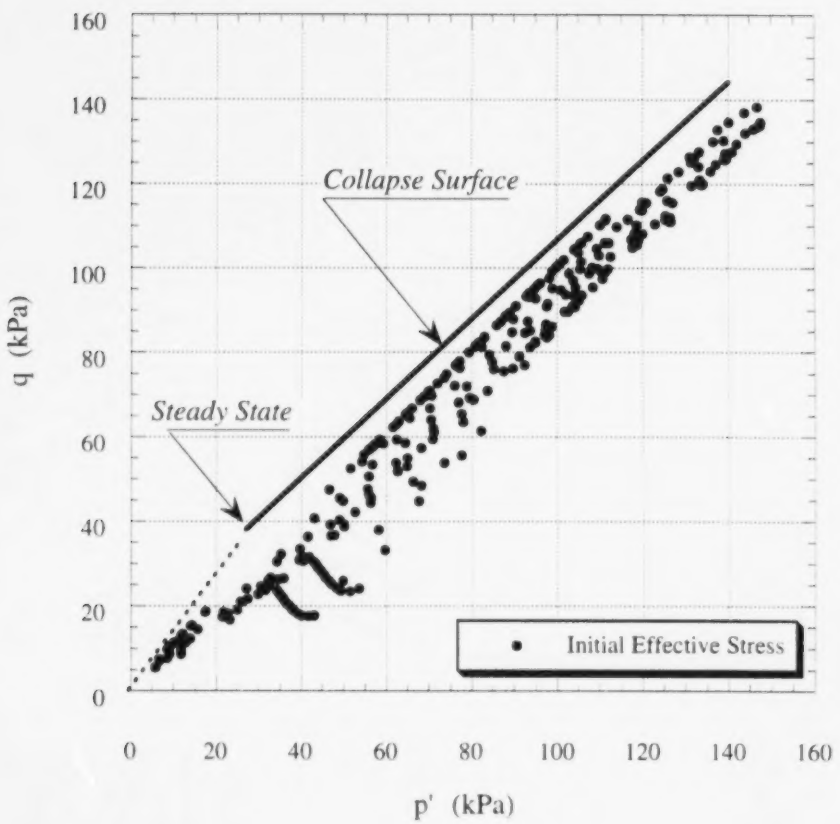

Fig. 4.17 Initial Effective Stress in Hydraulic Fill of Upper San Fernando Dam.

4.4.2 Liquefaction and Post-earthquake Deformation Analysis

An extended version of finite element program PISA for post-earthquake deformation and liquefaction analysis was utilized for this purpose.

To perform the analysis, distribution of excess pore water pressures induced by the earthquake in the hydraulic fill embankment should be known. Seed et al. (1975) combined the results of the dynamic response analysis and the cyclic triaxial tests, and showed that the highest excess pore water pressure was generated in the lower corner of the downstream hydraulic fill near the clay core, as indicated in Figure 4.7. A small area under the crest in the upstream hydraulic fill, as well as a limited area in the downstream hydraulic fill blanket, were also reported to be liquefied.

The excess pore water pressures induced by the earthquake are introduced to the analysis in the form of pore pressure ratios at the integration points of the elements. Here, the pore water pressure ratio is defined as u/u_m, where u is the pore water pressure induced directly by the earthquake and u_m is the maximum excess pore water pressure. The maximum excess pore water pressure is defined as the horizontal distance between the initial effective stress state (before earthquake) in a p-q' plane and the collapse surface as shown in Figure 4.18. Figure 4.19 shows the elements in which the maximum pore water pressure ratio was considered in the analysis.

The results from cyclic loading, conducted by Lee et al. (1975), showed that the alluvium foundation had a higher cycling loading strength than the hydraulic fill. The blow counts of SPT in the foundation were reported to be also considerably higher than that of the hydraulic fill embankment. Therefore, in the analysis the foundation was considered to be nonliquefiable.

4.4.2.1 Material Properties

Material properties used in the post-earthquake deformation analysis are estimated based on the laboratory and in situ tests and the analytical studies performed by Lee et al. (1975), Serf et al. (1976), Castro et al. (1992) and Gu et al. (1993a). These properties are presented in Table 4.4. In the following, discussions about the steady state strength of the hydraulic fill, the deformation modulus of the hydraulic fill and the post cyclic shear strength of the clay core are presented.

Steady State Strength of Hydraulic Fill Embankment

The key material property in the post-earthquake deformation analysis is the steady state strength of the liquefiable materials. There is no direct information about the steady state strength of the hydraulic fill in the Upper San Fernando Dam; however, a considerable number of data about the steady state strength of the hydraulic fill in the Lower San Fernando Dam is available.

According to Lee et al. (1975), the field and laboratory tests and trench inspection programs showed a strong similarity between the properties of the hydraulic fills in the Upper Dam and the Lower Dam. Therefore, it is not far from the reality to use the steady state strength results from the tests performed on the hydraulic fill of the Lower Dam for the hydraulic fill of the Upper Dam.

The steady state strength of the hydraulic fill of the Lower San Fernando Dam was evaluated from 1985 - 1987 by a joint group that included the University of California at Berkeley, Stanford University, Renseller Polytechnic Institute and GEI Consultants, Inc.. The joint group estimated the pre-earthquake steady state strength of the hydraulic fill of the Lower San Fernando Dam as presented in Table 4.5. Table 4.6 presents the overall estimates of pre-earthquake steady state strength at the base of the upstream hydraulic fill (which was liquefied directly by the earthquake) of the Lower San Fernando Dam.

Castro et al. (1992) have presented a comprehensive report on the work performed by the joint group, and detailed the different methods used to estimate pre-earthquake steady state strength of the hydraulic fill of the Lower Dam. They recommended that the strength values listed in Table 4.6 should be compared with the best estimate of the actual field strength of S_u = 400 to 500 psf (19.60 - 24.5 kPa). The average strength estimates in Table 4.6 (610 psf - 810 psf) is clearly unconservative compared with the estimated field values.

They concluded that "a conservative to a very conservative interpretation of the corrected laboratory test data (e.g., the use of a mean-minus-one-half to mean-minus-one-full-standard-deviation strength value) was necessary to provide a good agreement with the actual field strength back figured from the observation of the extent and timing of the slide."

Gu et al. (1993) utilized the concept of steady state strength in the modeling and analysis of the upstream failure of the Lower San Fernando Dam. They used steady state strengths reevaluated by Seed et al. (1989), which ranged from 333 psf - 800 psf (16 kPa - 38 kPa). In their analysis, they showed that a steady state strength as low as 16 kPa should be used so that the analysis will result in the upstream failure of the dam. This agrees with the conclusion made by Castro et al. (1992).

In the post-earthquake deformation analysis of the Upper San Fernando Dam, undrained steady state strength (S_u) in the range of 16 - 30 kPa was used. For S_u _ 19 kPa, deformation in the downstream hydraulic fill was triggered. Interestingly, the above value is in the range suggested by the joint group and agrees favourably with the concluding remarks made by Castro et al. (1992).

Table 4.4 Soil Parameters Used in Post-earthquake Deformation Analysis.

Soil Parameter	Symbol	Values used in The Analysis						
		Rolled Fill		Hydraulic Fill		Clay Core		Foundation
		above WT	below WT	above WT	Below WT	above WT	below WT	
Unit Weight	γ (kN/m^3)	22.05	12.25	19.24	9.43	19.24	9.43	10.53
Cohesion	c (kPa)	124.5	62.25			12	12	34
Friction Angle	$\phi°$	25	20					37
Young's Modulus	E(kPa)	0.8×10^4	0.4×10^4	0.36×10^5	0.82×10^4	0.55×10^4	0.34×10^4	0.4×10^5
Poison's Ratio	ν	0.3	0.48	0.35	0.48	0.40	0.48	0.40
Steady State Strength	S_u (kPa)			19	19			
Post-peak Parameter	a			0.05	0.05			
Angle of Hvorslev Surface	$\alpha_H°$			53	53			
Angle of Collapse Surface	$\alpha_c°$			43	43			
Pore pressure Parameters in Liquefaction analysis	A_o				0			
	A_m				5			
	B				1			

Table 4.5 Steady State Strength of Hydraulic Fill in Lower San Fernando Dam, psf (kPa).

Group	upstream		Downstream	
	range	Average	range	Average
Seed	291-1053 (14-51)	717 (34.5)	381-1322 (18.30-63.5)	896 (43.05)
GEI		640 (30.75) 1020 (49)	200-1600 (9.61-76.9) 200-2600 (9.61-125)	880 (42.3) 1380 (66.30)
RPI	150-2000 (7.21-96.1)	700 (33.6)		

Table 4.6 Overall Estimate of Pre-earthquake S_u at Base of Upstream Hydraulic Fill.

Strength evaluation level	S_u, psf (kPa)	
	Method A	Method B
Average (mean value)	610 (30.5)	810 (40.5)
Mean minus one-half standard deviation	490 (24.5)	650 (32.5)
Mean minus one standard deviation	360 (18.0)	480 (24.0)

key: Method A and Method B are two methods of analysis to estimate the possible void ratio changes that may have occurred during and after the earthquake.

Deformation Modulus of Hydraulic Fill after Liquefaction.

In addition to the steady state strength, the deformation modulus of the hydraulic fill affected by the earthquake-induced liquefaction also has to be evaluated. Previous researches have shown that earthquakes have the effect of decreasing the stiffness modulus of soils when drainage is not provided (Serf et al., 1976; Yasuda et al., 1992). It is clear that if the excess pore pressure increases, the shear strain under the same stress increases. This means that the inclination of the stress-stain curve, which can be viewed as an elastic modulus, decreases with increases in excess pore pressures.

Yasuda et al. (1992) conducted a number of shaking table, vane and cyclic torsional shear tests on 19 soil models, including clean sands and silty sands, and showed that at small strains, the elastic modulus decreases proportionally with increase in excess pore water pressure ratio ($\Delta u/p'$). For excess pore pressure ratios from 0.8 to 1.0, the reduction in the deformation modulus is reported to be significant (G/G_o = 0.01 - 0.001, where G_o is the elastic modulus when the excess pore pressure ratio is zero).

Post-Cyclic Shear Strength of Clay Core

Undrained shear strength of saturated cohesive soils after cyclic loading decreases and increases depending on whether the soil is initially normally consolidated or over consolidated, and whether drainage is included during or after cyclic loading. After conducting a number of cyclic triaxial tests, Yasuhara (1994) showed that undrained shear strength of normally consolidated clays after cyclic loading, without drainage, decreases. The post-cyclic shear strength is suggested to be calculated using the following equation.

$$\frac{S_{u,cy}}{S_{u,nc}} = \left(\frac{1}{1-\frac{\Delta u}{p'_i}}\right)^{\frac{\wedge o}{1-C_y/C_c}-1} \qquad [4.1]$$

where,

$S_{u,nc}$ = static undrained strength for normally consolidated saturated cohesive soils,

$S_{u,cy}$ = post-cyclic undrained strength without drainage,

p'_i = effective consolidation stress,

Δu = pore pressure induced by cyclic loading,

$\wedge_o$ = a material constant,

c_c = compressive index, and

c_s = swelling index.

To determine the experimental parameters, $\wedge_o$, c_c, and c_s in Equation [4.1], Yasuhara proposed the following empirical equations, initially introduced by Ue et al. (1991).

$$c_s/c_c = 0.185+0.002\ I_p \qquad [4.2]$$

$$\frac{\wedge_o}{1-c_s/c_c} = 0.939-0.002\ I_p \qquad [4.3]$$

where, I_p is the plasticity index of cohesive soils.

The plasticity index of the clay core of the Upper San Fernando dam ranged from 20 to 40. Using the above data in Equations [4.1] to [4.3], the post-earthquake undrained shear strengths of the clay core for a range of pore water pressure ratio (here, defined as $\Delta u/p'$) between 0.6 to 0.95 are calculated and summarized in Table 4.7.

Table 4.7 $\frac{S_{u,cy}}{S_{u,nc}}$ of Clay Core for Different Pore Water Pressure Ratios ($\frac{\Delta u}{p'_i}$)

	$\frac{\Delta u}{p'_i}$=0.6	0.7	0.8	0.9	0.95
I_p = 20	0.91	0.88	0.85	0.79	0.74
I_p = 40	0.88	0.84	0.80	0.72	0.66

key : $S_{u,nc}$ = static undrained strength of the clay core
$S_{u,cy}$ = post-cyclic undrained strength of the clay core without drainage
p'_i = effective mean normal stress
Δu = pore pressure induced by cyclic loading (i.e., earthquake)
I_p = plasticity index

4.4.2.2 Results of the analysis

In the first series of the analyses, it was assumed that the earthquake did not have any effects on the strength of the clay core. Based on this assumption, the analysis showed that the central part of the dam cross section, including the crest and the clay core, developed little deformations, especially in the horizontal direction, though the computed deformations in the downstream hydraulic fill were in reasonable agreement with the measured ones. Figure 4.20 shows these results indicating a relatively stable condition in the central part of the dam cross section.

The disagreement between the computed and the measured deformations in the central part of the dam necessitated a re-evaluation of the post-earthquake undrained shear strength of the clay core. Therefore, based on the foregoing discussion, the shear strength of the clay core was reduced to $S_{u,cy} = 0.66S_{u,nc}$, where $S_{u,cy}$ is the post-earthquake undrained shear strength of the clay core, and $S_{u,nc}$ is the static undrained strength of the clay core.

To facilitate the movement of the clay core in the same order of the downstream embankment movement, the deformation modulus of the clay core was reduced to a lower value; otherwise, the analysis tend to diverge due to the deformation contrast at the boundary of the clay core and the downstream hydraulic fill embankment. Another problem raised in the computation process was the occurrence of local divergence at the middle of the rolled fill. To overcome this problem, the deformation modulus of the rolled fill, in addition to that of the clay core, was also reduced. Considering the relatively low confining pressure in the rolled fill, together with the effect of earthquake shaking, this assumption is not far from the reality.

Based on the above discussion and knowledge of the distribution of the excess pore water pressure within the body of the dam, the final post-earthquake deformation analysis was carried out. Figure 4.21 shows the computed deformation. Figure 4.22 compares the measured and the computed deformations at the surface of the dam. This figure displays a

reasonable agreement between the measured and the computed deformations. The displacement field is presented by arrows in Figure 4.23.

The analysis was repeated for the steady state strength of the hydraulic fill (S_u) equal to 30 kPa and 24 kPa. These represent the average and the mean minus one-half standard deviation of steady state strength of the hydraulic fill, respectively (see Table 4.6). It is of interest that for these two cases, essentially no deformation in the dam was triggered.

4.4.2.3 Deformation Patterns in the Dam

Figure 4.23 shows three different patterns of deformation in the dam. The first one is related to the downstream hydraulic fill embankment. As mentioned, the hydraulic fill was recognized as the liquefiable material; therefore, by introducing high excess pore pressure ratio (> 0.8) for the liquefied elements, the flow deformation occurred in this part of the dam. The second pattern of the deformation is obvious in the centre of the dam cross section, including a small portion of the upstream hydraulic fill and the whole part of the rolled fill crest. As shown in Figure 4.19, a few elements in the lower part of the upstream shell close to the clay core were also liquefied by the earthquake. Introducing the maximum excess pore pressure ratio, u/u_m, for these elements resulted in a considerable settlement in this part of the upstream and, consequently, a large settlement in the crest.

The direct consequence of the above deformations was an extra loading on the clay core. This extra loading applied a downstream-directed pressure on the clay core and pushed it out towards the downstream of the dam. This could be considered the third pattern of deformation. The deformation in the clay core was the result of introducing the reduced shear strength, as well as the reduced stiffness modulus for this part of the dam, to the analysis .

4.4.2.4 Discussion

The main difficulty in the computation process of this type of analysis is the presence of different materials with appreciable difference in their strength and deformation

properties. The alluvium foundation did not cause any problem since it did not have any role in the earthquake-induced instability of the embankment. The rest of the dam comprises of 4 materials: the rolled fill crest, the clay core and the hydraulic fill (both below and above the phreatic surface). In such an analysis, each material tends to behave according to its own properties and model. Thus, harmonizing the behaviours of these materials requires some degree of judgment and modification, especially regarding the stiffness modulii of the materials. The problem may become more complicated when one differentiates between the properties of the liquefied part and the rest of the hydraulic fill.

The feature of the deformation at the Upper San Fernando Dam is that it is large (maximum of about 200 cm), although it is contained. Performing such a deformation analysis faces occasional numerical instability. The difficulty can be compounded when the embankment comprises more than one material.

4.5 SUMMARY AND CONCLUSION

The deformation induced in the Upper San Fernando Dam by the earthquake of February 9, 1971 was studied by the post-earthquake deformation analysis method. The computed results are favorably comparable with the deformations measured shortly after the earthquake.

In this analysis, the trigger of deformation is dependent on the value of the undrained steady state strength, S_u, of the hydraulic fill. The analysis with S_u = 19 kPa resulted in the most realistic results. This is consistent with the recommendation of Castro et al. that a conservative to a very conservative interpretation of the laboratory test strengths should be adopted. Some assumptions on the deformation modulii of the embankment materials were made to obtain the best fit to the measured deformations. The earthquake was taken to reduce deformation modulii. The output of the analysis also depends on the input excess pore water pressures induced by the earthquake. These excess pore water pressures were estimated based on the combined results of the dynamic analysis and the cyclic tests (Seed et al., 1975).

The finite element method is based on small strains and deformations. In this regard, some error is included in the analysis. Nonetheless, the method provides for practical purposes a reasonable basis for evaluating earthquake-induced deformations of soil structures.

The method of post-earthquake deformation analysis successfully explained the earthquake-induced upstream *failure* of the Lower San Fernando Dam (Gu et al., 1993a). The analysis of the Upper San Fernando Dam proved that the method can also evaluate earthquake-induced *deformations which are contained, but large*. Comparable strengths for the liquefiable material was found in both cases. More studies and back-analyses are needed to gain insight into the performance of soil structures subjected to earthquake loading and subsequent liquefaction.

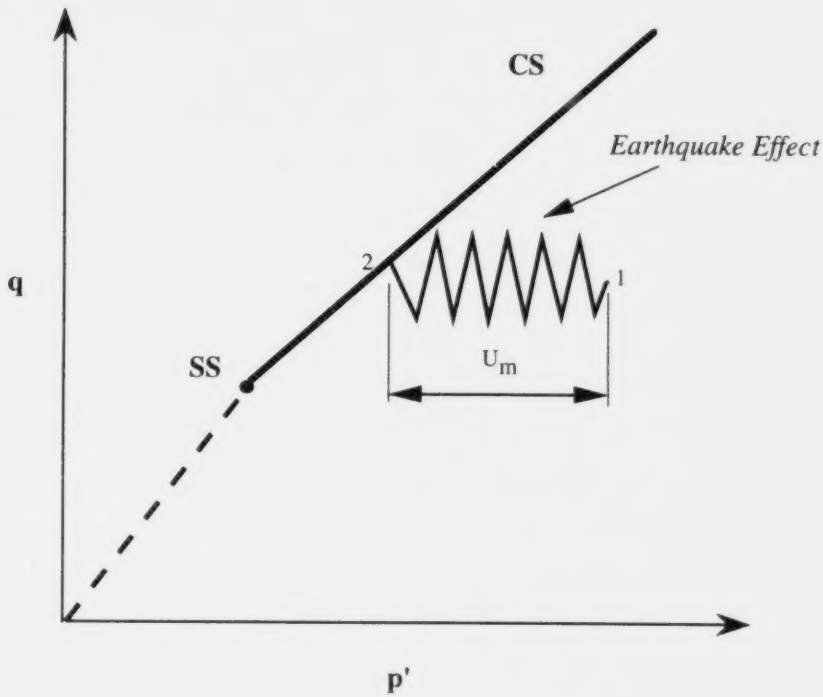

Legend :
- p' : mean normal effective stress
- q : deviator stress
- SS : steady state strength
- CS : collapse surface
- 1 : initial static effective stress
- 2 : effective stress after earthquake and before stress redistribution
- U_m : maximum excess pore pressure induced by earthquake

Fig. 4.18 Definition of Maximum Pore Water Pressure in Post-earthquake Deformation Analysis.

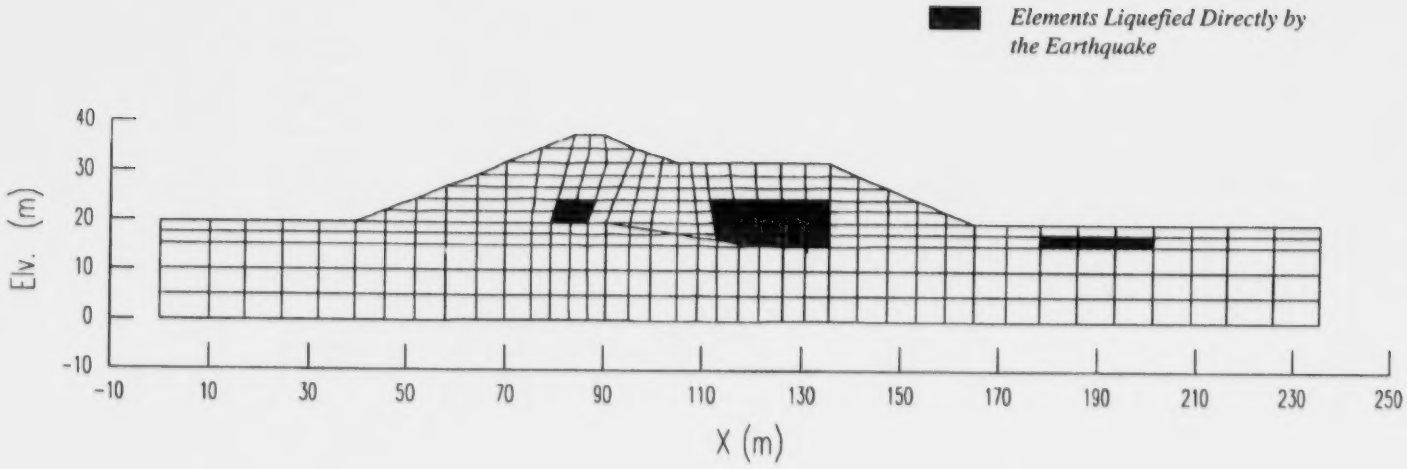

Fig. 4.19 Elements with Maximum Pore Water Pressure Ratio.

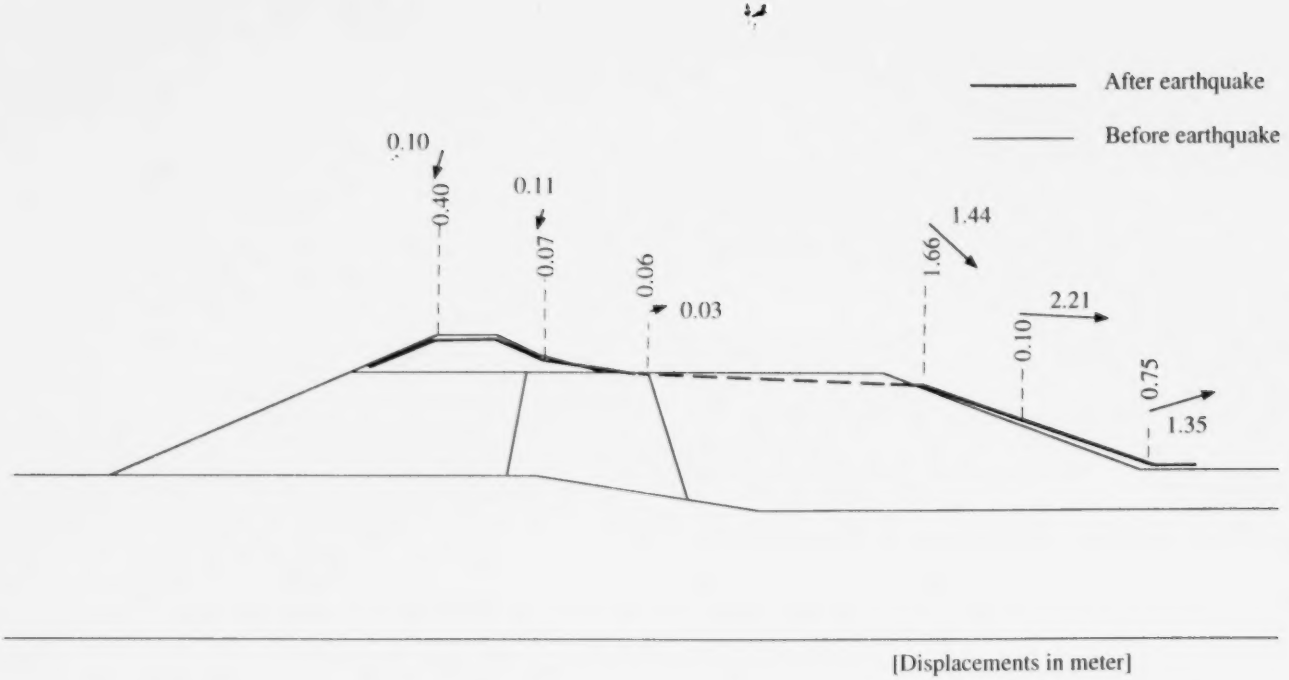

Fig. 4.20 Displacements Computed Using Non Modified Shear Strength of Clay Core.

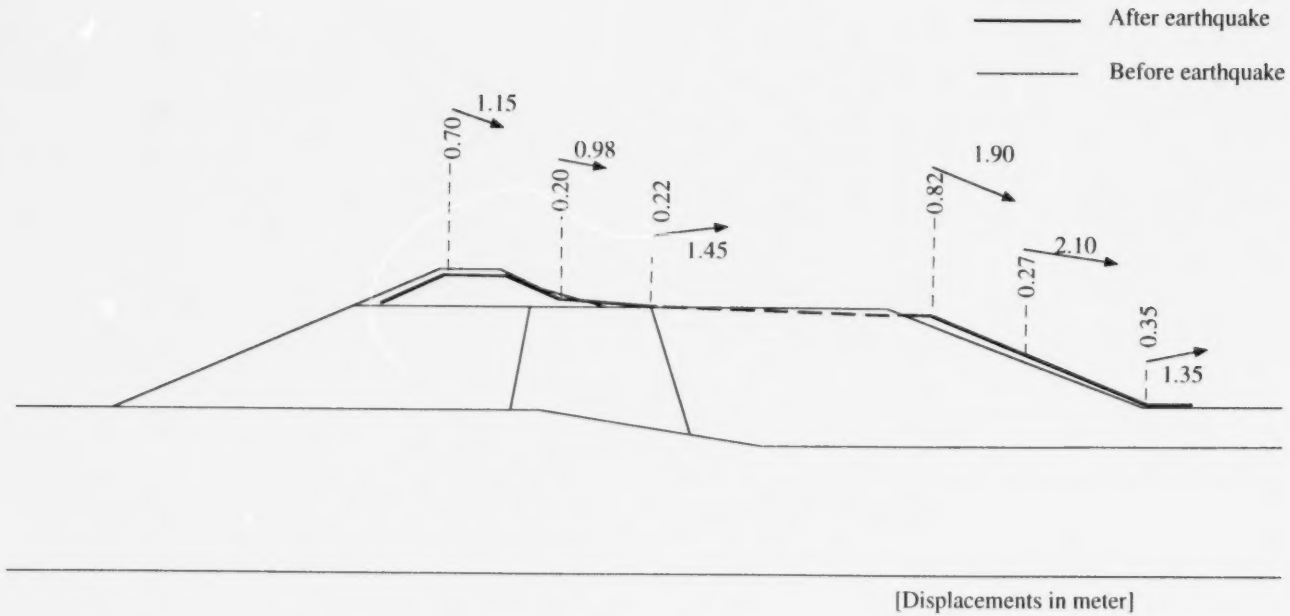

Fig. 4.21 Computed Displacements in Liquefaction Analysis (S_u =19 kPa, final analysis).

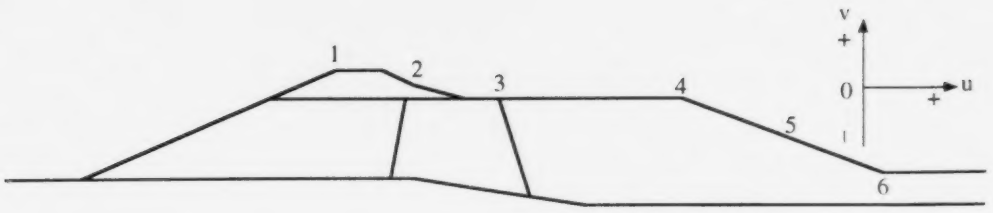

(a) Embankment Cross Section

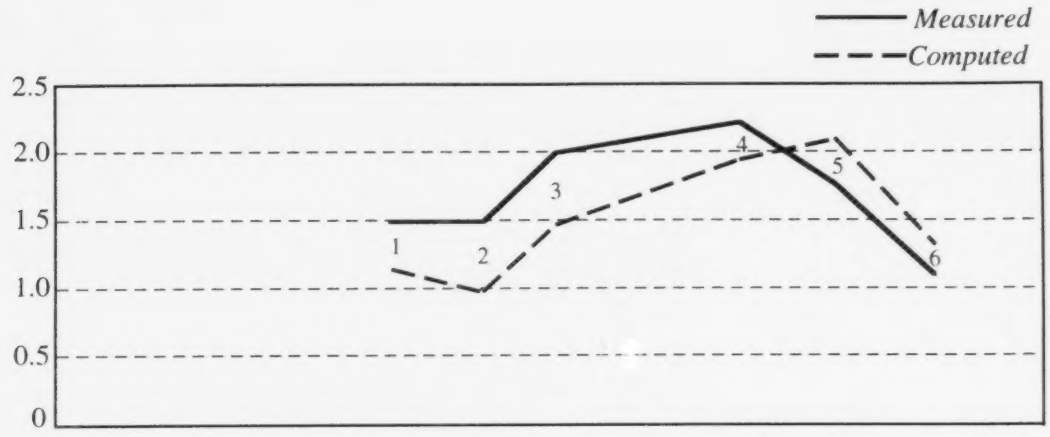

(b) Horizontal Deformation, u (m)

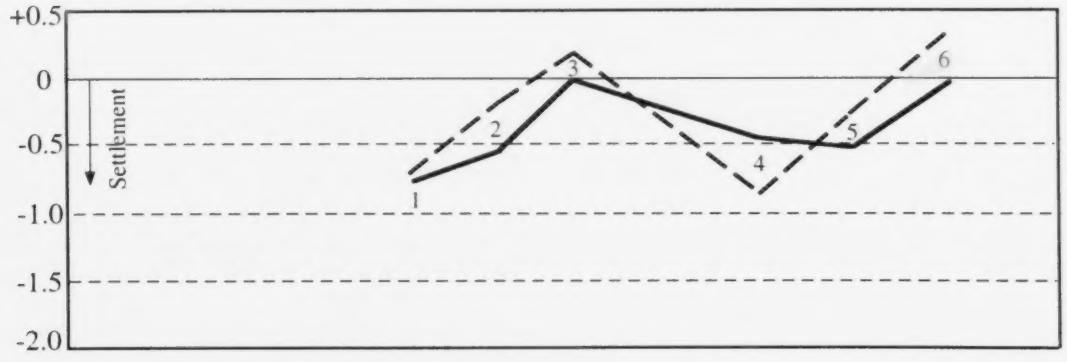

(c) Vertical Deformation, v (m)

Fig. 4.22 Comparison between Measured and Computed Deformation at Surface of The Dam.

Note : displacements induced by the gravity loads are not included

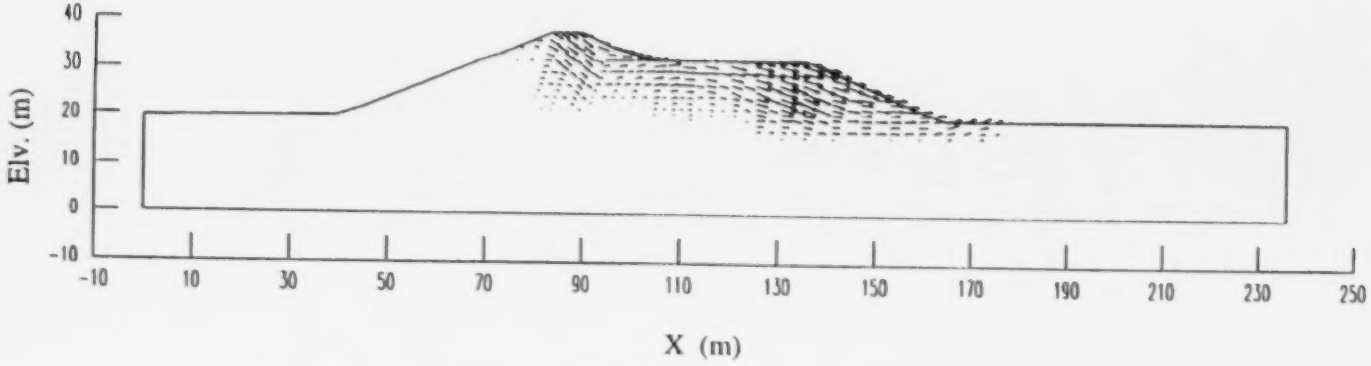

Fig. 4.23 Displacement Field Computed from Post-earthquake Deformation Analysis (displacement = arrow x 0.5).

Chapter 5

NUMERICAL MODELING AND ANALYSIS OF CANLEX PROJECT EXPERIMENTS

5.1 GENERAL INTRODUCTION

A major liquefaction sand study, entitled the Canadian Liquefaction Experiment, CANLEX, is being carried out by the geotechnical engineering community. CANLEX involves the characterization of sand in order to predict its liquefaction response. The third phase of CANLEX includes initiating a controlled full-scale liquefaction event in the field. The liquefaction event was designed to be carried out at the Syncrude Site near Fort McMurray, Alberta, during the Summer of 1995. Triggering of flow deformation was attempted by rapid construction of an embankment over a loose saturated sand layer.

As a complementary part of the numerical studies and the field event, a series of centrifuge tests were carried out at C-CORE Centrifuge Center, St. John's, Newfoundland. The centrifuge tests were conducted to aid in the design of the event and to facilitate calibration of the numerical models. The role of the field event and the centrifuge modeling in the overall project is shown in Figure 5.1.1.

The design of the event was based on field experience, centrifuge testing and numerical study. The numerical study was carried out to understand the liquefaction process of sand, to analyze and make predictions of both the centrifuge tests and the full-scale event, to compare the numerical forecast with the field measurements and to evaluate the current capability of the numerical modeling. The collapse surface plasticity model is adopted in the analysis. A comprehensive summary of the plasticity model was presented in Chapter 3.

This Chapter presents numerical modeling and analyses of the centrifuge tests and the field event in two separate sections. Each section has its own introduction and summary. A more detailed version of this Chapter, entitled "Numerical Study on the CANLEX Project", has been submitted to the CANLEX administration.

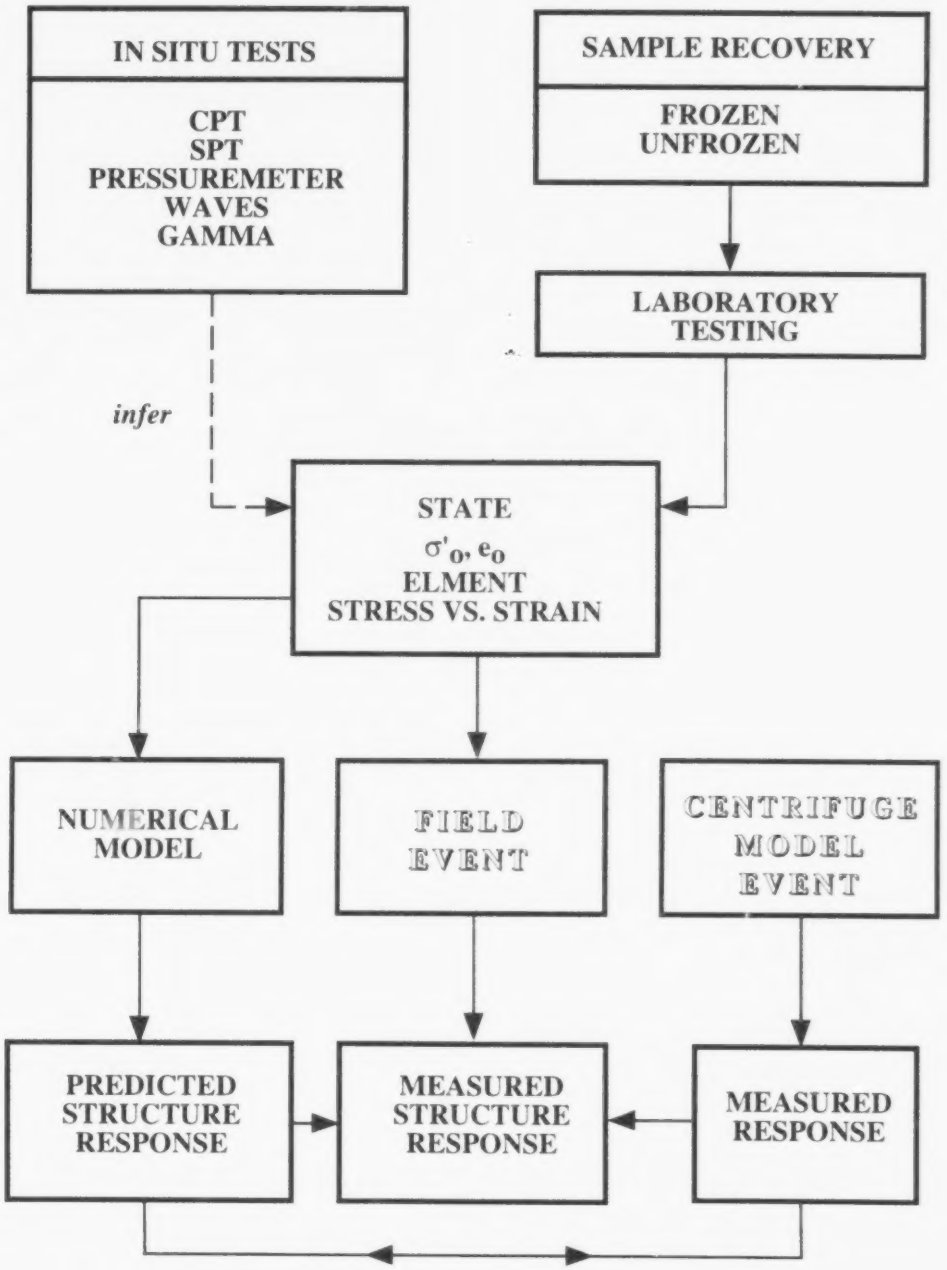

Fig. 5.1.1 Role of Centrifuge Modeling and Field Event in CANLEX Project [after Phillips and Byrne (1993)].

5.2 *LIQUEFACTION ANALYSIS OF THE CENTRIFUGE MODEL TESTING*[1]

5.2.1 INTRODUCTION

Geotechnical Engineers occasionally use centrifuge modeling in conjunction with theoretical analyses. A geotechnical centrifuge model might be tested when (1) it would be too difficult , expensive or dangerous to construct and test a full-scale structure or (2) improvement and calibration of the numerical models to study the full-scale structures are required. A centrifuge model is usually smaller than the prototype structure that it represents. The principles and applications of and discussions on centrifuge modeling are described by Schofield (1980).

In the framework of the CANLEX Project, centrifuge model tests were conducted to complement the numerical forecast and the field event planning. The tests were intended to aid in the design of the field event and to facilitate calibration of the numerical models. The centrifuge testing was divided into two stages. Stage 1 was to ascertain that a static liquefaction event could be induced through a centrifuge test. Numerical modeling

---

[1] A summarized version of this section was presented as a paper to the 48th Canadian Geotechnical Conference, Vancouver, Canada, September 25-27, 1995.

predictions from stage 1 were used to design a number of possible event triggers for stage 2 tests.

Two centrifuge tests, entitled CANLEX 1 and CANLEX 2, were carried out in Stage 1. On the basis of the numerical modeling of these two tests, the first test of Stage 2, named CANLEX3, was also conducted. CANLEX 3 simulates more closely the full-scale field event. Numerical simulation and analysis of the three centrifuge tests are presented in this Section. At the beginning a summary of the centrifuge model tests, including the technical development, the procedure and the results, is given. Fully detailed reports on the centrifuge model tests are provided by Phillips and Byrne (1993; 1994).

5.2.2 CENTRIFUGE MODEL TESTS

The centrifuge model tests were carried out at the C-CORE Centrifuge Center, St. John's, Newfoundland. The C-CORE centrifuge is an Acutronic 680-2 centrifuge with a nominal radius of 5 m and a maximum playload capacity of 220 g-tons. The centre and its facilities are described by Phillips et al. (1994). The tests were conducted on reconstituted tailings sand deposits shipped from Syncrude, Canada. Since it is important that the soil in the centrifuge is deformed under undrained conditions, higher viscosity fluid must be used to have the same drainage characteristics as the prototype. Therefore, Canola oil was used in the experiment as the pore fluid.

Material properties of the oil sand and the Canola oil determined at C-CORE are given in Table 5.2.1. The grain size distribution determined from dry sieving is shown in Figure 5.2.1. A number of drained and undrained triaxial extension and compression tests were also performed on water saturated oil sand with a relative density of 40% to obtain the material parameters for the model. The final results of the triaxial tests are summarized in Figure 5.2.2.

Figure 5.2.3 illustrates a configuration of the sand slope for CANLEX 1 and 2. The tests were carried out under a centrifuge force of 50 g, and therefore the model test represents a prototype of 50 times in its size. As shown, the experiment modeled a sand slope with a

flat top. To trigger the liquefaction event, a static trigger which imposed an undrained loading on the crest of the slope was adopted. The most technically appropriate static trigger was found to be loading the crest of the slope. The loading trigger selected was a steel drop weight. In CANLEX 1 and 2, the slope was totally submerged in the oil. Pore pressure transducers were installed at two locations, as shown in Figure 5.2.3. A video camera was used to record the process of the failure during the test. The tailings sand was placed by air pluviation in lifts of about 25 mm. The relative density of the sand was increased during saturation with relative density between 20 and 40 %.

Table 5.2.1 Properties of Oil Sand Tailings [after Phillips and Byrne, 1993].

Sand Type		Oil Sand	Silica Sand
Specific gravity	1	2.64	2.65
Maximum dry density	kg/m^3	1720	1650
Minimum dry density	kg/m^3	1350	1340
Maximum void ratio	1	0.96	0.98
Minimum void ratio	1	0.53	0.61
Mean grain size, d_{50}	mm	0.17	0.23
Effective grain size, d_{10}	mm	0.092	0.14
Uniformity coefficient, C_u	1	2.12	1.86
Natural water content	%	7 - 9	
Oil content	%	0.27	
Permeability to oil @ 21° C	m/s	3.25e-07	3.18e-06
at relative density, Dr	1	0.40	0.41
Permeability to water @ 21° C	m/s	1.56e-05	2.54e-04
at relative density, Dr	1	0.48	0.38

CANLEX 1

In CANLEX 1, the drop weight had a mass of 6.14 kg, corresponding to a surcharge of 43 kPa. Both pore pressure transducers recorded a pore pressure increase of 32 kPa from their equilibrium values. This pore pressure increase corresponded to a vertical total stress equal to 8 mm of steel above PPT1. The actual drop weight was 11 mm thick for the test. The lower response of the PPTs has been attributed by Phillips and Byrne (1993) to the possible influence of the compressibility of the pore fluid, partial saturation of the sand model, stress redistribution and consolidation. In this test no significant movements of the sand slope was observed by the video system.

CANLEX 2

In CANLEX 2, the mass of the drop weight was increased to 12.45 kg, corresponded to a surcharge of 88 kPa. The pore pressure transducers showed a significant increase in pore pressures. The sand slope failed under this higher dropped weight. As described by Phillips and Byrne (1993), no gross distortion of the slope was observed for a short period of about 1/4 second. The drop weight then punched vertically down into the crest of the slope and large deep-seated lateral flow movements occurred throughout the slope towards the toe over a 3 second period. The post-failure schematic configuration of CANLEX 2, together with the position of the drop weight and PPTs, are shown in Figure 5.2.4. Figure 5.2.5 shows the photo taken from the model slope after test CANLEX 2. Based on the failure of the sand, it was concluded that a static flow liquefaction event could be induced in a centrifuge test.

CANLEX 3

CANLEX 3 was conducted with a different configuration of the slope as shown in Figure 5.2.6. The test simulated a partially saturated 5 m high slope over a 10 m saturated loose sand layer. The main objectives of conducting CANLEX3 were:

(1) to provide more support for analytical modeling and liquefaction event planning

(2) to optimize centrifuge testing procedures of the Syncrude tailings sand

(3) to conduct centrifuge testing on Syncrude sand to assist in the design of a static liquefaction full-scale field event and for analytical work

The experimental technique for CANLEX 3 was improved over that of CANLEX 1 and 2 to prevent slumping of the slope prior to the test, acquire additional pore pressure measurements, and record sand surface settlements. Due to possible dynamic effects involved in dropping the weight in CANLEX 1 and 2, the weight for CANLEX 3 was placed as close to the crest as possible. The drop weight consisted of two 9 kg steel plates, corresponded to 60 kPa surcharge. Five pore pressure transducers, three under the slope and two near the toe, were located in the sand model. The average relative density of the sand after achieving equilibrium at 50 g was 29 %. The first load was placed on the crest between 14 and 16 seconds after the equilibrium. The second plate was located on the first plate between 18 to 21 seconds.

All recorded images, the videos and the surface settlement data indicated that the liquefaction and the flow deformation occurred during application of the first steel plate, and the movement stopped prior to application of the second plate. Flow liquefaction of the slope was apparent from the nature and pattern of the subsurface deformation during application of the first surcharge. LDT18 and LDT19 shown in Figure 5.2.6 monitored surface displacements of the crest and the toe plane of the slope respectively. LDT19 recorded 2.7 mm heave of the toe plane immediately after application of the surcharge. The profile of the whole sand surface after the centrifuge test, compared with the pre-test profile, is illustrated in Figure 5.2.7. The vector displacement field, obtained from the recorded images, is shown in Figure 5.2.8.

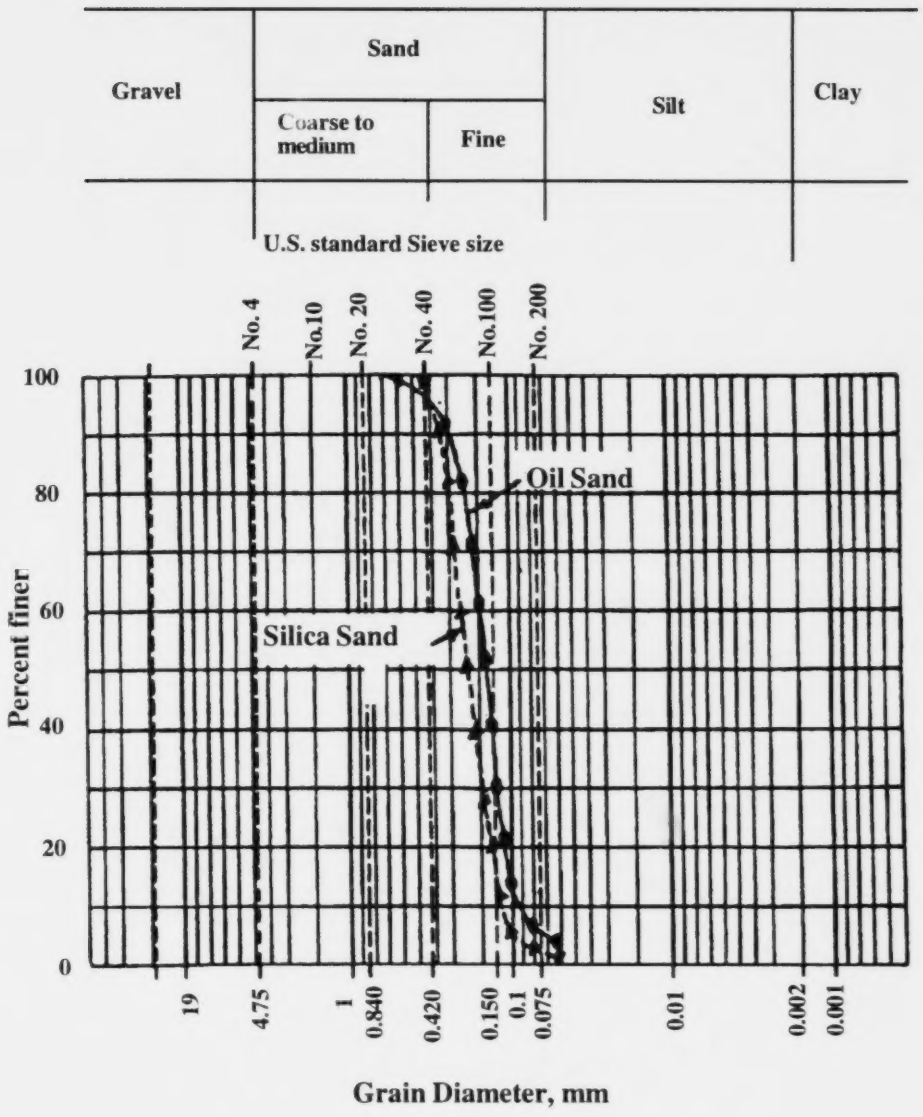

Fig.5.2.1 Grain Size Distribution of Oil Sand.

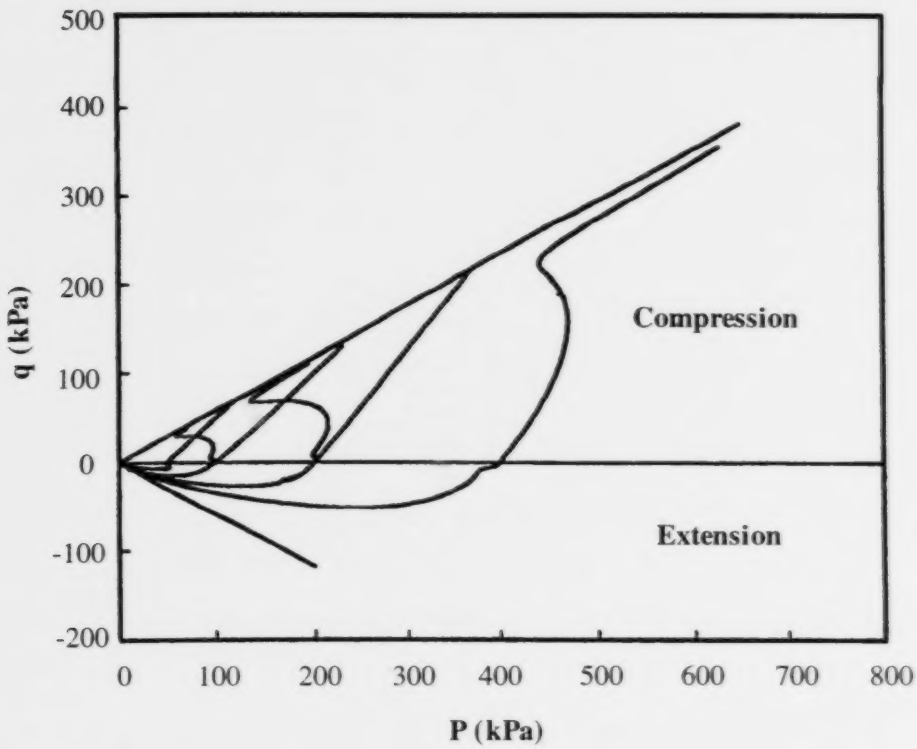

Fig. 5.2.2 Summary of Triaxial Test Results
[modified after Phillips and Byrne (1993)].

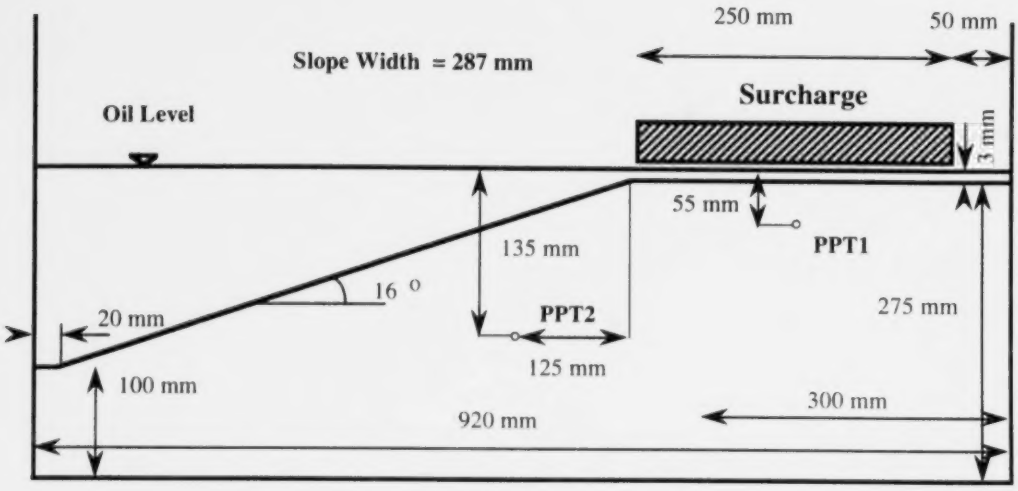

Fig. 5.2.3 CANLEX 1 and 2- Initial Configuration of Model Slope.

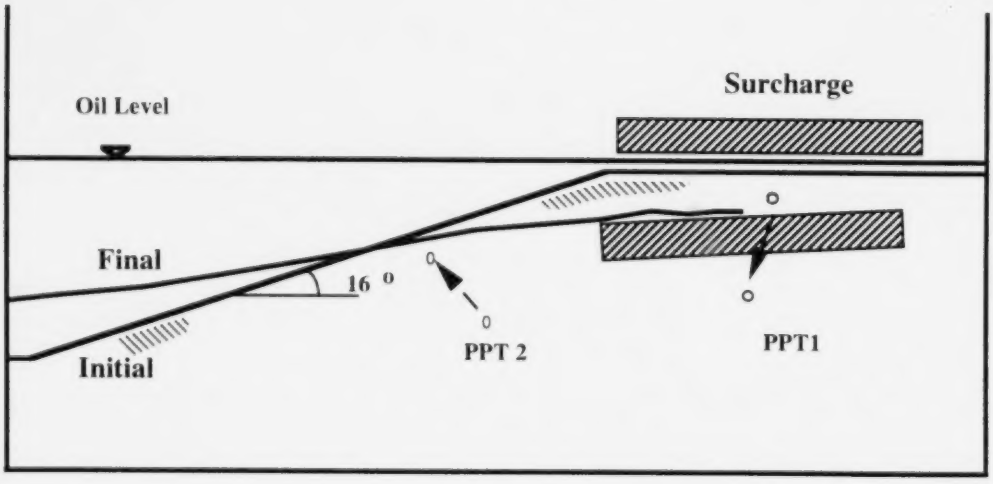

Fig. 5.2.4 CANLEX 2- Observed Post Failure Configuration .

Fig. 5.2.5 CANLEX 2- Model Slope after Failure [modified after Phillips and Byrne, 1993].

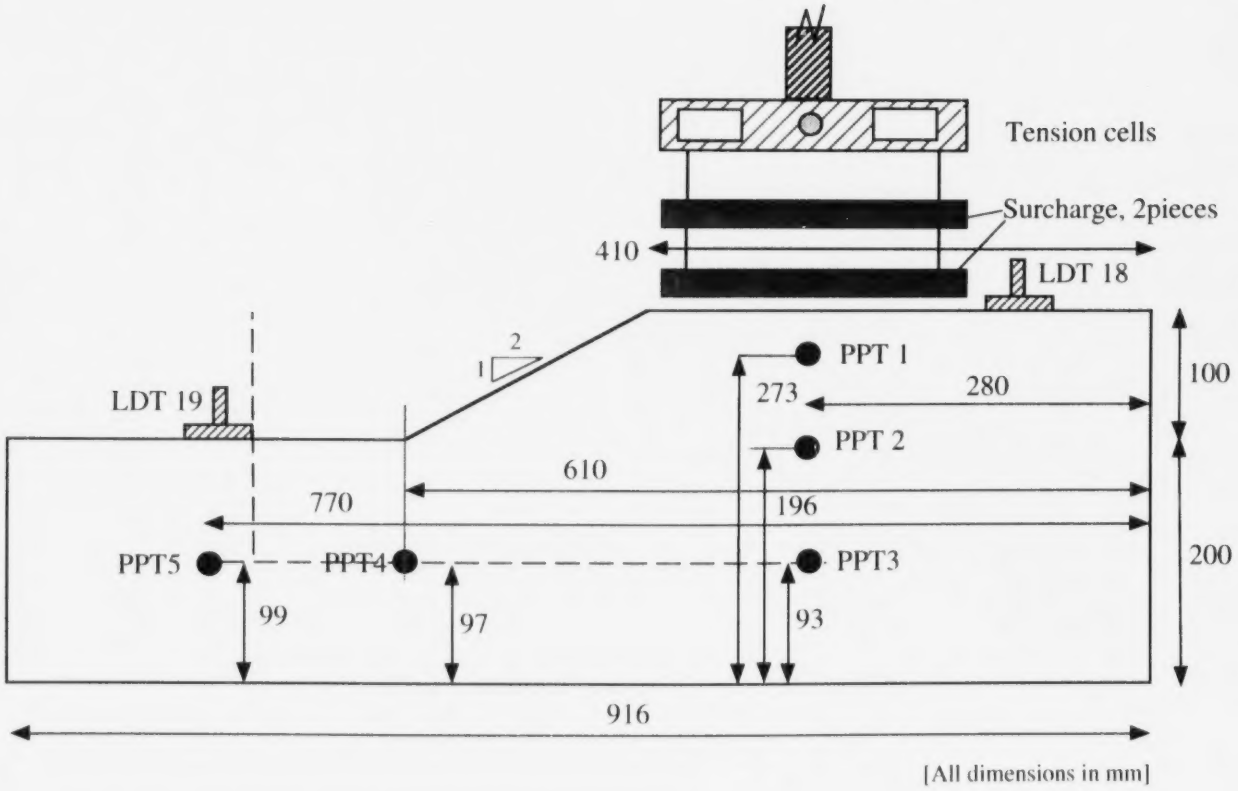

Fig. 5.2.6 CANLEX 3- Model Test Configuration.

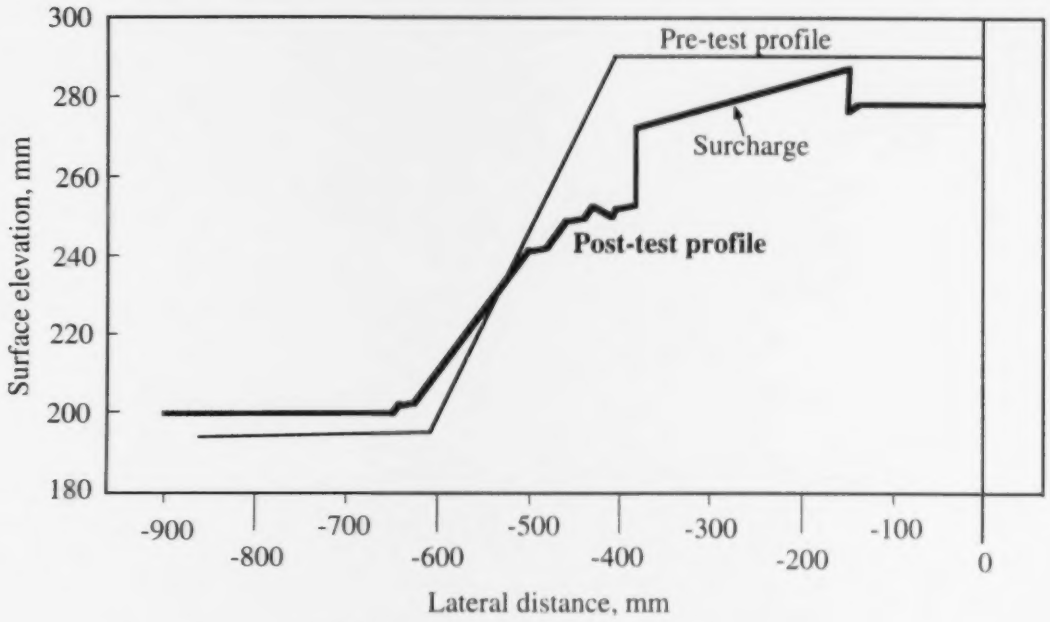

Fig. 5.2.7 CANLEX3 - Pre & Post Test Surface Profiles.

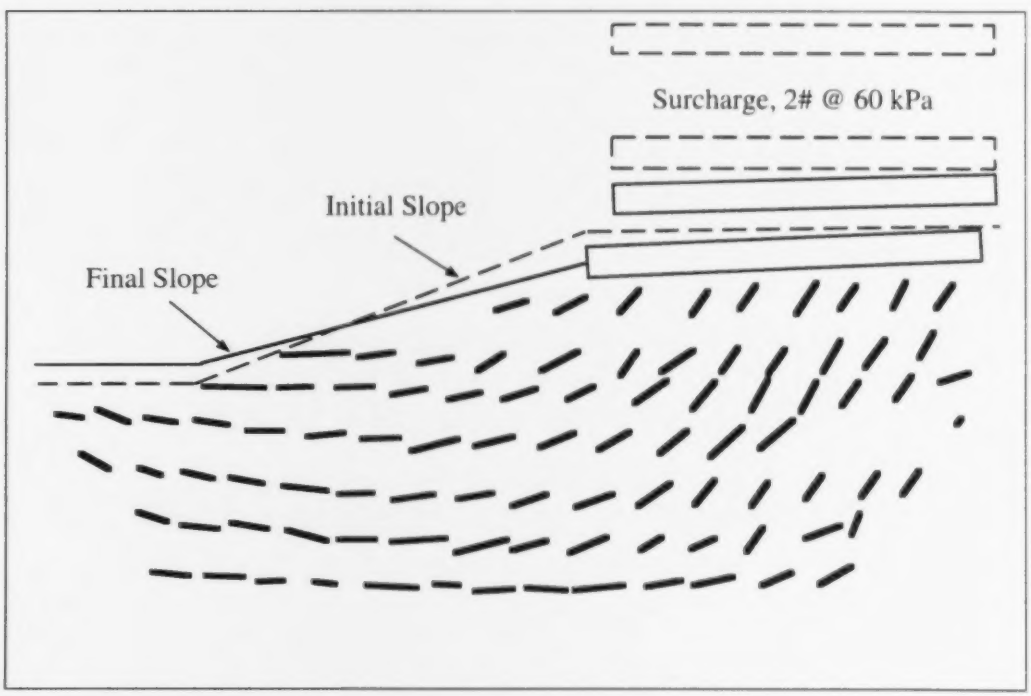

Fig. 5.2.8 CANLEX 3- Observed Deformation Field.

5.2.3 NUMERICAL MODELING AND ANALYSIS

The centrifuge tests were modeled using the finite element program PISA-L. The program has incorporated the collapse surface plasticity model for modeling undrained deformation of sand. To evaluate the model, one of the isotropically consolidated undrained triaxial compression tests on the Syncrude sand, conducted at Laval university, was simulated. Figure 5.2.9 shows an axisymmetric finite element model of the triaxial sample. The predicted and observed response of the test for a confining pressure of 728 kPa are compared in Figure 5.2.10. It can be seen that the computed response, stress-strain relationship and pore pressure, are reasonably comparable with the measured response of the test. Table 5.2.2 shows the parameters used in the analysis. The parameters were chosen to obtain the optimum fit to the measured data.

Figure 5.2.11 illustrates the steps involved in the numerical modeling of the centrifuge tests. The first step, indicated by point 1, shows the effective stress state of the sand after achieving equilibrium at 50 g. The second step, marked by the curved arrow, represents the effect of the surcharge which exerts undrained loading on the slope. The third step, represented by the downward straight arrow, displays the stress path followed by the liquefied elements during the collapse of the soil. The material parameters used in the liquefaction analysis are shown in Table 5.2.3. These parameters are determined based on the triaxial tests results. The pore pressure parameters were back calculated from the Henkel's Equation using the observed pore pressure response in the centrifuge tests.

Table 5.2.2 Parameters Used in Analysis of Triaxial Test.

E (kN/m^2)	ν	ϕ_s (°)	ϕ_c (°)	a	A_o	A_m	β	S_u (kN/m^2)
0.3×10^5	0.3	34	23.0	0.001	0	5	0.90	115

Key: E = Young's Modulus
ν = Poisson's ratio
ϕ_s = friction angle at steady state
ϕ_c = angle of collapse surface
a = post peak factor in hyperbolic model
A_o, A_m, and β = pore pressure parameters in the effective stress path model
S_u = undrained steady state strength

Table 5.2.3 Material Parameters Used in Finite Element Liquefaction Analysis.

Case	γ_b (kN/m^3)	E (kPa)	ν	ϕ_s (°)	ϕ_c (°)	a	A_o	A_m	α	S_u (kPa)
CANLEX1	9.87	900	0.3	36	24	0.001	0	5	0.3	20
CANLEX2	9.87	900	0.3	36	24	0.001	0	5	0.3	20
CANLEX3	9.00	9000	0.3	33	24	0.001	0	5	0.3	0.2*

Notes:

- * - S_u/p ratio
- γ_b - Submerged unit weight in Canola oil
- E - Young's Modulus
- ν - Poisson's Ratio
- ϕ_s - Steady state friction angle
- ϕ_c - Collapse surface friction angle
- a - Post peak factor in hyperbolic softening model (Chan and Morgenstern, 1989)
- A_o - Pore pressure parameters in liquefaction model (Gu et al., 1992)
- α - Henkel's pore pressure parameter; $\beta = 0.97$ was used in all analyses
- S_u - Undrained shear strength at steady state

In order to back calculate the pore pressure parameter α, the following steps were carried out.

(1) A total stress analysis was performed to calculate the changes in the total principle stresses (σ_1, σ_2, and σ_3) under the pressure of the drop weight.

(2) By subtracting the initial σ_1, σ_2, and σ_3 from the above values, the increments of total principle stresses $\Delta\sigma_1$, $\Delta\sigma_2$, and $\Delta\sigma_3$ were determined.

(3) The observed Δu is available from the piezometers.

(4) Using the equation proposed by Henkel (1960), the value of α was back calculated.

β is the pore pressure parameter for the change in mean normal stress and α is the pore pressure parameter for the change in deviator stress. β is reported to be 0.97 in the tests.

In the centrifuge tests, a two dimensional plain strain finite element mesh was used to model the prototype embankment. Figure 5.2.12 and 5.2.13 show the finite element idealization of CANLEX 1 & 2 and CANLEX 3, respectively.

A static effective stress switch on gravity analysis was performed to determine effective stresses after applying the centrifugal loading on the sand. For CANLEX 1 and 2, the application of the drop weight was modeled using a uniform boundary pressure. For CANLEX 3, the application of the drop weight was modeled using both uniform boundary pressure and rigid body elements. The numerical model assumes the soil deforms in an undrained manner with pore pressures determined from pore pressure parameters. Stresses in the soil after application of the surcharge are determined and then compared with the collapse boundary surface. If the stresses result in a collapsible state, collapse analyses will be performed and the stresses and pore pressures will be redistributed to obtain a new equilibrium state.

5.2.3.1 Results of the Analyses

CANLEX 1

The effective stress state immediately after application of the surcharge imposed on the initial effective stress state is shown in Figure 5.2.14(a). Figure 5.2.14(b) shows the effective stress state in the sand after the liquefaction analysis. As shown, a number of elements have liquefied and reached the steady state. However, most of the elements are below the collapse boundary surface. Figure 5.2.15 displays the yield condition after the completion of stress redistribution. The yield zone shown in Figure 5.2.15 is contained, indicating the overall stability of the slope. Figure 5.2.16 displays contours of excess pore pressures immediately after application of the surcharge. The observed and the calculated pore pressure responses at the PPTs due to the application of the surcharge are compared in Figure 5.2.17. A reasonable agreement between the calculated and the observed pore pressures can be seen. The model underestimates the response to the drop weight at PPT 2, but the equilibrium pore pressures compare reasonably with the predicted values.

CANLEX 2

The slope liquefied and failed as a result of loading and increase in pore pressure caused by the drop weight. This is indicated by the effective stress state lying outside the boundary surface, as illustrated in Figure 5.2.18(a). After the excess stresses were distributed, collapse and progressive deformation in the slope occurred. Figure 5.2.18(b) displays the post-failure effective stress distribution in the sand slope. Almost all of the elements have failed on the collapse surface and eventually reached the steady state.

Figure 5.2.19 presents the yield conditions in the sand slope after application of the surcharge, but before stress redistribution. It can be seen that a substantial area below the crest and the slope surface has yielded. In CANLEX 2, unlike CANLEX 1, the yield zone has been large enough to expand and result in overall instability of the slope. The failure shape, shown in Figure 5.2.20, compares favourably with the post-failure configuration of the slope given in Figure 5.2.4. The failure displacement field, shown in Figure 5.2.21, indicates a deep failure, which is in good agreement with that observed in the test.

Contours of excess pore pressures immediately after application of the surcharge are displayed in Figure 5.2.22. Figure 5.2.23 compares the observed and calculated pore pressure responses at the PPTs. As indicated, the calculated responses from the undrained analysis are in good agreement with the observed values.

CANLEX 3

In CANLEX 3, liquefaction and flow deformation happened as the result of the first plate and the deformation stopped prior to the application of the second plate. Therefore, in the finite element simulation, only the first plate was included. The surcharge effect was simulated by both boundary pressure and rigid body elements. No appreciable differences between the results from the above two modeling techniques were observed.

Previous analyses of CANLEX 1 and 2 were conducted using a constant value of undrained steady state strength for the entire slope assuming a uniform initial void ratio. Since it is known that the undrained steady state strength increases with increase in mean

normal effective stress, a constant S_u/p' ratio is more realistic. A S_u/p' ratio of 0.2 was used in the analysis. The analysis indicated failure of the slope after the application of the first weight. The calculated deformed mesh shown in Figure 5.2.24 compares favourably with the observed failure shape shown in Figure 5.2.7. Figure 5.2.25 shows the displacement field, which is comparable with the displacement vectors recorded during the test. The calculated and the observed pore pressures are shown and compared in Table 5.2.4.

The liquefaction evaluation was also performed with a single value of the undrained steady state strength (S_u = 20 kPa). Figures 5.2.26 and 5.2.27 show, respectively, displacement field and deformed finite element mesh when the effect of the surcharge is simulated by boundary pressure on the crest of the slope.

Table 5.2.4 CANLEX 3- Observed and Computed Excess Pore Pressures at PPTs, (kPa).

	PPT2		PPT3		PPT4	
	Observed	Measured	Observed	Measured	Observed	Measured
Immediately after application of the first surcharge	42	36	64	55	35	15
After liquefaction due to the first surcharge	25	32	50	45	45	38

5.2.3.2 Discussion on Steady State Strength, S_u

A key input parameter in the liquefaction analysis is the undrained steady state strength, S_u. S_u controls initiation of the collapse of the liquefiable soils. In order that the liquefaction analysis of the sand slope result in progressive deformation, it is not enough that S_u be smaller than the shear stress of the elements which are liquefied directly by the undrained loading. S_u also should be sufficiently small so that stress redistribution can

create expansion of the yield zone and, consequently, result in progressive deformation. For the first estimation of the undrained steady state strength of the sand slope, the value of 20 kPa was selected. As mentioned for S_u = 20 kPa, liquefaction analysis of CANLEX 1 did not show any collapse, while liquefaction analyses of CANLEX 2 and CANLEX 3 indicated collapse and flow failure of the sand.

In an attempt to investigate effects of any increases in the value of S_u on the results, S_u was increased to 22 kPa and then to 24 kPa; and the liquefaction analysis was repeated. Interestingly, CANLEX 2 did not fail for S_u greater than 20 kPa. Referring to Figure 5.2.18(a), it can be seen that for S_u = 24 kPa ($q_{ss} = 2S_u$ = 48 kPa), q_{ss} is smaller than the deviator stresses of a considerable number of liquefied elements (liquefied elements in this Figure are those points which are on or behind the strength boundary). However, q_{ss} is not sufficiently small to create conditions of collapse in the sand.

Looking at the steady state strength from the laboratory point of view is also instructive. Figure 5.2.28 shows the steady state strength results in the e-log p' plane with data from tests conducted at the University of Alberta and CANLEX. As indicated, the steady state line has a gentle slope. Therefore, any small change in void ratio results in a substantial change in mean normal effective stress at the steady state, p'_{ss}. p'_{ss} is correlated to the steady state strength by $2S_u = q_{ss} = M\ p'_{ss}$, where M is the tangent of the angle of the Hvorslev surface in a q - p' plane.

The upper bound and the lower bound of the void ratio in the centrifuge tests are also illustrated in Figure 5.2.28. The upper bound of the void ratio (e = 0.87) is related to a relative density of about 21% and the lower bound of the void ratio (e = 0.79) is associated with a relative density of about 40%. The average void ratio becomes about 0.83, which corresponds to a steady state strength of 20 kPa ($2\ S_u = M\ p_{ss}$; M=1.33).

The above discussion, based on the liquefaction analyses and the laboratory tests results, supports S_u = 20 kPa as a realistic average value for the steady state strength of the sand in the centrifuge model tests.

5.2.3.3 Limit Equilibrium Analysis versus Liquefaction Analysis

In order to evaluate the mechanism of failure (liquefaction flow failure versus instability along a potential slip surface) in the centrifuge tests, a limit equilibrium slope stability analysis of CANLEX 2 was carried out. A general slip surface (Morgenstern and Price, 1965) was adopted. It was assumed that the instability occurs under undrained conditions. Hence, an internal friction angle of zero was introduced to the analysis. Assuming a Factor of Safety equal to one, undrained shear strength of the sand was back calculated. The largest, in depth and width, possible slip surface was specified. This specification agrees with the general form of the observed failure shape.

From the limit equilibrium stability analysis, the undrained shear strength of the sand was back calculated equal to 22 kPa, which is close to the undrained steady state strength value used in the liquefaction analyses (S_u = 20 kPa). Therefore, the above stability analysis is not able to help to explore the mechanism of failure of the sand embankment in CANLEX 2. However, observations from the failure of the sand in CANLEX 2, reported by Phillips and Byrne (1993), support the idea of a typical flow failure of the mass of the sand rather than slipping of the sand along an obvious slip surface.

Therefore, it is reasonable to conclude that the failure of the sand embankment in CANLEX 2 and CANLEX 3 has most probably been, initially, due to the liquefaction of some area in the sand. This liquefaction has resulted in stress redistribution, further liquefaction and yielding of the surrounding area and, finally, collapse and flow deformation of the embankment.

5.2.4 SUMMARY

Numerical modeling and analyses of three centrifuge tests were described in this section. The tests were modeled using the collapse surface plasticity finite element model which simulates the collapse behaviour of liquefiable soils. The finite element model was evaluated by numerical simulation of an undrained triaxial compression test. The

predicted response of the model was comparable with the observed response during the triaxial test.

The centrifuge tests were carried out to investigate the feasibility of inducing a static liquefaction event in the field and to calibrate numerical models. Pore pressures and deformations calculated from the analyses were compared with the pore pressures and deformations observed during the tests. The calculated pore pressures are generally in good agreement with the observed values. The calculated deformation patterns compare favourably with the patterns observed in the tests.

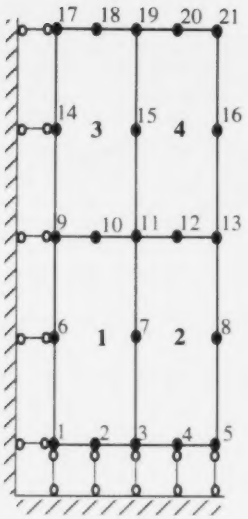

Fig. 5.2.9 Axisymmetric Finite Element Model of Triaxial Test.

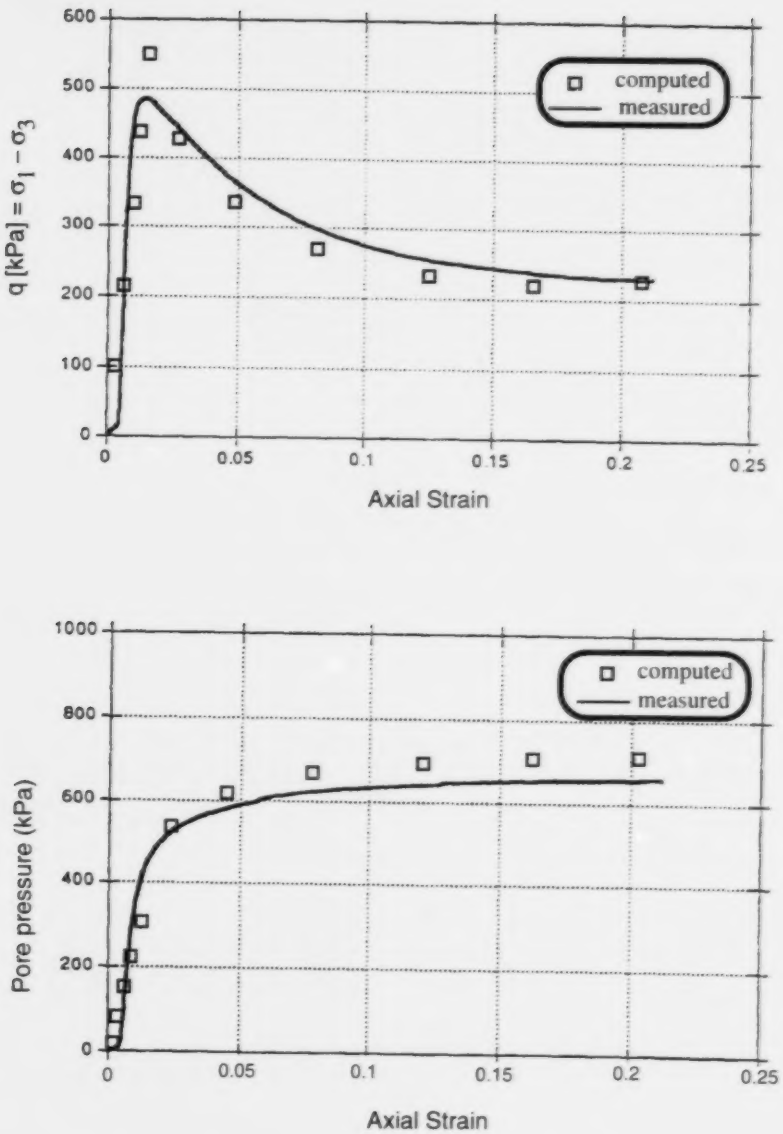

Fig. 5.2.10 Triaxial Test (Laval #3), Measured and Calculated Results.

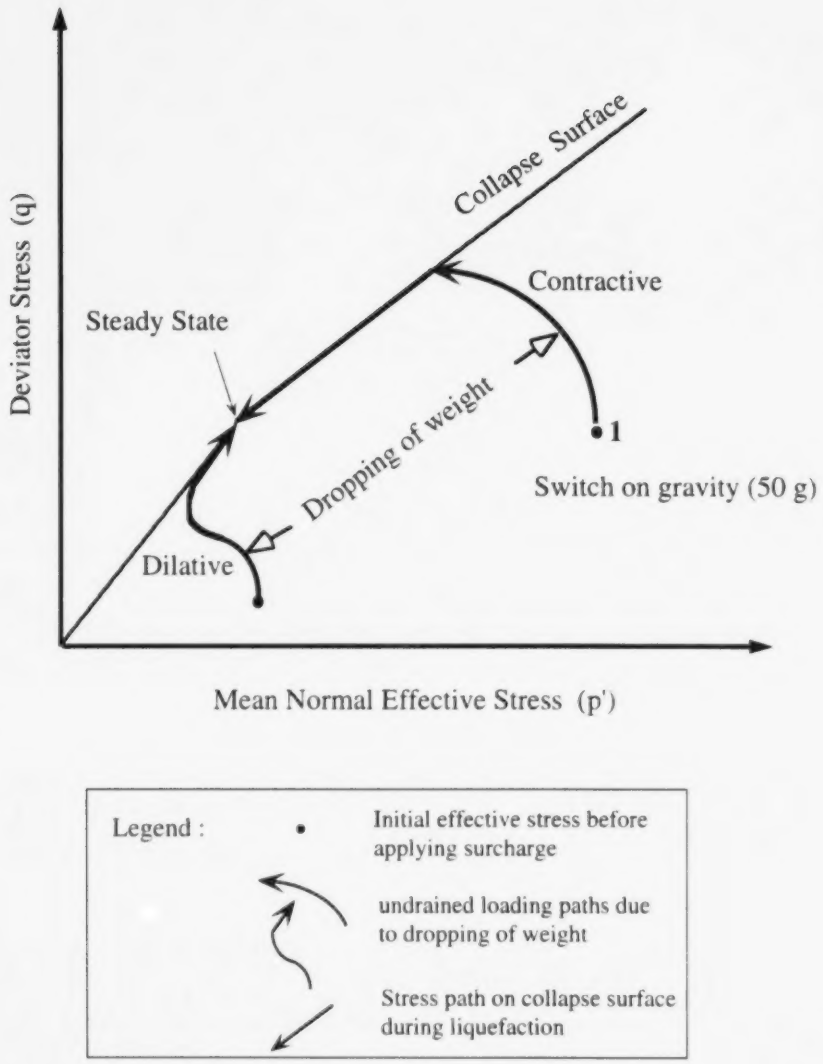

Fig. 5.2.11 Schematic Steps of Numerical Modeling.

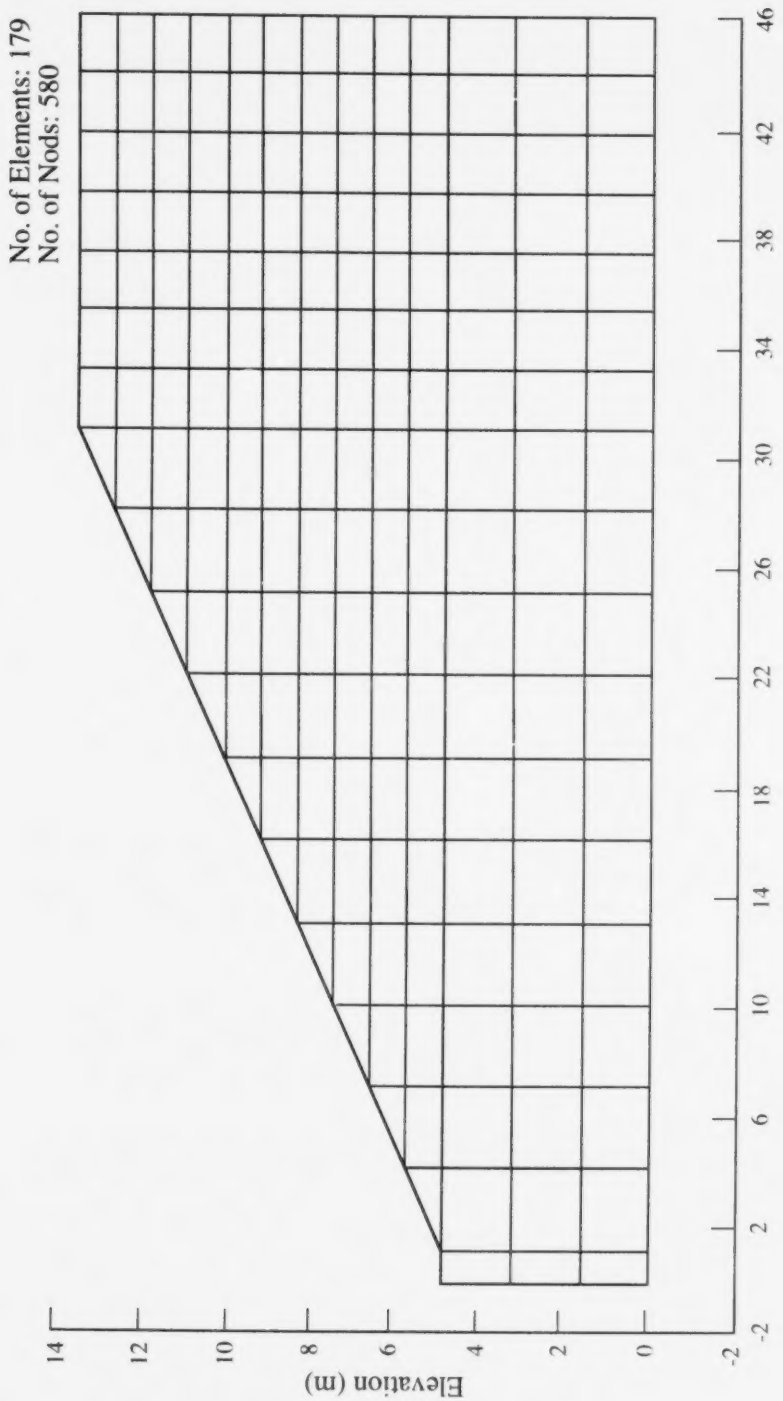

Fig. 5.2.12 CANLEX 1 and 2- Finite Element Idealization.

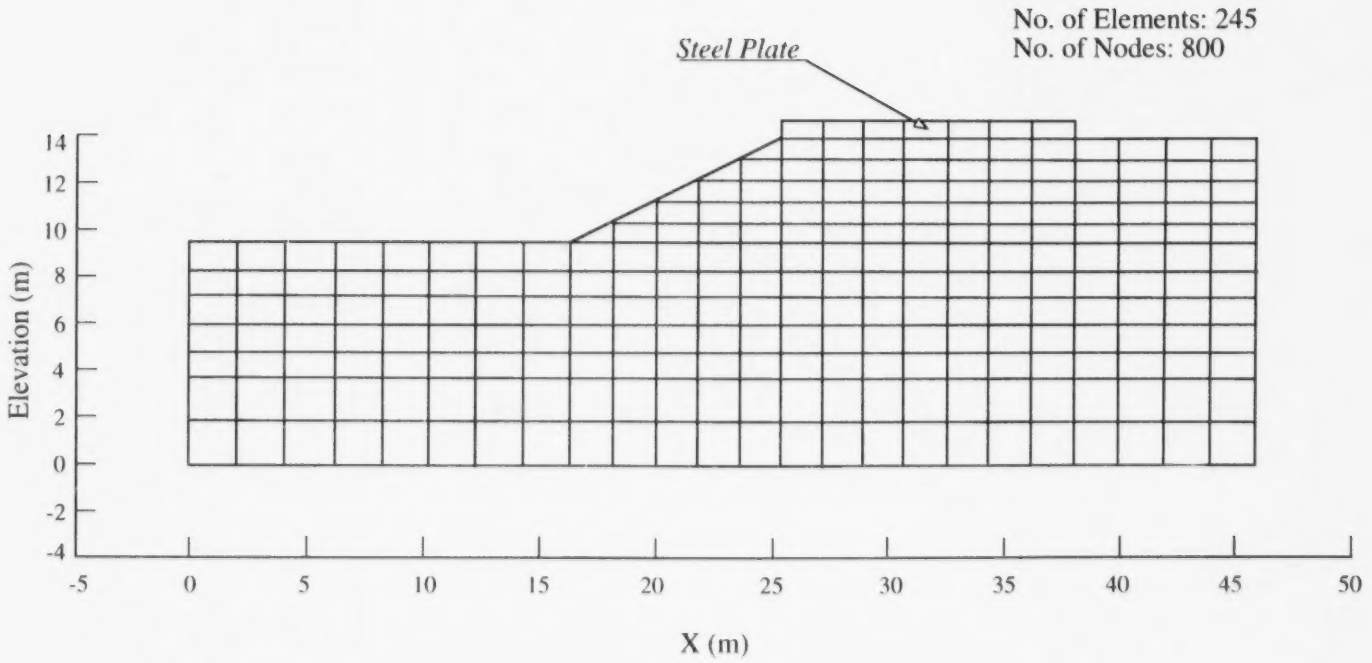

Fig. 5.2.13 CANLEX 3- Finite Element Idealization.

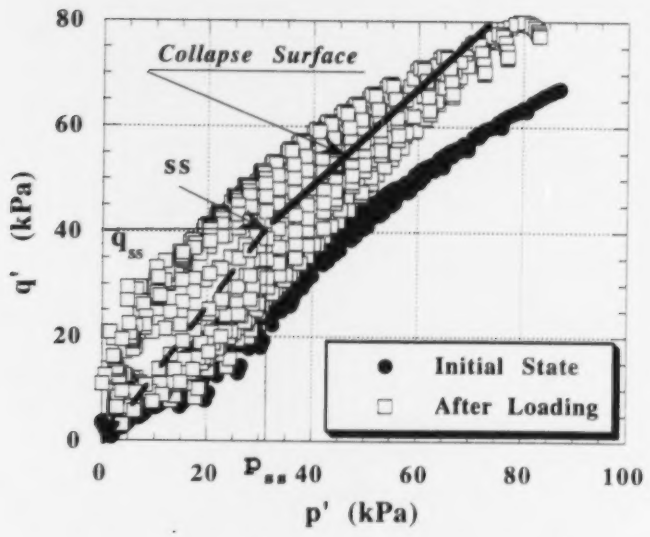

(a) Before Stress Redistrbution

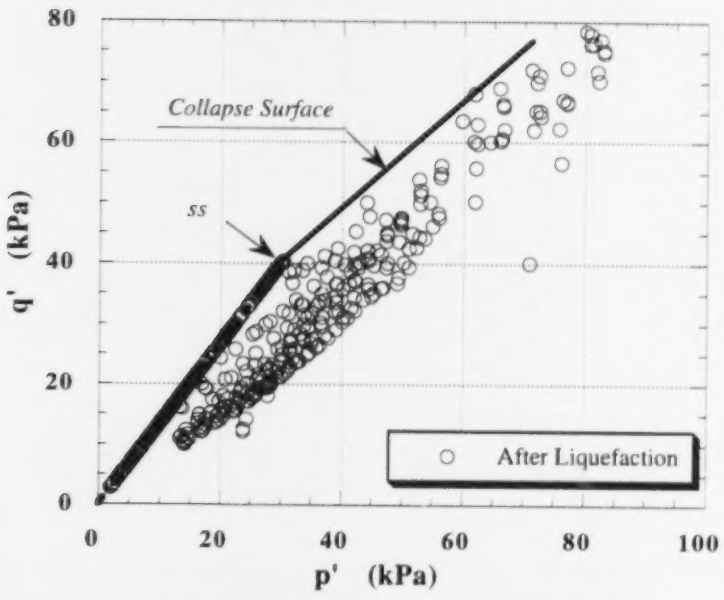

(b) After Stress Redistribution

Fig. 5.2.14 CANLEX 1- Effective Stress Distribution after Drop of Weight.

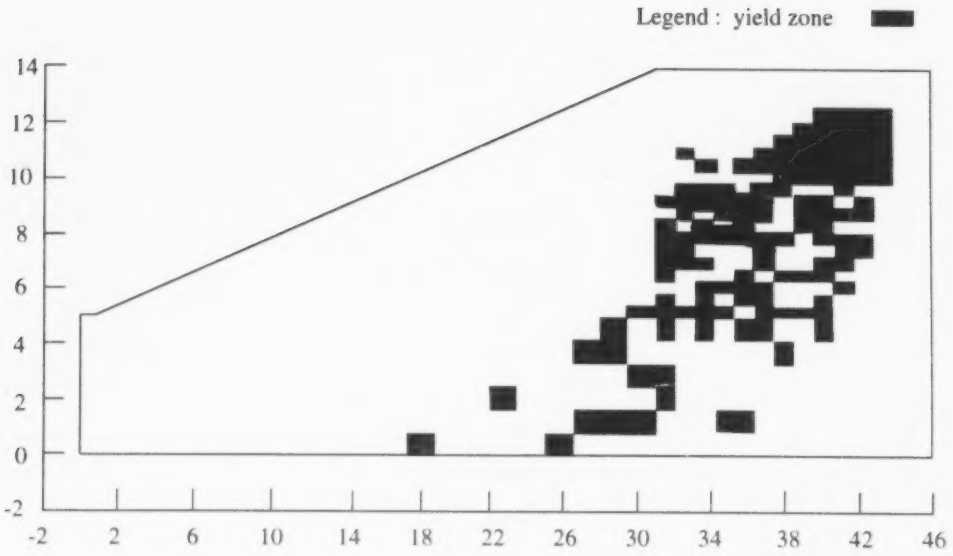

Fig. 5.2.15 CANLEX 1- Yield Zone after Stress Redistribution.

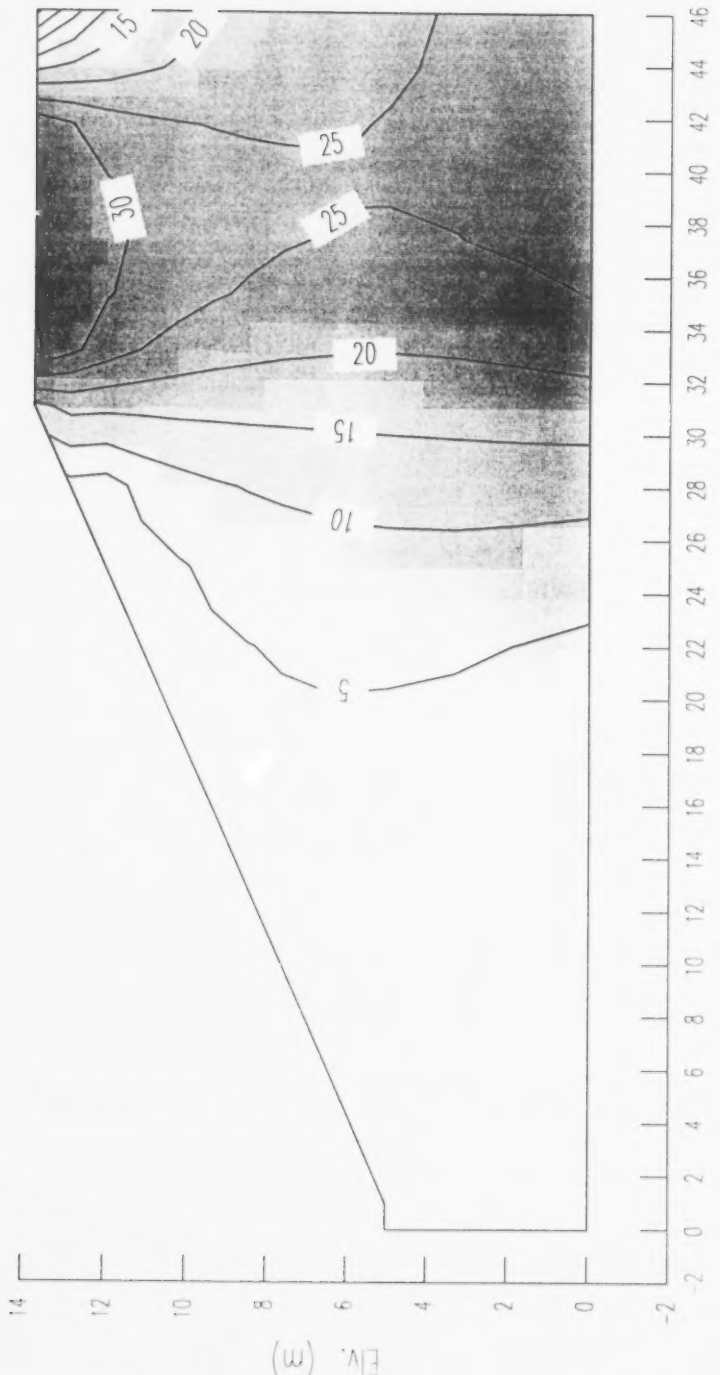

Fig. 5.2.16 CANLEX 1- Contours of Excess Pore Pressures Induced by Dropping the Weight (kPa).

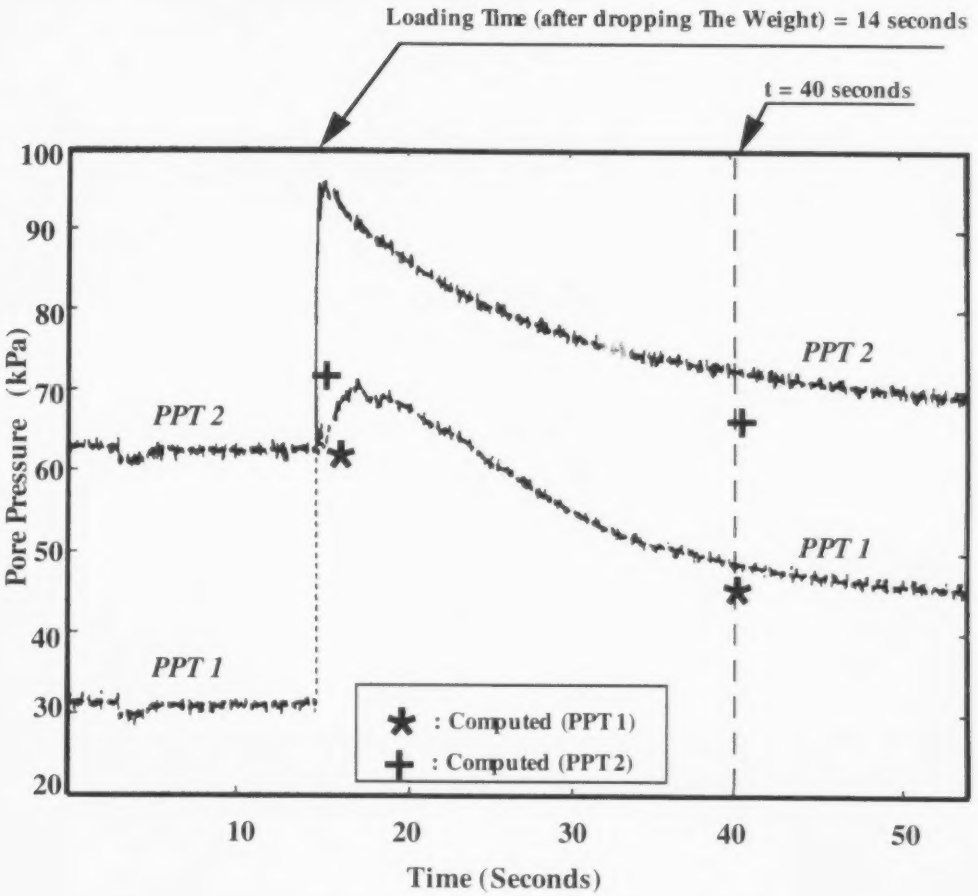

Fig.5.2.17 CANLEX 1- Comparison Between Computed and Observed Pore Pressures.

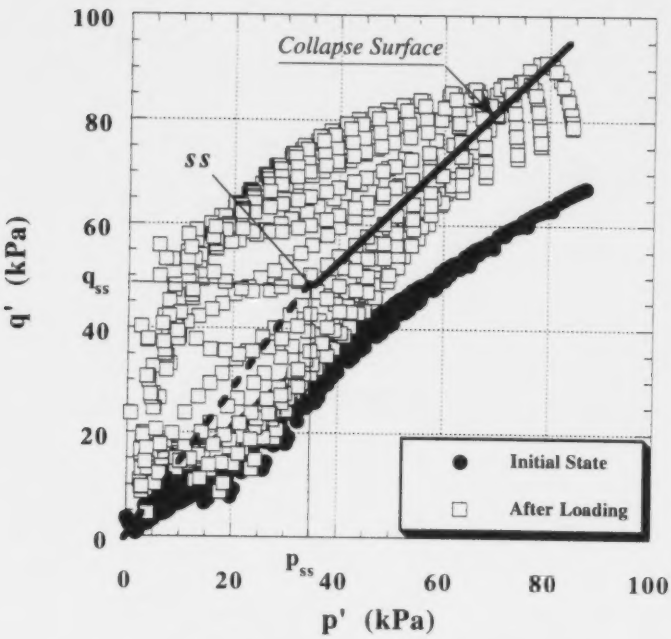

(a) Before Stress Redistribution

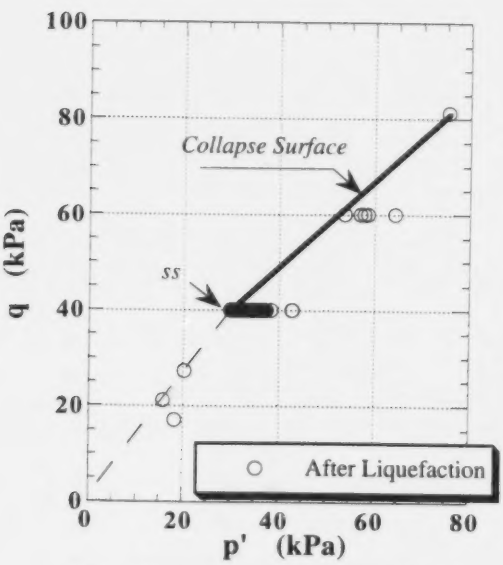

(b) After Stress Redistribution

Fig. 5.2.18 CANLEX 2- Effective Stress Distribution after Driop of Weight.

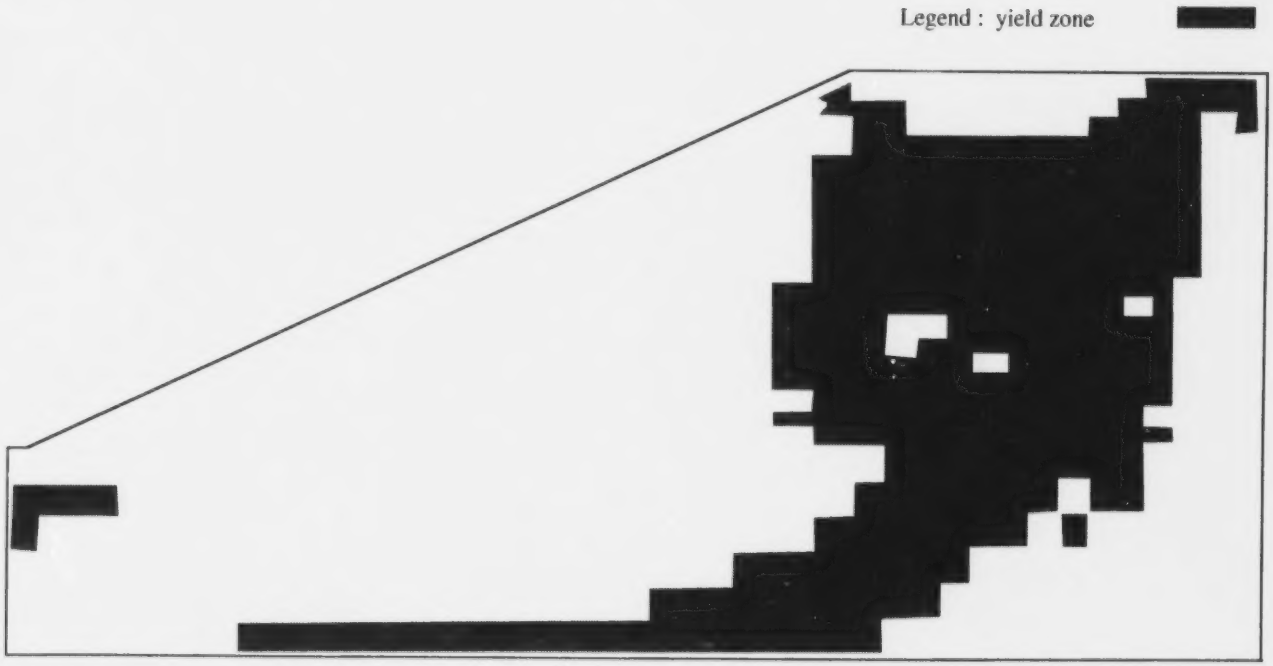

Fig. 5.2.19 CANLEX 2- Yield Zone after Drop of Weight and befor Stress Redistribution.

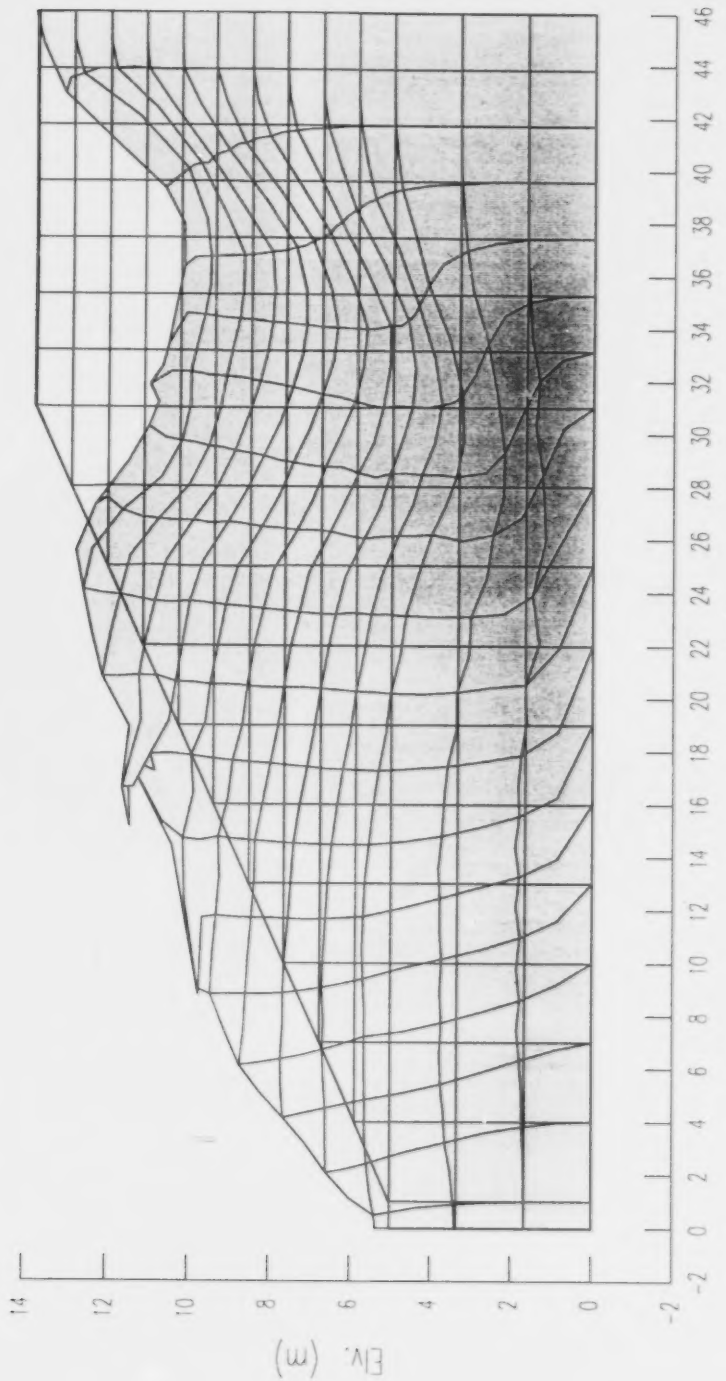

Fig. 5.2.20 CANLEX 2- Deformed Mesh after Liquefaction Analysis.

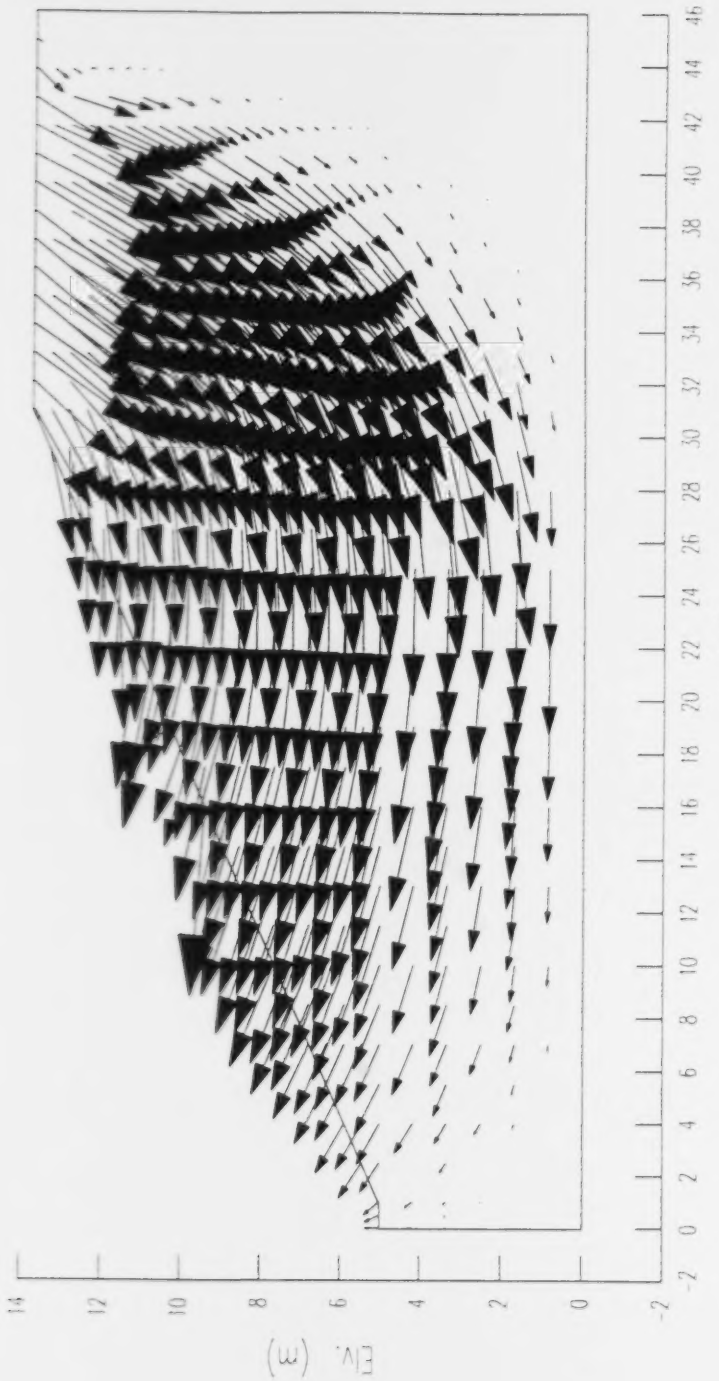

Fig. 5.2.21 CANLEX 2- Displacement Field after Liquefaction Analysis.

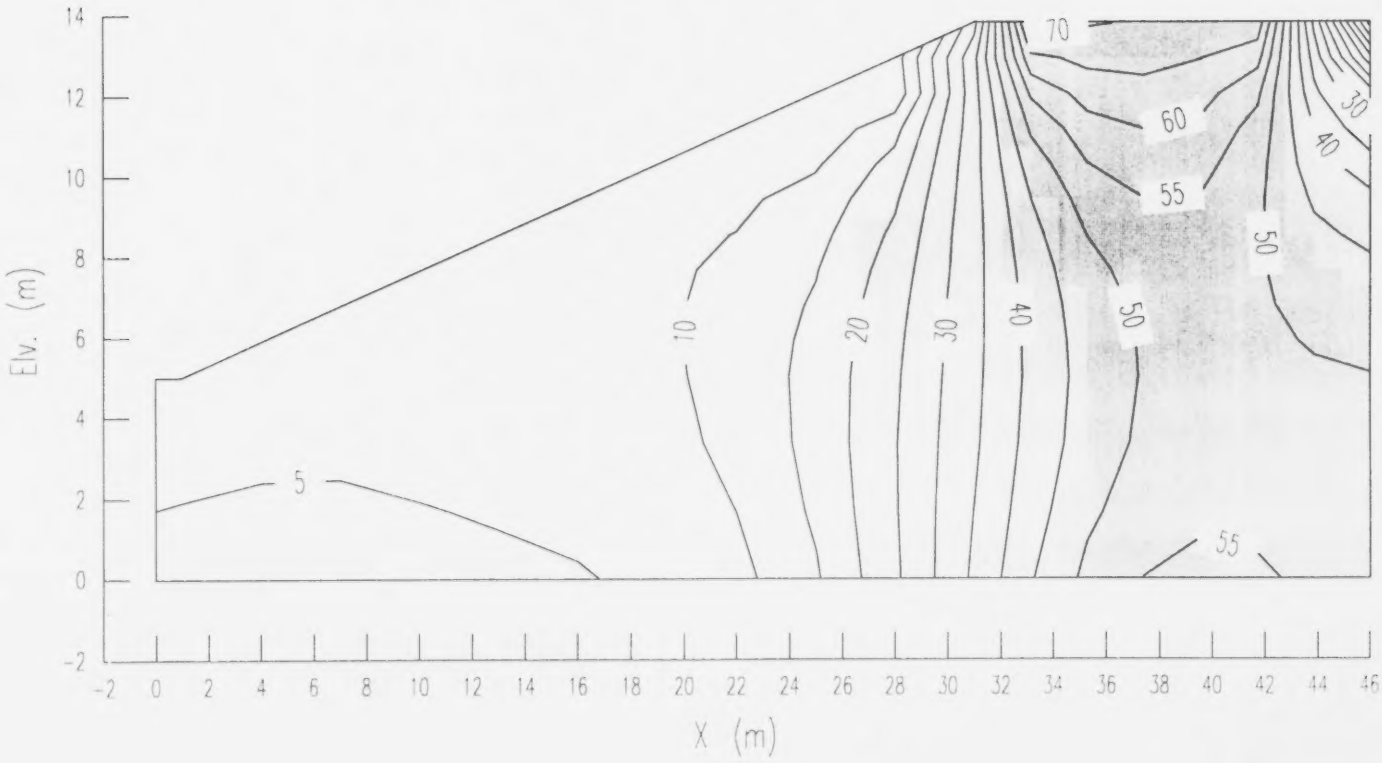

Fig. 5.2.22 CANLEX 2- Contours of Excess Pore Pressures Induced by Dropping the Weight (kPa).

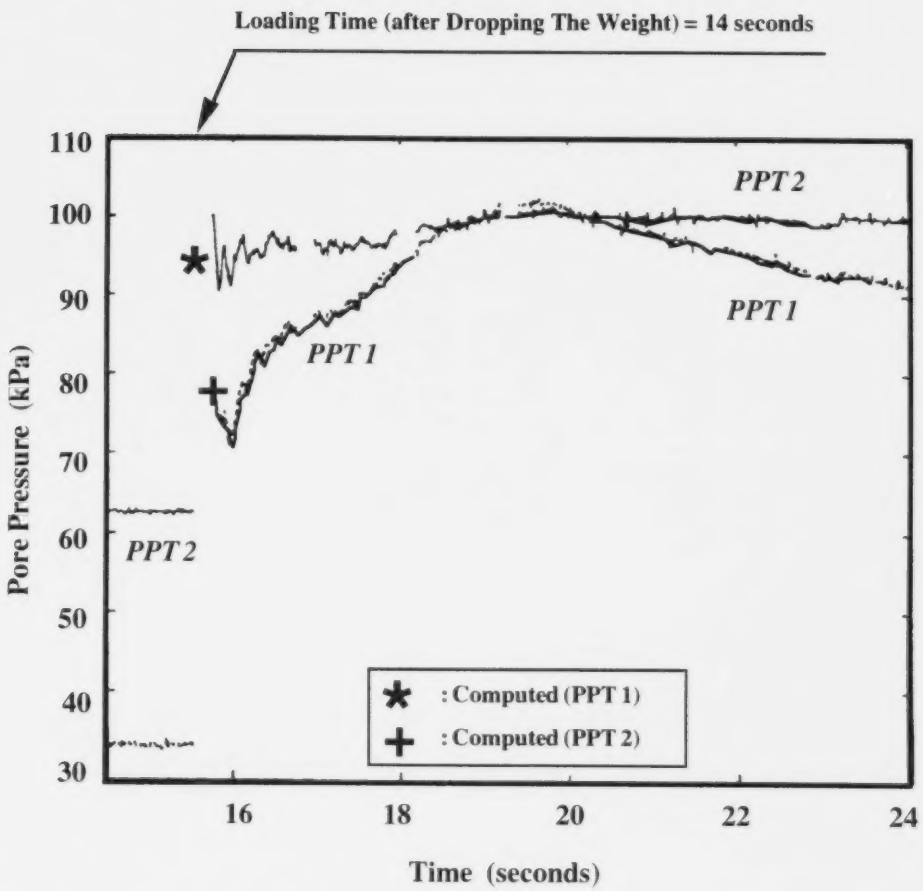

Fig. 5.2.23 Canlex 2- Comparison Between Computed And Observed Pore Pressures .

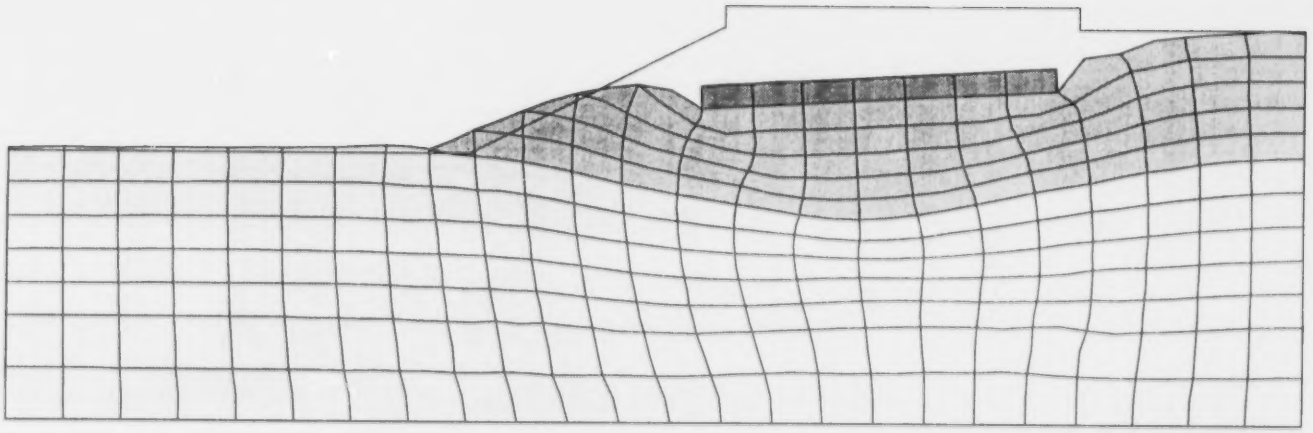

Fig. 5.2.24 CANLEX 3- Deformed Mesh after Liquefaction Analysis, $S_u = 0.2\ p'$
[surcharge is simulated by rigid elements].

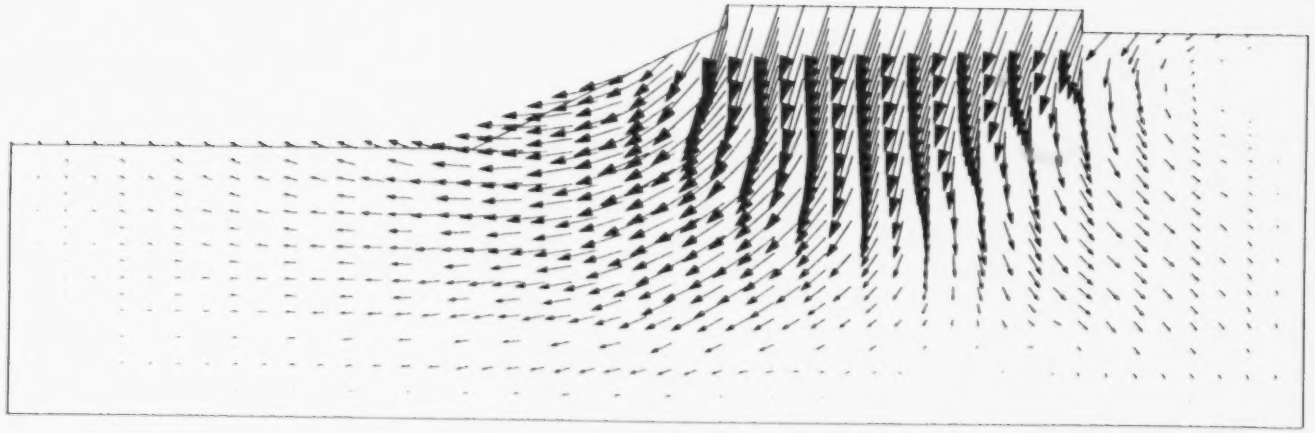

[arrow = displacement]

Fig. 5.2.25 CANLEX 3- Displacement Field after Liquefaction Analysis, $S_u = 0.2\ p'$
[surcharge is simulated by rigid elements].

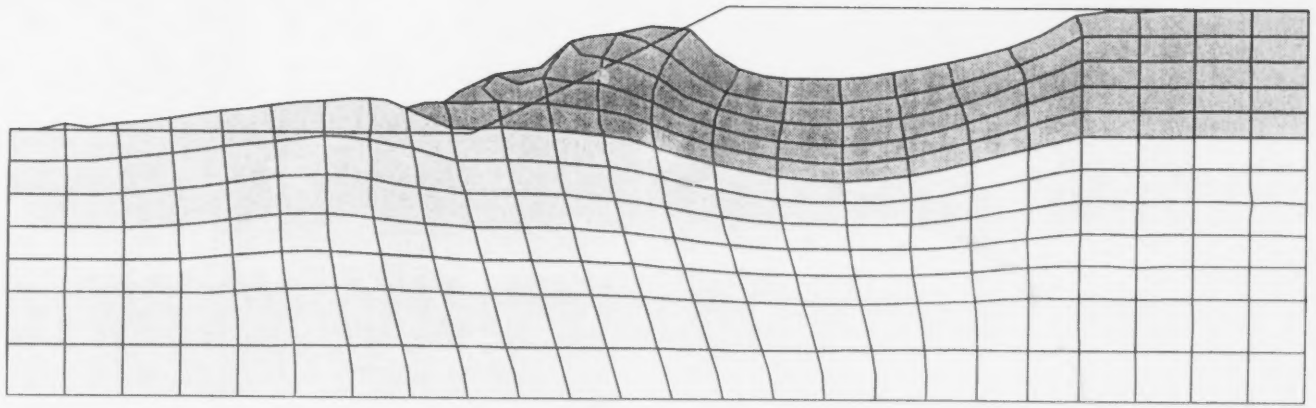

[magnification = 1.0]

Fig. 5.2.26 CANLEX 3- Deformed Mesh after Liquefaction Analysis, S_u = 20 kPa
[surcharge is simulated by boundary pressure].

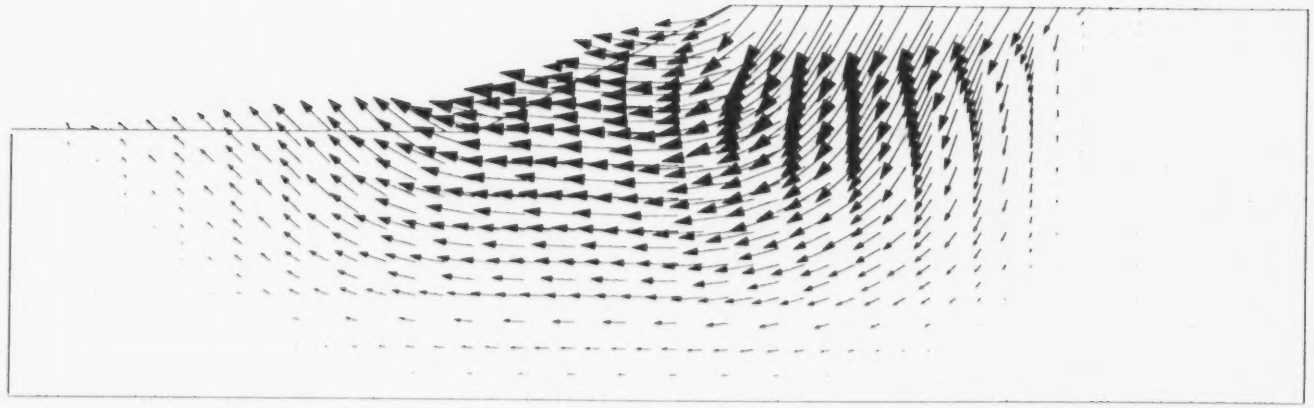

[arrow = displacement]

Fig. 5.2.27 CANLEX 3- Displacement Field after Liquefaction Analysis, S_u = 20 kPa
[surcharge is simulated by boundary pressure].

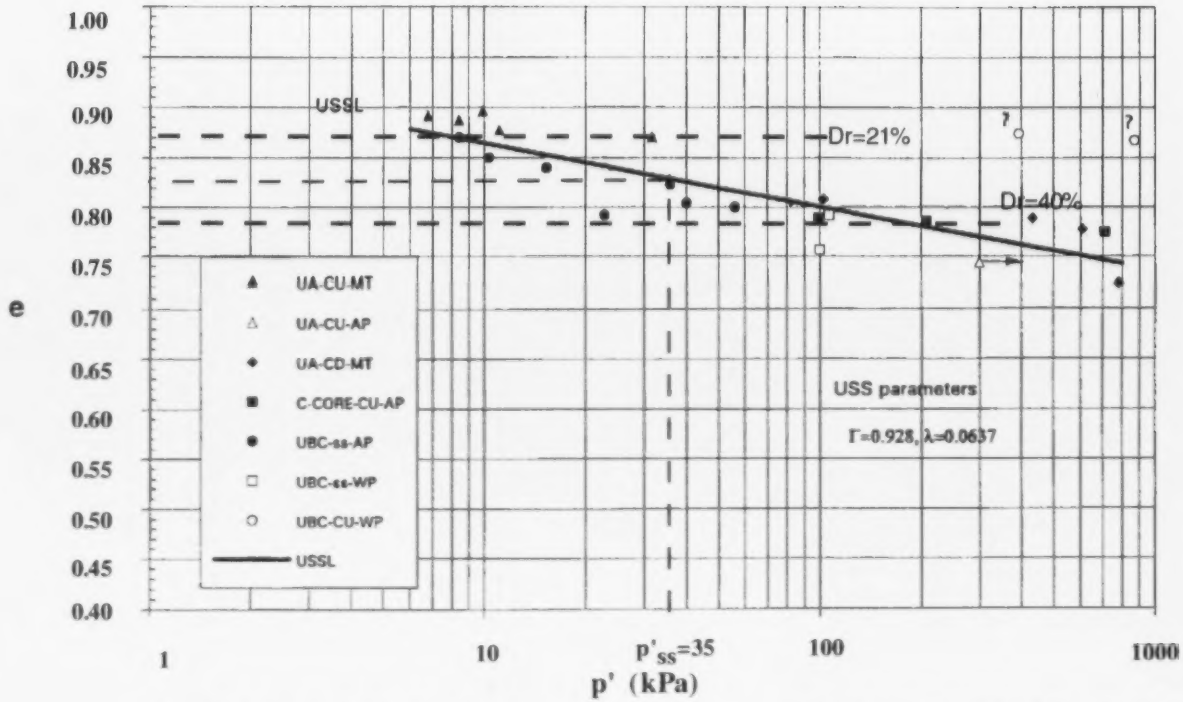

Fig. 5.2.28 Syncrude Sand Steady State Results in e - log p' plane [modified after Cunning (1993)].

5.3 LIQUEFACTION ANALYSIS OF THE FIELD EVENT[1]

5.3.1 INTRODUCTION

The previous Section of this Chapter presented the numerical modeling, the liquefaction analyses, and the results of the centrifuge model tests. Conducting the centrifuge model tests followed by the numerical modeling and the liquefaction analyses benefitted the project in the following ways:

(1) It ascertained that static liquefaction can occur in the centrifuge model tests and therefore it could happen in the full scale field event.

(2) The field event can be proposed based on the technical and analytical experiences from the centrifuge tests.

(3) The numerical model was adopted for the case of static liquefaction.

(4) The numerical model used in the liquefaction analyses of the centrifuge tests proved to be able to evaluate static liquefaction failures and forecast qualitatively and quantitatively failure configurations and pore pressure responses.

On the basis of the experiences gained through the numerical modeling and the analyses of the centrifuge tests, the field event was proposed. The event was intended to provide a

---

[1] A summarized version of this section is submitted as a paper to the 49th Canadian Geotechnical Conference, St. John's, Newfoundland, Canada, September 23-25, 1996.

static liquefaction failure in the field similar to the upstream liquefaction failures that occurred at the Suncor Tar Island Tailings Pond in the 1970's. The overall picture of the field event is that tailings from Syncrude, Canada, were loosely deposited under water in a constructed test cell. Afterward, a test berm was constructed up to a certain height on top of the tailings in order to induce static liquefaction failure in the loosely deposited tailings.

The design of the field event was an ongoing project at the time that its modeling and analysis were being carried out. At first, a preliminary design for the event was proposed (Plewes, 1994). This design is entitled *proposed field event* throughout this Section. On the basis of a number of influential factors and the results from the analysis of the *proposed field event*, the event design changed. The new design is named *final designed field event* in this Section.

The present Section of Chapter 5 is mainly devoted to the numerical modeling and analysis of the *final designed field event*. However, at the beginning, a summary of the numerical modeling and analysis of the *proposed field event* will be presented.

5.3.2 PROPOSED FIELD EVENT

A preliminary field event was proposed by Plewes (1994) based on a number of design criteria and geometrical features. The design criteria were required to induce static liquefaction failure in the loosely deposited tailings. The criteria were proposed as follows:

(1) A test cell is to be constructed to contain about 10 m of tailings which will be deposited under water in a loose state. The test cell should be constructed to sufficiently restrict seepage losses in order to maintain the tailings in a saturated state with hydrostatic pore pressure conditions .

(2) The density of the tailings sand should be equivalent to $(N_1)_{60} = 8$ or less.

(3) The test berm is to be constructed on top of the tailings in lifts of 2 m to 5 m to a maximum height of 15 m. A period for dissipation of excess pore pressures will be provided between construction lifts in order to permit construction equipment to safely travel on the surface of the berm.

Geometrical dimensions and construction requirements for the field event were determined from the information about the Suncor failure events and other similar experiences. These are as follows:

(1) The test cell should be long enough to provide free boundary conditions for the berm.

(2) The test cell should be wide enough to provide plain strain condition for the failure of the tailings and the berm, i.e., width of the cell should be at least 6 times the berm height. Figures 5.3.1 and 5.3.2 present, respectively, the plan and the cross-section of the *proposed field event*, and are determined based on the above criteria and requirements.

5.3.2.1 Numerical Modeling and Analysis

Figure 5.3.3 illustrates the different steps involved in the numerical modeling of the *proposed field event.* The first step marked by point 1 shows the effective stress state of the deposited tailings before construction of the berm. The second step designated by curved arrows represents the lifts of berm construction. The construction lifts will be fast enough to exert undrained loading on the loosely deposited tailings. The dissipation of excess pore pressures generated by the lifts of berm construction is shown by straight dashed arrows. The final step, shown by downward straight arrows, displays the stress path followed by liquefied tailings during the collapse. This scenario is repeated for all five lifts.

Table 5.3.1 presents properties of the tailings used in the analyses. The values of internal friction angle at steady state, ϕ_{ss} and the angle of collapse surface, α_c have been selected from the tests results conducted on Syncrude tailings sand for the CANLEX project. The sensitivity of the analysis to the undrained steady state strength ratio (S_u/p') of the tailings was reasonably covered by assuming a range of S_u/p' ratio between 0.15 and 0.45.

5.3.2.2 Results

Liquefaction analyses were performed for the last three lifts of berm construction where the berm height was to be raised to 9, 12 and 15 m through three equal lifts. For the purpose of brevity, only the results of the case analysis where the berm height equals to 15m and the undrained steady state strength ratio of the tailings equals to 0.2 are presented.

Figure 5.3.4 shows displacement field in the form of arrows. A pattern of deep-seated flow deformation can be seen. This is comparable with the pattern that resulted from the liquefaction analysis of the centrifuge model tests, CANLEX 2 and CANLEX 3. Figure 5.3.5 illustrates the post-failure configuration of the proposed event in the form of the deformed finite element mesh. A large slumping of the crest and bulging of the toe area in the slope surface, and on a large portion of the tailings surface, is obvious in this

Figure. Almost the entire area of the tailings, except for about 20 m near the right side dyke of the cell, have failed.

The overall results for different heights of the berm, in terms of S_u/p' ratio, are synthesized graphically in Figure 5.3.6. Using the results compiled in this Figure, one can describe possibility of the liquefaction failure of the event for different heights of the embankment in terms of the Su/p' ratio of the tailings. Here, failure is tentatively defined as the occurrence of deformations greater than about 3 meter. Figure 5.3.6 indicates that failure of the tailings and the berm may occur after construction of 9 m of the berm if the S_u/p' ratio of the tailings is less than 0.2. If $0.2 \leq S_u/p' \leq 0.3$, the berm might slump in the upstream corner of the crest. If $0.3 < S_u/p' < 0.45$, the berm will remain stable though some slumping in the crest and bulging in the tailings near the berm toe have been calculated.

In the case where the height of the berm is 12 m, the complete failure of the berm and the tailings could happen if $S_u/p' \leq 0.25$. If $0.25 < S_u/p' \leq 0.3$, large slumping for the crest and lateral deformation for the toe and the nearby tailings are calculated. If $0.3 < S_u/p' < 0.45$, large bulging in the toe and tailings beach close to the toe may occur; however, the event remains stable. When the height of the berm is raised to 15 m, the results of the liquefaction analyses indicate that failure might occur if $S_u/p' \leq 0.3$. If $0.3 < S_u/p' \leq 0.45$, the berm and the tailings will suffer from large deformation; however, they remain stable. For the case that $S_u > 0.45$, no significant deformation was obtained.

The numerical modeling and liquefaction analysis of the proposed field event further increased the confidence in the numerical model. The results of the analysis also helped the CANLEX Scientific Committee design the required instrumentation for the event.

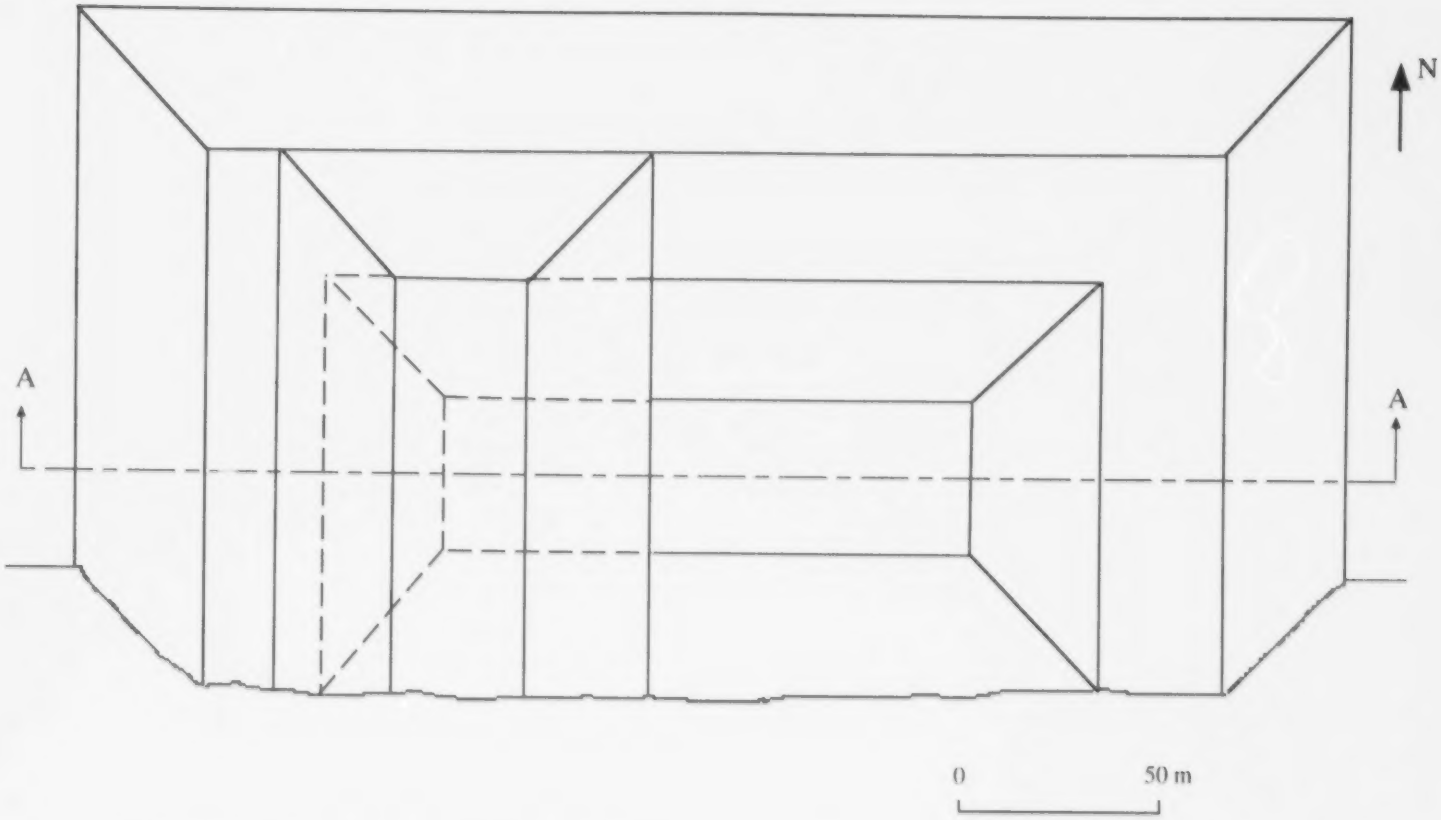

Fig. 5.3.1 Proposed Plan of The Field Event.

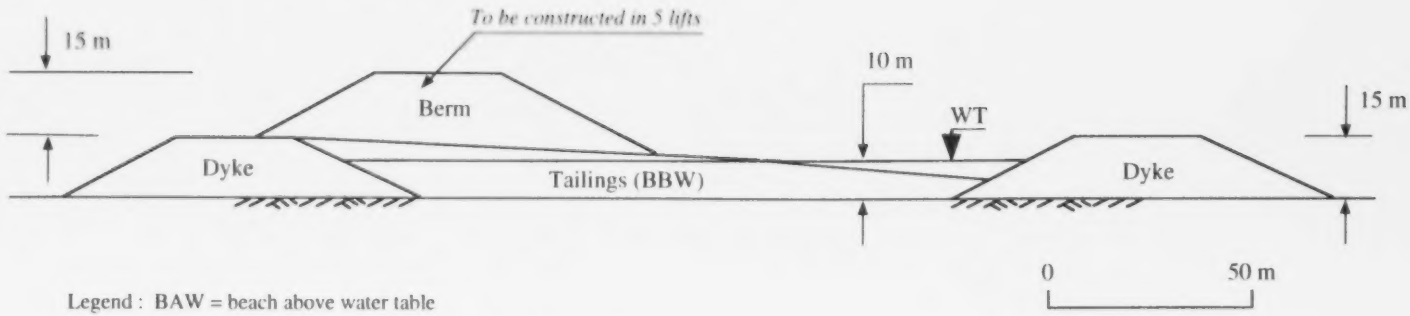

Fig. 5.3.2 Section A-A of the proposed Field Event.

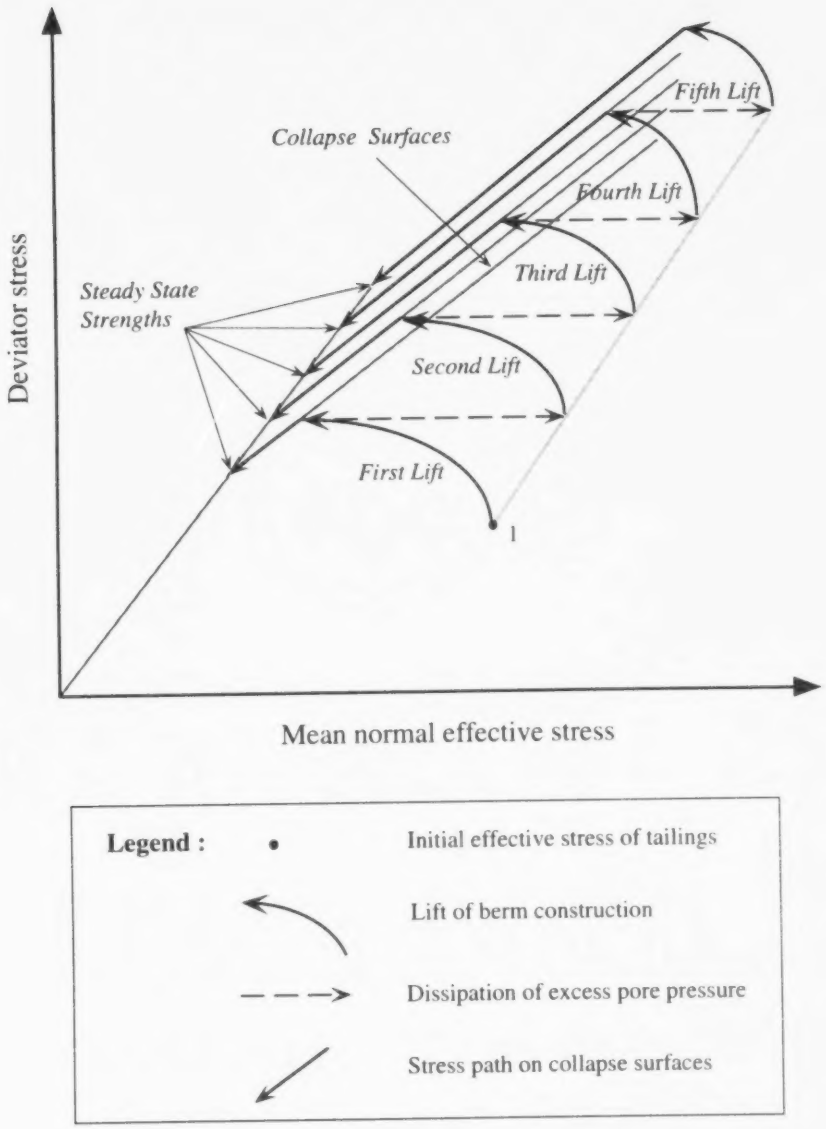

Fig. 5.3.3 Illustration of Field Event Modeling.

Table 5.3.1 Material Properties of Tailings Used in Liquefaction Analysis of Proposed Field Event.

Soil	γ_s (kN /m^3)	γ_b (kN /m^3)	E (kN /m^2)	ν	ϕ_{ss} (°)	α_c (°)	S_u/p'	a	A_o	A_m	B
Tailings (BBW)	15.5	5.7	0.10×10^5	0.49	33	24	0.15-0.45	0.001	0	5	1
Tailings (BAW)	15.5		0.10×10^5	0.3							
Berm	20		0.45×10^5	0.3							

Key: γ_s = saturated unit weight of oil sand

γ_b = submerged unit weight

E = Young's Modulus

ν = Poisson's ratio

α_c = angle of collapse surface in p'-q plane

S_u/p' = undrained steady state strength ratio

a = post peak factor in hyperbolic model

A_o, A_m, and B = pore pressure parameters in the effective stress path model

BBW and BAW: Beach Below (Above) Water Table

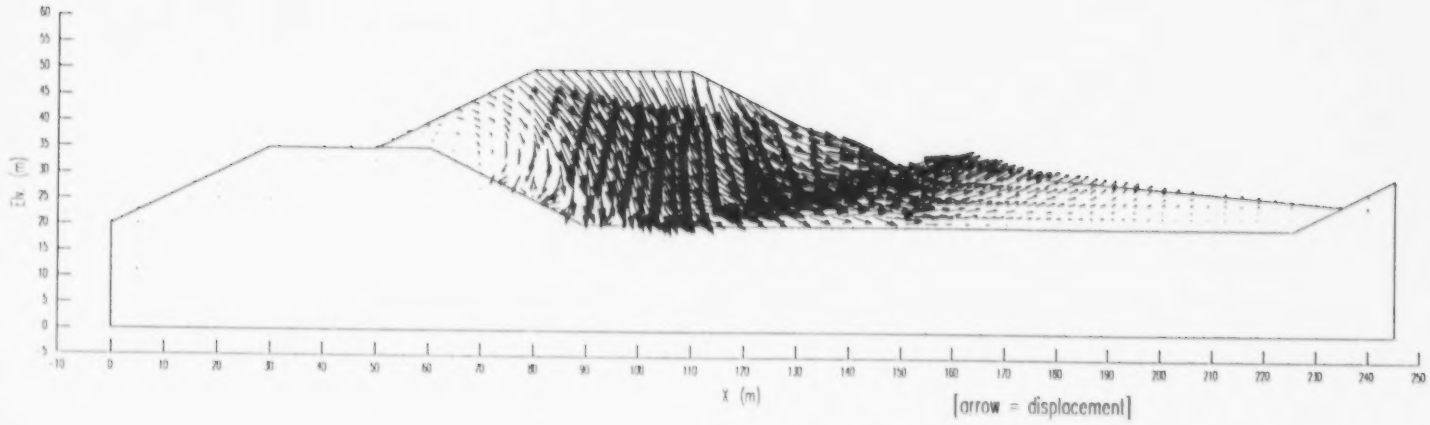

Fig. 5.3.4 Displacement Field after Liquefaction Analysis (H_{berm} = 15m, Su/p' = 0.2).

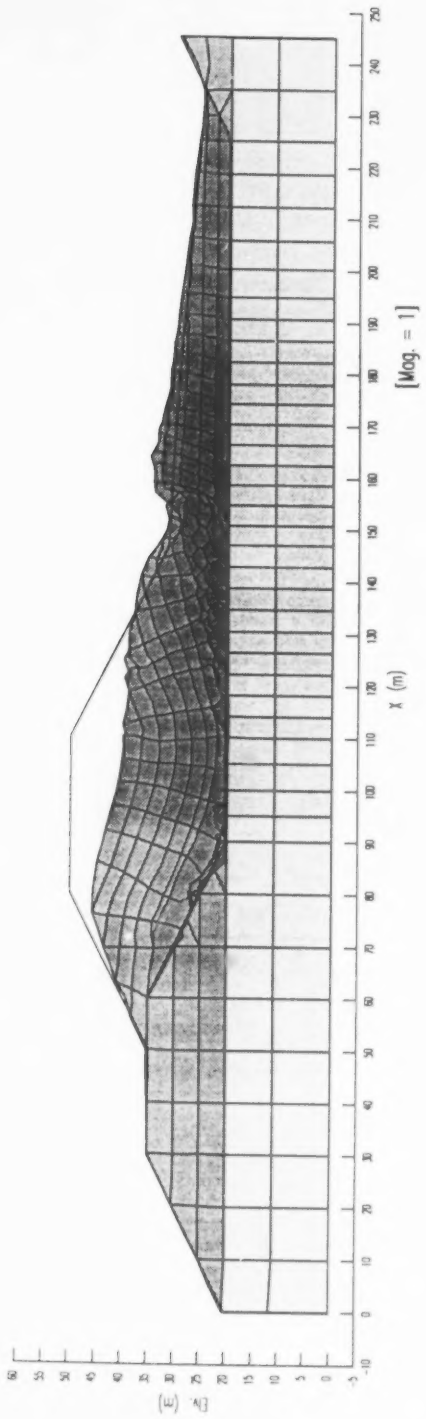

Fig. 5.3.5 Deformed Finite Element Mesh after Liquefaction Analysis (H_{berm} = 15 m, S_u/p' = 0.2).

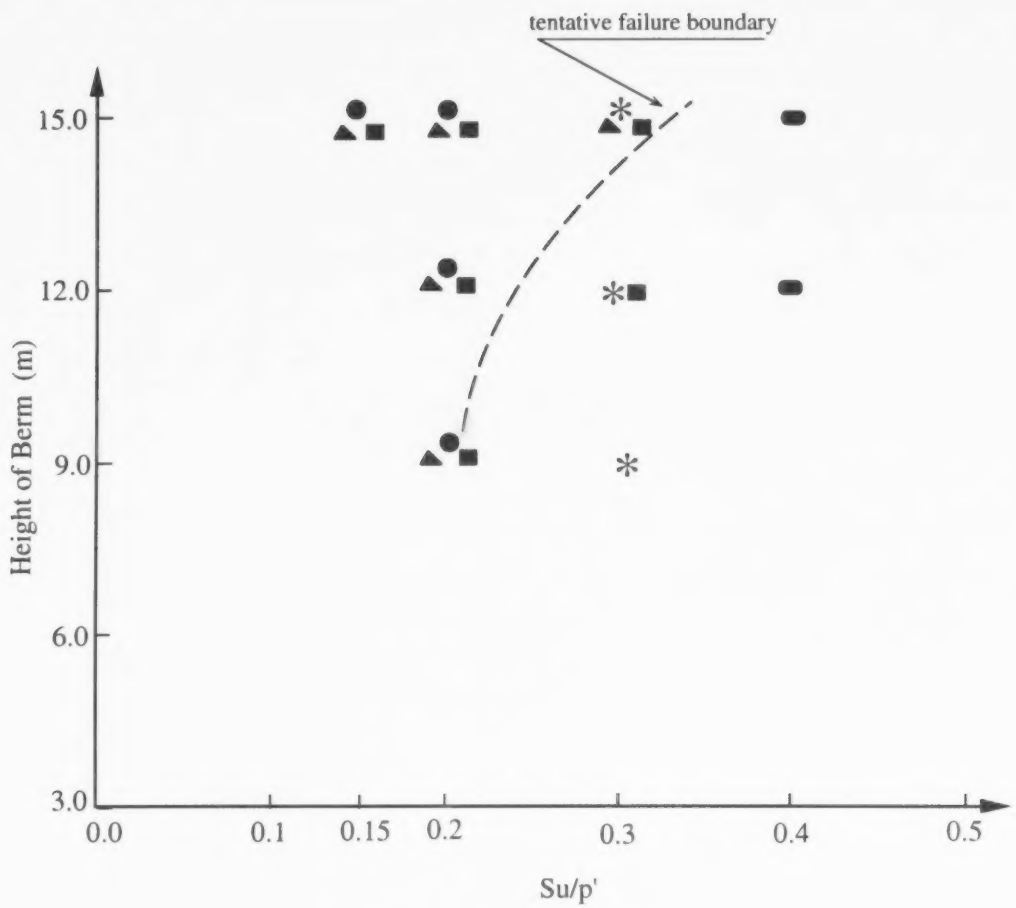

Legend : ✻ = slumping of the crest

● = slumping and lateral deformation of the crest

▲ = slumping or lateral deformation of the D/S slope surface

■ = bulging and lateral deformation of the toe and the beach near the toe

⬬ = bulging of the toe and the beach near the toe

Fig. 5.3.6 Failure Cases of the Field Event

[failure is defined any diplacements > about 3 m].

5.3.3 LIQUEFACTION ANALYSIS OF THE FINAL DESIGNED FIELD EVENT

A number of influential factors changed the design of the field event. Safety to life, safety to equipment, construction procedure compatible with Syncrude procedures and costs were the major factors. It was agreed that the trigger mechanism should be a static one comprising both rapid loading as well as boundary water loading, leading to transient seepage. Details of the liquefaction event planning are given by Byrne et al. (1995).

The maximum height of the embankment was limited primarily to 10 m (8 plus 2) based on safety concerns and then to 8 m due to the cost. The event took place in J-pit on the Syncrude, Canada Site near Fort McMurray. The pit is approximately 400 m long by 300 m wide and 10 m deep, and at the time of construction was almost full of water. Figure 5.3.7 shows the location and the size of J-pit. The pit was filled with about 11 m of submerged tailings sand.

The test embankment was constructed in the north west corner of J-pit. The tailings sand was contained between the clay dyke and a compacted sand structure, as shown in Figure 5.3.8. The contained tailings were deposited in water so that the soil structure was subjected to a rapid loading.

Finite element deformation analysis of the event was carried out in 2 stages: (1) pre-event prediction and (2) during-construction prediction. Results of the above analyses were submitted to the CANLEX administration in the form of two prediction reports. In the following Section, comprehensive summaries of these reports are presented. A number of comments on the post-event conditions will also be provided.

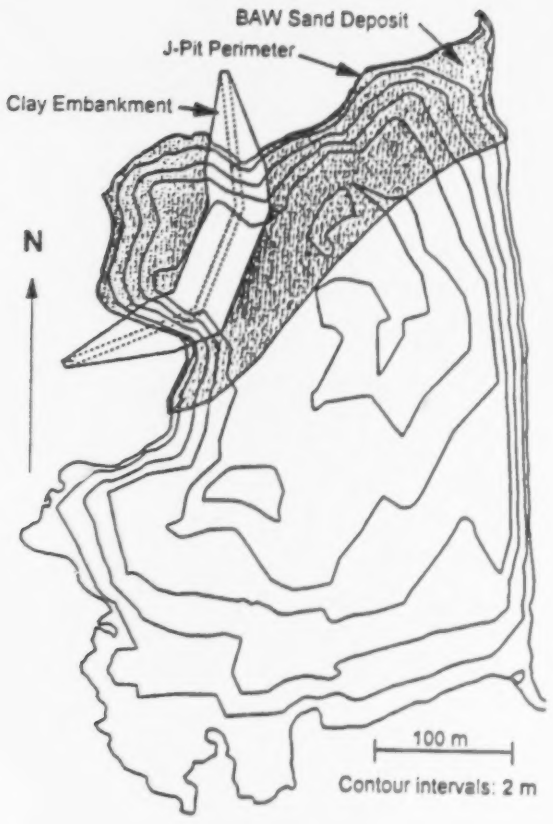

Fig. 5.3.7 Plan View of Field Event in J-Pit.

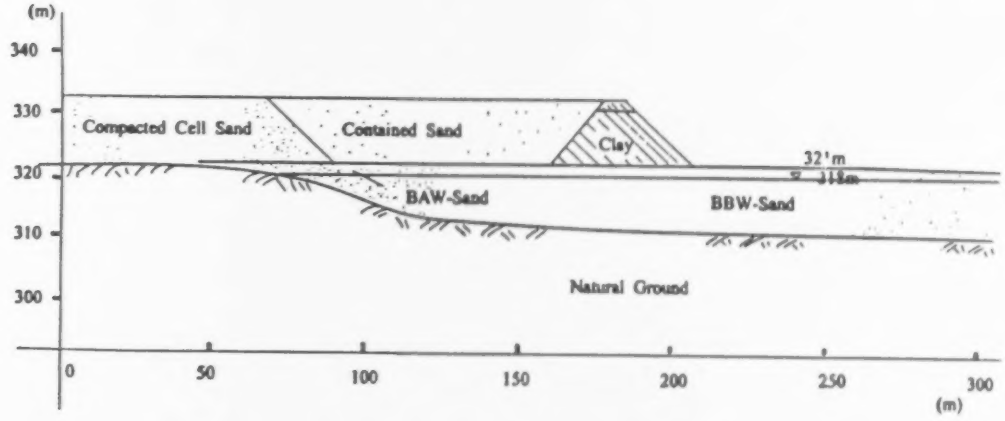

Fig .5.3.8 Field Event Geometry and Soil Types.

5.3.3.1 Pre-Event Analyses

Based on the Final Design Report on the Liquefaction Event, Figure 5.3.9 presents the field event cross section including 11 m of submerged tailings sand, and a 10 m clay embankment over the tailings. The tailings sand is assumed to be fully submerged. According to the information on site characterization, about 1.5 m of soft clay exists between the tailings sand and the foundation material. The contained tailings will be piped behind the clay embankment in order to exert an undrained loading on the tailings sand to trigger a static liquefaction failure. The tailings sand has a surface slope of approximately 1%. The upstream and downstream slopes of the first 8 m and the top 2 m of the embankment are 2.5:1 and 1:1, respectively.

Finite element analysis using the computer code PISA-L was carried out. Figure 5.3.10 presents a plain strain two dimensional model and the boundary conditions of the field event. Since it was not known at the time of the analysis that the upstream and downstream faces of the first 8 meter of the clay embankment will be constructed at 2:1 or 2.5:1 slopes, the elements in these areas are generated in such a way that the analysis can examine either case. A certain depth of the foundation is also included in the finite element mesh; and the mesh is extended to about 100 m beyond the clay embankment to minimize boundary effects.

Material properties used in the static analysis are presented in Table 5.3.2. The unit weight of the tailings sand is assumed based on an average relative density of 34% (e_{max} = 0.96, e_{min} = 0.53, and G = 2.64 kN./m3). Strength and deformation parameters of the tailings sand are estimated from the average cone resistance obtained during site characterization. The site characterization indicates that the top 3 m of the tailings sand is generally denser than the lower 8 m. Therefore, the unit weight of this part of the tailings was assumed to be slightly higher. Pore pressure parameters α and β in Table 5.3.2 are the same values used in the analysis of the centrifuge model tests and the *proposed field event*. For the soft clay layer at the bottom of the tailings sand, a residual internal friction angle of 8 degree is assumed (Alencar et al., 1994).

Table 5.3.2 Parameters Used in Effective Stress Static Analysis of the Field Event.

Material	γ (kN/m3)	γ' (kN/m3)	E'(kN/m2)	ν'	ϕ'	c'(kN/m2)	α pore pressure parameters	β
Foundation	19		70,000	0.3	38	25		
Clay Layer	19		10,000	0.47	8	1	0.3	0.97
Tailings (low 8 m)	18.75	8.95	14,000	0.3	34	1	0.3	0.97
Tailings (top 3 m)	19.2	9.4	18,000	0.3	36	1	0.3	0.97
Compacted Sand	19.25		100,000	0.3	45	1		
Clay Embankment	19		15,000	0.37	25	25		
Contained Tailings	18.75	8.95	10,000	0.3	28	1		

Key: γ = total unit weight

γ_b = submerged unit weight

E' = Young's Modulus

ν' = Poisson's ratio

ϕ' = internal friction angle

c' = cohesion

α and β = Henkel's pore pressure parameters

Drained Analysis of the Embankment Construction

A drained static analysis, using the elasto-plastic Mohr Coulomb Model, was performed to simulate the very slow construction rate of the clay embankment over the submerged tailings sand. In this analysis, the tailings are considered to be fully drained during the embankment construction. This type of construction most probably will not be followed in the field due to the finite amount of time it takes for pore pressures to dissipate. However, the drained condition represents an extreme case to evaluate the stability of the embankment. Sequence of the analysis is summarized in Table 5.3.3. This is the same sequence suggested in the Final Design Report of the Liquefaction Event and is expected to be followed in the field.

Table. 5.3.3 Sequence of Fully Drained Analysis of Clay Embankment.

STEP	ANALYSIS
1	Foundation, soft clay layer, and submerged tailings (switch on gravity analysis)
2	First layer of clay embankment (2m), drained loading
3	Second layer of clay embankment (2m), drained loading
4	Third layer of clay embankment (2m), drained loading
5	Fourth layer of clay embankment (2m), drained loading
6	Fifth layer of clay embankment (2m), drained loading
7	Construction of the compacted sand Dyke

Results of Drained Analysis

The results of the analysis indicate no large deformation occurs in the tailings sand and clay embankment. Therefore, the model indicates that construction of the clay embankment over the tailings sand under drained conditions should be stable and no failure is expected.

Undrained Analysis of the Embankment Construction

An undrained effective stress analysis of the clay embankment construction over the submerged tailings sand was performed. The undrained analysis represents the other extreme condition which will be experienced by the tailings sand. In modeling, the 10 m high embankment was divided into 9 lifts. Between each lift, no dissipation of the excess pore water pressure was allowed. Results of the analysis show that failure occurs at the early stage of the embankment construction which corresponds to the first 2 m lift. Pore pressures as high as 40 kPa was generated.

Partially Drained Analysis of the Embankment Construction

The above two cases represent the extreme conditions the sand will experience during construction of the clay embankment. Realistically, partial drainage (or complete drainage, depending on the permeability of the tailings sand and the rate of construction) will occur. In order to simulate partial dissipation of pore pressures between each lift of fill, an undrained analysis was carried out with excess pore pressures in the sand being reduced between lifts. The pore pressure was reduced to an amount which will result in subsequent stable construction of the clay embankment. Instability is indicated by non-converging results in the finite element model.

Results of Partially Drained Analysis

Results of the analysis are presented in Table 5.3.4. This table shows the maximum allowable excess pore water pressure in the tailings sand in order to avoid instability. According to the analysis, the construction of the last 3 m of the embankment is critical. The maximum excess pore pressure should not exceed 45 kPa for the last 2 lifts of

construction. The results are plotted in Figure 5.3.11 in terms of "the maximum safe excess pore pressure in the tailings between the construction lifts" versus "the embankment height before the lift".

Table 5.3.4 Maximum Allowed Excess Pore Pressure in the Tailings in Order to Safely Construct the Clay Embankment.

Lift No.	Embank. Height before Lift (m)	Lift Height (m)	(Δu)max. or [Δh] to safely construct the next lift (kPa), [m]
1	0	1.8	0 [0]
2	1.8	1.2	20 [2.04]
3	3	1	26 [2.65]
4	4	1	36 [3.67]
5	5	1	45 [4.60]
6	6	1	45 [4.60]
7	7	1	50 [5.10]
8	8	1	45 [4.60]
9	9	1	45 [4.60]

Note: Δu = Excess pore water pressure

Δh = Excess piezometer head

Liquefaction Analysis

Liquefaction analysis of the field event was performed for the drained case assuming that all excess pore water pressures generated by the clay embankment have been dissipated. The contained tailings are assumed to be filled rapidly between the embankment and the compacted sand dyke so that it imposes an undrained loading on the submerged tailings sand.

A liquefaction analysis was performed at the final stage of filling of the contained tailings when the height of the tailings has reached the crest of the clay embankment. The properties of the tailings are summarized in Table 5.3.5. The analysis was carried out using different undrained steady state strength ratios (S_u/p') of 0.3, 0.2, and 0.1. It is believed that the average (S_u/p') ratio is close to 0.1 based on the CPT and SPT results

(Ishihara, 1993). An increase in S_u/p' ratio is expected due to the loading imposed and the dissipation of pore pressure allowed in the tailings.

Table 5.3.5 Parameters of Tailings Sand Used in Liquefaction Analysis of the Final Designed Field Event.

Material	γ' (kN/m3)	E (kN/m2)	ν	ϕ_s	ϕ_c	A_o	A_m	S_u/p'
Tailings (low 8 m)	8.95	14,000	0.49	34	24	0	5	0.3, 0.2, 0.1
Tailings (top 3 m)	9.4	18,000	0.49	36	25	0	5	0.3, 0.2, 0.1

Key : ϕ_S = friction angle at steady state

ϕ_C = angle of collapse surface

A_o, A_m = pore pressure parameters in liquefaction analysis

S_u/p' = undrained steady state strength ratio

Results of Liquefaction Analysis

The results of the liquefaction analyses show that static liquefaction flow failure of the field event will not occur if S_u/p' ratio of the tailings sand is greater than 0.1. The computed deformed finite element mesh after the liquefaction analysis for the case of $S_u/p' = 0.1$ is presented in Figure 5.3.12. As indicated, a type of deep-seated flow large deformation in the tailings is obvious. The failure is caused by simultaneous increase of pore water pressures and shear stresses in the elements of the tailings beneath the clay embankment due to rapid filling of the contained tailings. The excess pore pressures in the above elements, generated during the filling of the contained tailings, increased incrementally during the solution process in the liquefaction analysis. Their values range from 30 kPa (downstream) to 100 kPa (upstream).

Summary of the Pre-event Analyses

(1) Slow construction of the clay embankment (drained conditions) is expected to be safe and no failure should occur due to the embankment construction.

(2) Construction of the embankment under fully undrained conditions, with no dissipation of excess pore water pressures in the tailings between lifts, is unsafe and may lead to failure of the clay embankment.

(3) Partially drained conditions allowing dissipation of pore water pressures between lifts can result in stable construction of the embankment.

(4) Assuming that all excess pore water pressures induced in the tailings sands during the embankment construction are dissipated, the rapid filling of the tailings behind the embankment will trigger liquefaction flow failure in the submerged tailings sand if the undrained steady state ratio of the tailings does not exceed 0.1.

More liquefaction analyses will be performed considering the combination effects of different Su/p', height of the contained tailings behind the clay embankment and excess pore water pressure distribution in the tailings sand due to the seepage.

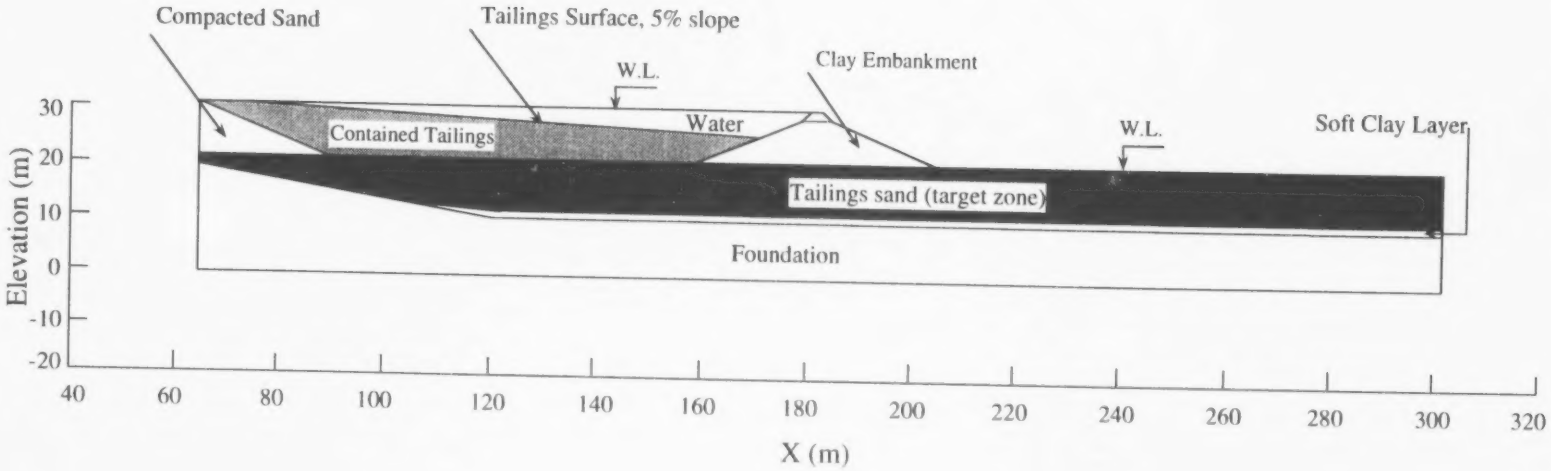

Fig. 5.3.9 Cross-section of the Final Designed Field Event.

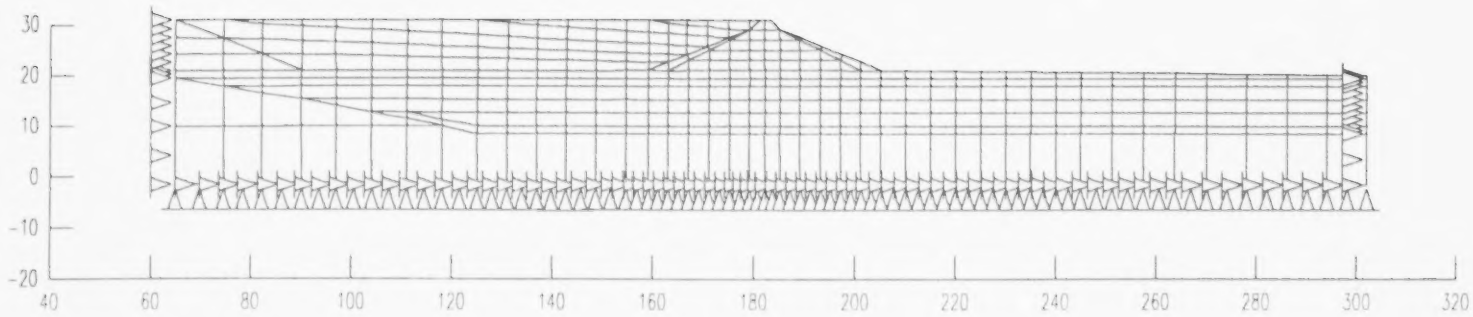

Fig. 5.3.10 Finite Element Idealization of the Field Event.

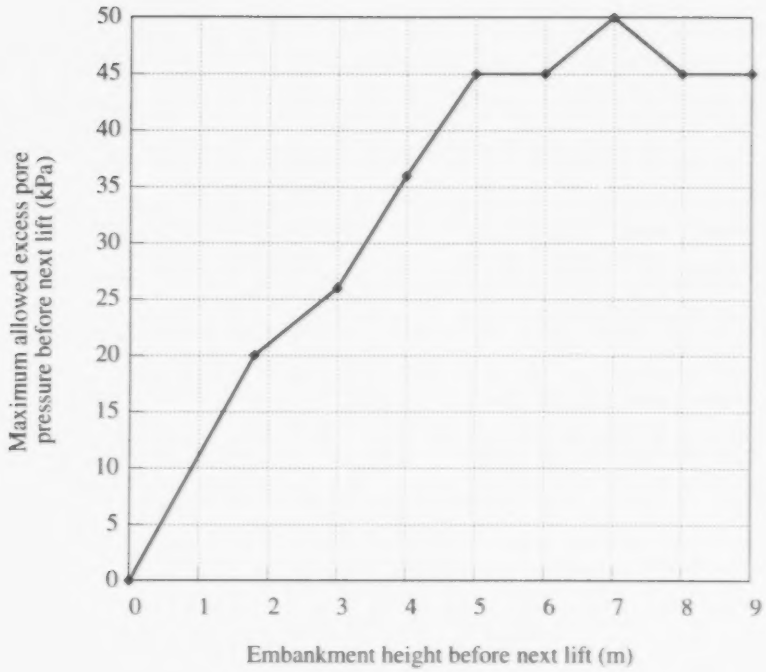

Fig.5.3.11 Maximum Excess Pore Pressure at Mid-depth of Tailings Sands (under centre-line of embankment) for Safe Construction of Embankment.

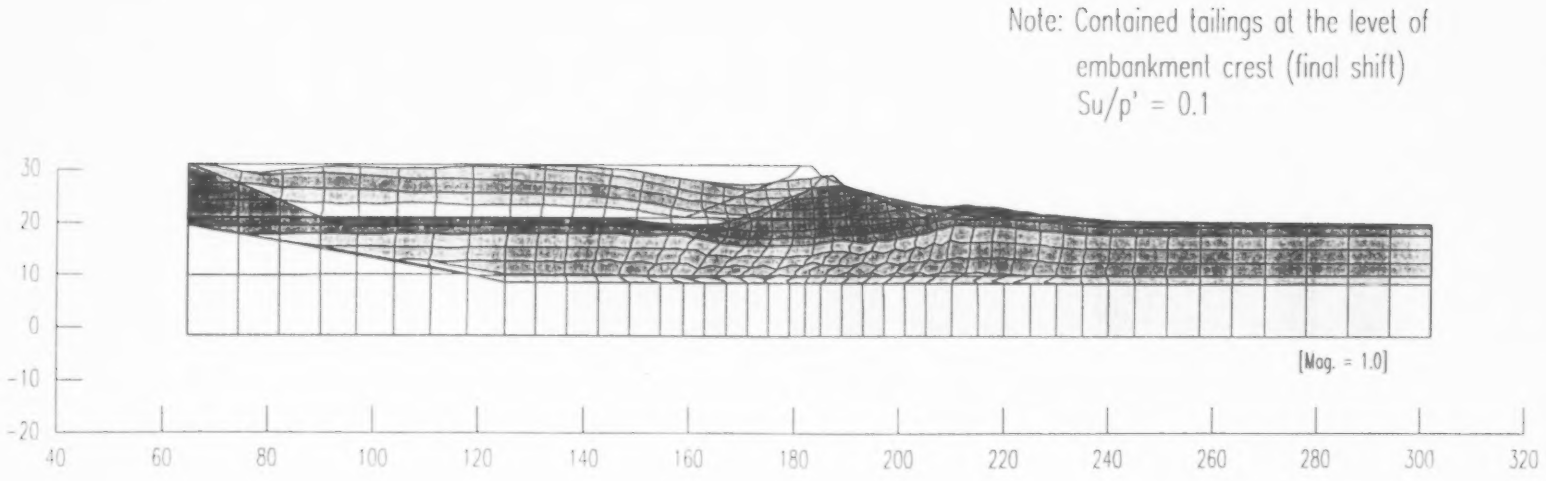

Fig. 5.3.12 Deformed Mesh after Liquefaction Analysis (Su/p' = 0.1).

5.3.3.2 During-Event Analyses

The pre-event analyses concluded that if the clay embankment is constructed under drained or partially drained conditions, allowing partial dissipation of excess pore water pressures between lifts, no failure of the clay embankment will occur. The liquefaction analysis indicated that liquefaction flow failure due to the filling of contained tailings behind the clay embankment will occur if (1) the loading is achieved in undrained conditions and (2) the undrained steady state strength ratio (S_u/p') of the tailings sands is equal to or less than 0.1.

Following the first prediction report, more liquefaction analyses were carried out to investigate the effect of contained tailings on the stability of the embankment. In these analyses, contained tailings were assumed to be placed after all excess pore water pressures in the tailings sands due to the embankment construction had been dissipated. This assumption was made based on the observed piezometers response which indicated relatively fast dissipation of the excess pore water pressure in the tailings sands. The analyses are categorized into three main cases:

Case 1- The contained tailings were assumed to be piped rapidly between the embankment and the compacted sand dyke so that the tailings imposed undrained loadings on the structure. No dissipation of excess pore water pressures was assumed during filling.

Case 2- Steady state flow of water through the tailings sands is established due to filling of the contained tailings.

Case 3- The contained tailings were assumed to be placed in 3 lifts with reduction of excess pore pressures in the tailings sands between lifts. This analysis was performed to study the effect of the loading rate on the stability of the embankment

Case 1 assumes that the contained tailings imposes loading on the tailings sands in undrained conditions, which is a short term effect. Case 2 assumes that filling of the contained tailings results in drained loading with steady state water flow conditions,

which is a long term effect. Case 3 is an intermediate case which assumes partially drained conditions during the loading.

In situ testing, including CPT and SPT, before the embankment construction indicated that the tailings sands are generally loose although highly non-homogeneous. Based on the in situ test results, the average undrained steady state strength ratio of the tailings sands (S_u/p') before the embankment construction was estimated to be about 0.1 (Ishihara, 1993). S_u/p' ratios in the range of 0.1-0.2 were used in the analysis to examine its sensitivity on the results. In order to investigate the effect of higher strength at the top 3 m of the tailings sands on the possibility of a liquefaction flow failure, analyses were carried out with higher S_u/p' ratios for the top 3 m of the tailings. An increase in the S_u/p' ratio of the tailings sands under the clay embankment was also expected due to consolidation. In order to examine the effects of this increase in S_u/p' ratio on the results, a number of analyses were carried out with higher S_u/p' ratios for the tailings under the embankment. Cases 1, 2 and 3 analyses with different S_u/p' ratios are summarized in Table 5.3.6. In the following, results of the analyses for the above cases are described.

Table 5.3.6. Summary of The Analyses of Loading due to Contained Tailings.

	S_u/p'	Case 1	Case 2	Case 3
Constant S_u/p'	0.1	Failure	No Failure	No Failure
	>0.1	No Failure	No Failure	No Failure
(S_u/p') of the top 3 m tailings is higher*	0.15	Failure	No Failure	–
	>0.2	No Failure	No Failure	–
S_u/p' of tailings right under embankment is higher•	0.15	Failure	No Failure	–
	0.2	No Failure	No Failure	–

* A value of 0.1 is used for S_u/p' ratio of the low 8 m of the tailings.

• A value of 0.1 is used for S_u/p' ratio of the tailings which are not located under the clay embankment

Case 1- Liquefaction Analysis Assuming Undrained Loading

The analysis was performed at the final stage of filling of the contained tailings when the height of the contained tailings had reached the crest of the clay embankment. The analysis results indicated that liquefaction flow failure occurs for the case where S_u/p' ratio of the top 3 m of the tailings sands was increased to 0.2. However, the magnitude of the computed deformations were smaller than that using S_u/p' ratio equal 0.1 for the whole layer (see Figure 5.3.12). The reason for the occurrence of flow failure even with S_u/p' ratio of 0.2 for the top 3 m of the tailings sands is that the flow failure is deep-seated and is almost independent of the shallow higher strength elements of the tailings sands.

As mentioned, a possible increase in S_u/p' ratio of the tailings sands right under the clay embankment due to consolidation of the tailings sands was expected. In order to examine the effect of this increase in S_u/p' on the liquefaction flow failure, analyses were performed assuming that the tailings under the clay embankment have higher steady state strengths than the remainder of the tailings. A range of S_u/p' ratio between 0.1 to 0.2 for this part of the tailings was assumed while S_u/p' ratio of the rest of the tailings were kept constant (0.1) throughout the analyses. The analysis results indicated that failure will not occur if S_u/p' ratio of the tailings sands under the embankment is increased to 0.2. The high strength tailings under the clay embankment acts as a thick strong wall which prevents large slumping and lateral deformation of the embankment.

Case 2- Liquefaction Analysis Following Steady State Seepage Conditions

In this case, the effect of the contained tailings on the tailings sands was assumed to be loading under drained conditions, with seepage pore pressures established in the tailings sands. The following steps were performed in this analysis.

(1) A static total stress analysis was carried out for the case where the contained tailings is pumped behind the embankment. Total unit weights were used in this step.

(2) A steady state seepage analysis was carried out. The permeability of the tailings sands in the horizontal direction (K_X) was assumed to be 10 times of the permeability in the vertical direction (K_Y).

(3) The output pore pressure from the steady state seepage analysis was introduced to the total stress results obtained in Step 1 in order to determine the effective stress distribution in the tailings due to steady state seepage conditions.

Figure 5.3.13 shows contours of equal potentials resulting from the seepage analysis. Figure 5.3.14 presents the deformed finite element mesh after liquefaction analysis for constant S_u/p' ratio of 0.1 for all elements. As shown in Figure 5.3.14, the tailings under the downstream face of the embankment have a considerable amount of deformation. However, the deformations of the elements under the upstream face of the clay embankment are not sufficient to cause a flow failure. Figure 5.3.14 also indicates that the tailings sands under the upstream face of the embankment are relatively stable. The maximum deformation is concentrated under the embankment toe where the seepage pore pressures are relatively high compared to the total stresses.

The above analysis was repeated for higher S_u/p' ratios of 0.15 and 0.2 for the tailings sands under the clay embankment. As expected, the displacements decreased with increase in the S_u/p' ratio.

Case 3- Liquefaction Analysis Assuming Partially Drained Conditions

In this case, the contained tailings were assumed to be placed in 3 lifts with reduction of excess pore pressures in the tailings sands between lifts. This analysis was performed to study the effect of the loading rate on the stability of the embankment. The analysis results indicated that liquefaction flow failure will not occur in this case. Figure 5.3.15 shows contours of computed excess pore water pressures at the end of loading.

Summary of the During-event Analysis

Based on the information summarized in Table 5.3.6, the major findings of the liquefaction analyses are:

1) Rapid filling of the contained tailings behind the clay embankment, with no dissipation of excess pore water pressures during filling, will trigger liquefaction flow failure in the tailings sands if the undrained steady state strength ratio of the tailings sands does not exceed 0.1.

2) Liquefaction flow failure (if any) will occur after the undrained loading before the steady state seepage is established in the tailings sands.

3) Results of case 3 analysis indicated that if loading is not fast enough, liquefaction failure will not occur. Rapid loading of the contained tailings is essential in order to trigger a flow failure. It was therefore recommended that the contained tailings should be filled continuously and be completed in about 24 hours to minimize dissipation of excess pore water pressures in the tailings sands.

4) If the S_u/p' ratio of the tailings sands under the embankment is increased to 0.2 due to construction of the clay embankment, failure will not occur.

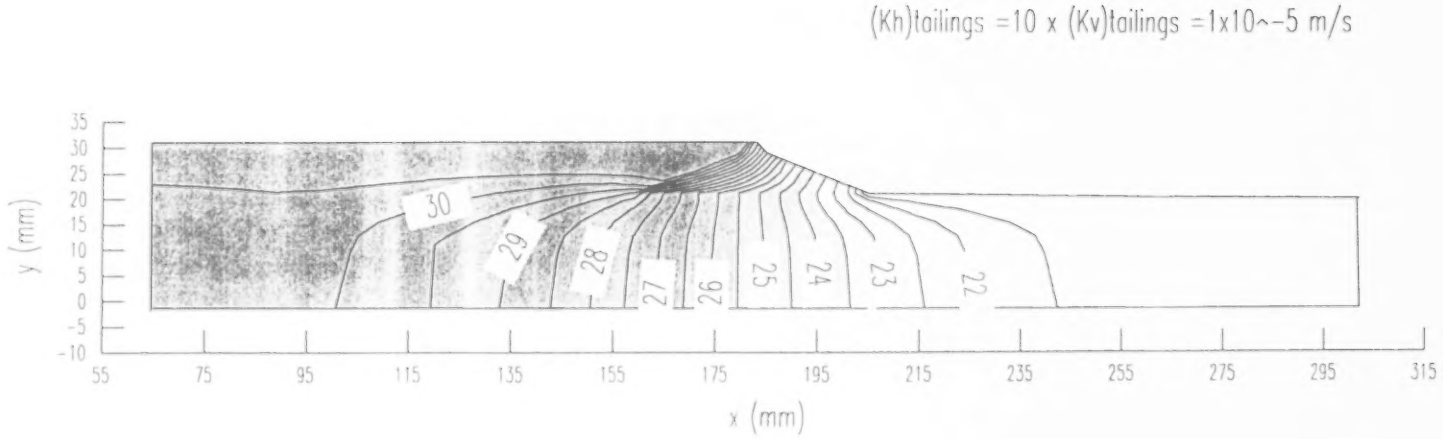

Fig. 5.3.13 Contours of Equal Potential in Seepage Analysis (m).

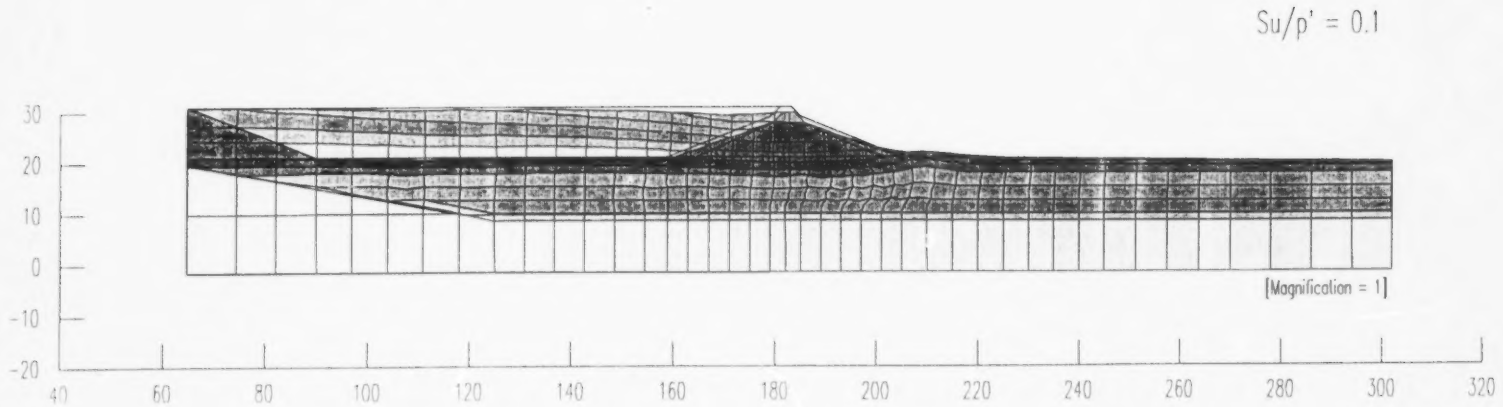

Fig. 5.3.14 Deformed Mesh after Liquefaction Analysis [Case 2].

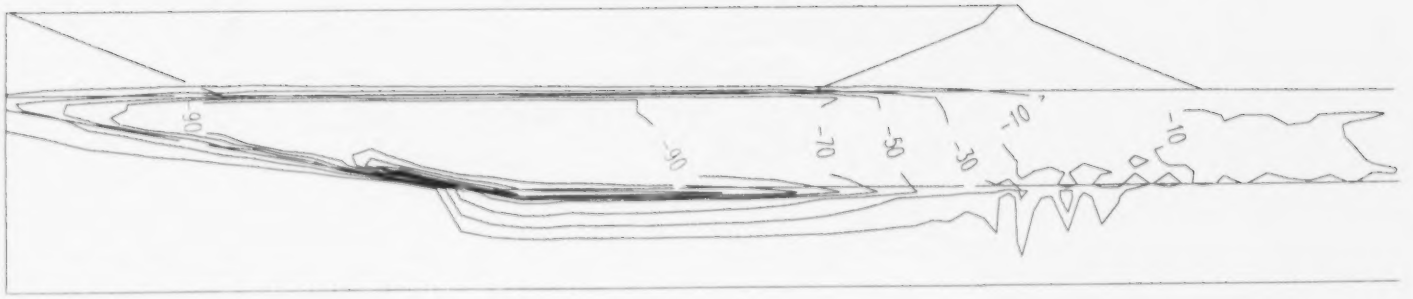

Note: negative sign means compressive (positive pore pressure).

Fig. 5.3.15 Contours of Excess Pore Water Pressures at the End of Loading [Case 3].

5.3.3.3 Post-Event Comments

The field event began on September 18, 1995. Water and tailings were poured in the cell behind the clay embankment. The water level was raised to a height of 7.5 m and the sand was placed to a height of 7 m. Loading lasted for about 36 hours and the embankment moved very little during the loading. A number of possible factors may have contributed to the stability (non-failure) of the embankment. Major factors are listed as follows:

1. Rate of Loading Compare to Rate of Excess Pore Pressure Dissipation

Although from a feasibility point of view the loading rate was relatively fast, it was not fast enough to induce high enough excess pore pressures in the tailings to reach a state of instability. It is important that the rate of loading be studied together with the rate of dissipation of excess pore water pressure. Piezometer measurements during the clay embankment construction showed that the tailings sands are highly permeable. Almost half of the induced pore water pressures were dissipated after 12 hours from the beginning of lift construction. Also piezometer response during loading behind the embankment indicated that a large amount of excess pore pressures had been dissipated during loading. Results of Case 3 analysis showed that if the loading was not fast enough, i.e. most of the excess pore pressures dissipate during the loading, no liquefaction flow failure will occur. Table 5.3.7 compares the observed and calculated changes in water level for Case 3 in Line 1 of the instrumented section. The piezometers location in Line 1 is shown in Figure 5.3.16. Line 1 instrumented section showed the highest pore pressure response during the experiment.

Figure 5.3.17 compares the measured excess pore water pressure at piezometer P18-A during loading with calculated excess pore water pressures for cases 1, 2 and 3. As indicated, the computed excess pore water pressure from case 1, which assumes fully undrained conditions, is much higher than the observed excess pore water pressure. However, the excess pore water pressures calculated from cases 2 and 3 are close to the

measured value. These results indicate that the assumption of fully undrained loading was not realistic due to relatively high permeability of the tailings sands.

It should be noted that the purpose of the above discussion is only to show that the tailings sands were not loaded under fully undrained conditions. From the above discussion one cannot conclude that liquefaction flow failure of loose sands will not occur when *external* loading is applied under partially drained (or drained) conditions. Sasitharan et al. (1993) conducted a number of drained and undrained triaxial compression tests and showed that it is possible to induce liquefaction failure of the sand subjected to external loading under fully drained conditions. They suggested that the loading under drained conditions brought the sand to the state boundary surface (i.e. the collapse surface). As the sand lay on the collapse surface, it behaved in a strain softening manner, resulting in a high increase in excess pore water pressures and failure of the sand in *internally* undrained conditions.

Table 5.3.7. Comparison between the Observed and Calculated Changes in Water Level for Case 3 in Line 1 of the Instrumented Section (change in water level in meter).

	P18A	P13A	P13B	PF19C2	P09A	PF19T2
Observed	6.8	3.4	3.8	1.8	1.6	0.7
Calculated	7.1	2.9	3.4	1.2	1.0	0.9

2. Stress Path Dependency of the Undrained Behavior of Tailings Sands

Recent laboratory testing carried out after the field event on both undisturbed and reconstituted samples of the tailings sands showed that the potential for liquefaction of Syncrude sand at a given void ratio is dependent on the stress path during undrained shear as well as the initial consolidation stress. Figure 5.3.18 shows typical results of the tests. The test results showed that for a given initial state (void ratio and confining stress) the sand under undrained loading is slightly strain softening in triaxial compression loading and highly strain softening in triaxial extension loading. The test results in simple shear condition tend to lie between that of the triaxial compression and extension tests. The

undrained steady state strength ratio based on undisturbed samples was about 0.3 in triaxial compression and about 0.03 in triaxial extension.

Based on the above results, it is useful to investigate stress paths in the tailings sands during loading. Figure 5.3.19 shows contours of the angle (α) between the major principle stress (σ_1) and the depositional (vertical) direction. As indicated most of the tailings, including the tailings under upstream of the embankment are sheared predominantly in compression. Only the surface material near the toe are subjected to extension mode. Therefore it is reasonable to conclude that a rigorous liquefaction analysis based on the above undrained steady state strength ratios (0.3 for compression and 0.03 for extension) most likely will result in standing (non-failure) of the embankment.

3. Relative Density of the Tailings Sands

The field and laboratory tests data showed that the tailings are strongly non-homogeneous. The laboratory tests on the undisturbed frozen samples of the sand indicated that most of the samples lay on the dense side of the steady state line; hence, most of them may not behaved in a strain softening manner during loading. Despite both CPT and SPT results indicated that the tailings sands are generally loose, they may not be loose enough, compared to the steady state line, to have static flow liquefaction.

In addition to the above factors, the method by which the tailings sands were placed could have some effects on its response. In the field experiment the tailings sands were deposited under water. Laboratory tests on Syncrude sands showed that the sands reconstituted by air pluviation is much more prone to liquefaction than its water pluviated counterpart (Vaid et al., 1995). It should be noted that the sand in the centrifuge tests was deposited by air pluviation.

5.3.3.4 Summary of the Event Analysis

Numerical modeling and liquefaction analyses of the field event were carried out. Results of the analyses were periodically submitted to the CANLEX administration. The analysis of the *proposed field event* helped in designing the optimum instrumentation for the event. The analysis also proved useful in the final design of the event.

Results of the partially drained analysis of the clay embankment construction helped the embankment to be constructed safely in the shortest possible time. The observed pore pressures during the embankment construction were comparable with the computed values, which were recommended for safe construction of the embankment.

The effect of loading of the contained tailings was numerically simulated under drained, undrained and partially drained conditions. The model predicted that rapid loading of the under-water deposited tailings sands can trigger liquefaction flow failure provided that (1) the undrained steady state strength ratio of the tailings does not exceed 0.1 and (2) the loading be rapid with no dissipation of excess pore pressures. The embankment did not fail and moved very little during the loading. A number of possible influential factors, including the relatively high permeability of the tailings and the stress-path dependency of the undrained behavior of the tailings sands were discussed. Results of the recent laboratory tests on the undisturbed frozen samples of the Syncrude sand can be useful for further analyses.

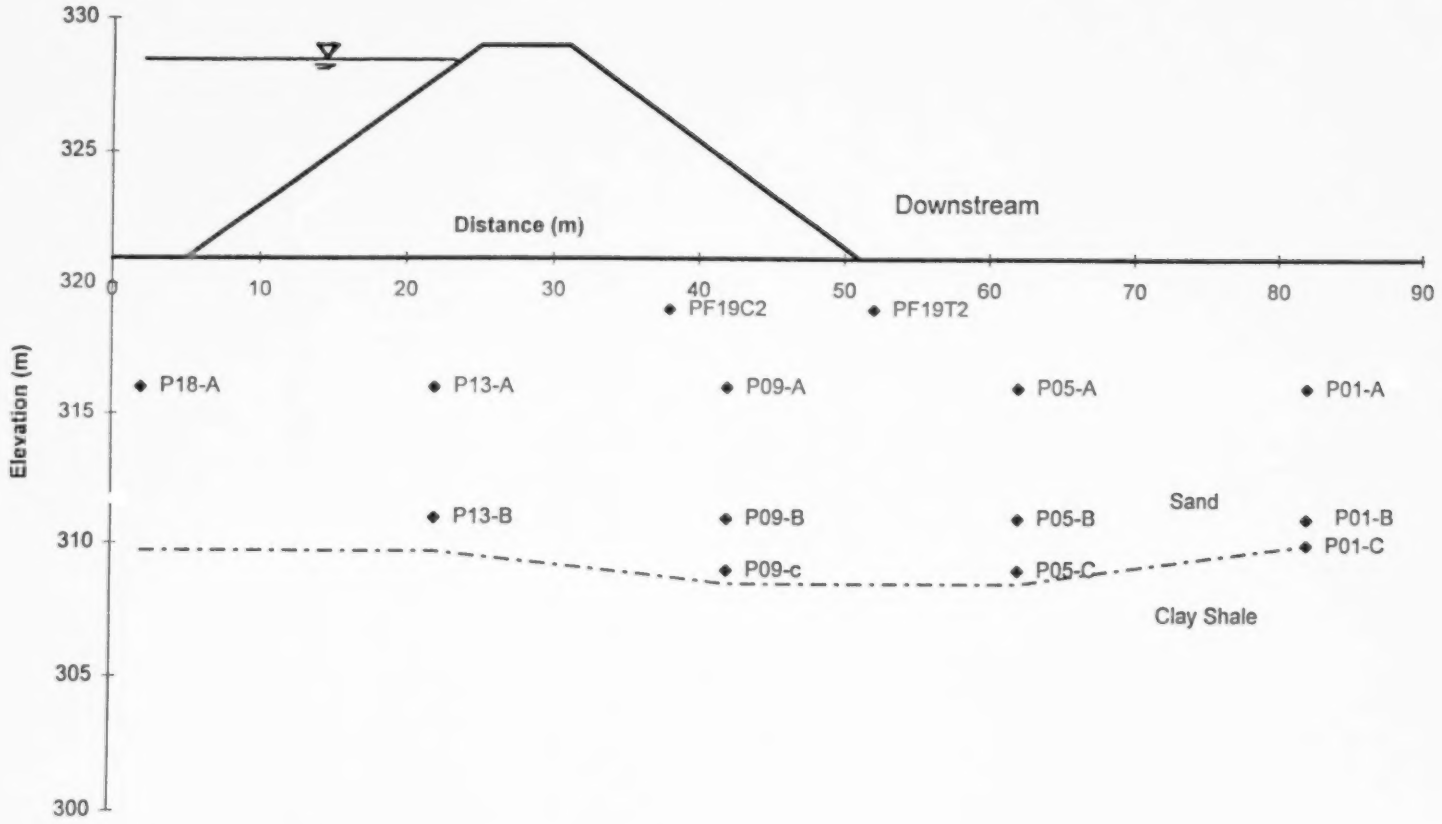

Fig. 5.3.16 Location of Piezometer Tips of Line 1 Instrumented Section.

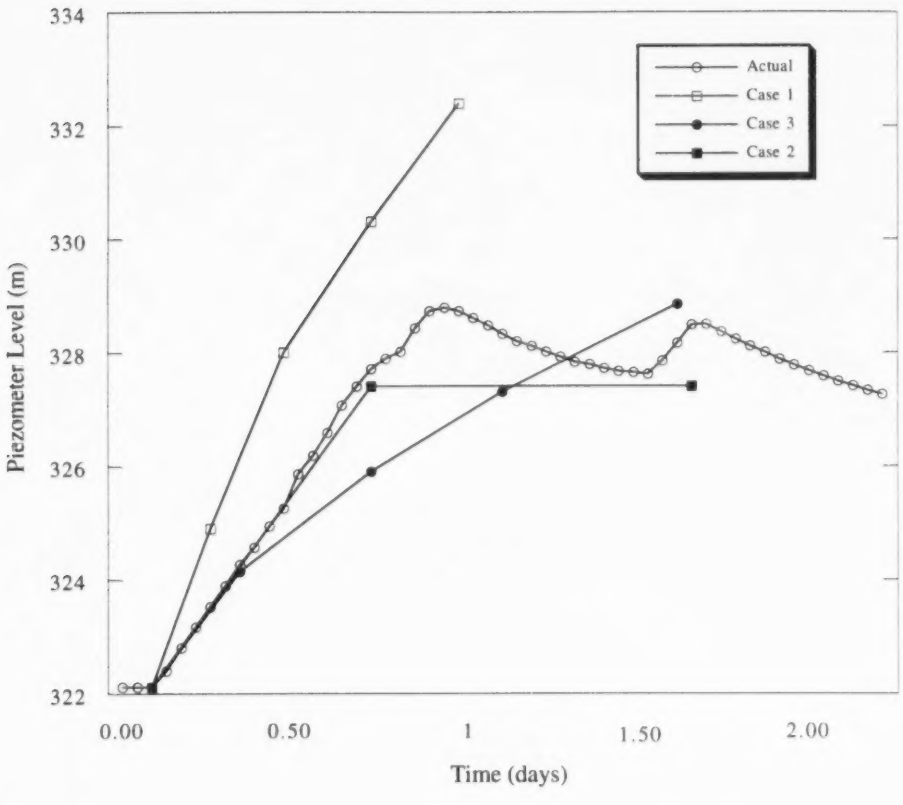

Fig. 5.3.17 Comparison of Observed and Computed Pore Pressures at P18A, Line 1.

(a) isotropically consolidated

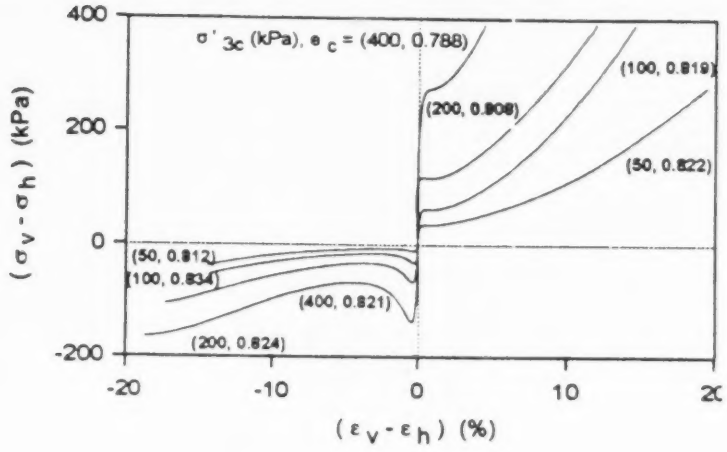

(b) anisotropically consolidated

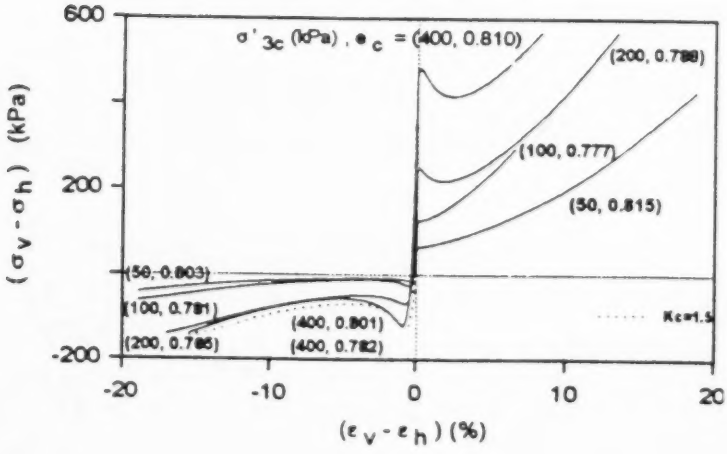

Fig. 5.3.18 **Triaxial Compression and Extension Undrained Behavior of Water Pluviated Syncrude Sand** [after Vaid et al., 1995].

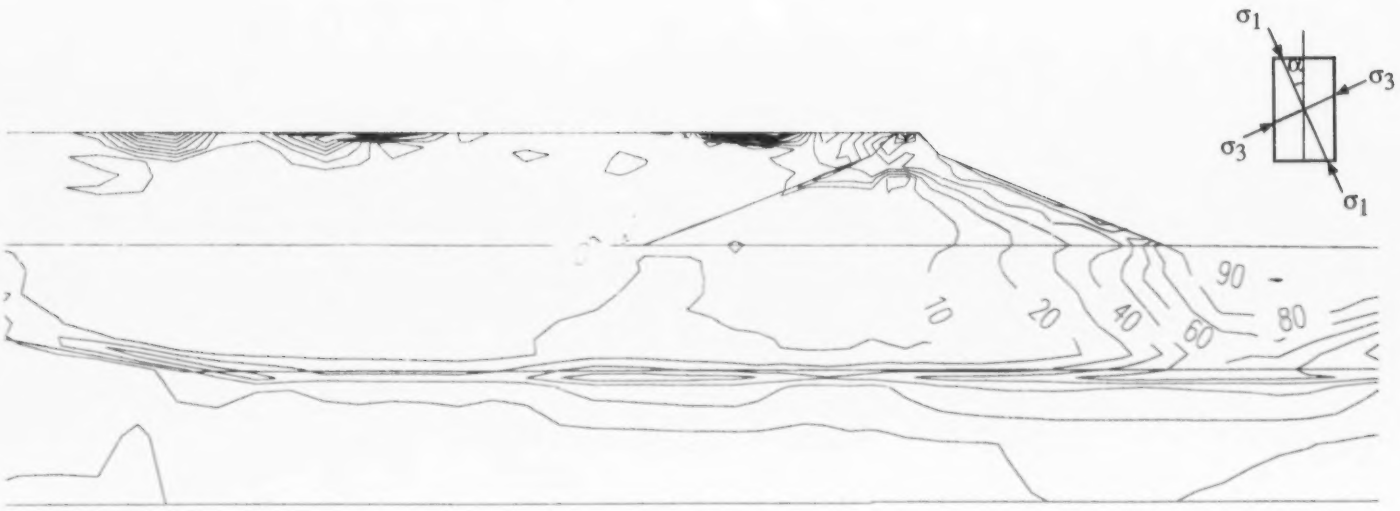

Fig. 5.3.19 Contours of the Angle (α) between Major Principle Stress (σ_1) and Depositional (vertical) Direction (α is in degree).

Chapter 6

LATERAL SPREADING DUE TO EARTHQUAKE-INDUCED LIQUEFACTION

6.1 INTRODUCTION

Lateral spreading of the ground induced by liquefaction of gently sloping granular materials is the most significant and common cause of damage during and shortly after earthquakes. Permanent ground displacements, predominantly horizontal, ranging from a few centimeters to some meters have been recorded. There are numerous cases in which lifeline facilities, underground structures, canals, buried pipelines, roads and foundations of buildings have been seriously damaged by lateral spreads induced by liquefaction (Bartlett and Youd, 1992; Doi and Hamada, 1992; Darragh et al. 1992; Isoyama, 1994; Wakamatsu and Yoshida, 1994; Davis and Brdet, 1994; Vahdani et al., 1994). Figure 6.1 illustrates schematically the liquefaction and its associated lateral spread damage effects. In order to be consistent with the literature, "lateral spreading" and "large ground deformations (or displacements)" will be used alternatively to refer to the subject throughout the present Chapter.

From a geotechnical perspective, it is important to verify lateral spreading in both qualitative and quantitative manners. There are three research subjects on liquefaction-induced lateral spreads. The first one is to investigate the mechanism of the occurrence of the ground displacement of several meters and to develop proper analytical models. The second is to evaluate quantitatively the effect of the ground displacements on in-ground structures such as foundations and buried pipes, and the third is to study means of mitigating effects of liquefaction and large ground displacements.

Many documented cases of lateral spread have been reported. Two of them, including the magnitude of the ground displacement, geology, and properties of the ground, will be described. Summarized information about many other cases of lateral spread, including the maximum magnitude of ground displacement, the type of the liquefied soil, the ground surface gradient and the SPT value (N) of each case are presented in Table 6.1. This data will be used to discuss the possible mechanism of lateral spreading later. Then, a summary of damaging effects of some cases will be presented.

In addition, empirical correlations based on the data from some of the past earthquakes to predict the liquefaction-induced lateral spreading will be discussed. The experimental studies performed on the subject, including shaking table and centrifuge model tests, will be summarized. A summary of the various thoughts about the possible mechanism of lateral spreading and the proposed analytical models, together with a number of conclusions from the literature review will also be presented. A numerical model to evaluate lateral spreading will be suggested.

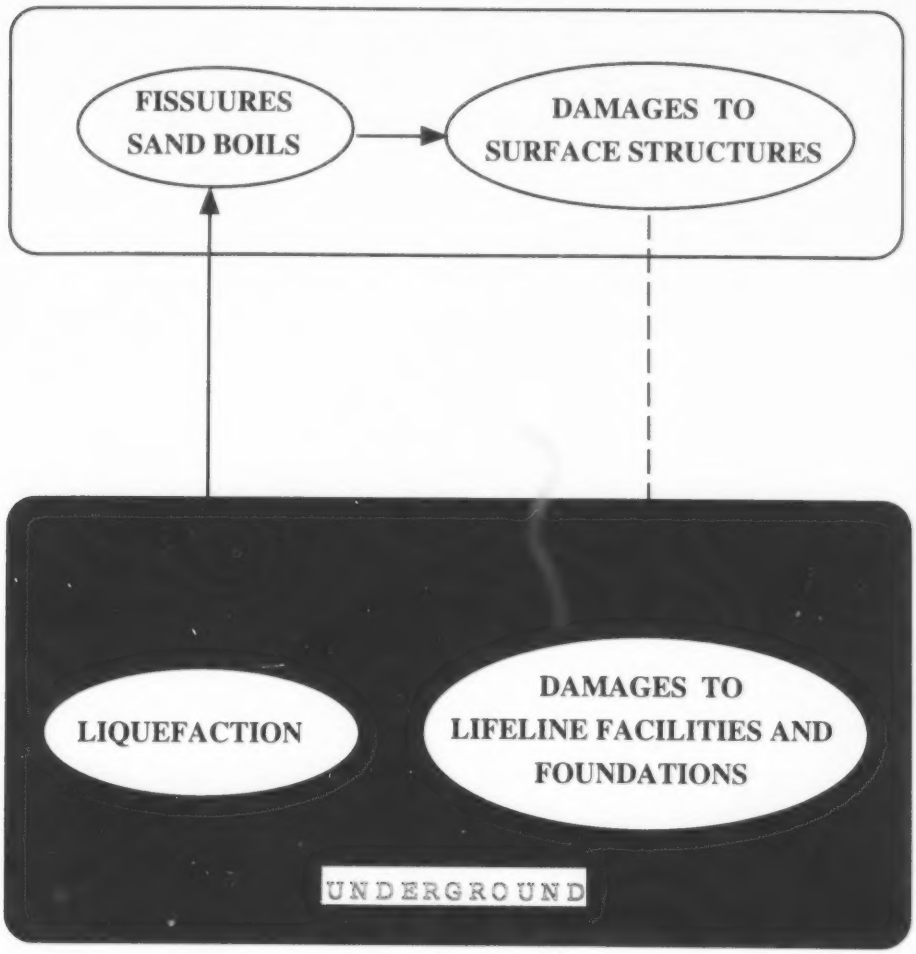

Fig. 6.1 A Model of Liquefaction Damaging Effects.

Table 6.1 Summary of Lateral Spread Case Histories.

Earthquake	Location	M	Soil type	N	Average surface gradient (%)	Ground boundary conditions	Maximum subsidence (m)	*Maximum horizontal displace-ment (m)*	Reference (s)
Niigata (Japan) 1964	Niigata City	7.5	Fluvial	3-15	2	GSG RB	3	***11***	Doi and Hamada (1992) Hamada et al. (1994) Ishihara and Takeuchi (1991)
Fukui (Japan) 1948	Morita Area		Fluvial		1	GSG RB	1-2	***4***	Doi and Hamada (1992)
San Fernando (USA) 1971	Upper Van Norman Reservoir	6.6	Loose to medium dense alluvium	9-24	2.6 max=5.2	GSG	0.6	***2.3***	Hamada et al. (1994)
Nihonkai Chubu (Japan) 1983	Noshiro City	7.7	Sand dune	5-20	3	GSG	1	***5***	Hamada et al. (1994)
Luzan (Philippines) 1990	Dagupan City	7.8	Alluvium	5-30	~ 0	RB	-	***8***	Ishihara et al. (1991) Hamada et al. (1994)
Manjil (Iran) 1990	Rudbaneh	7.3	Fluvial plain	5-10	~ 0	CB	-	***2.5***	Ishihara et al. (1992)

Legend: GSG = Gently Sloping Ground, RB = River Bank, CB = Canal Bank

Table 6.1 Summary of Lateral Spread Case Histories (contiued).

Earthquake	Location	M	Soil type	N	Average surface gradient (%)	Ground boundary conditions	Maximum subsidence (m)	*Maximum horizontal displace-ment (m)*	Reference (s)
Hokkaido-nansei-oki (Japan) July 1993	Shiribeshi toshibetsu area	7.8 (JMA)	alluvial lands	1-4	RB GSB		1.00	***3.00***	Isoyama (1994)
Kushiro-oki (Japan) January 1993	Midoriga oka District, Kushiro City	7.8 (JMA)		<5			0.30	***0.50***	Wakamatsu and Yoshida (1994)

Legend: GSG = Gently Sloping Ground, RB = River Bank, CB = Canal Bank

6.2 CASE HISTORIES OF LATERAL SPREADING

(1) Ebigase Area, Niigata Earthquake (1964)

The Niigata earthquake with a magnitude of 7.5 occurred on June 16, 1964 and caused extensive soil liquefaction in Niigata City and its surrounding areas. Many buildings, bridges, quay walls, and lifeline systems such as electricity, gas, water and telecommunication were severely damaged due to liquefaction. The liquefaction induced by the Niigata earthquake also caused large ground displacements, which resulted in extensive damage to foundation piles and buried pipes.

Figure 6.2 shows the liquefaction-induced ground displacement at the Ebigase area in Niigata City. The vectors represent the horizontal ground displacements and the numbers in the parentheses are vertical displacements. It can be seen that the ground displaced from the natural levee with a higher elevation toward the old river bed with a lower elevation. The mean gradient of the ground surface at Ebigase Area was about 2%. The maximum horizontal displacement in the area close to the Ohgata Primary School, which was located on top of the natural levee, was over 8 m. The primary school and its vicinity, where the ground has a higher elevation, subsided greatly to a maximum of 2.0 m. However, the ground heaved at many points in the neighbourhood of the Tsusen River where the ground has a lower elevation.

As shown in Figure 6.2, numerous ground fissures developed in the vicinity of the primary school. Witnesses in the area reported that several fissures with a width of about 3 m formed. The road, which had been straight before the earthquake, deformed due to the ground movement. In the low area of the Tsusen River a large number of sand boils were observed. It was reported that a considerable amount of sand and water spouted from the river and the river bed rose about the water level, enabling people to cross the river on foot.

Figure 6.3 shows the soil conditions along Section A-A' in Figure 6.2. The estimated liquefied soil with a thickness of about 5.00 m was distributed from the primary school to

the river. The boundary between the estimated liquefied layer and non-liquefied layer above it inclined toward the river with a gradient of about 1%. The blow counts from the Standard Penetration Test (SPT) ranged from 3-15. More detailed information about the case is given by Doi and Hamada (1992) and Hamada et al. (1994).

(2) Upper Van Norman Reservoir, San Fernando Earthquake (1971)

The San Fernando Earthquake, with a magnitude of 6.4, occurred on February 9, 1971. In addition to the near catastrophic upstream failure of the Lower San Fernando Dam and the downstream movement of the Upper San Fernando Dam, the earthquake caused liquefaction, large ground deformations and extensive damage to lifeline facilities.

One of the significant features of the earthquake was its influence on lifeline facilities. Nearly 900,000 customers in the area were affected by electrical power outrages. The damage was especially severe for buried conduits, including water supply, gas, liquid fuel and waste water pipelines. Most permanent ground displacement was concentrated in two areas: the Van Norman Reservoir Complex and along the San Fernando Fault. The Van Norman Reservoir supplied 80% of the water to the City of Los Angeles. Liquefaction-induced soil movement affected main pipelines, channels, pump stations and filtration facilities within and adjacent to the complex.

Figure 6.4 displays the ground displacements in the east of the Upper Van Norman Reservoir in the San Fernando Valley. The vectors show the horizontal displacements and the numbers show the vertical displacements in centimeters. A maximum horizontal displacement of 2.30 m was observed by the aerial photograph survey. The mean and maximum gradients of ground surface was about 2.6% and 5.2% respectively. Figure 6.5 shows the soil profile along the cross section of A-A' in the dominant direction of the lateral spreading. The subsurface soil consisted of three main soil types: artificial fill, loose to medium dense alluvium and dense alluvium. The thickness of the loose alluvium was in the central part of the ground maximum and was up to 15 m. The water table varied from 3 to 6 m below the ground surface. More details of this case are described by O'Rourke et al. (1992).

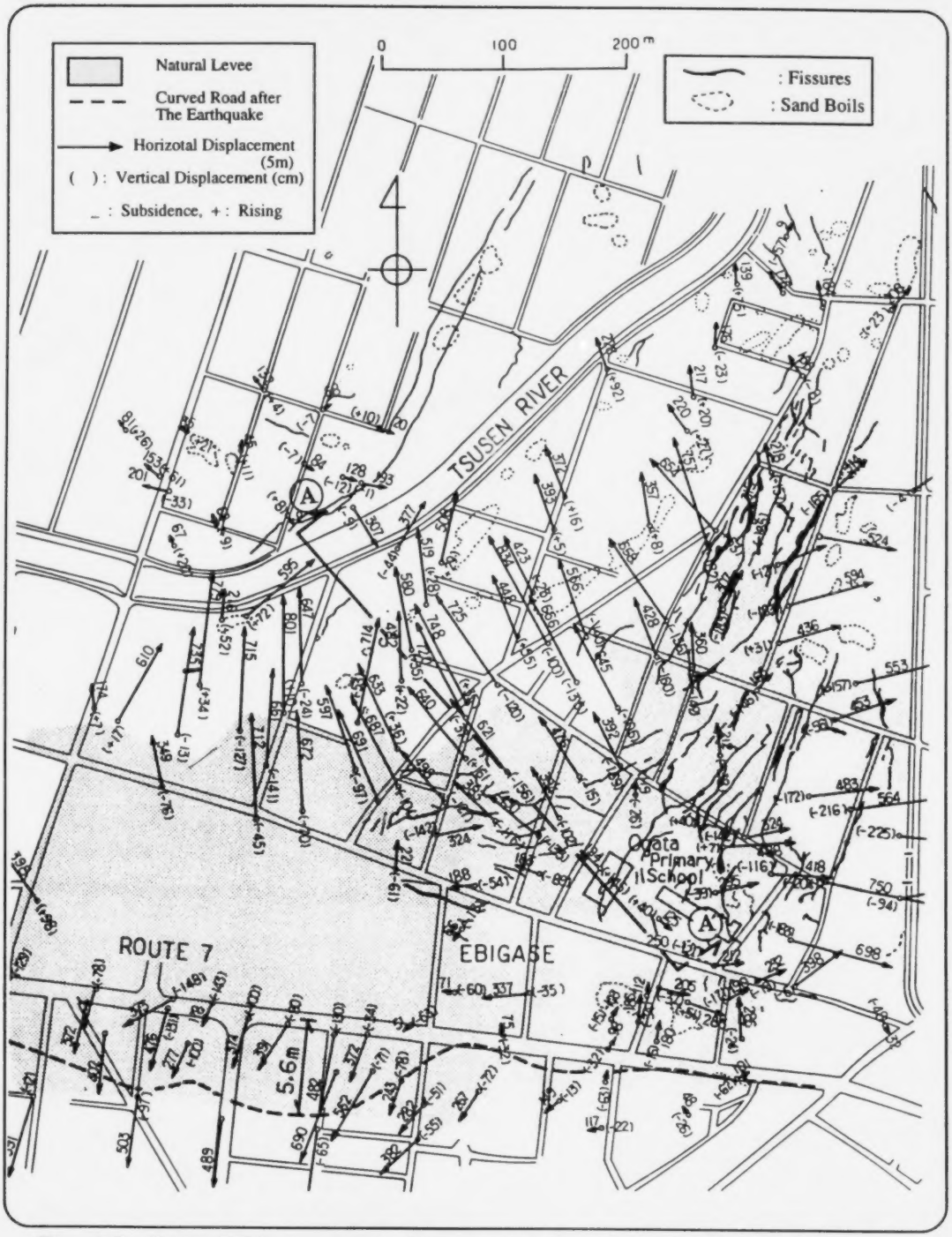

Fig. 6.2 Ground Displacements, Fissures and Sand Boils in the Vicinity of the Ohgat Primary School during the 1964 Niigata Earthquake [modified after Hamada et al.,1994].

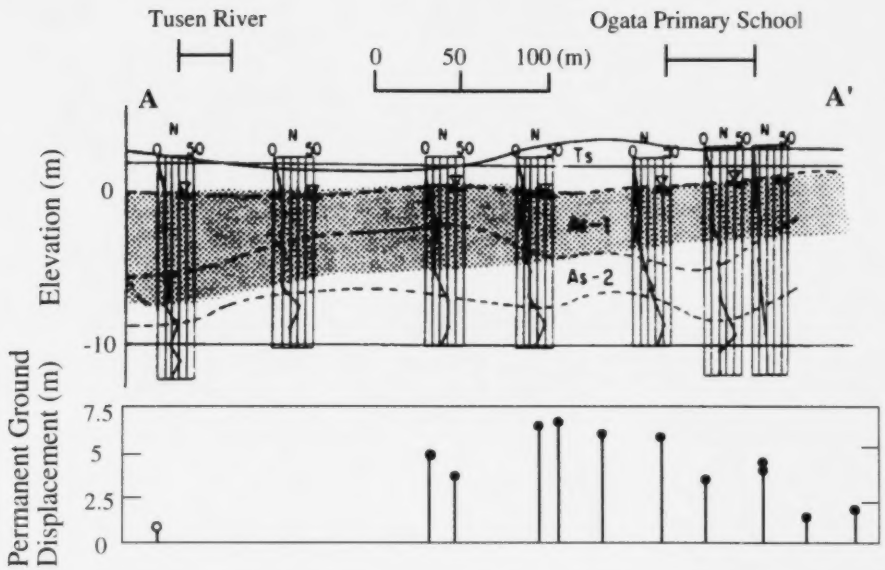

Fig. 6.3 Soil Conditions, Ground Displacement and Estimated Liquefied Layer along Section A-A' at Ebigase Area in Niigata City
[modified after Hamada et al., 1994].

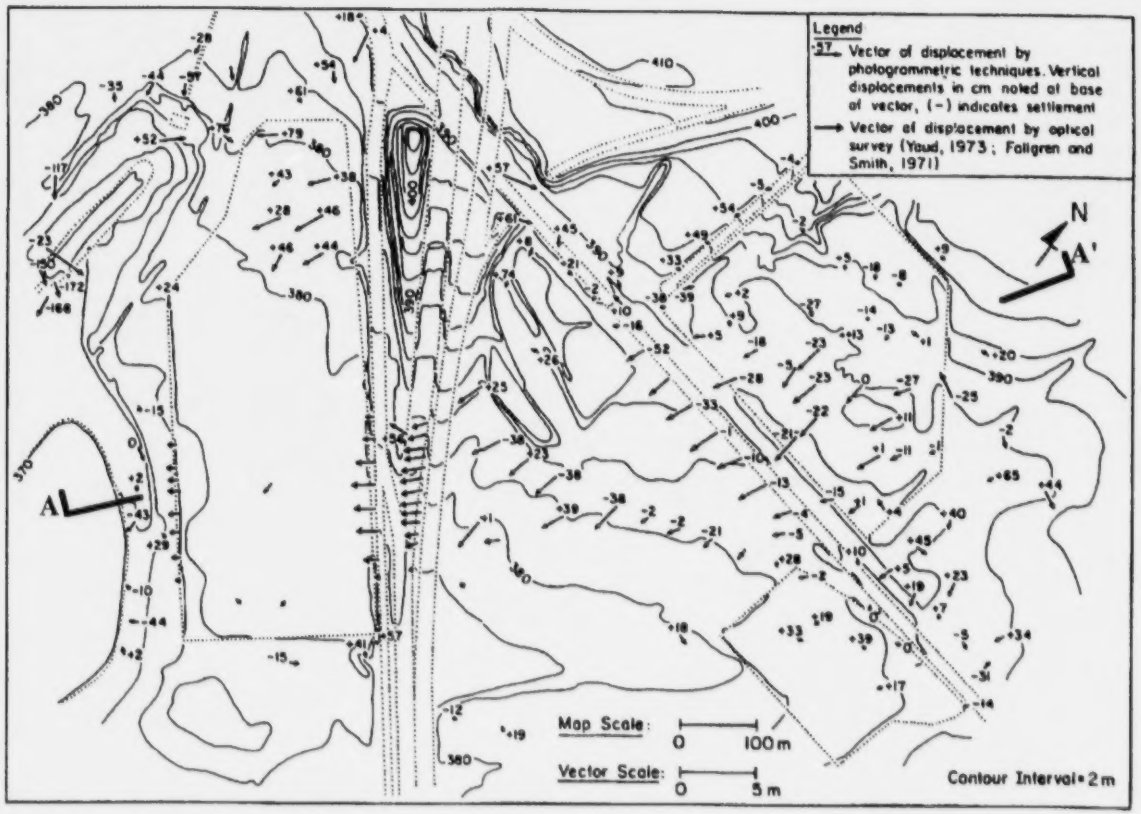
Legend
Vector of displacement by photogrammetric techniques. Vertical displacements in cm noted at base of vector, (-) indicates settlement
Vector of displacement by optical survey (Yaud, 1973; Foligren and Smith, 1971)
N
A
A'
Map Scale: 0 100 m
Vector Scale: 0 5 m
Contour Interval = 2 m

Fig. 6.4 Liquefaction-induced Ground Displacement, East of Upper Van Norman Reservoir (1971 San Fernando Earthquake) [after O'Rourke et al., 1992].

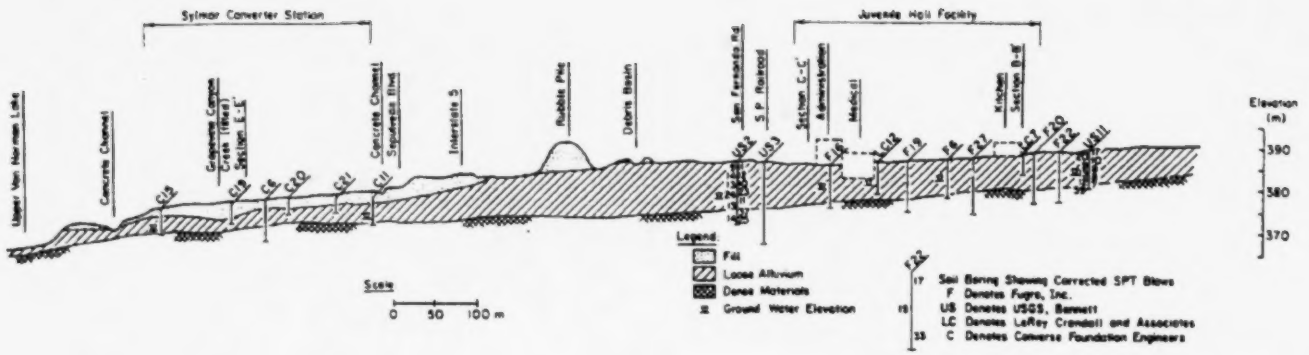

Fig. 6.5 Soil profile at Cross-Section A - A', East of Upper Van Norman Reservoir, (1971 San Fernando Earthquake) [modified after O'Rourke et al., 1992].

6.3 EFFECTS OF SPREADING ON IN-GROUND STRUCTURES

The information about the ground deformation pattern along the vertical direction is instructive for clarifying the mechanism of lateral spreading. The deformation of the damaged piles in Niigata City and the movement of the waste water pipes in Noshiro City may provide some information about the distribution of the ground deformations and also about the possible mechanism of lateral spreading. Detailed information about these two cases can be found in Doi and Hamada (1992), and Hamada and O'Rourke (1992).

(1) Damage to Foundation Piles during the Niigata Earthquake (1964)

Figure 6.6 displays damage to the foundation piles and soil conditions at two buildings, the Court House and the old NHK building, in the earthquake area. The Court House was a four story building constructed on concrete pile foundations, each with a diameter of 35 cm. The building inclined due to differential settlement of the ground caused by the earthquake, indicating that the foundation piles were damaged. However, after minor repairs were made to the inclined floors, the building was used for 25 years. The damage to the piles was observed during reconstruction of the building.

The ground in the area consisted of a loose sandy layer with N values of less than 10 down to -8.0 m. It was assumed that the submerged sandy soil layer between -1.70 m and -8.0 m was liquefied due to the earthquake. It was reported that the piles of this building were damaged at two locations, as shown in Figure 6.6(a). The two locations roughly coincide with the boundaries between the estimated liquefied layer and non-liquefied layers on the top and below the liquefied layer. Figure 6.6(c) indicates that at the upper location the concrete was crushed and steel bars were severely bent.

Figure 6.6 (b) shows the damage to the piles of the two story NHK building. As shown, the concrete piles with a diameter of 35 cm are broken at two elevations, about 3 m from the top of the pile and 2.5 m from the bottom. The subsurface soil at the building site consisted mostly of loose sand with SPT values of 5 to 10 down to -10 m. This sand was considered to have been liquefied due to the earthquake. The lower damaged point

generally coincides with the interface between the estimated liquefied layer and the underlying non-liquefied soil. Moreover, it was observed that the upper damaged position of the piles coincides with the boundary between the liquefied soil and the overlying non-liquefied layer.

Doi and Hamada (1992) concluded that the damage pattern of the piles and the estimated depth of the liquefied soil suggest that the ground displacement was not caused simply by the slippage at the interface between the overlying non-liquefied layer and the estimated liquefied soil, but by deformation throughout the whole thickness of the liquefied layer.

(2) Damage to the Sewage Pipes during the Nihonkai-Chubu Earthquake, Japan, 1983

Figure 6.7 shows the horizontal displacements of the ground surface and the movement of a cement sewage pipe with a diameter of 30 cm in Noshiro City at the time of the Nihonkai-Chubu Earthquake. The ground displacements were measured by using pre- and post-earthquake aerial photographs. The movement of the sewage pipe was measured as the relative displacement between the pipe axis after the earthquake and the line between the two neighbouring manholes. The maximum relative displacement of the pipe was more than 160 cm, but the maximum displacement of the ground was about 80 cm. This suggested that the liquefied layer moved more than the upper non-liquefied layer.

Figure 6.8 displays the movement in Section A-A' of Figure 6.7(a). The total displacement of the pipe was estimated to be 255 cm. Figure 6.8 also shows the N values of the ground at a site about 50 m north of the pipe. The subsurface soil consisted of sandy fill and sand dunes, and the ground water table was at -1.70 m below the ground surface. The soil layer between -1.70 m and -4.20 m was evaluated as the liquefied soil during the earthquake.

6.4 CONCLUSIONS FROM CASE STUDIES

From the above-mentioned case studies of liquefaction-induced ground displacements and their damaging effects, as well as the other cases summarized in Table 6.1, the following conclusions can be made. These conclusions may help to understand the

mechanism of liquefaction-induced ground displacement and their effects on underground structures and lifeline facilities.

1) The general direction of the lateral spread is from higher elevations to lower elevations. No case has been reported in which the ground displacements were caused in the upward direction of the slope.

2) In most cases, the ground displacements in the higher elevations are accompanied by fissures and the ground surface largely subsides. However, in the area where the ground has a lower elevation, a large number of sand and water boils is observed and the ground heaves.

3) The magnitude of the horizontal component of the ground displacement has a reasonable correlation with the thickness of the estimated liquefied layer; the thicker the liquefied layer, the greater the horizontal displacement.

4) From the damages to the piles, shown in Figure 6.6, it is obvious that the displacement of the ground was not caused simply by the slippage of the upper non-liquefied layer on the liquefied soil, but by the flow movement of the whole mass of the liquefied soil.

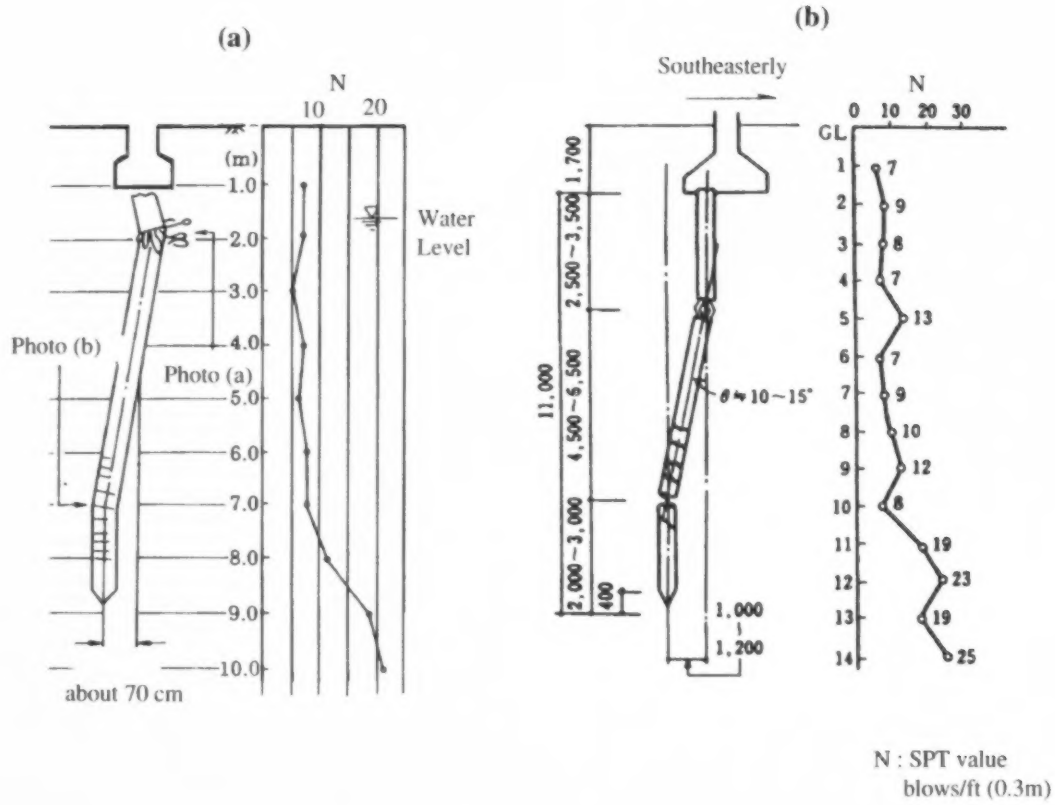

Fig. 6.6 Damages to the Foundation Piles, (a) Court House Building, (b) Old NHK Building [modified after Doi and Hamada, 1992].

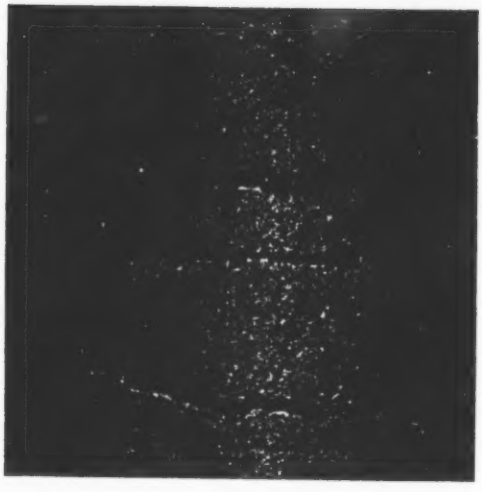

(c) Upper Part of Pile of Court House (d) Lower Part of Pile of Court House

Fig. 6.6 (continued).

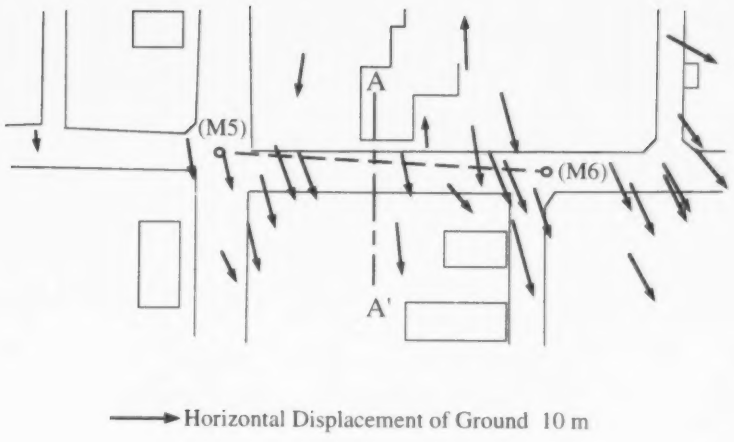

(a) Ground Displacements

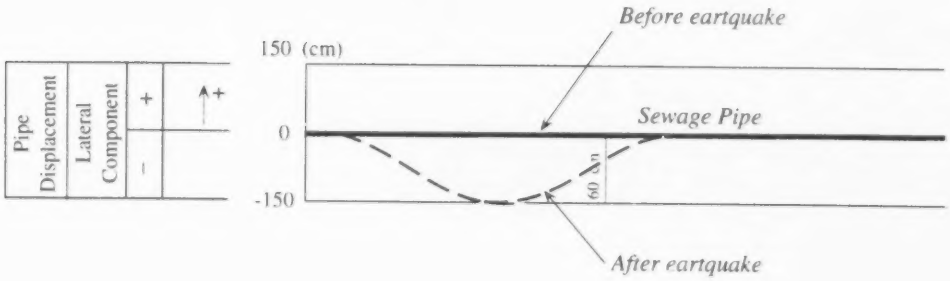

(b) Movement of Sewage Pipe

Fig. 6.7 Horizontal Displacement of the Ground Surface and Movement of Sewage Pipe.

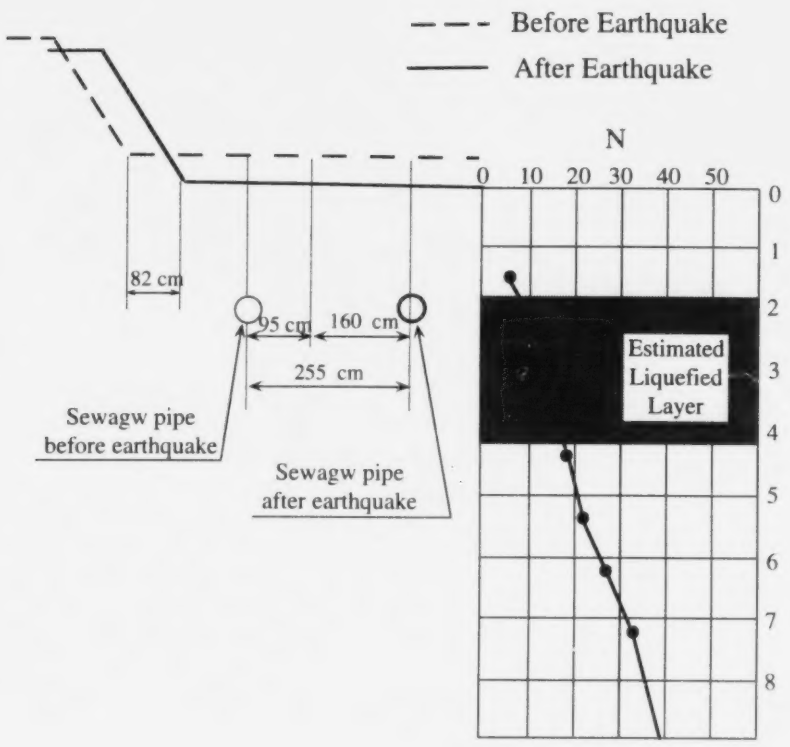

Fig. 6.8 Ground Displacement and Movement of Sewagw Pipe in Cross-Section A-A' of Figure 7(b).

6.5 EMPIRICAL PREDICTION OF LATERAL SPREADING

Correlations between the ground displacement and various factors, such as the thickness of the liquefiable soil, the ground surface gradient, the earthquake magnitude and so on, have been developed, and some empirical formulae have been proposed. Bartlett and Youd (1992) compiled data from case histories of liquefaction-induced lateral spreads and developed an empirical model for predicting the horizontal ground displacement at potentially liquefiable sites. They analyzed earthquake, topographical, geographical and soil factors associated with eight major earthquakes in U.S. and Japan. They used multiple linear regression to find which factors are most closely correlated to lateral spread, and developed empirical formulae from those factors. The formulae are:

for free face conditions,

$$Log\,(D_H + 0.01) = -16.366 + 1.178M - 0.927\,Log\,R - 0.013\,R + 0.657\,Log\,W + 0.348\,Log\,T_{15} + 4.527\,Log\,(100 - F_{15}) - 0.922\,D50_{15} \qquad [6.1\text{-a}]$$

and for ground slope conditions,

$$Log\,(D_H + 0.01) = -15.787 + 1.178M - 0.927\,Log\,R - 0.013\,R + 0.429\,Log\,S + 0.348\,Log\,T_{15} + 4.527\,Log\,(100 - F_{15}) - 0.922\,D50_{15} \qquad [6.1\text{-b}]$$

where,

M = Earthquake magnitude,

R = Horizontal distance from the seismic energy source (km),

W = 100 * (height (H) of the free face / distance (L) from the free face),

S = Ground slope (%),

T_{15} = Cumulative thickness of saturated granular layers with $N1_{60} \leq 15$ (m),

F_{15} = Average fines content of saturated granular layers included in T_{15} (%) and

$D50_{15}$ = Average mean grain size in layers included in T_{15} (mm).

Formula (6.1-a) was developed from the cases of the area along the river and the sea sides while formula (6.1-b) is for cases of gently sloping grounds. The above formulae are only applicable to earthquakes with magnitude between 6.0 and 8.0 and affected sites underlain by continuous layers of sandy soils with $T_{15} > 0.3$. Figure 6.9 shows the measured horizontal displacements versus the displacements predicted using the above empirical correlation. As shown, the predicted displacements are scattered between half and twice the measured ones.

Hamada et al. (1986) conducted regression analyses using the data from the 1964 Niigata, 1971 San Fernando and 1983 Nihonkai-Chubu earthquakes, and proposed the following empirical correlation

$$D = \sqrt[2]{H} \cdot \sqrt[3]{\theta} \qquad [6.2]$$

where,

D: Magnitude of ground displacement in the horizontal direction (m)

H: Thickness of liquefied layer (m), and

θ: The greater value of the gradient of ground surface or that of lower boundary of liquefied layer.

The measured ground displacements are generally scattered between half and twice the values given by the above equation, as shown in Figure 6.10. This empirical correlation indicates a comparatively low correlation between the ground displacement (D) and the gradient (θ) of the ground surface or the lower boundary of the liquefied layer. Taking advantage of this, Hamada et al (1994) suggested that the ground displacements were

caused by fluid behaviour of the liquefied soil because the gradient of the fluid surface has little effect on the magnitude of the fluid displacement, but does affect its velocity.

The advantages of the correlation developed by Bartlett and Youd (1992) over the correlation proposed by Hamada et al. (1986) are:

(1) The database on which the Bartlett and Youd model is developed is much greater than the one used by Hamada et al., 8 earthquakes over 3 earthquakes.

(2) The number of factors encountered in the Bartlett and Youd model is more than the number of factors used by Hamada et al., 7 factors versus 2 factors.

(3) In the Bartlett and Youd method, the "free face conditions" and the "ground slope conditions" have been studied separately.

Darragh et al. (1992) studied liquefaction effects of the 1906 San Francisco Earthquake and the 1989 Loma Prieta Earthquake on the lifeline facilities throughout the San Francisco Bay area. They observed that the maximum lateral spreads are directly proportional to the surface gradient. They found this to be the most important conclusion of their liquefaction studies. This suggests that the extent of lateral spreading is governed by gravity.

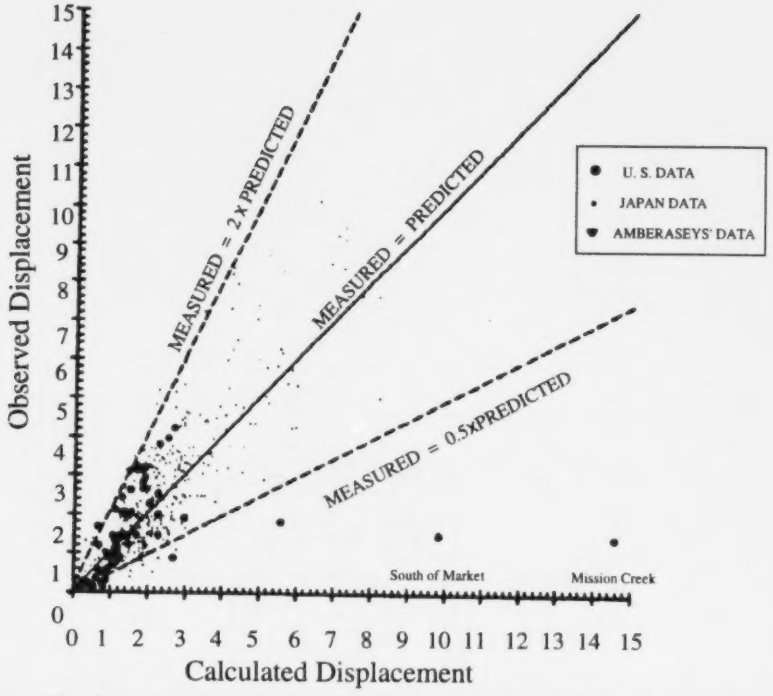

Fig. 6.9 Measured Displacements versus Predicted Displacements [modified after Bartlett and Youd, 1992].

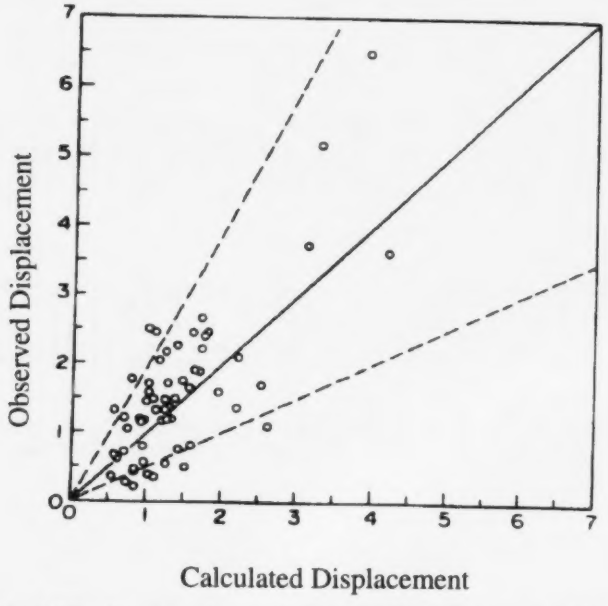

Fig. 6.10 Comparison of the Predicted Ground Displacement with the Observed Ground Displcement [modified after Hamada et al., 1986].

6.6 EXPERIMENTAL STUDIES ON LIQUEFACTION-INDUCED GROUND DISPLACEMENT

6.6.1 Shaking Table Test under 1g Gravitational Stress

Shaking table tests have been widely conducted to investigate the mechanism of permanent ground displacement due to liquefaction. Yasuda et al. (1991) conducted a number of shaking table tests and evaluated the effects of the relative density, the gradients of the upper and the lower boundaries of the liquefied soil, and the thickness of the liquefiable layer on the pattern and the magnitude of ground displacements. From the test results, they concluded that the liquefaction-induced displacement did not occur at the boundary between the liquefied layer and the non-liquefied layer, but rather occurred with a somewhat constant shear strain in the liquefied layer.

According to the test results, the effect of the thickness and the surface gradient of the liquefied soil was stronger than that expected from the empirical formula proposed by Hamada et al. (1986), indicating the strong effect of the static gravity. The results also showed that the displacement of loose sand was greater than that of medium sand, and the displacement of silty sand was less than that of clean sand. Yasuda et al. (1992) also conducted vane shear tests on the liquefied soil to examine the rate of the shear strength reduction in the process of liquefaction. According to the vane shear test results, the undrained shear strength decreased to about 1/100 to 1/500 of the original strength due to liquefaction. The decrease in the shear strength was rather proportional to the increase in the pore water pressure and the decrease in the effective mean normal stresse.

Miyajima et al. (1991) examined the effects of the thickness, the depth and the gradient of the liquefied soil by conducting a series of shaking table tests. Based on the test results, they found that the time duration of ground deformation and the thickness of the liquefied soil showed a good correlation. The velocity of ground deformation and slope of the loose sand layer also correlated with each other. According to the test results, the

magnitude of horizontal ground displacements are mostly proportional to the gradient of the ground surface and the thickness of the liquefied layer. This suggests that the lateral spreading is significantly affected by the static shear stress.

Sasaki et al. (1991) carried out a series of shaking table tests to examine the effects of the thickness of the liquefied layer, the slope of the ground and the input motion. A summary of the main conclusions made by Sasaki et al. at the end of the tests is as follows:

1) The lateral ground flow is strongly affected by the slope of the ground surface, and it is almost independent of the slope of the lower boundary of the liquefiable soil.

2) The direction of excitation has no significant influence on the direction of the lateral flow displacement, and the lateral ground deformation is related to the direction of the slope surface, i. e., the direction of the initial shear stress in the liquefiable layer before the excitation. The excitation is not the direct cause for ground displacement, but the cause for soil liquefaction.

3) After stopping the vibration, the lateral displacement almost stopped. This contradicts the observed phenomenon of delayed response, which has been observed in many cases of lateral spread. According to this phenomenon , deformations and excess pore pressures in soil structures subjected to earthquakes may continue long after the earthquake. The delayed response was described in detail in Chapter 1. The above contradiction can be related to the small size of the shaking table test compared with the dimensions of the soil mass in the field.

Hamada et al. (1990) vibrated a model test in the direction perpendicular to the surface slope. They observed large ground displacements in the direction of the slope. This indicates that the ground displacements were not caused by the inertia force due to the acceleration, but by the component of the gravity in the slope direction.

Based on these shaking table test studies, the following conclusions describe the fundamental characteristics of the liquefaction-induced ground displacement:

1) The ground displacement does not occur at the boundary between the liquefied and non-liquefied layer, but occurs in the whole mass of the liquefiable soil.

2) The ground displacement is not caused directly by the shaking force, but by the component of the gravity in the slope direction; the effect of the shaking is to increase the pore water pressure, and subsequently to reduce the global strength and the stiffness of the liquefied material.

3) The magnitude of lateral ground displacement is mostly proportional to the ground surface gradient and the thickness of the liquefied layer.

6.6.2 Centrifuge Modeling

Fiegel and Kutter (1994) used seismic centrifuge modeling to study the behaviour of two mildly sloping ground models subjected to earthquake loading and liquefaction. The first model consisted of a uniform layer of saturated sand, and the second one consisted of a layer of sand overlaid by a relatively impermeable layer of silt. In both tests, 0.8 m of prototype lateral displacement was measured at the surface. Almost all the lateral displacement occurred during shaking.

In the first model test, the lateral displacement was distributed throughout much of the sand, increasing from the bottom to the surface. In the second model test, lateral displacement was concentrated in a narrow zone at the interface of the sand and silt. This contradicts the conclusion from the case histories (Section 6.4) and the shaking table tests (Section 6.6.61) that the liquefaction-induced spreads were caused by the flow movement of the whole mass of the liquefiable soil, not simply by the slippage of the upper non-liquefiable layer over the liquefiable layer. It should be noted that the sand in the centrifuge tests was much denser (Dr = 60%) than most of the liquefied sands involved in the case histories and shaking table tests.

In an attempt to resemble the lateral sliding observed at Valdez during the 1964 Alaska earthquake, Zeng and Arulanandan (1995) conducted a centrifuge test to study the mechanism of lateral sliding of a soil slope due to liquefaction of a sand layer. The

centrifuge model was a submerged slope made of silt with a thin horizontal layer of sand placed at mid-height of the slope. The model was subjected to base shaking at a centrifuge acceleration of 50g. The test resulted in failure of the slope as a result of liquefaction of the sand layer.

An important finding from the test was the response of one of the piezometers placed in the top silt layer. The piezometer recorded negative excess pore pressures during the shaking. After the shaking was stopped, pore pressures in this piezometer began to rise and continued to increase to a positive value, even after the slope movement had stopped. The negative pore pressure at the time of shaking was due to the dilation of the silt. The increase in pore pressures after stopping both the shaking and the movement has been the result of the slope movement and pore pressure redistribution in the soil.

The big advantage of the centrifuge tests over the shaking table tests is that the centrifuge tests provide almost the same stress conditions which exist in the field. However, the drainage conditions, including the boundary conditions and the drainage path, in the centrifuge tests are yet different from those in the field.

6.6.3 Laboratory Tests on Post-Liquefaction Behavior of Sand

Laboratory tests have studied the post-liquefaction stress-strain relationship of sand (Yasuda et al., 1991, 1992a and 1993; Yoshida et al., 1994). Yasuda et al. conducted a number of torsional shear tests under several conditions to study the post-liquefaction behaviour of sand. In these tests, a prescribed number of cyclic loading were applied first, then a monotonic undrained loading was applied. They showed that the stress strain curves were affected by the excess pore pressure ratio and by the severity of liquefaction. The shear modulus decreased to about 1/1000 due to liquefaction. However, after some amount of strain, the stiffness of the liquefied soil increased. The amount of shear strain after which the shear modulus starts to increase depends on several conditions, including the excess pore pressure ratio, the initial relative density of the sand and the magnitude, as well as the duration of the earthquake shaking.

6.7 ANALYTICAL MODELING OF LIQUEFACTION-INDUCED GROUND DISPLACEMENT

There is presently no agreement among researchers on how to model the mechanical response of liquefied media. Depending on the assumed mechanism by which the ground displacement is generated, a variety of analytical models have been developed. From an analytical point of view, mechanisms causing liquefaction-induced large ground displacement can be classified into three categories:

1) The ground behaves as a liquid during liquefaction.

2) The upper layer of the ground, which is assumed to be non-liquefiable, slides on a thin weak layer formed at the upper boundary of the liquefied layer.

3) Liquefied layer behaves as a solid, but shear strength and stiffness of the soil are greatly reduced due to liquefaction.

6.7.1 Behavior As A Fluid

After conducting a series of shaking table tests, Hamada et al. (1993) simulated the liquefied model ground by a one-dimensional viscous-flow model. Figure 6.11 illustrates schematically the model test. The liquefaction of the model ground was caused by shaking the soil box in the direction perpendicular to the direction of the ground slope, so that the effect of the inertia force on the deformation of the soil can be eliminated. The ground velocity was calculated by an integration of the measured time history of the ground displacement. The one dimensional viscous flow shown in Figure 6.12 was used to calculate the extent of deformation.

Towahata et al. (1992) conducted three series of shaking table tests. Observing the results, they assumed that the liquefied soil behaves like a liquid, leading to the notion that the ground displacement is governed by the principle of minimum potential energy. This analysis is made in a static manner under the assumption that the seismic inertia

force is not important in the prediction of the permanent displacement, though it induces soil liquefaction. They assumed that the lateral displacement has a sinusoidal distribution in the vertical direction. In this model, the ground surface becomes flat after the ground movement if there is no overlying non-liquefied layer. They compared observed and calculated displacements for a number of actual cases to show the reliability of the model. In most cases, the calculated results are greater than the observed ones. Figure 6.13 shows a comparison between the calculated displacements and the observed displacements along the section line at Ohgata Site in Niigata City, shown in Figure 6.2.

The basic assumption embedded in the models simulating the liquefied soil as a fluid is that the liquefied soil has a zero residual strength. However, as previously described, the liquefied soil can sustain some strength which is called steady state strength. Another assumption is that the ground surface becomes flat after its deformation. This contradicts what happens in the field. Moreover, the fluid-like models are dependent upon parameters not well known for liquefied soils. Fundamental characteristics of soil, even during liquefaction, are different from those of liquid.

6.7.2 Sliding Soil Block Model

According to this model, the overlying non-liquefiable layer slides on a thin, weak layer, which is formed at the upper boundary of the liquefiable soil layer due to liquefaction. Dobry and Baziar (1992) assumed that inertia force exceeding the steady state shear strength causes lateral movement of the ground. The idea was initially proposed by Newmark et al. (1965), as shown in Figure 6.14.

Figure 6.15 shows the type of analytical model developed for the evaluation of lateral spreading. A rigid soil block slides down along the sloping failure surface due to the combined effect of gravity and inertia forces associated with the base acceleration, a(t). In this method, it is assumed that the soil immediately above the failure surface is loose and liquefiable, and only its post-liquefaction steady state strength is available to resist the sliding. They extended the method for 2-block and 3- block models.

The authors also conducted triaxial compression tests on loose silty sand containing 50% silt and 50% sand. The test results indicated that the soil behaviour was contractive in the specified range of consolidation pressure. On the basis of the results, they adopted the rigid perfectly plastic model to explain the stress strain behaviour of the soil in large strains.

In this model, the magnitude of lateral spreading is computed by double integration from the difference between the earthquake and the yield accelerations. The yield acceleration, associated with the steady state strength of the soil, can be calculated simply from equilibrium mechanics equations. They evaluated the model by case studies in some sites of the U.S. where the ground was supposed to be silty sand, and compared the calculated displacements with the Liquefaction Severity Index (LSI) criteria defined by Youd and Perkines (1987).

The following comments pertain to the use of the sliding soil block model for evaluating liquefaction-induced lateral spreads:

1) According to this method, the ground movement suddenly stops when the ground acceleration ceases. This contradicts the observed phenomenon of delayed response, which suggests that the ground displacement and stress redistribution in the soil may continue even after the earthquake shaking is terminated.

2) The sliding soil block model can explain the magnitude of displacement at the ground surface. However, it is not able to explain the ground deformation pattern along the vertical direction within the liquefied layer. This is due to the fact that the model ignores the accumulated deformations in the mass of the liquefied layer and only concentrates on the boundary between the liquefied soil and the overlying non-liquefied layer. The damage pattern of the foundation piles, shown in Figure 6.6, suggested that the ground displacement was not caused simply by the sliding of the overlying non-liquefied layer over the liquefied soil, but by deformation throughout the mass of the liquefied soil.

3) The assumptions on which the model is based make it independent of the thickness of the liquefied layer. This clearly ignores facts realized through the empirical

correlations based on the past case histories of lateral spread (Bartlett et al., 1992; Hamada et al., 1986), and also ignores the important conclusion obtained from the shaking table tests (Hamada et al., 1990; Yasuda et al., 1992; Sasaki et al., 1991; Miyajima et al., 1991).

4) This model offers no suggestion for evaluating the earthquake-induced pore water pressure in the ground.

5) It cannot explain movements in directions other than the direction of the inertia force.

6.7.3 Behavior As A Solid

According to this mechanism, liquefied soil is assumed to behave as a solid, but shear strength and shear stiffness of the soil dramatically decrease due to liquefaction. This mechanism has been more popular among researchers than the other two previously described mechanisms.

Several analytical models have been developed based on the above mechanism. Yoshida (1989) developed a finite element model based on a large deformation theory, assuming that effective stress ratios of liquefiable elements decrease proportionally according to the development of liquefaction. The hyperbolic model was used, and shear modulus at small strain and shear strength were defined as functions of effective stress. According to Hamada et al. (1994), this method requires huge computing time, considering the change of both material property and geometry during the iterative calculation.

Finn et al. (1991) assumed that shear strength decreases with the progress of liquefaction. One of the predominant factors of ground movement, shear strength, can be controlled directly in this model.

Yasuda et al. (1992-a) proposed a simplified procedure based on linear static total stress finite element analysis. They assumed that the liquefaction-induced ground movement occurs under an undrained condition. Hence, they used a Poisson's ratio close to 0.5 for the liquefied layer in the total undrained analysis. Moreover, they reduced Young's

modulus to simulate the effect of liquefaction. Two static switch on gravity analyses were conducted: (1) the analysis using the original material properties and (2) the one using the material properties during liquefaction. The difference between the two analyses gives the ground displacement due to the liquefaction. The authors also analyzed the ground displacement in the vicinity of the Niigata Railway Station, and concluded that the result of the analysis when Young modulus was reduced to 1/1000 of the initial value is the closest one to the observed displacements.

In an attempt to unify the solid-like and liquid-like approaches into a single model, Aydan (1994) developed a visco-elastic model in which the mechanical response of the liquefied soil is associated with strain for a solid-like behaviour and strain rate for a fluid-like behaviour of the liquefied material. Noting that large deformations of the liquefied ground take place due to purely gravitational loading long after the main shock wave passed away, he developed closed form solutions and a finite element model for the dynamic shear response of a one-dimensional infinitely long visco-elastic layer under gravitational loading. The constitutive law used in this model is given as:

$$\tau = G\gamma + \eta\dot{\gamma} \qquad [6.7]$$

where,

τ = shear stress,

G = elastic shear modulus,

γ = shear strain,

η = viscous shear modulus, and

$\dot{\gamma}$ = shear strain rate.

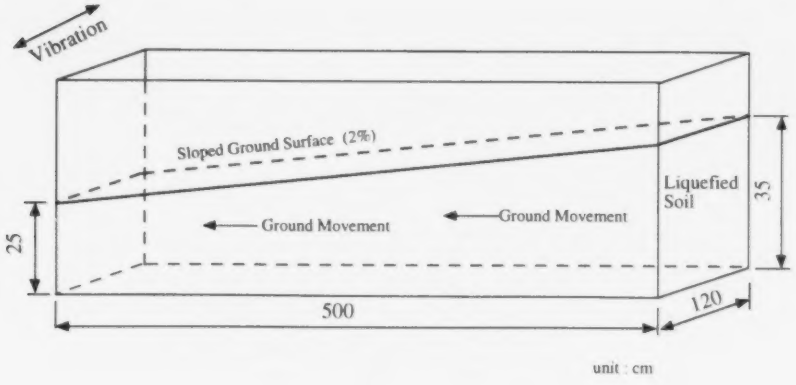

Fig. 6.11 Experiment on Liquefaction -Induced Ground Displacement [modified after Hamada et al., 1986].

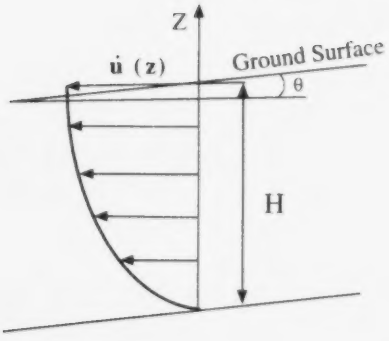

Fig. 6.12 Viscous Flow of Ground Displacement.

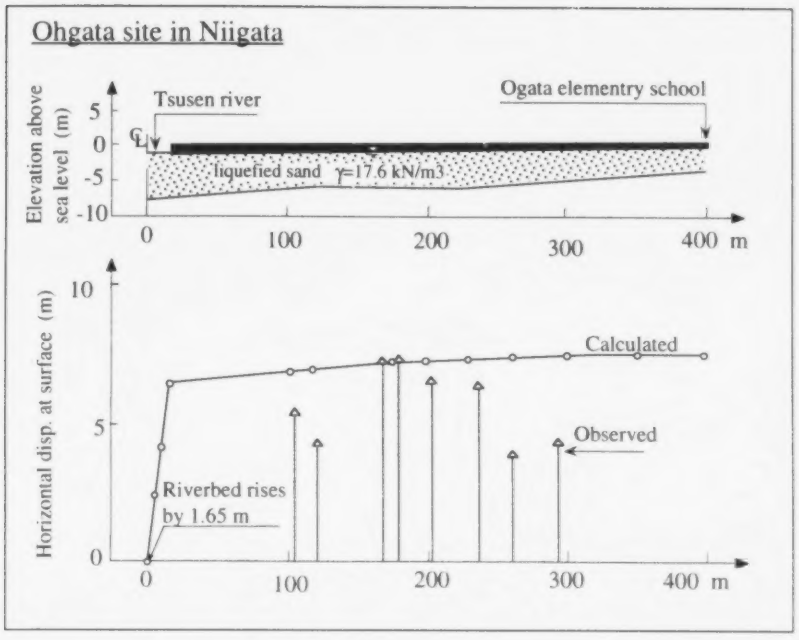

Fig. 6.13 Case History Study in Ohgata Area [modified after Towhata et al., 1992].

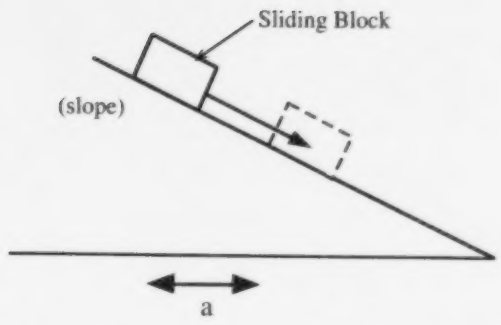

Fig. 6.14 Newmark Sliding Block Model.

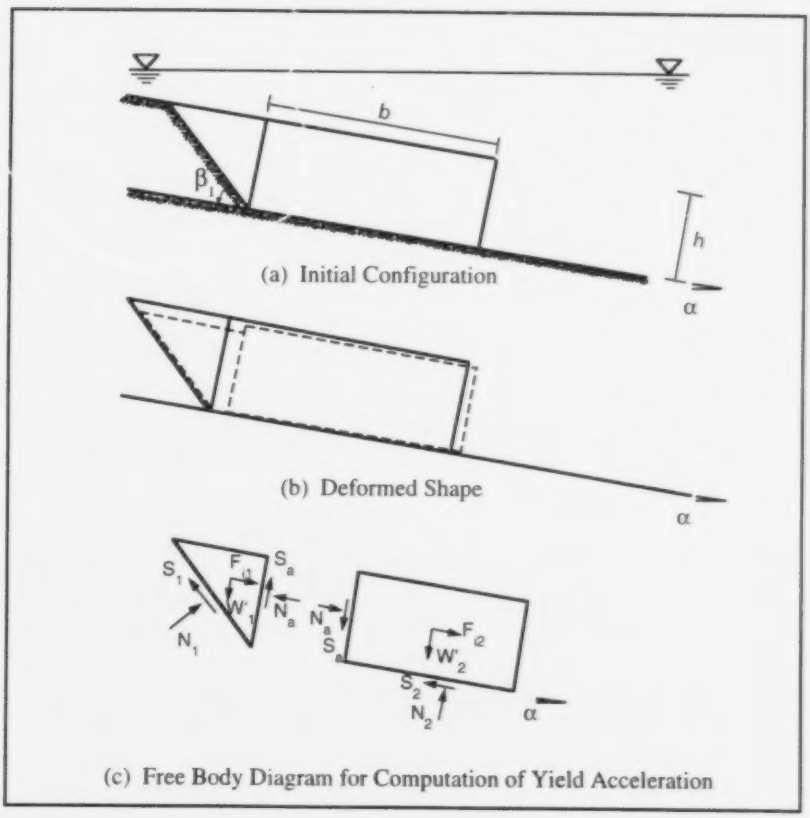

Fig. 6.15 Two-Block Soil Model for Analysis of Spreading with Free Face and Graben Proposed by Dobry and Baziar (1992).

6.8 DISCUSSION

6.8.1 Comparison between Behaviour of Liquefied Soil in Test Models and in the Field

From the literature review, performances of liquefied sand deposits both in the field and in the laboratory were introduced and discussed. Similar behaviour, irrespective of whether it is in the field or in the lab, was observed. However, one important difference between them seems to exist: *soil behaviour after stopping of shaking*. In all model tests, deformations stopped almost when the shaking was terminated. However, many field cases in which large deformations occurred after the earthquake shaking have been reported. This fact was previously discussed in the context of the delayed response phenomenon and a number of cases, in which this phenomenon had been observed, were noted.

The above difference in soil behaviour can be attributed reasonably to the difference between the sizes of small-scale model tests and the real field situation. The time required to bring about the deformation in the field is much longer than the similar time for small-scale model tests. In the model test, the liquefied soil deforms quickly; as the shaking stops, the soil has already deformed sufficiently and stopped and reached a new geometry which satisfies equilibrium conditions. In other words, the model is small enough to be able to fully liquefy and deform within the short period of time. On the other hand, it takes longer time for a mass of soil in the field to deform. Therefore, the larger the soil mass, the longer the time required to liquefy and to deform. In addition to the size factor, drainage conditions, fines percent and boundary conditions influence the different behaviour of the soil in the model tests and the field.

The difference between the post-shaking behaviour of the liquefied soil in the small-scale test and in the field can be clarified in the context of stress redistribution. In the small-scale test, almost all elements of the soil will liquefy at the period of the shaking. The

processes of liquefaction, stress redistribution and pore water pressure redistribution take place in a short period, most likely shorter than the period of shaking. However, in nature, the above processes take real time and can continue long after the earthquake. The above processes during and after the earthquake are presented as a flow chart in Figure 6.16.

Ishihara and Takeuchi (1991) have suggested that the difference between the nature of shaking could be another reason for the different behaviour of the soil in the field and in the model tests. They mentioned that in most of the tests, a shaking with uniform amplitude is applied so that liquefaction can be achieved quickly during the early stage of shaking. Therefore, the strength of liquefied soil reduces to the undrained steady state strength at the early stage of shaking. However, the cycles of earthquake shaking are not uniform, and liquefaction in the field generally occurs at a later stage of the main shaking, and there is no time for the soil to undergo any more shaking when it is in steady state. Hence, most of the deformation in the field occurs after earthquake shaking.

6.8.2 Trigger Mechanism in Lateral Spreading

Deformation analysis of the seismically-induced liquefaction of soils is very complicated and involves the effect of both cyclic and gravity forces. Literature review of the case histories and the experimental studies of lateral spreading, especially shaking table tests in which the effect of shaking was eliminated by shaking the table tests in the direction perpendicular to the slope of the ground (Hamada et al., 1990 and Sasaki et al., 1991), suggest that large lateral spreads are essentially driven by gravity forces. The idea is reinforced by delayed response phenomena as described in Chapter 1. Therefore a deformation analysis, in which the gravity force is considered, is essential.

On the basis of a number of case studies and experimental works of lateral spreading, Ishihara and Takeuchi (1991) described a clear picture of liquefaction-induced lateral spreading. They concluded that this type of permanent deformation develops during a period of small-intensity to non-shaking following the main shock, due to the static driving shear stress which exceeds the undrained steady state strength of the liquefied

soil; hence, if the steady state strength is small enough, large deformations can develop in any ground conditions even if the driving shear stress is very small, which is the case in gently sloping grounds.

From the above information and discussions, one can reasonably conclude that large spreading of liquefied ground is induced by static gravity forces. The earthquake motion increases pore water pressures, and if the induced pore water pressures are high enough, the soil will be brought on or close to the state of collapse. The earthquake also degrades the global stiffness of the soil mass. In other words, the gravity force is the immediate cause while the shaking force is the indirect cause of large deformations.

If the soil has a high enough shear stress, it will soften on the collapse surface and induce unbalanced loads, which by turn may cause liquefaction of the neighbouring elements. This leads to the process of stress redistribution until the soil reaches the steady state strength and equilibrium conditions are satisfied. If the soil has a low shear stress, it may go to the state of shear stress reversal during the shaking time, and may reach the state of zero effective stress (p') where the soil has almost a zero shear strength. Therefore, soils with low driving shear stresses in gently slopping grounds may also liquefy and largely deform because of having a very low or even zero steady state strength. In this process, the relatively small stiffness of the soil, degraded by cyclic loading and an increase in excess pore pressures, facilitates large deformation of the soil. Figure 6.17 schematically illustrates the above mechanism.

6.9 NUMERICAL MODEL FOR LATERAL SPREADING

The elasto-plastic finite element model presented in Chapter 3 using a constant undrained steady state strength ratio (S_u/p') and a reduced stiffness proportional to excess pore pressures, enables one to evaluate lateral spreading of the liquefied ground. The assumption of S_u/p' = constant, which is also S_u/q = constant, can properly define the undrained shear strength of liquefiable soils with both high and low driving shear stresses, as indicated in Figure 6.17. The model can introduce very low undrained shear

strengths for soils with low driving shear stresses. This agrees with what happens in the field.

The previously described case histories and the laboratory model tests suggested that the ground deformation does not occur at the boundary between the liquefied and non-liquefied layer; rather, it occurs in the whole mass and involves the entire depth of the liquefiable soil. Such a deformation pattern can be produced from a post-earthquake deformation analysis using a constant steady state strength ratio.

Gu et al. (1993b) employed the method of post-earthquake deformation analysis to evaluate the liquefaction event in the Wildlife site in California during the 1987 earthquake. They obtained comparable deformations with the deformations recorded in the site shortly after the earthquake. The deformation in the Wildlife site was not very large (maximum of about 20 cm). For lateral spreading cases where the deformations are as large as several meters, the finite element model should be extended for large deformation and large strain analyses to obtain more precise deformations.

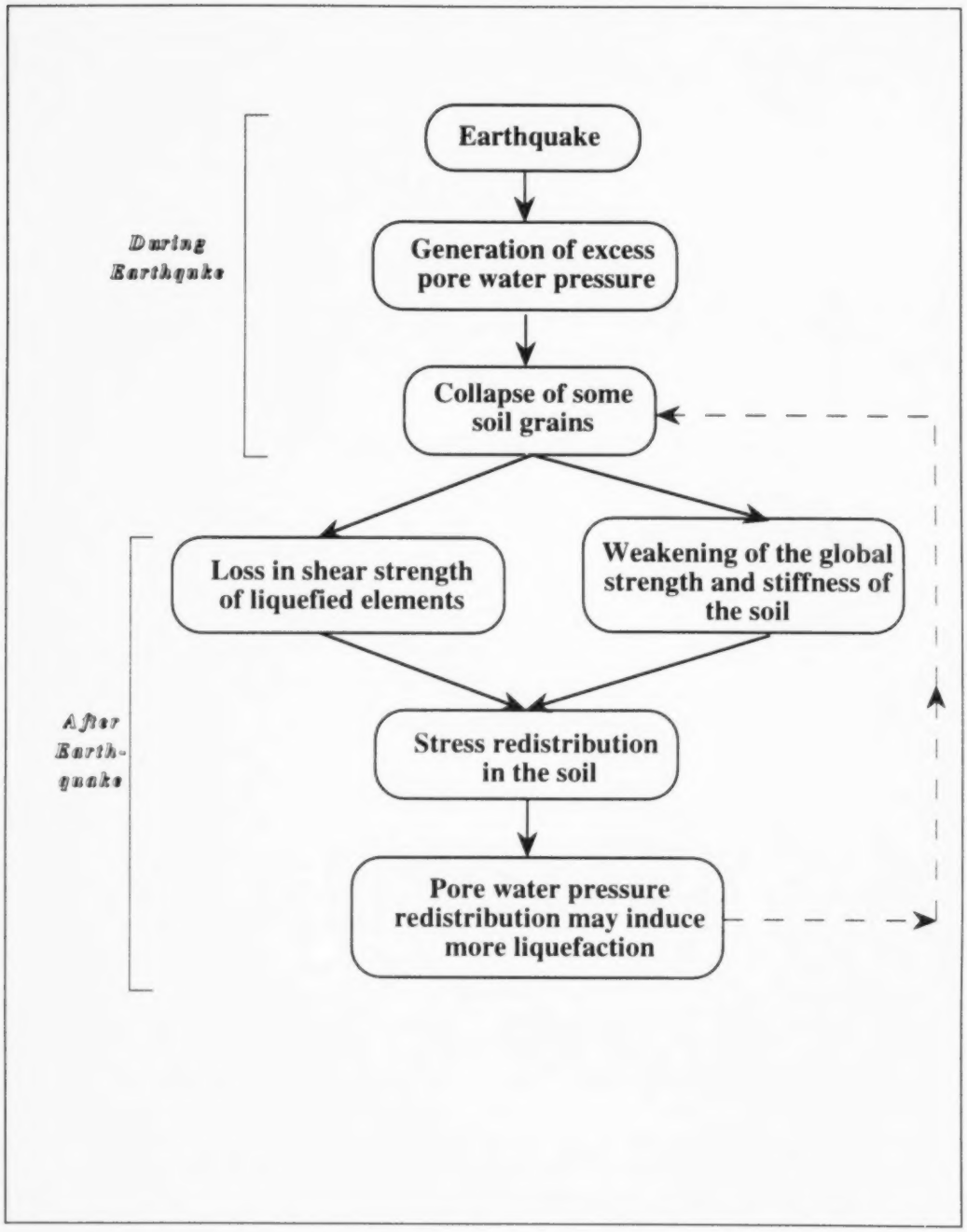
Earthquake
During Earthquake
Generation of excess pore water pressure
Collapse of some soil grains
Loss in shear strength of liquefied elements
Weakening of the global strength and stiffness of the soil
After Earth-quake
Stress redistribution in the soil
Pore water pressure redistribution may induce more liquefaction

Fig. 6.16 Simpified Process during and after Earthquake.

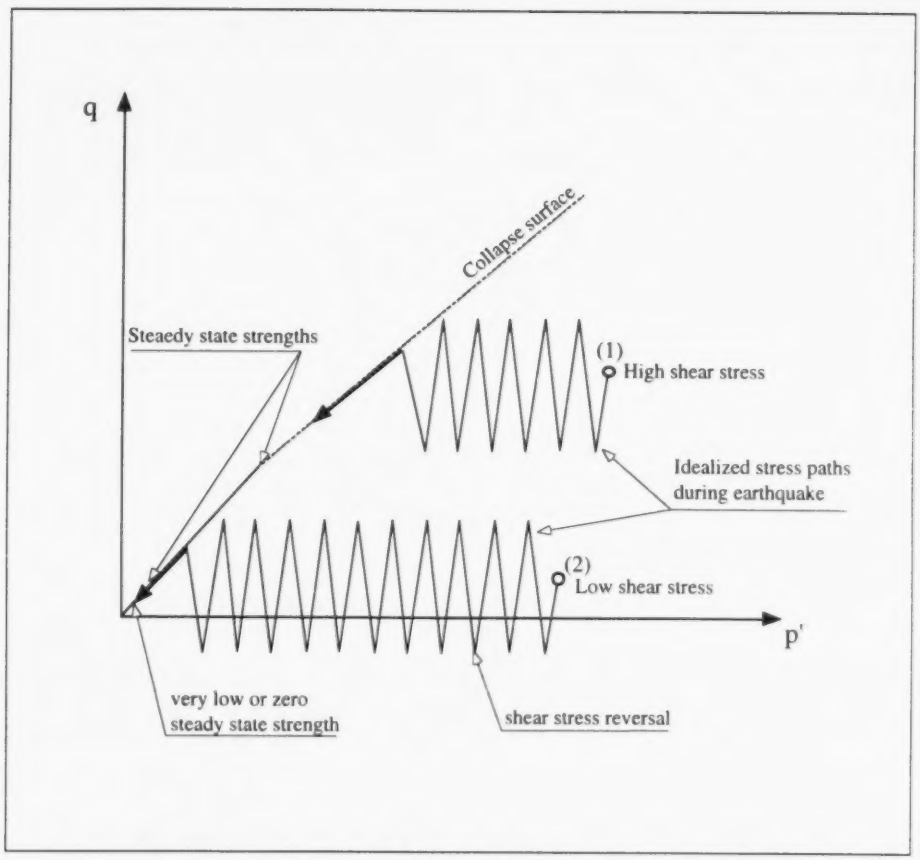

Fig. 6.17 Mechanism of Earthquake-induced Liquefaction and Lateral Spreading.

6.10 MITIGATING METHODS OF LIQUEFACTION AND SPREADING

The deformation of liquefied grounds and its damaging effects on lifeline facilities and underground structures can be reduced by a variety of special techniques. Methods for the mitigation of liquefaction and its associated ground displacements can be classified into the following four categories:

1) Improvement of density by compaction, including sand compaction piles, vibrofloatation and dynamic consolidation.

2) Dissipation of excess pore water pressure by drains, including gravel piles or walls, drainage pipes and so on.

3) Solidification, including deep grouting and mixing methods and lime piles.

4) Restraint of ground displacement by using sheet piles, retaining walls and diaphragm walls.

Each of the above methods has its own advantages and disadvantages. Compaction methods are more cost effective and used widely in the United States (Darragh et al., 1992; Mitchell, 1995) and Japan (Fujii et al., 1992). However, the method induces noise and can harm the surrounding area and structures. Therefore, it is not suitable for some urban areas. From an environmental point of view, drainage is more appropriate. Deep soil mixing methods require removal and replacement of utilities prior to stabilization. Grouting would not require utility removal, but could damage the utilities.

Design of the above mitigating methods, especially the first three methods, are mostly based on past field experience and, recently, small scale model tests. Some analyses have been performed to evaluate the performance of the previously employed mitigating means. Finn et al. (1994) performed the analysis of the pile reinforced sections of Sardis Dam and computed the deformation of and the force acting on the piles.

Experimental studies, mostly using shaking table tests, have been performed to evaluate the performance and effectiveness of different mitigating methods of liquefaction ground displacements. Miyajima et al. (1992) conducted a series of shaking table tests and experimentally investigated the application of a gravel drain system for buried pipelines as a countermeasure against soil liquefaction and lateral spreading. They realized that the gravel drain system, including gravel walls and/or gravel pipes, was effective in reducing the maximum excess pore water pressure and duration of liquefaction.

Yasuda et al. (1992) conducted a number of shaking table tests to study the effectiveness of different mitigating methods against the permanent ground displacements due to liquefaction. They classified large ground displacements due to liquefaction into two groups: (1) permanent ground displacement along a gentle slope and (2) lateral flow near banks and seashores. For the first case, they studied countermeasures by strengthening the ground with compacted sand piles, steel piles, compaction of the ground along a narrow band, concrete or steel continuous walls, and steel piles with drain holes. The most effective method was found to be the continuous wall method. For the second case, they studied the effectiveness of improving the ground behind the quay walls and strengthening quay walls and retaining walls to prevent damage.

Ito et al. (1994) conducted shaking table tests to evaluate the liquefaction resistance of soil treated with Quick Lime Consolidated Briquettes (QCB). They suggested that QCBs used in the form of driven piles adsorb water and their swelling will compress the voids in the soil and thus increase its density. The authors compared the results of shaking table tests on non-treated soil with those of treated with QCBs, and concluded that QCBs are efficient to reduce the liquefaction potential.

6.11 SUMMARY AND CONCLUSION

This Chapter presented a thorough literature review of lateral spreading of the ground due to earthquakes. The literature review provided a number of case histories on lateral spreading, where the ground moved several meters, and its damaging effects on in-ground structures. Experimental works on lateral spreading, including shaking table tests, centrifuge experiments and torsional shear tests, were reviewed. On the basis of the data from many of spreading cases, a number of empirical correlations to predict lateral spreads have been developed. These correlations were introduced and compared. The developed analytical models to evaluate liquefaction-induced ground displacements have been summarized and their physical concepts probed.

Based on the information provided through the literature, it can be said that lateral spreading is driven by the shearing component of gravity. Earthquake shaking has an indirect effect on the spreading. The shaking increases pore water pressures, bringing the soil on or close to the state of collapse, and degrades the global stiffness of the soil mass. The result will be failure and large deformation of the liquefied soils.

The previously described case histories and the laboratory model tests suggest that the ground displacement does not occur at the boundary between the liquefied and non-liquefied layer; rather, it occurs in the whole mass involving the entire depth of the liquefiable soil. The exact distribution of strains at depth depends on a number of factors, including boundary conditions and the contrast in relative density and permeability of the liquefied soil and the overlying as well as underlying non-liquefiable soils.

Finally, the elasto plastic collapse model, using a constant steady state strength ratio and a reduced stiffness, was suggested for evaluating lateral spreads. An assumption that the spreading occurs under fully undrained conditions is embeded in the model. However, spreading may occur under partially drained conditions (depending on the permeability of

the soil and boundary conditions). Therefore, there is a need to include drainage, both during and after spreading, in the model.

At the end, mitigating methods of liquefaction-induced large ground displacements were reviewed and the current practice was introduced.

Chapter 7

CONCLUSIONS AND RECOMMENDATIONS

7.1 CONCLUSIONS

Earthquake-induced liquefaction is a complicated process involving seismic loading, excess pore water pressure generation, strain softening, stress redistribution and reconsolidation both during and after earthquake. During the collapse of elements liquefied directly by the earthquake, a major part of the load previously carried by these elements will be transferred to the neighboring elements, causing further liquefaction and yielding. This process may result in progressive deformation continuing until the whole body of the soil structure comes to a new equilibrium. If that part of the soil which is liquefied directly by the earthquake is sufficiently large, stress redistribution may cause large deformations or complete failure of the structure. Stress redistribution followed by progressive deformation is not an instantaneous phenomenon, rather it is a process in which time is involved.

In earthquake-induced liquefaction, large deformations (or collapses) are controlled by the gravity force. The earthquake shaking increases pore water pressures, bringing the soil on or close to the state of collapse, and degrades the global stiffness of the soil mass.

The result may be failure or large deformations of the structure under the gravity force. Therefore, a deformation analysis in which the driving force is gravity is required.

According to the observed phenomenon of delayed response, response of a saturated soil structure to an earthquake will continue long after that the earthquake shaking is stopped. Hence, the critical period for a soil structure subjected to earthquake shaking is not only the period of shaking, but also a long period following the earthquake. This time could vary from a few seconds to several hours depending on a variety of conditions, including the permeability and the boundary conditions of the structure.

The observation of the delayed response phenomenon is not limited to earth dams. A similar response has been observed in earthquake-induced liquefaction of gently sloping grounds where the gradient of the ground surface does not exceed 10%. Therefore, a post-earthquake deformation analysis may be essential in liquefaction stability evaluations of soil structures.

A summary of the elasto-plastic collapse model for post-earthquake deformation analyses of soil structures developed by Gu (1992) was presented. Large deformations (or failure) are assumed to be triggered by gravity in this model. The model, which numerically evaluates post-earthquake-deformations, is based on the critical state boundary surface theory and the concepts of steady state strength and collapse surface. The post-peak strain softening behaviour of liquefiable soils is simulated in the model by the hyperbolic strain softening model. The model is useful in explaining the delayed response, although it is not intrinsically time-dependent.

The post-earthquake deformation analysis of the Upper San Fernando Dam, which suffered *large deformations* as a result of the 1971 San Fernando Earthquake, was carried out. The maximum deformation at the surface of the dam was 220 cm. The computed results are in reasonable agreement with the deformations measured shortly after the earthquake. The analysis appears to provide overall a reasonable evaluation of the liquefaction-induced large deformations of the dam. This increased the confidence in the

numerical model and indicated that the model is able to evaluate the earthquake-induced deformations which are contained but large.

The collapse surface plasticity model was essentially developed for analyses of earthquake-induced liquefaction in soil structures. Fundamentals of the soil behaviour during static liquefaction and during earthquake-induced liquefaction are the same. However, there are differences in stress paths by which the soil is brought to the state of collapse. The plasticity model was adapted for analyses of static liquefaction failures induced by undrained monotonic loading, similar to the effect of rapid construction of an embankment over a loose, saturated sand deposit.

The finite element model was also extended for the case where the undrained steady state strength of the liquefiable soil is not a single value for the entire zone of the liquefiable soil; rather, it is a function of mean normal effective stress. This is the case for very loose granular materials, which are very prone to liquefaction. In the extended version of the model, the strength parameter of the liquefied soil is introduced to the analysis in the form of undrained steady state strength ratio (S_u/p'). Introducing S_u/p' ratio, instead of a single value of steady state strength, to the analysis prevents early instability in the process of calculation. This allows calculation of liquefaction-induced deformations and pore water pressures without facing divergence during computational iterations. The extended finite element model was successfully evaluated by numerical simulation of an undrained triaxial compression test.

In addition to earthquake-induced liquefaction, static liquefaction has also been a major cause of damage to soil structures consisting of loose to medium dense granular materials. The third phase of the Canadian Liquefaction Experiment, CANLEX, included initiating a controlled full-scale static liquefaction event in the field. As a complementary part of numerical studies and design of the event, a series of centrifuge modeling tests were carried out at C-CORE Centrifuge Center. Numerical modeling and liquefaction analyses of three of the centrifuge experiments and the field event were carried out.

The first centrifuge experiment indicated no failure of the slope while the second experiment resulted in liquefaction flow failure of the sand. The results of the centrifuge experiments were compared with the numerical model and reasonable agreements between the calculated and observed pore pressures and deformations were obtained. The third centrifuge experiment was carried out to closely model the anticipated field event. The application of a surcharge resulted in failure of the soil, which was also captured by the numerical model. The analyses indicated that the finite element model is able to capture the static liquefaction-induced failure mechanics and pore pressure response of the sand.

Construction of the clay embankment in the field event was also numerically modeled. The results of the partially drained analysis helped to construct the embankment in the shortest feasible time. The observed pore pressures during construction of the clay embankment were favorably comparable with the computed values, which was recommended for a safe construction of the embankment.

The liquefaction analyses of the event predicted that the event will fail after rapid filling of the contained tailings if the undrained steady state strength of the tailings does not exceed 0.1. The event did not fail and it moved very little during the loading. A number of influential factors which may have contributed to the stability of the event, including the stress-path dependency of the undrained behaviour of the tailings sand, have been counted. These factors have been discussed and a number of conclusions have been made.

Lateral spreading of gently sloping grounds was thoroughly reviewed from the literature. All aspects of the subject, including a number of case histories, damage effects of the ground displacement on in-ground structures, the experimental work and the theoretical studies on the lateral spreading were discussed.

Based on the information provided through the literature, it was suggested that large deformations in lateral spreading are induced by the gravity force. This notion is reinforced by the delayed response phenomenon. The earthquake shaking has an indirect

effect on the triggering. The shaking increases pore water pressures, bringing the soil on or close to the state of collapse, and degrades the global stiffness of the soil mass, resulting in large deformations of the ground. The elasto plastic collapse model, using a constant steady state strength ratio and a reduced stiffness was suggested for evaluating lateral spreads. Since lateral spreading may occur under partially drained conditions, consolidation, both during and after spreading, should be included in the model.

7.2 RECOMMENDATIONS

The ideal deformation analysis for liquefaction failure should be a large strain, large displacement and discontinuity problem. If the purpose of analysis is to capture the deformation that may cause a liquefaction failure, the analysis can be done by the small strain and small deformation finite element formulation. This is the case for the evaluation of safety of structures in which safety is the main concern rather than the post-failure configuration. The current finite element model can properly carry out such evaluations. However, if the amount of deformation is required with high degrees of precision, the model should be reformulated based on the large strain and large deformation finite element formulations.

In order to provide a comprehensive numerical study on earthquake-induced liquefaction, a time-dependent model should be developed. The model should be able to simulate effects of earthquake shaking, development of pore water pressures, yielding of very first elements of the soil, stress redistribution and consolidation of the soil both during and after the shaking. Of course, such a model is complicated, and it can be more complicated if the simultaneous effects of the above processes are to be included in the modeling.

Recent laboratory tests indicated that the undrained behaviour of loose granular soils is highly stress-path dependent. The triaxial tests conducted by Vaid et al. (1995) showed that the potential for liquefaction of water pluviated Syncrude sand at a given void ratio is dependent on the stress path during undrained shear as well as the initial consolidation stress. The test results showed that for a given initial state, the sand on an undrained

loading is dilative in triaxial compression but contractive in triaxial extension. Under initial static shear, Syncrude sand showed to be contractive in both compression and extension modes. The more the initial static shear, the more contractive is the behaviour of sand in the compression mode.

The finite element model can be modified to include the above behavioural characteristics of liquefiable soils. This can be done by defining the stress-strain relationship of each element according to the stress path of the element during the undrained loading. The model can be modified so that it automatically incorporates such a feature.

More laboratory tests on granular soils are necessary to study their behaviour under different stress paths with different initial shear stress. Since the method of sample preparation affects undrained behaviour of the sample, undisturbed frozen samples are preferred.

Laboratory tests to study the post-liquefaction stress-strain relationship of sand showed that the shear modulus, G, of the saturated sand decreases according to increases in pore water pressure ratio, $\Delta u/p'$. In order to incorporate this shear modulus degradation, the modulus can be defined as a function of excess pore water pressure ratio in the finite element model.

Numerical modeling and analysis of lateral spreading of gently sloping grounds is the most complicated liquefaction problem. Evaluation of detailed input parameteres is certainly the most important task in the analysis. Moreover, the empirical correlations showed that the extent of deformation in lateral spreading depends on so many factors, including the earthquake magnitude, the horizontal distance from the seismic energy source, the slope of the ground, the thickness of saturated granular layer, and so on. It is difficult to develop a numerical model based on all these factors.

However, developing a numerical model based on the *main* factors which affect lateral spreading is not unreachable, although development and application of such a model require a considerable amount of time and cost. Hence, it seems that the simplified

numerical models, developed based on the results of laboratory tests and centrifuge modeling, are more economic and they can be used for most practical purposes.

In geotechnical engineering analyses, a major concern is to provide representative material parameters as input data for modeling and analysis. Sophisticated numerical analyses can lead to wrong, and even misleading, results when non-representative parameters are used. Field response provided through instrumentational monitoring remains an excellent tool to back calculate the most representative parameters. The field response can also be used for calibration and modification of numerical models.

BIBLIOGRAPHY

Alencar, J., Morgenstern, N.R. and Chan, D.H. (1994), "Analysis of Foundation Deformation Beneath the Syncrude Tailings Dyke," Canadian Geotechnical Journal, Vol. 31, pp 868-884.

Arulanandan, K., Yogachandran, C., Muraleetharan, K. K., Kutter, B. L., and Chang, G. S. (1988) "Seismically Induced Flow Slide on Centrifuge," Journal of Geotechnical Engineering Division, ASCE, Vol. 114, No. 12, pp 1442-1449.

Atkinson, J. (1993), "An Introduction to the Mechanics of Soils and Foundations, McGraw - Hill International (UK) Limited.

Aydan, O. (1994), "The Dynamic Shear Response of an Infinitely Long Visco-Elastic Layer under Gravitational Loading," Soil Dynamics and Earthquake Engineering, Vol. 13, pp 181-186.

Bartlett, S. F. and Youd, T. L. (1992), "Empirical Prediction of Lateral Spread Displacement," Proceedings from the Fourth Japan-U. S. Workshop on Earthquake Resistant Design of Lifeline Facilities and Countermeasures for Soil Liquefaction, Vol. 1, pp 351-365.

Baziar, M. H. and Dobry, R. (1991), "Liquefaction Ground Deformation Predicted from Laboratory Tests," Proceedings: Second International Conference on Recent Advances in Geotechnical Earthquake Engineering and Soil Dynamics, Vol. 1, Paper No. 3.28, pp 451-458.

Been, K., Jefferies, M. G. and Hachey, J. (1991), "The Critical State of Sands," Geotechnique, Vol. 41, No. 3, pp 365-381.

Been, K., Jefferies, M. G. and Hachey, J. (1992), "Discussion: The Critical State of Sands," Geotechnique, Vol. 42, No. 4, pp 665-663.

Byrne, P.M., Robertson, P.K., Plewes, H.D., List, B. and Tan, S. (1995), "Liquefaction Event Planning," Proceedings of the 48th Canadian Geotechnical Conference, Vol. 1, pp 341 - 352.

Casagrande, A. (1936), "Characteristics of Cohesionless Soils Affecting the Stability of Slopes and Earth Fills," Journal of the Boston Society of Civil Engineers, reprinted in Contributions to Soil Mechanics, 1925 to 1940, Boston Society for Civil Engineers, 1940, pp 257-276.

Casagrande, A. (1971), "On Liquefaction Phenomenon," Geotechnique, Vol. 21, pp 197-202.

Castro, G. (1975), "Liquefaction and Cyclic Mobility of Saturated Sands," ASCE, Journal of Geotechnical Engineering, Vol. 101, No. 6, pp 551-569.

Castro, G. (1987), "On the Behavior of Soils During Earthquake - Liquefaction," Soil Dynamics and Liquefaction, pp 169-204.

Castro, G., Seed, R. B., and Keller, T. O. (1992), "Steady State Strength of Lower San Fernando Slide," Journal of the Geotechnical Engineering, ASCE, Vol. 118, No. 3, pp 406-427.

Chan, D. H. (1986), "Finite Element Analysis of Strain Softening Materials," Ph. D. Thesis, University of Alberta.

Chan, D. H. and Morgenstern, N. R. (1989), "Bearing Capacity of Strain Softening Soil," Victor deMello Volume, Edited by J. E. Moreira, Rie de Janeiro, pp 59-68.

Cunning, J.C. (1994), "Shear Wave Velocity Measurement of Cohesionless Soils for Evaluation of In Situ State, M. Sc. Thesis, Department of Civil Engineering, University of Alberta, Edmonton, Alberta.

Darragh, R. R., Taylore, H. T., Scawthorn, C., Seidel, D., and Ng, C. (1992), "Liquefaction Study, Sullivan March And Mission Creek, San Francisco, California," Proceedings from the Fourth Japan-U. S. Workshop on Earthquake Resistant Design of Lifeline Facilities and Countermeasures for Soil Liquefaction, Vol. 1, pp 205-221.

Davis, C. A. and Bardet, J. P. (1994), "Geotechnical observations at the Van Norman Complex after the 1994 Northridge Earthquake ," Proceedings from the fifth Japan-U. S. Workshop on Earthquake Resistant Design of Lifeline Facilities and Countermeasures for Soil Liquefaction, pp 63-77.

Dobry, R. and Baziar, M. H. (1992), "Modeling of Lateral Spreads in Silty Sands by Sliding Soil Blocks," Stability and Performance of Slopes and Embankments-II, A 25 Year Perspective," Vol. 1, ASCE, Geotechnical Special Publication, Berkeley, California, pp 625-652.

Doi, M. and Hamada, M. (1992), "A Summary of Case Studies on Liquefaction Induced Ground Displacements," Proceedings from the Fourth Japan-U. S. Workshop on Earthquake Resistant Design of Lifeline Facilities and Countermeasures for Soil Liquefaction, Vol. 1, pp 115-129.

Duncan, J. M. and Chang, C. Y. (1970), "Nonlinear Analysis of Stress and Strain in Soils, " Journal of the Soil Mechanics and Foundation Division, ASCE, Vol. 96, No. SM5, pp 1629-1653.

Eckersley, D. (1990), " Instrumented Laboratory Flow-Slides," Geotechnique, Vol. 40, No. 3. pp 489-502.

Elgamal, A-W. and Zeghal, M. (1992), "Analysis of Wildlife Site Liquefaction during the 1987 Superstition Hills Earthquake," Proceedings from the Fourth Japan-U.S. Workshop on Earthquake Resistant Design of Lifeline Facilities and Countermeasures for Soil Liquefaction, Vol. 1, pp 87-96.

Fear, C.E. and Robertson, P.K. (1995), "Estimating the Undrained Strength of Sand: A Theoretical Framework," Canadian Geotechnical Journal, Vol. 32 , pp 859-870.

Fiegel, G. and Kutter, B. L. (1994), "Liquefaction-induced Lateral Spreading of Mildly Sloping Ground," Journal of Geotechnical Engineering, ASCE, Vol. 120, No. 2, pp 2236- 2243.

Finn, W. D. L., Ledbetter, R, H., and Wu, G. (1994), "Liquefaction in Silty Soils, Design and Analysis," Ground Failure under Seismic Conditions, ASCE, Geotechnical Special Volume, Publication No. 44, pp 51-76.

Fujii, Y., Ohtomo, K., Arai, H., and Hasegawa, H. (1992)," The State of the Art in Mitigation of Liquefaction for Lifeline Facilities in Japan," Proceedings from the Fourth Japan-U. S. Workshop on Earthquake Resistant Design of Lifeline Facilities and Countermeasures for Soil Liquefaction, Vol. 2 pp 889-909.

Gu, W. H. (1992), "Liquefaction and Post-Earthquake Deformation Analysis," Ph.D. Thesis, University of Alberta.

Gu, W. H., Morgenstern, N. R., and Robertson, P. K. (1993-a), "Progressive Failure of the Lower San Fernando Dam," Journal of Geotechnical Engineering, ASCE, Vol. 119, No. 2, pp 333-348.

Gu, W. H., Morgenstern, N. R., and Robertson, P. K. (1993-b), "Post-Earthquake Deformation Analysis of Wildlife Site," Journal of Geotechnical Engineering, ASCE, Vol. 120, No. 2 , pp 274-285.

Gu, W. H., Morgenstern, N. R., and Robertson, P. K. (1994), "An Elasto-Plastic Model for Liquefaction Deformation Analysis," Performance of Ground and Soil Structures during Earthquakes, XIII ICSMFM, New Delhi, India : 219 - 226.

Hamada, M., O'Rourke, T. D. and Yoshida, N. (1994), "Liquefaction-induced Large Ground Displacements," Performance of Ground and Soil Structures during Earthquakes, 13th ICSMFE, New Delhi, JSSMFE, pp 93-108.

Henkel, D. J. (1960), "The Shear Strength of Saturated Remolded Clay," Proceedings of the ASCE Research Conference on Shear Strength of Cohesive Soil, Boulder, Colorado, pp 533-544.

Holzer, T. L., Youd, T. L. and Hanks, T. C. (1989), "Dynamics of Liquefaction during the 1987 Superstition Hills, California Earthquake," Science, Vol. 224, pp 56-59.

Ishihara, K. (1993), "Thirty-third Rankine Lecture: Liquefaction and Flow Failure during Earthquakes," Geotechnique, Vol. 43, No. 3, pp 349-415.

Ishihara, K., Haeri, S. M., Moinfar, A. A., Towhata, I., and Tsujino, S. (1992), "Geotechnical Aspects of the June 20, 1990 Manjil Earthquake in Iran," Soils and Foundations, Vol. 32, No. 3, pp 61-78.

Ishihara, K. and Takeuchi, M. (1991), "Flow Failure of Liquefied Sand in Large-Scale Shaking Tables," Proceedings: Second International Conference on Recent Advances in Geotechnical Earthquake Engineering and Soil Dynamics, St. Louis, Missouri, Paper No. SOA5, pp 1753-1766.

Ishihara, K., Verdugo, R., and Acacio, A. A. (1991), "Characteristics of Cyclic Behavior of Sand and Post-seismic Stability Analyses," Proceedings of the 9th Asian Regional Conference on Soil Mechanics and Foundation, Bangkok, Thailand, Vol. 2, pp 17-40.

Ishihara, K., Tatsuka, F. and Yasuda, S. (1975), "Undrained Deformation and Liquefaction of Sand under Cyclic Stress," Soil and Foundations, 15 (1), pp 29-44.

Isoyama, R. (1994), "Liquefaction-induced Ground Failures and Displacements along the Shiribeshi-toshibetsu River Caused by the 1993 Hokkaido-nansei-oki Earthquake," Proceedings from the Fifth Japan-U. S. Workshop on Earthquake

Resistant Design of Lifeline Facilities and Countermeasures for Soil Liquefaction, pp 1-26.

Ito, T., Mori, Yoshinobu, and Asada, A. (1994), "Evaluation of Resistance to Liquefaction Caused by Earthquakes in Sandy Soil Stabilized with Quick-Lime Consolidated Briquette Piles," Soils on Foundations, Vol. 34, pp 33-40.

Kulhaway, F. H. and Duncan, J. M. (1972), "Stresses and Movements in Oreville Dam," Journal of the Soil Mechanics and Foundation Division, ASCE, Vol. 98, No. SM7, pp 653-665.

Lee, K. L., Seed, H. B., Idriss, I. M., and Makdisi, F. I. (1975), "Properties of Soils in the San Fernando Hydraulic Fill Dams," Journal of the Geotechnical Engineering Division, ASCE, Vol. 101, No. GT8, pp 801-821.

Mc Robast, E. C. and Sladen, J. A. (1992), "Observations on Static and Cyclic Sand-Liquefaction Methodologies," Canadian Geotechnical Journal, Vol. 29, pp 650-665.

Miyajima, M., Kitaura, M., and Ando, K. (1991), "Experiments on Liquefaction-induced Large Ground Deformation, "Proceedings from the Third Japan-U. S. Workshop on Earthquake Resistant Design of Lifeline Facilities and Countermeasures for Soil Liquefaction, pp 269-278.

Morgenstern, N. R. and Price, V. E. (1965), "The Analysis of the Stability of General Slip Surface," Geotechnique, Vol. 15, No. 1, pp 79 - 93

Morgenstern, N. R. (1994), "Observations on the Collapse of Granular Materials," The Kersten Lecture, Proceedings: 42nd Annual Geotechnical Engineering Conference, Minneapolis, Minnesota.

O'Rourke, T. D., Roth, B. L., and Hamada, M. (1992), "Large Ground Deformations and their Effects on Lifeline Facilities: 1971 San Fernando Earthquake," Case Histories of Liquefaction and Lifeline Performance during Past Earthquakes, Vol. 2, United States Case Studies, Technical Report NCEER-92-0002, pp 3-1, 3-85.

O'Rourke, T. D. and Hamada, M. (1992), Case Histories of Liquefaction and Lifeline Performance during Past Earthquakes, Vol. 2, United States Case Studies, Technical Report NCEER-92-0002, National Center for Earthquake Engineering Research, Buffalo.

Phillips, R. and Byrne, P. M. (1993) "CANLEX, Phase 1, Activity 8e - Stage 1, Centrifuge Model Testing," Contract Report for CANLEX, C-CORE, Contract Number 93-C14.

Phillips, R. And Byrne, P. M., (1994) "CANLEX, Phase 2, Activity II-6D - Test 1, Centrifuge Testing," Contract Report for CANLEX, C-CORE, Contract Number 94-C18.

Plews (1994), "Feasibility Level Design for Field Event," Internal Report, CANLEX.

Poulos, S. J. (1981), "The Steady State of Deformation," Journal of Geotechnical Engineering, ASCE, Vol. 107, No.GT5, pp 553-562.

Poulos, S. J., Castro, G., and France, J. W. (1985), "Liquefaction Evaluation Procedure," Journal of Geotechnical Engineering, ASCE, Vol. 111, No. 6, pp 772-791.

Poulos, S. J., Robinsky, E. I., and Keller, T. O. (1985)," Liquefaction Resistance of Thickened Tailings," Journal of Geotechnical Engineering, ASCE, Vol. 111, pp 1380-1394.

Robertson, P. K. and Fear, C. E. (1995), "Liquefaction of Sands and its Evaluation," IS TOKYO 95, First International Conference on Earthquake Geotechnical Engineering, Keynote Lecture, in Press.

Robertson, P. K. (1994), "Suggested Terminology for Liquefaction," Proceedings of 47th Canadian Geotechnical Conference, pp 277-286.

Roscoe, K. H., Schofield, A. N. and Worth, C. P. (1958), "On the Yielding of Sands," Geotechnique, Vol. 8, pp 22-53.

Sasaki, Y., Tokida, K-I., Matsumoto, H., and Saya, S. (1991), "Experimental Study on Lateral Flow of the Ground due to Soil Liquefaction," Proceedings: Second International Conference on Recent Advances in Geotechnical Earthquake Engineering and Soil Dynamics, St. Louis, Missouri, pp 263-270.

Sasitharan, S., Robertson, P. K., Sego, D. C., and Morgenstern, N. R. (1993), "Collapse Behavior of Sand," Canadian Geotechnical Journal, Vol. 30, pp 569-577.

Sasitharan, S., Robertson, P. K., Sego, D. C., and Morgenstern, N. R. (1994), "State-Boundary Surface for Very Loose Sand And Its Practical Implications," Canadian Geotechnical Journal, Vol. 31, pp 321-334.

Seed, H. B. (1966), "A Method for Earthquake Resistant Design of Earth Dams," Journal of the Geotechnical Engineering Division, ASCE, Vol. 92, No. SM1, Proc. Paper 4616, pp 13-41.

Seed, H. B., Lee, K. L., Idriss, I. M., and Makdisi, F. I. (1975), " The Slides in the San Fernando Dams during the Earthquake of February 9, 1971, "Journal of the Geotechnical Engineering Division, ASCE, Vol. 101, No. GT7, pp 651-688.

Seed, H., B. (1979), Nineteenth Rankine Lecture: "Consideration in the Earthquake Resistance Design of Earth and Rockfill Dams", Geotechnique 29, pp 215-263.

Serf, N., Seed, H. B., Makdisi, F. I. and Chang, C. -Y. (1976), " Earthquake Induced Deformations of Earth Dams, " Report No. EERC. 74-6, University of California, Berkeley, California.

Sladen, J. A., D'Hollander, R. D., and Krahn, J. (1985-a), " The Liquefaction of Sands, A Collapse Surface Approach," Canadian Geotechnical Journal, Vol. 22, pp 564-578.

Sladen, J. A., D'Hollander, R, D., and Krahn, J. (1985-b), "Back Analysis of the Nerlerk Berm Liquefaction Slides," Canadian Geotechnical Journal, Vol. 22, pp 579-588.

Tinsley J. C. and Durpe, W. R. (1992), "Liquefaction Hazard Mapping, Depositional Faces, and Lateral Spreading Ground failure in the Montery Bay Area, Central

California, during the 10/17/89 Loma Prieta Earthquake," Proceedings from the Fourth Japan-U. S. Workshop on Earthquake Resistant Design of Lifeline Facilities And Countermeasures for Soil Liquefaction, Vol. 1, pp 71-85.

Tokimatsu, K., Suzuki, Y., and Tamura, S. (1994), "Preliminary Report on the Geotechnical Aspects of the Hokkadio-Nansei-Oki Earthquake of July 12, 1993," Performance of Ground and Soil Structures, Special Volume for 13th Int. Conf. on Soil Mechanics and Foundation Engineering, New Delhi, January 1994.

Vahdani, S., Pyke, R. and Siriprusunen, U. (1994), "Liquefaction of Calcareous Sands and Lateral Spreading Experienced in Guam Earthquake," Proceedings from the fifth Japan-U. S. Workshop on Earthquake Resistant Design of Lifeline Facilities and Countermeasures for Soil Liquefaction, pp 117-134.

Vaid, Y.P., Sivathayalan, S., Uthayakumar, M., and Eliadorani, A. (1995), "Liquefaction Potential of reconstituted Syncrude Sand," Proceedings of the 48th Canadian Geotechnical Conference, Vol. 1, pp 319 - 329.

Watkamtsu, K. and Yoshida, N. (1994), "Ground Deformations and their Effects on Structures in Midorigaoka District, Kushiro City, during the Kushiro-oki Earthquake of January 15, 1993," Proceedings from the fifth Japan-U. S. Workshop on Earthquake Resistant Design of Lifeline Facilities and Countermeasures for Soil Liquefaction, pp 41-62.

Whitman, R. V. (1970), "Hydraulic Fills to Support Loads," Journal of the Geotechnical Engineering Division, ASCE, Vol. 96, No. SM1, pp 23-47.

Yasuda, S., Nagase, H., and Kiku, H. (1991), "Shaking Table Tests on Permanent Ground Displacements Due to Liquefaction", Proceedings: Second International Conference on Recent Advances in Geotechnical Earthquake Engineering and Soil Dynamics, March 11-15, 1991, St. Louis, Missouri, Paper No. 2.19, pp 245-252.

Yasuda, S., Nagase, H., Kiku, H., and Uchida, Y. (1992-a), "The Mechanism and A Simplified Procedure for the Analysis of Permanent Ground Displacement due to Liquefaction," Soils And Foundations, Vol. 32, No. 1, pp 149-160.

Yasuda, S., Nagase, H., Kiku, H., and Uchida, Y. (1992-b), "Shaking Table Test on Countermeasures against Large Ground Displacement due to Liquefaction," "Proceedings from the Fourth Japan-U. S. Workshop on Earthquake Resistant Design of Lifeline Facilities and Countermeasures for Soil Liquefaction, Vol. 1, pp 367-380.

Yasuda, S., Kiku, H., Masuda, T., and Itufuji, S. (1993), "Torsional Shear Tests on Post Liquefaction Behavior of sand," Preprint, Japan-U.S. Seminar on Dynamic Behavior and Failure of Ground, Napa Valley, California.

Yasuhara, K. (1994), "Post-cyclic Degradation and Recovery in Undrained Strength of The Clays," Performance of Ground and Soil Structures during Earthquakes, 13th ICSMFE, New Delhi, JSSMFE, pp 93-108.

Yoshida, N. Yasuda S., Kiku, M., Musuda, T., and Finn, W. D. L. (1994), Behavior of Sand after Liquefaction," Proceedings from the fifth Japan-U. S. Workshop on Earthquake Resistant Design of Lifeline Facilities and Countermeasures for Soil Liquefaction, pp 181-198.

Youd, T. L. and Holzer, T. L. (1994), "Piezometer Performance at Wildlife Liquefaction Site," Journal of Geotechnical Engineering, ASCE, Vol. 120, No. 6, pp 975-995.

Youd, L. T. and Perkines, M. D. (1987), "Mapping of Liquefaction Severity Index," Journal of Geotechnical Engineering, ASCE, Vol. 113, No. 11, pp 1374-1392.

Zeng, X. and Arulanandan, K. (1996), "Modeling Lateral Sliding of Slope due to Liquefaction of Sand Layer," Journal of Geotechnical Engineering, ASCE, Vol. 121, No. 11, pp 814-816.